

Linköping Studies in Science and Technology. Dissertations.  
No. 1990

# Flight Test System Identification

Roger Larsson



**li.u** LINKÖPING  
UNIVERSITY

# Flight Test System Identification

**Roger Larsson**

**Cover illustration:** The JAS 39 Gripen test aircraft no. 2. Foto Saab.

Linköping studies in science and technology. Dissertations.  
No. 1990

**Flight Test System Identification**

Roger Larsson

*roger.larsson@liu.se*  
*www.control.isy.liu.se*  
*Division of Automatic Control*  
*Department of Electrical Engineering*  
*Linköping University*  
*SE-581 83 Linköping*  
*Sweden*

ISBN 978-91-7685-070-1      ISSN 0345-7524

Copyright © 2019 Roger Larsson

Printed by LiU-Tryck, Linköping, Sweden 2019

*To my family!*



## Abstract

With the demand for more advanced fighter aircraft, relying on unstable flight mechanical characteristics to gain flight performance, more focus has been put on model-based system engineering to help with the design work. The flight control system design is one important part that relies on this modeling. Therefore, it has become more important to develop flight mechanical models that are highly accurate in the whole flight envelope. For today's modern fighter aircraft, the basic flight mechanical characteristics change between linear and nonlinear as well as stable and unstable as an effect of the desired capability of advanced maneuvering at subsonic, transonic and supersonic speeds.

This thesis combines the subject of system identification, which is the art of building mathematical models of dynamical systems based on measurements, with aeronautical engineering in order to find methods for identifying flight mechanical characteristics. Here, some challenging aeronautical identification problems, estimating model parameters from flight-testing, are treated.

Two aspects are considered. The first is online identification during flight-testing with the intent to aid the engineers in the analysis process when looking at the flight mechanical characteristics. This will also ensure that enough information is available in the resulting test data for post-flight analysis. Here, a frequency domain method is used. An existing method has been developed further by including an Instrumental Variable approach to take care of noisy data including atmospheric turbulence and by a sensor-fusion step to handle varying excitation during an experiment. The method treats linear systems that can be both stable and unstable working under feedback control. An experiment has been performed on a radio-controlled demonstrator aircraft. For this, multisine input signals have been designed and the results show that it is possible to perform more time-efficient flight-testing compared with standard input signals.

The other aspect is post-flight identification of nonlinear characteristics. Here the properties of a parameterized observer approach, using a prediction-error method, are investigated. This approach is compared with four other methods for some test cases. It is shown that this parameterized observer approach is the most robust one with respect to noise disturbances and initial offsets. Another attractive property is that no user parameters have to be tuned by the engineers in order to get the best performance.

All methods in this thesis have been validated on simulated data where the system is known, and have also been tested on real flight test data. Both of the investigated approaches show promising results.



## Populärvetenskaplig sammanfattning

Modellering och simulering används idag flitigt i flygindustrin. Detta görs för att på ett säkert och kostnadseffektivt sätt undersöka flygegenskaper hos såväl nya som befintliga flygfarkoster. Att från uppmätta data skapa matematiska modeller av ett dynamiskt system, så som ett flygplans rörelse, kallas systemidentifiering. Genom att ställa upp rörelseekvationerna och fylla dessa med uppmätta data kan man optimera fram den modell som på bästa sätt beskriver rörelsen. Optimeringen kan påverkas av olika störningskällor. Dessa kan komma från omgivningen, så som turbulens, där farkostens rörelse påverkas, eller från mätningen i sig och det är därför viktigt att den metod man använder vid systemidentifieringen kan hantera dessa störningar så att en så bra modell som möjligt kan erhållas. För att få ett bevis på att den framtagna modellen är tillräckligt bra behövs även ett test på ny data.

I denna avhandling undersöks två typer av identifieringsalgoritmer. Den första är tänkt att användas medan flygfarkosten är i luften för att förse provingenjörer med information som kan användas för olika beslut under flygningen. Information om huruvida insamlad provdata stämmer överens med befintliga modeller kan leda till att man ger klartecken att fortsätta provningen eller att man vill avbryta för att utföra en noggrannare analys. För detta syfte har en redan befintlig metod utvärderats och vidareutvecklats så att den har blivit mer robust mot olika typer av störningar samt varierande informationsinnehåll i datan.

Den andra typen av algoritmer behandlar identifiering av en flygfarkosts mer avancerade egenskaper. Denna analys utförs efter avslutat prov och är till för svårmodellerade flygegenskaper. I denna undersökning har en relativt enkel och robust metod jämförts med fyra andra. Resultatet visar att den förstnämnda metoden fungerar bättre än de övriga i de undersökta fallen.

Alla de använda metoderna har analyserats på simulerade data med kända egenskaper. Tester har även utförts på riktiga flygprovdata som ett bevis på att metoderna kan användas i praktiken.





## Acknowledgments

Everything is possible! This thesis is a proof of that. The research herein would however not have been possible without the open minds at the department of Electrical Engineering at Linköping University and at Saab Aeronautics working together in the Vinnova Competence Center LINK-SIC - Linköping Center for Sensor Informatics and Control.

I would like to thank my two university supervisors; Dr. Martin Enqvist and Professor Emeritus Lennart Ljung for opening the door to this research and for guiding me on my way as well as sharing their knowledge. I had been away from higher education for a long time before I started this journey, which now has taken over ten years to complete, but being stubborn as a mule I now stand at the finishing line.

I would like to thank Lic. Mattias Sillén and Dr. Gunnar Holmberg for being the ones who opened the door at Saab Aeronautics. This was also an important enabler for this research. However, I actually first came in contact with this work when Dr. Ola Härkegård, former PhD student at the automatic control group at Linköping University and co-worker at Saab, asked me to help him with the writing of a PhD proposal. This was aimed at improving the tools used at Saab Aeronautics for system identification when evaluating flight test data. Later I got the question if I would like to take on the task described in the proposal. As can be seen I accepted, so thank you Ola.

In addition, I want to thank all those both at Saab and at Linköping University who have supported me in my everyday struggle, helped me with proof reading and giving helpful hints, making this thesis what it is today. When writing, reading and rewriting something several times, it is easy to get blind to mistakes made. Special thanks should also go to Lic. Alejandro Sobron and Dr. David Lundström for the opportunity to use the radio-controlled subscale aircraft GFF as an experimental platform. This was a great experience and fun as well!

I have on numerous occasions said that: I spend 100% at work, 100% at the university and 100% at home, i.e., no more than 300%. Unfortunately, there is only 100% to go around, so sacrifices have had to be made. Some of that sacrifice has been time that I could have spent with my family. Therefore, I want to thank them for their patience when I was away or put time on my studies at home. I can only hope that the sacrifices will be worthwhile in the end!

*Linköping, May 2019*  
*Roger Larsson*



---

# Contents

<b>Notation</b>	<b>xv</b>
<b>1 Introduction</b>	<b>1</b>
1.1 Background . . . . .	1
1.2 Research motivation . . . . .	3
1.3 Goal . . . . .	4
1.4 System . . . . .	4
1.5 Contributions . . . . .	8
1.6 Thesis outline . . . . .	9
<b>2 System identification</b>	<b>11</b>
2.1 System . . . . .	11
2.2 Modeling . . . . .	15
2.3 Methods . . . . .	18
2.3.1 Prediction-error method . . . . .	21
2.3.2 State and parameter estimation method . . . . .	23
2.3.3 Instrumental variable method . . . . .	24
2.3.4 State estimation method . . . . .	24
2.4 Testing . . . . .	24
2.5 Simple example . . . . .	25
<b>3 Aeronautics</b>	<b>29</b>
3.1 Definitions . . . . .	29
3.2 Flight mechanics . . . . .	33
3.3 Modeling . . . . .	36
3.3.1 System modeling . . . . .	36
3.3.2 Noise modeling . . . . .	39
3.3.3 Total model . . . . .	41
<b>4 Flight testing</b>	<b>45</b>
4.1 Pre-flight activities . . . . .	46
4.1.1 The analysis and design phase . . . . .	46
4.1.2 The production and implementation phase . . . . .	48

4.1.3	The integration and test phase . . . . .	48
4.2	Flight testing . . . . .	48
4.3	System identification . . . . .	55
<b>5</b>	<b>Sequential identification</b>	<b>59</b>
5.1	Problem formulation . . . . .	60
5.2	Methods . . . . .	61
5.2.1	Sequential frequency domain method . . . . .	61
5.2.2	Recursive time-domain method . . . . .	72
5.2.3	Instrumental variables . . . . .	78
5.2.4	Data fusion . . . . .	93
5.3	Convergence and consistency analysis . . . . .	98
5.4	Estimation on real data . . . . .	110
5.5	A six degrees-of-freedom model . . . . .	112
5.6	Conclusions . . . . .	119
<b>6</b>	<b>Generic future fighter</b>	<b>121</b>
6.1	Introduction . . . . .	122
6.2	Input design using simulated data . . . . .	123
6.3	Experimental setup . . . . .	129
6.4	Results using real flight test data . . . . .	132
6.5	Post flight analysis . . . . .	138
6.6	Conclusions . . . . .	140
<b>7</b>	<b>The parameterized observer method</b>	<b>143</b>
7.1	Problem formulation . . . . .	144
7.2	Method . . . . .	145
7.3	Noise . . . . .	146
7.4	Stability of nonlinear systems . . . . .	147
7.5	Piecewise affine systems . . . . .	149
7.6	Simple example . . . . .	150
7.7	Simulation study . . . . .	153
7.8	Conclusions . . . . .	156
<b>8</b>	<b>Identification of unstable nonlinear systems</b>	<b>157</b>
8.1	The identification methods . . . . .	157
8.1.1	Prediction-error methods . . . . .	158
8.1.2	State estimation method . . . . .	160
8.1.3	Parameter and state optimization method . . . . .	161
8.2	Estimation on simulated data . . . . .	162
8.3	Estimation on real data . . . . .	183
8.4	Conclusions . . . . .	184
<b>9</b>	<b>Discussion</b>	<b>187</b>
<b>A</b>	<b>Nonlinear aircraft model</b>	<b>191</b>

---

<b>B</b>	<b>Some mathematics</b>	<b>201</b>
<b>C</b>	<b>Sequential algorithms</b>	<b>203</b>
<b>D</b>	<b>Complementary results to the sequential identification</b>	<b>209</b>
<b>E</b>	<b>GFF test card</b>	<b>271</b>
<b>F</b>	<b>Kalman filters</b>	<b>277</b>
	F.1 Extended Kalman filter (EKF) . . . . .	278
	F.2 Unscented Kalman filter (UKF) . . . . .	279
<b>G</b>	<b>Complementary results to the identification of unstable nonlinear systems</b>	<b>281</b>
	G.1 Tuning results from the noise (SNR) sensitivity study . . . . .	282
	G.2 Complementary results for the SNR sensitivity study . . . . .	284
	G.3 Tuning results from the initial offset ( $\theta_0$ ) sensitivity study . . . . .	284
	<b>Bibliography</b>	<b>295</b>



---

# Notation

## MATH SYMBOLS

---

Notation	Meaning
$\mathbb{N}$	Set of natural numbers
$\mathbb{R}$	Set of real numbers
$\mathbb{C}$	Set of complex numbers
Cov	Covariance
E	Expectation
$\forall$	For all
Im	Imaginary part
Re	Real part
$I$	Identity matrix
sup	Supremum or least upper bound
$\sigma$	Standard deviation
*	Superscript for equilibrium
*	Complex transpose
$\hat{\cdot}$	Predictor notation
$\hat{\cdot}$	Estimate notation
$\bar{\cdot}$	Mean notation
$\tilde{\cdot}$	Fourier transform notation
$ x $	Euclidean vector norm
$\ x\ _2$	$L_2$ -norm

---



## SYSTEM IDENTIFICATION

Notation	Meaning
$A, B, C, D$	Linear system and measurement matrices, continuous time
$a, c$	Nonlinear system and measurement function, continuous time
$F, G, H, J$	Linear system and measurement matrices, discrete time
$f, g$	Nonlinear system and measurement function, discrete time
$F_y$	Feedback gain
$F_r$	Feed-forward gain
$F(m, Z)$	Model fit for model $m$ using dataset $Z$
$K$	Gain matrix
$k$	Discrete time index corresponding to the actual time $t = T_s k$
$N$	Number of time samples
$P$	Covariance matrix
$S$	General notation for a system
$T_s$	Sample time
$t$	Time
$u$	Input vector
$V_N(\theta, Z^N)$	Cost function for $\theta$ based on the dataset $Z^N$
$v$	Measurement noise
$w$	Process noise
$x$	State vector
$y$	Measurement or output vector
$Z$	Dataset, e.g., an estimation dataset $Z_e^N = \{u_k, y_k\}_{k=1}^N$ with $N$ input and output data points
$z$	System response vector
$\epsilon$	Prediction error matrix
$\varepsilon$	Prediction error vector
$\Phi$	Regressor matrix
$\phi$	Regressor vector
$\lambda_{LM}$	Levenberg-Marquardt regularization parameter
$\Theta$	Parameter matrix
$\theta$	Parameter vector
$\vartheta$	Parameter vector augmented with the state vector
$\omega$	Angular frequency
$Z$	Instrumental variable matrix
$\zeta$	Instrumental variable vector

## AERONAUTICS

Notation	Meaning
$a$	Speed of sound
$b$	Reference span
$c$	Reference chord
$S$	Reference area
$S_B$	Body-fixed system
$S_E$	Earth-fixed system
$g$	Gravity constant
$m$	Mass
$x, y, z$	Cartesian coordinates
$u, v, w$	Velocities in Cartesian coordinates
$V, \alpha, \beta$	Velocities in spherical coordinates, speed, angle-of-attack and angle-of-sideslip
$\Phi, \Theta, \Psi$	Euler angles, roll, pitch and yaw
$p, q, r$	Roll, pitch and yaw angular velocities
$\delta_a, \delta_e, \delta_r$	Aileron, elevator and rudder deflection angles
$\delta_c$	Canard deflection angle
$\delta_{LE}, \delta_{TE}$	Leading edge and trailing edge deflection angles
$F$	Force
$F_u, F_v, F_w$	Turbulence force filter in Cartesian coordinates
$F_p, F_q, F_r$	Turbulence moment filter in Cartesian coordinates
$H_p$	Pressure altitude
$M$	Moment
$M$	Mach number $M = V/a$
$P$	Position
$I$	Moment of inertia
$T_a$	Ambient temperature
$F_p, M_p$	Propulsive force and moment
$T_e$	Engine thrust
$F_A, M_A$	Aerodynamic force and moment
$L, D$	Aerodynamic lift and drag force
$X, Y, Z$	Aerodynamic forces in the Cartesian coordinates
$T, C, N$	Aerodynamic tangential ( $= -X$ ), side ( $= -Y$ ) and normal force ( $= -Z$ )
$\mathcal{L}, \mathcal{M}, \mathcal{N}$	Aerodynamic rolling, pitching and yawing moments
$C_x$	Aerodynamic coefficient $C_x = X/(q_a S y)$ , where $x \in \{L, D, T, C, N, l, m, n\}$ , $X \in \{L, D, T, C, N, \mathcal{L}, \mathcal{M}, \mathcal{N}\}$ and $y \in \{1, 1, 1, 1, 1, b, c, b\}$
$q_a$	Dynamic pressure $0.5 \rho V^2$
$\rho$	Density
$\omega$	Angular velocity

**ABBREVIATIONS**

---

<b>Abbreviation</b>	<b>Meaning</b>
ARES	Aircraft rigid-body engineering simulator
BIBO	Bounded-input bounded-output
CFD	Computational fluid dynamics
DOF	Degrees-of-freedom
EKF	Extended Kalman filter
FCS	Flight control system
IFAC	International federation of automatic control
ISA	International standard atmosphere
ISO	International organization for standardization
IV	Instrumental variable
JAS	Jakt (fighter), attack, spaning (reconnaissance)
MC	Monte Carlo
PLA	Power leverage angle
RLS	Recursive least-squares
SAAB	Svenska aeroplan aktiebolaget
UKF	Unscented Kalman filter

---

# 1

---

## Introduction

*“Cause and effect are two sides of one fact.”*  
- Ralph Waldo Emerson (1803 - 1882)

This thesis is a combination of two subjects, system identification from the academic world and flight mechanics from aeronautical engineering in the industrial world. Combining the two subjects leads to interesting research problems to be studied in academia and enhanced capabilities that can be used in industry, a typical win-win situation.

### 1.1 Background

Ever since the dawn of time there has been cause and effect, action and reaction. We humans have observed these phenomena in order to try to understand the world in which we are living. Many things in our world can be looked upon as some kind of a system. A general definition of a system is a bounded set of components or rules that form an integrated whole. The boundary separates the system from its surroundings. The system can be affected by inputs from the surroundings, some of which can be controlled. The effect of the inputs can be observed from the surroundings as outputs. Figure 1.1 shows a schematic description of a general system.

Our understandings of the world have been put into theories, which in some cases have been used to produce models of systems. With the introduction of computers, numerical simulations of systems using these models became possible. This has led to many conceivable ways to learn more about the behavior of the systems in a safe and structured manner.

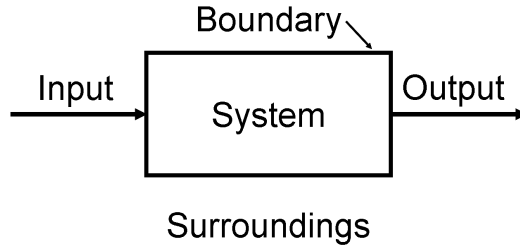


*Figure 1.1: A schematic diagram of a system.*

System identification is the art of building mathematical models of systems based on measurements of input and output signals. The subject is associated with dynamic systems, i.e., systems that have a memory of the states in which they have been. A static system is, in contrast, a system that only takes the current input and converts it to the current output regardless of earlier inputs. A very simple example of a dynamic system is a falling apple. Isaac Newton studied the dynamics of this system. The falling apple is autonomous, meaning that it falls without a controlled input. Another example is a shower. This system is, in contrast to the falling apple, controllable. The flow and temperature of the water can be changed to a comfortable state. We can measure this state as an output with receptors in our skin and control the input until we are satisfied.

The dynamic system of interest in this thesis is the aircraft, with a focus on the flight mechanical characteristics. An aircraft is an example of an aeronautical system. The word aeronautics comes from the Greek words for air and seaman-ship, giving the meaning of - sailing the air. Looking up in the sky, this is what the birds are doing. The dream of flying has been and still is shared by many people. In China, kites were used in 200 B.C. In the 15th century, Leonardo da Vinci looked at ways to mimic the birds as the concept of flight. A major advancement from this was when George Cayley separated lift and propulsion at the end of the 18th century. In the following century, Otto Lilienthal conducted stability tests with his gliders. One cornerstone to achieve sustained, three-axis controlled, manned motorized flight was when the Wright brothers added a lightweight engine and the means to control flight using a wing-warping technique for twisting the wing tips like the birds do when turning in the air. The brothers also used a movable horizontal surface for pitching the nose up and down and a movable vertical surface for pointing the aircraft right and left, leading to their 12 s (37 m) pioneering flight with the Flier I, on the 17th of December in 1903 at Kill Devils Hill, North Carolina, USA. A later analysis made by Culick [2001] shows that this aircraft had both unstable and nonlinear aerodynamic pitch characteristics. Fortunately, the characteristics were no worse than the brothers could handle. As design of aircraft led to higher speeds, it was necessary to turn to inherently pitch stable solutions. From the first successful flight until the present day, the understanding of the dynamics of flight has enhanced enormously.

## 1.2 Research motivation

Modern fighter aircraft operate in a large envelope including flight at subsonic, transonic as well as supersonic speeds at different altitudes, see Figure 1.2. Together with aggressive maneuvering this results in different combinations of stable/unstable and linear/nonlinear flight mechanical characteristics. Robustly designed *Flight Control Systems* (FCSs) aid the pilot in flying the aircraft in this complex physical environment. In order to design the control laws, high quality simulation models are needed. During an aircraft project, the fidelity of these models is successively increased. Flight-testing is the last step in this process. The data from these tests are highly valuable since a lot of time and effort have been put into the project. It is therefore desirable to have tools that can make the most of the evaluation of these test data.

Today on-line flight test evaluation software runs almost in real-time. This type of software is used to monitor if set boundaries are crossed and to analyze the flight characteristics so that safe and cost effective testing can be conducted. The tool used for the aerodynamic analysis delivers resultant forces and moments. A tool that, in a robust way, can divide these forces and moments into their components of stability and control would increase the understanding of the observed flight mechanical characteristics so that correct decisions can be made. If this tool also gives an indication of the information content for post flight analysis, a potential reduction of expensive repetitions and thereby a cost reduction can be made.

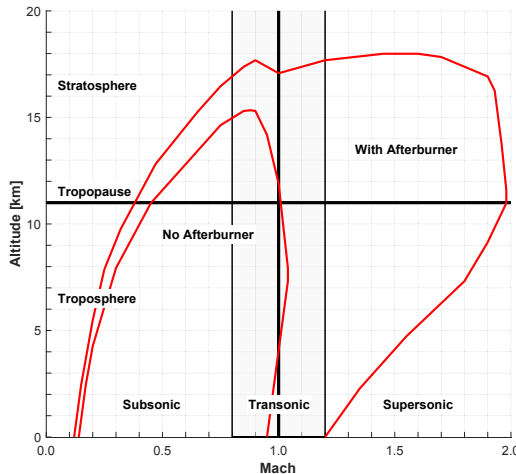


**Figure 1.2:** Typical flight envelope for a fighter aircraft with an afterburner. The envelope covers altitudes from the Troposphere (0 – 11 km) past the Tropopause up to the Stratosphere (11 – 47 km), for subsonic (Mach 0 – 0.8) past transonic (Mach 0.8 – 1.2) into supersonic (Mach  $\geq 1.2$ ) speed.

Post flight tools for aerodynamic evaluation already exist, but for the nonlinear parts there are still a need for more efficient tools. It is therefore desirable to be able to use robust methods that require a minimum of input from the engineer, but still give accurate enough results. This is a challenging task that leads to interesting research problems.

### 1.3 Goal

*The goal* of the work described in this thesis is to provide aircraft companies with robust methods for identification of flight mechanical characteristics.

*The aim* is to improve the tools used in industry today, making the modeling process easier for the engineers, leading to a more time and cost effective way of working.

This will hopefully result in increased time for the engineers to ponder and better understand the results from the identification process and thereby increasing the accuracy of the models used for simulation and control law design.

### 1.4 System

Here, a short overview of the systems used is given to provide the reader with the understanding of similarities and differences. The flight mechanical motion of jet fighter aircraft is used as the system of choice since fighter aircraft is the main product of Saab Aeronautics. However, not all the aircraft used in this thesis are of Saab design. Six aircraft have been studied in this thesis. The geometrical shape differs a bit between these. Three have a close-coupled canard delta-wing layout, two are of conventional tail-plane configuration and one has a double-delta wing. The difference between these layouts is shown in Figure 1.3.

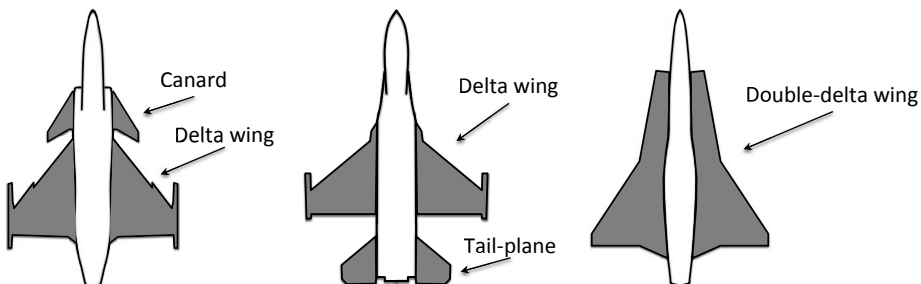


**Figure 1.3:** Aircraft configurations: Canard, Tail-plane and Double-delta.

The **JAS 39C Gripen**, shown in Figure 1.4, is a single seat, single-engine multi-role aircraft, meaning that it can perform fighter, attack and reconnaissance missions. The aircraft has a maximum take-off weight of 14000 kg, a wing area of  $30\text{ m}^2$  and is powered by the Volvo RM12 low by-pass afterburning turbofan engine, giving a thrust of 54 kN dry and up to 80.5 kN using the afterburner. The aircraft is developed by Saab and has a close-coupled delta-wing canard configuration. The JAS 39 is aerodynamically static unstable (subsonically) and has a fly-by-wire flight control system for stability and control. This means that the pilot gives inputs to a computer that sends electric signals via wires to the actuators for control. The first flight was performed on the 9th of December 1988 and the aircraft was introduced into the Swedish Air Force in November 1997. More about this aircraft can be found in Keijsper [2004].

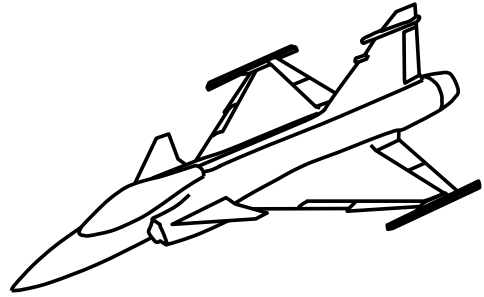


*Figure 1.4: JAS 39C Gripen.*

**Vegas & ADMIRE** are two simulation model aircraft based on the same Generic Aerodata Model presented in Backström [1997]. This generic model was developed at SAAB to be used for research purposes of a close-coupled canard delta-wing configuration similar to the JAS 39 Gripen (see Figure 1.5). “Vegas” is a rigid body simulation model used at Saab. The aircraft, with a wing area of  $45\text{ m}^2$  and a maximum take-off weight of 10000 kg, is a slightly larger aircraft than the JAS 39 Gripen. The model has a single afterburning turbofan engine giving a thrust of 56.9 kN dry and 134.7 kN with the afterburner running. The model called ADMIRE [Forssel and Nilsson, 2005], with the same size and mass as Vegas, developed by Swedish Defense Materiel Administration (FOI), has been used for research of clearance of flight control laws both in Sweden and internationally in GARTEUR (Group for Aeronautical Research and Technology in Europe), see Forssell and Hydén [2003] and Menon et al. [2005]. Some data from the ADMIRE model is given in Appendix A.

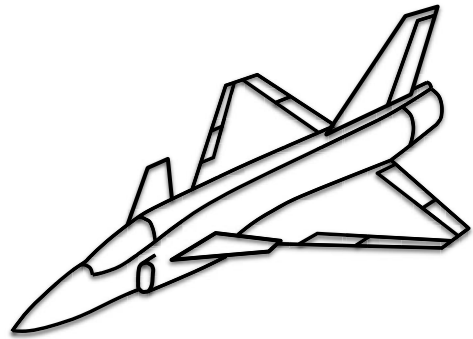


*Figure 1.5: Vegas & ADMIRE.*



The **F-104G Starfighter**, shown in Figure 1.6, is a single seat, single-engine, supersonic point defense interceptor designed by Lockheed as a product of the Korean war. An interceptor is a type of aircraft that usually attacks enemy non-fighters. The F-104 has a maximum take-off weight of about 13000 kg and is designed with a slender low aspect ratio wing with an area of  $16.66\text{ m}^2$ . Powered by a GE-J79 turbo-jet afterburner engine with a thrust of 44 kN dry and 69 kN using the afterburner it has an overemphasized rate-of-climb and brute speed. The Starfighter was the first aircraft to hold simultaneous official world records for speed, altitude and time-to-climb. The first flight was performed on the 17th of February 1956 and it was introduced into the U.S. Air Force in February 1958. This aircraft is called "a missile with a man in it". More about this aircraft can be found in Upton [2003].

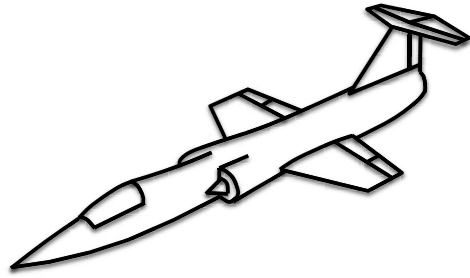


*Figure 1.6: F-104G Starfighter.*

The **F-16C Fighting Falcon**, shown in Figure 1.7, is a single seat, single-engine multi-role fighter, first designed as a air superiority fighter, meaning that it should go into enemy territory and take control over the air space, preventing the enemy to use its air force. Developed by General Dynamics, the aircraft first flight was performed on the 20th of January in 1974 and it was introduced into the U.S. Air Force in August 1978. This aircraft is aerodynamically static unstable (subsonically) and has a fly-by-wire flight control system. The layout is a conventional wing tail-plane configuration where the horizontal tail is all moving for pitch and roll control. With a wing area of  $28\text{ m}^2$  and a maximum take-off weight of 19200 kg, it is an aircraft of roughly the same size as the JAS 39 Gripen. The F-16 is powered by the F110-GE-129 Afterburner turbofan engine, which gives a thrust of 76.3 kN dry and 127 kN using the afterburner. Details can be found in Hamilton [2012].

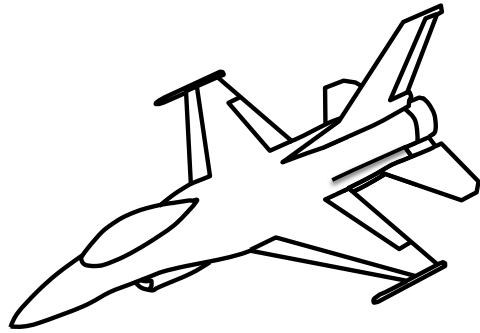


*Figure 1.7: F-16C.*

The **GFF** [Jouannet et al., 2012], shown in Figure 1.8, is a single-engine Generic Future Multi-role Fighter demonstrator. It is a sub-scale research aircraft developed by Saab, the Swedish Defense Research Agency (FOI), Volvo Aero, Linköping University (LiU) and the Royal Institute of Technology (KTH), ordered by the Swedish Material Board (FMV) in 2006. The main objective was to look at a future multi-role fighter with stealth, super cruise and long range capabilities. The aircraft has an all-moving canard configuration with a fixed V-tail. The maiden flight was in November 2009. The full-scale aircraft design has a wing area of  $47 \text{ m}^2$  and a maximum take-off weight of 23500 kg, being significantly larger than the JAS 39 Gripen. The engine is estimated to have a max thrust of 170 kN using the afterburner. The GFF has a JetCat P160 model jet engine capable of delivering 160 N thrust.

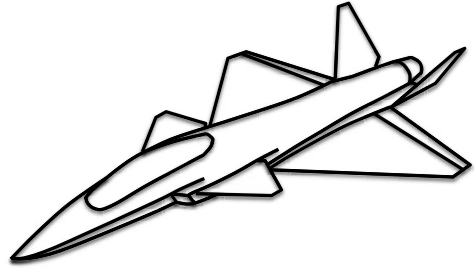


**Figure 1.8:** GFF.

The **Saab 35 Draken** was a Swedish fighter of the cold war (1946-1991). It was Saab's first supersonic aircraft with a max speed over two times the speed of sound. Its double-delta wing configuration was designed so that both low- and high-speed flight requirements could be met. The aerodynamics of the wing was first tested with small-scale (0.92 m span) wire-controlled model aircraft, then with a sub-scaled (4.88 m span) manned demonstrator aircraft (Saab 210, Figure 1.9) before finally testing the real full-scale aircraft. The Draken, shown in Figure 1.10, has a wing area of  $49.2 \text{ m}^2$  and a maximum take-off weight of about 16000 kg. The engine produced a thrust of 56.5 kN dry and 78.4 kN with the afterburner. Draken first flew on the 25th of October 1955 and was introduced into the Swedish Air Force in March 1960. The Draken history is found in Jørgensen [2015].

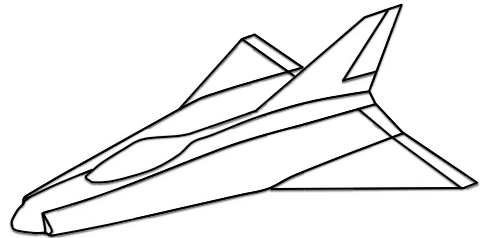


**Figure 1.9:** Saab 210 Lill-Draken.

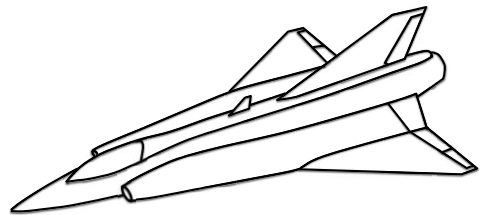


**Figure 1.10:** Saab 35 Draken.

## 1.5 Contributions

The subject of system identification applied to aircraft is not new. Several books have been published on the subject, like Klein and Morelli [2016], Jategaonkar [2015] and Tischler and Remple [2012]. A historical perspective of the subject is given in 'The Evolution of Flight Vehicle System Identification', presented in Hamel and Jategaonkar [1996]. Research is still continued to develop more effective methods supporting the development of new aircraft. One research topic, described in this thesis, is a sequential method used for identification during flight-testing. The aim of this method is to aid the aeronautical engineer in making decisions if to repeat, proceed or abort the testing. These decisions are based on the estimated parameters compared to an already existing model, but also on the estimated amount of information content in data. An existing frequency domain method by Klein and Morelli [2016] was implemented both at Linköping University and at Saab Aeronautics. The first contribution consists of the analysis of a correctly implemented finite Fourier transform of the time derivative used in the method and the second contribution is the implementation of an Instrumental Variable (IV) approach together with data fusion to take care of system noise such as atmospheric turbulence and varying excitation. The method in Klein and Morelli [2016] has been compared to the improved method as well as to a recursive time domain method. Results are published in the following articles

R. Larsson and M. Enqvist. Real-time aerodynamic model parameter identification. In *Society of Flight Test Engineers International Symposium*, Linköping and Stockholm, Sweden, September 2009.

R. Larsson and M. Enqvist. Sequential aerodynamic model parameter identification. In *Proceedings of the 16th IFAC Symposium on System Identification*, pages 1413–1418, Brussels, Belgium, July 2012a.

The third contribution is a test of the frequency domain method. An experiment was designed using multisine input signals and the GFF subscale demonstrator aircraft was used as a test platform. The test execution and results from this are given in

A. Sobron, D. Lundström, P. Krus, R. Larsson, and C. Jouannet. Methods for efficient flight testing and modelling of remotely piloted aircraft within visual line-of-sight. In *Proceedings of the 31th Congress of the International Council of the Aeronautical Sciences*, 2018.

R. Larsson, A. Sobron, D. Lundström, and M. Enqvist. Multisine inputs for a subscale demonstrator aircraft. *Submitted to Control Engineering Practice*, March 2019.

Another research topic is the identification of unstable and nonlinear systems working under feedback. This is a complex task. The aim is to simplify the modeling process for the aeronautical engineer making nonlinear models post flight. For this purpose, a benchmark problem has been formulated. This can in itself

be seen as a contribution, but the results of the comparison are more important. The fourth contribution is the analysis of the properties of a method that includes a parameterized observer that stabilizes the predictor used. This method is compared with four other direct identification methods with respect to how they are affected by different noise sources. Effects of both white measurement noise and process noise in the form of atmospheric turbulence have been investigated. An interesting result is that the implemented parameterized observer method that, in contrast to the other methods, is without any tuning parameters seems to be least sensitive to noise and initial offset of the model parameters for the studied cases. The methods and results are published in the following articles

R. Larsson, Z. Sjanic, M. Enqvist, and L. Ljung. Direct prediction-error identification of unstable nonlinear systems applied to flight test data. In *Proceedings of the 15th IFAC Symposium on System Identification*, pages 144–149, Saint-Malo, France, July 2009.

R. Larsson and M. Enqvist. Nonlinear aerodynamic modeling of unstable aircraft using flight test data. In *Proceedings of the 28th Congress of the International Council of the Aeronautical Sciences*, Brisbane, Australia, September 2012b.

R. Larsson and M. Enqvist. An easy to use engineering method for identification of complex flight dynamics from flight test data. In *Proceedings of 16th AIAA Aviation Technology, Integration, and Operations Conference, AIAA Aviation 2016*, Washington DC, USA, June 2016.

## 1.6 Thesis outline

This thesis is a continuation of the Licentiate thesis Larsson [2013]. The thesis begins with a general description of system identification in Chapter 2 and an introduction to flight mechanics and flight-testing in Chapter 3 and 4 respectively. These three chapters are meant to give a foundation for the understanding of the chapters that present the contributions. In Chapter 5 the sequential identification is presented and in Chapter 6 the GFF flight test experiment is described. Chapter 7 presents the parameterized observer (PO) for identification of unstable and nonlinear systems. An analysis of the PO predictor characteristics, including a comparison with four other methods is given in Chapter 8. A discussion of the results is then presented in Chapter 9. Some background theory and complementary results are given in the appendices.



# 2

---

## System identification

"When you have eliminated the impossible, whatever remains, however improbable, must be the truth."

- Sherlock Holmes, The sign of the four (1890)

As stated in the introduction, system identification is the art of building mathematical models of dynamical systems based on measurements of input and output signals. These models can then be used to study the system response for different inputs. Hopefully, these studies lead to an understanding of the system properties that then can be used, for example, to improve the system behavior by adding a control system. In this chapter, some basics of system identification are presented. The main concepts of this subject are the true system under investigation, the model structure that is used to describe the true system, experimental design to get the information for the identification and the method used to estimate the model that should describe the true system in a satisfactory way. Some standard references on the subject of system identification are Söderström and Stoica [1989], Ljung [1999] and Pintelon and Schoukens [2012]. These books cover the details of the subject, both for time and frequency domain system identification. An overview of the subject can be found in Ljung [2008].

### 2.1 System

What is a dynamical system? A system can be almost anything. One way of defining a system is to let a human observer put a boundary around something that he or she wants to investigate. A *dynamical* system is a system that includes some time history dependence. This means that the state  $x(t)$  of the dynamical system at time  $t$  is dependent on the state at earlier times. A system  $S$  can be influenced by a controllable input  $u(t)$ , which can come from a desired reference

$r(t)$  and also as a feedback of measured quantities from the system. Process noise  $w(t)$  is another source of influence, which in contrast to  $u(t)$  is a disturbance that can affect the system without any predetermined intention. The influence of both the input and process noise leads to a response  $z(t)$  of the system. Observations can be made by measuring the output  $y(t)$ , which reflects some or all response properties. The measurements can be affected by noise  $v(t)$  that come from the sensors or the environment that these sensors are placed in. The measured output of the system can mathematically be described as a function

$$y(t) = S(u(t), w(t), v(t)) \quad (2.1)$$

Note that the function describes the entire signals from  $t = -\infty$  to  $t = +\infty$ . However, the aircraft application studied in this thesis is causal, meaning that the output at the current time is only affected by the history, of the input and noise, up to the present time.

An important property of dynamical systems is the stability characteristics. There exist several different types of stability concepts [Khalil, 2002] and [Cook, 1994]. Here, some versions used in system identification are given.

Consider a nonlinear system  $S$  described by a state-space equation

$$\begin{aligned} \dot{x}(t) &= a_S(x(t), u(t), w(t)), \quad x(t_0) = x_0 \\ y(t) &= c_S(x(t), u(t), v(t)) \end{aligned} \quad (2.2)$$

where  $a_S(x(t), u(t), w(t))$  is the function that describes the time history dependency of the system state given the input and process noise. Initially the system will be in some state  $x(t_0) = x_0$ . Observations of the states are then described by the measurement function  $c_S(x(t), u(t), v(t))$  and depend on the input and the measurement noise. An equilibrium  $(x^*(t), u^*(t))$  of the system is defined as  $a_S(x^*(t), u^*(t), 0) = 0$ . This equilibrium can have different stability characteristics. According to Khalil [2002], the equilibrium of the system (2.2) is said to be stable if for any given  $\epsilon > 0$  there exists a  $\delta > 0$  such that

$$|x^*(t) - x(t_0)| < \delta \Rightarrow |x^*(t) - x(t)| < \epsilon \quad \forall t \geq t_0 \quad (2.3)$$

Otherwise the system is unstable. The system is convergent if there exist a  $\delta > 0$  such that

$$|x^*(t) - x(t_0)| < \delta \Rightarrow |x^*(t) - x(t)| \rightarrow 0 \quad \text{as } t \rightarrow \infty \quad (2.4)$$

An equilibrium is said to be asymptotically stable if it is both stable and convergent. Figure 2.1 shows an example of the three different stability cases of an equilibrium both for non-oscillative and oscillative cases. With this stability definition it is possible to analyze the falling apple, mentioned in the introduction.

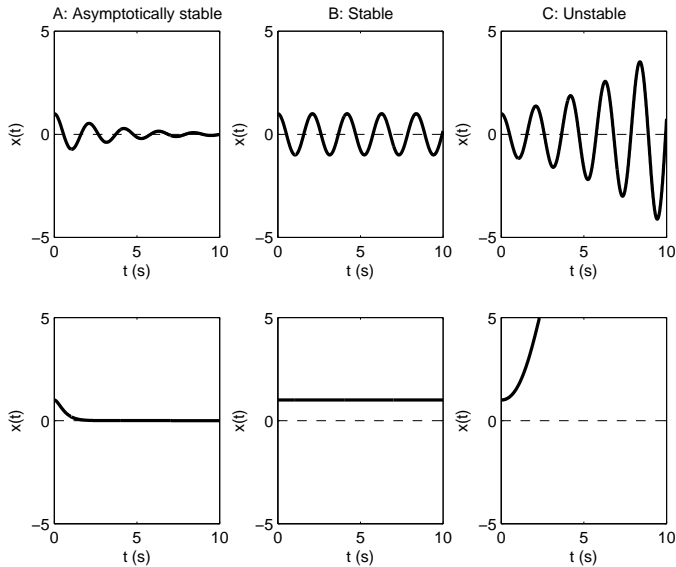


**Figure 2.1:** Behavior of asymptotically stable (A), stable (B) and unstable (C) systems for both oscillative (top) and non-oscillative (bottom) cases.

### Example 2.1: Falling apple

Assume that there is an apple balancing on a branch in an apple tree. Let the position be measured from this point, which is an equilibrium since the time derivative of the states, position  $P(t)$  and speed  $V(t)$ , both are zero. A wind disturbs the tree at time  $t = 0$  and the apple falls down. The true system and the observer are shown to the left in Figure 2.2. To the right is a block diagram, which in the control community is a common way to graphically describe a dynamic system.

This system is autonomous, meaning that it has no time dependent input. The apple falls towards the ground by the influence of gravity, which is here considered to be process noise. This gravitational force determines the trajectory that the apple will follow. By looking at this trajectory it is possible to make observations of the position of the apple as it falls. The accuracy of the observations is affected by the observer's eyesight and maybe even the atmospheric properties around the person. For example, the observations would be degraded if the apple falls in rain. The apple will fall away from its initial condition. This means that the distance from the initial position will grow to infinity (or in this case until it hits the ground and finds a new equilibrium). The behavior of the apple is unstable with respect to the equilibrium on the branch and can be described by the lower right picture in Figure 2.1.



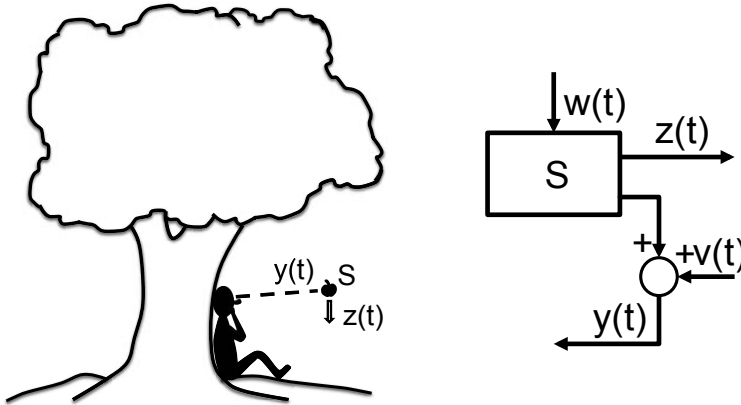


**Figure 2.2:** The true system and block diagram used for the falling apple.

Another type of stability is called bounded-input, bounded-output (BIBO) stability. In this case the system (2.2) is said to be BIBO-stable if there exists a finite constant  $\eta$  such that for a bounded input  $u(t)$  with  $|u(t)| \leq \delta$ ,  $\delta > 0$ , it holds that

$$\sup |y(t)| \leq \eta \sup |u(t)| \quad \forall t \geq t_0 \quad (2.5)$$

which means that the output is limited so that it does not grow to infinity.

The stability characteristics of a system can be affected by adding a control system. One part of the control system can change the input based on the measured output. This principle is called feedback and is denoted  $F_y$ . In addition to this, a part that changes the input based on a user, or reference, signal is called feed-forward and is denoted  $F_r$ . As an example consider the shower mentioned in the introduction.

### Example 2.2: Shower

The true system and block diagram are shown in Figure 2.3. Here, the reference is a desired water flow and temperature, which in this case is controlled by turning the water mixer lever. The flow and temperature can be measured by putting a hand into the shower. The user can then adjust the mixer until the water reaches the desired state. Here, the user and the mixer together act as both a feed-forward and feedback system that mixes the cold and hot water, which is the input to the system. In modern mixers there can also be a thermo element working as a feedback system that takes care of minor changes in input temperature that could be caused by pressure disturbances originating from the fact that other people use the tap water system. This kind of disturbances is more common in

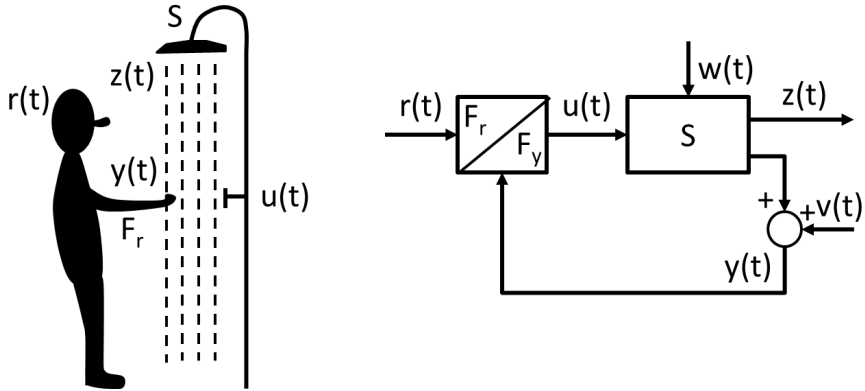


Figure 2.3: The real system and block diagram used for the shower example.

old houses. The shower system is usually both asymptotically stable and BIBO-stable since the temperature and flow will normally settle to an equilibrium after a disturbance or user input.

## 2.2 Modeling

The exact details about the true system stability and controllability characteristics may be unknown, but by performing experiments and observing the response it is possible to make mathematical models that mimic the true system. The modeling can be done in several ways. As an example, a parameterized state-space structure ( $\mathcal{M}$ )

$$\begin{aligned}\dot{x}(t) &= a(x(t), u(t), w(t); \theta) \\ y(t) &= c(x(t), u(t), v(t); \theta)\end{aligned}\tag{2.6}$$

can be used. Here,  $x(t)$  is a  $n_x \times 1$  state vector,  $u(t)$  is a  $n_u \times 1$  input vector and  $w(t)$  is the modeled process noise. The nonlinear continuous function  $a$  describes the dynamics of the model. The output  $y(t)$  is a  $n_y \times 1$  vector and  $v(t)$  is the modeled measurement noise. The nonlinear continuous function  $c$  describes the measurements. The vector  $\theta$  contains the  $n_p$  parameters to be estimated so that the model in (2.6) describes the physics of, for example, the nonlinear system (2.2). In some cases the measurement and/or process noise are assumed to be white, meaning that the power spectrum is flat. White noise is usually denoted with  $e(t)$  to separate it from general noise characteristics. A state-space model of a physical system can sometimes be obtained by 'first principles', i.e., based on some established physical law. For example, modeling the motion of the falling apple is usually done using Newton's second law.

Measured data is often given in discrete time. Therefore (2.6) has a discrete-time state-space formulation

$$\begin{aligned}x_{k+1} &= f(x_k, u_k, w_k; \theta) \\ y_k &= h(x_k, u_k, v_k; \theta),\end{aligned}\tag{2.7}$$

which normally is an approximation when (2.6) and (2.7) are compared. Here,  $t = T_s k$ , which means that  $x_k$  is the discrete state sample corresponding to  $x(t) = x(T_s k)$ . Note here the abuse of notation of  $w$  and  $v$ . These are not the same noise terms as in (2.6), but they represent the same type of noise, i.e., process and measurement noise, respectively.

Special, and simpler, cases of (2.6) and (2.7) are obtained if the models are linear, such that the equations can be written as

$$\begin{aligned}\dot{x}(t) &= A(\theta)x(t) + B(\theta)u(t) + w(t) \\ y(t) &= C(\theta)x(t) + D(\theta)u(t) + v(t)\end{aligned}\tag{2.8}$$

for the continuous-time case and

$$\begin{aligned}x_{k+1} &= F(\theta)x_k + G(\theta)u_k + w_k \\ y_k &= H(\theta)x_k + J(\theta)u_k + v_k\end{aligned}\tag{2.9}$$

for the discrete-time case.

It is important to use a model that is complex enough to describe the phenomenon of interest, but not more complex than that. So, the model complexity ( $\mathcal{C}$ ) has to be considered. The complexity could be represented by the number of parameters,  $n_p$ , to be estimated or by whether the model structure to be used should be linear or nonlinear. As an example, consider again the falling apple in Example 2.1.

---

### Example 2.3: Falling apple continued

---

If the apple falls from a tree its motion could, to an acceptable accuracy, be modeled as

$$\begin{aligned}\begin{bmatrix} \dot{P}(t) \\ \dot{V}(t) \end{bmatrix} &= \begin{bmatrix} 0 & 1 \\ 0 & 0 \end{bmatrix} \begin{bmatrix} P(t) \\ V(t) \end{bmatrix} + \begin{bmatrix} 0 \\ g \end{bmatrix} \\ P_m(t) &= \begin{bmatrix} 1 & 0 \end{bmatrix} \begin{bmatrix} P(t) \\ V(t) \end{bmatrix},\end{aligned}\tag{2.10}$$

i.e., as a continuous-time linear system with the position  $P(t)$  and velocity  $V(t)$  as states, influenced by gravity  $g$ . Capital letters have been used for the states to avoid mixing the notation of the velocity  $V(t)$  with the measurement noise  $v(t)$ . The measurement is the observed position  $P_m(t)$  of the apple with the origin at the initial apple position and positive direction towards the center of the earth. This model could for example be used to estimate the gravity constant. Now, if the apple were to be dropped from a hot air balloon flying at some high altitude, the

model (2.10) would not be accurate enough. The reason for this is that the speed of the apple would increase so much that the air resistance would significantly affect the motion. The model would have to be modified as

$$\begin{aligned} \begin{bmatrix} \dot{P}(t) \\ \dot{V}(t) \end{bmatrix} &= \begin{bmatrix} V(t) \\ -\frac{\rho C_D S V^2(t)}{2m} \end{bmatrix} + \begin{bmatrix} 0 \\ g \end{bmatrix} \\ P_m(t) &= \begin{bmatrix} 1 & 0 \end{bmatrix} \begin{bmatrix} P(t) \\ V(t) \end{bmatrix} \end{aligned} \quad (2.11)$$

where  $\rho$  is the air density,  $m$  is the apple mass,  $C_D$  is a drag coefficient describing the friction and pressure on the apple due to the air passing around it and  $S$  is the cross section area. Note that the velocity  $V(t)$  now enters the equation both in a linear and a quadratic way. Hence, this is a nonlinear model. The difference in position when using the linear or the nonlinear model approach is shown in Figure 2.4. It is easy to see that after only 1 second and about 4 meters the outputs from the two models differ.

The apple will actually reach a constant speed, using the nonlinear model, after falling some time in the atmosphere. This speed is called the terminal speed. In this example it is possible to measure it from Figure 2.4 as  $V_{terminal} \approx 16(m/s)$ .

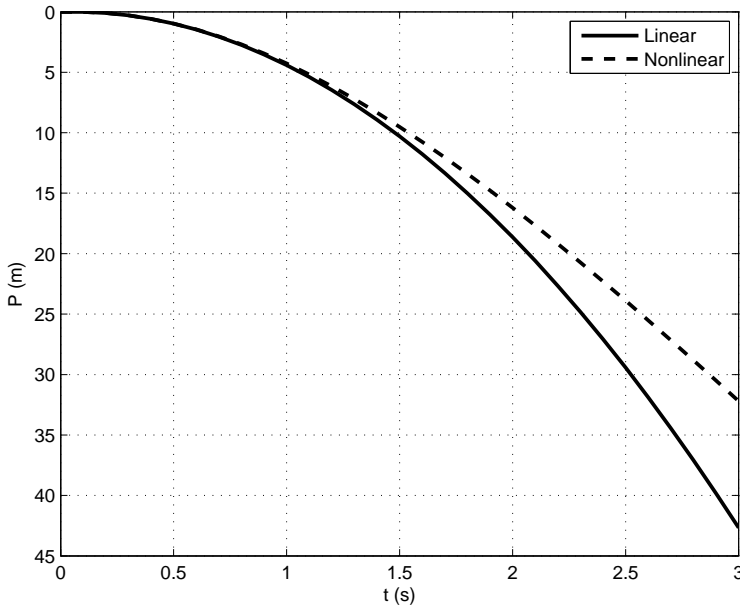


**Figure 2.4:** Difference in position between the linear (2.10) and nonlinear (2.11) model used for the falling apple.

The model of the falling apple can be made even more complicated if one would consider atmospheric turbulence. This will not be shown here, but an atmospheric model has been implemented for the use of process noise investigations in Chapters 5 - 8. This has been done using another type of model structure based on transfer functions. The transfer function description is based on a differential equation of the form

$$\frac{d^n}{dt^n} w(t) + d_1 \frac{d^{n-1}}{dt^{n-1}} w(t) + \dots + d_n w(t) = c_1 \frac{d^m}{dt^m} e(t) + c_2 \frac{d^{m-1}}{dt^{m-1}} e(t) + \dots + c_m e(t). \quad (2.12)$$

The transfer function  $H(s)$  can be obtained by applying the Laplace transform to (2.12), which results in

$$W(s) = H(s)E(s) = \frac{c_1 s^m + c_2 s^{m-1} + \dots + c_m}{s^n + d_1 s^{n-1} + \dots + d_n} E(s). \quad (2.13)$$

The model description given here was of a fairly general type. In Chapter 3, a dynamical model for aircraft and atmospheric turbulence will be presented in more detail. The next question in the present chapter is, how can the model be estimated?

## 2.3 Methods

Identification of the system ( $S$ ) using a model structure ( $\mathcal{M}$ ) and the information in a data set  $Z_e^N = \{u_k, y_k\}_{k=1}^N$  is the process of finding a model ( $m$ ) that is usable for the purpose of the application. Consider a discrete-time formulation

$$\{y_k\}_{k=0}^N = S(\{u_k\}_{k=0}^N, \{w_k\}_{k=0}^N, \{v_k\}_{k=0}^N) \quad (2.14)$$

of the general system (2.1) with the signal time interval  $t = 0$  to  $t = T_s N$ . It is possible that the mathematical structure of the system is unknown, and then some non-parametric or a general parametric identification method can be used. An example of a non-parametric approach is to use a kernel based method described in Roll [2003] where the estimation can be given as

$$\hat{y}(t_i) = \sum_{k=0}^N W_k y_k. \quad (2.15)$$

Here  $W_k$  are weights applied to each output data point  $y_k$  in the data set to make an estimate  $\hat{y}(t_i)$  of  $y(t_i)$ . Figure 2.5 shows an estimation  $\hat{y}(5.5)$  with a weight coinciding with the triangular kernel of the form

$$W_k = K(t_k, a, t_i) = \begin{cases} \frac{1}{a^2}(a - |t_k - t_i|) & \text{if } a - |t_k - t_i| \leq a \\ 0 & \text{otherwise,} \end{cases} \quad (2.16)$$

which has a base of  $2a$  and a height of  $1/a$ .

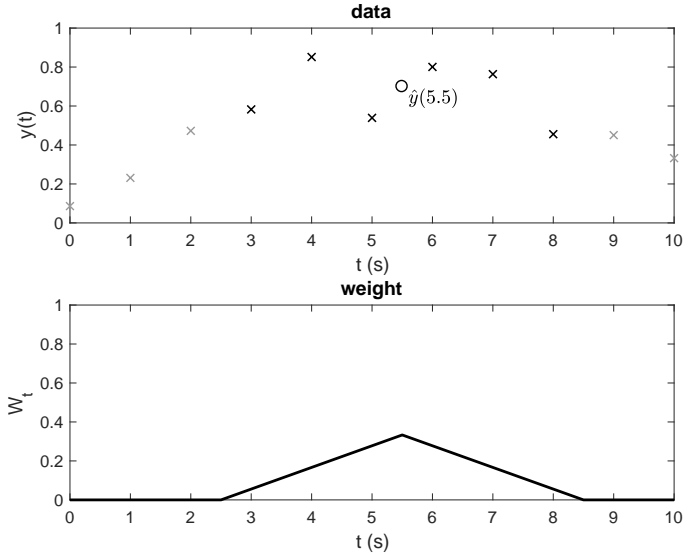


**Figure 2.5:** A non-parametric estimation,  $\hat{y}(5.5)$ , using a triangular kernel.

An ordinary Least-Squares method with a polynomial model in a linear regression problem formulation can be used as an example for the general parametric identification method. The regression formulation is given as

$$y_k = \phi_k^T \theta \quad (2.17)$$

where  $\phi_k^T = [y_{k-1} \ u_{k-1} \ y_{k-1}^2 \ y_{k-1}u_{k-1} \ u_{k-1}^2 \ \dots]^T$  and  $\theta = [a_1 \ b_1 \ a_2 \ c_2 \ b_2 \ \dots]^T$ . Caution must be taken to the polynomial degree, so undesirable characteristics are avoided in the model. Particular caution is required for estimation outside the data set. Here the polynomial can grow rapidly. Consider for example the polynomial

$$y = a_0x^0 + a_1x^1 + a_2x^2 + a_3x^3 + e \quad (2.18)$$

with a data set given in Figure 2.6. In the figure, three different models are suggested for polynomial degree one, three and nine. As can be seen, all the models give reasonable amplitudes of  $y$  within the given data set, but grow outside this range. The three models fit the data set differently giving different accuracy, which is no surprise. The model with degree one gives a poor estimate, underfitting the data. On the other hand, the model with degree nine seems to give the best estimate. This is even better than for the model with the true degree. However, since the data is noisy some of the unwanted noise characteristics is included in the model, leading to an overfitting of the data to the system.

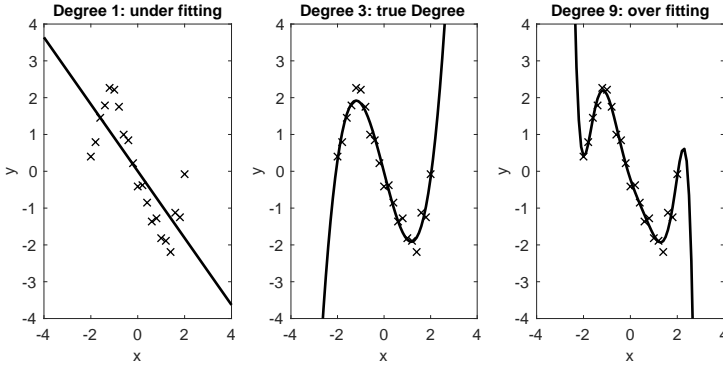


**Figure 2.6:** A general parametric method using a polynomial.

In this thesis, the mathematical structure is known since it is assumed that the true system, for the studied aircraft application, can be described by a state-space equation

$$\begin{aligned} x_{k+1} &= f_S(x_k, u_k, w_k) \\ y_k &= h_S(x_k, u_k, v_k). \end{aligned} \quad (2.19)$$

The desired result from the system identification is a simulation model that can be used for investigation of flight mechanical characteristics. Such a model has the following model structure

$$\begin{aligned} x_{k+1} &= f(x_k, u_k; \theta) \\ y_k &= h(x_k, u_k; \theta) \end{aligned} \quad (2.20)$$

Note that this model has no noise model. During the identification process a noise model can be needed as a way to take proper care of noisy input and output data.

When the parameters have been estimated, the quality of the model has to be validated using a data set  $Z_v^N$  that is different from the set used for the estimation. This has to be done in order to ensure that the model is useful in general, i.e., that the model fit  $F(m, Z)$  is good for all possible data sets from the system and not just the specific data set used during the estimation. Here

$$F(m, Z) = 100 \left( 1 - \frac{\|y_k - \hat{y}_k(\theta)\|_2}{\|y_k - \bar{y}_k\|_2} \right) \quad (2.21)$$

where  $\hat{y}_k(\theta)$  is the estimated output when using the parameters  $\theta$  and  $\bar{y}_k$  is the mean of the output. It should be noted that it is in general good to have a high model fit value, but a perfect model fit of 100% is not expected if noise is present in the validation data.

The identification methods presented here are described in a general sense. A more specific description used for the aircraft application will be given in Chapters 5 to 8.

### 2.3.1 Prediction-error method

The Prediction-Error Method (PEM) [Ljung, 1999] uses model predictions  $\hat{y}_k(\theta)$  of the present outputs, influenced by past inputs and outputs, to compare with the present outputs. A simple predictor for a stable discrete-time nonlinear state-space model can be written as

$$\begin{aligned}\hat{x}_{k+1}(\theta) &= f(\hat{x}_k(\theta), u_k, y_k; \theta) \\ \hat{y}_k(\theta) &= h(\hat{x}_k(\theta), u_k; \theta)\end{aligned}\quad (2.22)$$

where the dynamic model  $f$  is influenced by the measured inputs and outputs. The prediction error is the difference between the measurement and the prediction, given as

$$\varepsilon_k(\theta) = y_k - \hat{y}_k(\theta). \quad (2.23)$$

The PEM is based on the strategy to minimize the prediction-error with respect to the model parameters. This can in general be described as an unconstrained optimization problem with the cost function

$$V_N(\theta, Z^N) = \frac{1}{N} \sum_{k=1}^N l(L(q)\varepsilon_k(\theta)) \quad (2.24)$$

where  $q$  is the time shift operator ( $qy_k = y_{k+1}$ ),  $L(q)$  is a stable linear filter and  $l(\cdot)$  is a nonnegative scalar-valued function. In this thesis, a special choice,  $L(q) = 1$  and  $l(\cdot) = \frac{1}{2}\varepsilon_k(\theta)^T \varepsilon_k(\theta)$ , is used. With this choice the optimization problem of minimizing  $V_N(\theta, Z^N)$  w.r.t  $\theta$  can be written as

$$\underset{\theta}{\text{minimize}} \quad \frac{1}{N} \sum_{k=1}^N \frac{1}{2} \varepsilon_k(\theta)^T \varepsilon_k(\theta) \quad (2.25)$$

or in vector form

$$\underset{\theta}{\text{minimize}} \quad \frac{1}{N} \frac{1}{2} \varepsilon(\theta)^T \varepsilon(\theta) \quad (2.26)$$

where  $\varepsilon(\theta) = [\varepsilon_1(\theta)^T \ \varepsilon_2(\theta)^T \ \dots \ \varepsilon_N(\theta)^T]^T$ . The argument that gives the solution to this problem is denoted  $\hat{\theta}$ . It should be noted that, even though the optimization is unconstrained, the predictors used in this thesis have to be stable, which gives a kind of internal constraint.

If  $\hat{y}_k(\theta)$  can be written as a linear regression,  $\hat{y}_k(\theta) = \phi_k^T \theta$ , where  $\phi_k$  are regressors that include past inputs and outputs. The solution to the minimization in (2.25) and (2.26) can be expressed analytically as

$$\hat{\theta}^{LS} = \left( \frac{1}{N} \sum_{k=1}^N \phi_k \phi_k^T \right)^{-1} \frac{1}{N} \sum_{k=1}^N \phi_k y_k = (\Phi^T \Phi)^{-1} \Phi^T y \quad (2.27)$$



where  $\Phi = [\phi_1 \ \phi_2 \ \dots \ \phi_N]^T$ . This is called the Least-Squares approach and will give a solution to the problem provided that the inverse exists. Assume that the true output in (2.19) can be written as

$$y = \Phi^T \theta_0 + v_0 \quad (2.28)$$

where  $\theta_0$  contains the true parameters and  $v_0$  is the true measurement noise. Using the true output in (2.27) gives

$$\hat{\theta}^{LS} = (\Phi^T \Phi)^{-1} \Phi^T y = \theta_0 + (\Phi^T \Phi)^{-1} \Phi^T v_0. \quad (2.29)$$

The expectation  $E[\hat{\theta}^{LS}]$  of the estimated parameters and the associated covariance  $\text{Cov}[\hat{\theta}^{LS}] = E[(\hat{\theta}^{LS} - E[\hat{\theta}^{LS}])(\hat{\theta}^{LS} - E[\hat{\theta}^{LS}])^T]$  are given as

$$E[\hat{\theta}^{LS}] = \theta_0 + E[(\Phi^T \Phi)^{-1} \Phi^T v_0] \quad (2.30a)$$

$$\begin{aligned} \text{Cov}[\hat{\theta}^{LS}] &= E[(\Phi^T \Phi)^{-1} \Phi^T v_0 v_0^T \Phi (\Phi^T \Phi)^{-1}] \\ &\quad - (E[(\Phi^T \Phi)^{-1} \Phi^T v_0])(E[(\Phi^T \Phi)^{-1} \Phi^T v_0])^T. \end{aligned} \quad (2.30b)$$

To have an unbiased estimate, the second term in the expectation  $E[\hat{\theta}^{LS}]$  in (2.30a) has to be zero. This will be the case if the inverse exists, the noise  $v_0$  has zero mean, i.e.  $E[v_0] = 0$ , and is independent of the regressors  $\Phi$ . If  $E[v_0 v_0^T] = \sigma^2 I$  is the covariance of  $v_0$ , then

$$E[\hat{\theta}^{LS}] = \theta_0 \quad (2.31a)$$

$$\text{Cov}[\hat{\theta}^{LS}] = \sigma^2 (\Phi^T \Phi)^{-1}. \quad (2.31b)$$

In the cases when (2.25) cannot be solved analytically a numerical approach has to be used. Then some method that searches for a sequence of  $\theta$ -values that iteratively improves  $V_N(\theta, Z^N)$  can be used. A general type of search routine is given by

$$\hat{\theta}^{i+1} = \hat{\theta}^i - \mu^i [R_N^i]^{-1} V_N'(\hat{\theta}^i, Z^N) \quad (2.32)$$

where  $i$  indicates the iteration number and  $\mu^i$  is the step length that should be chosen such that the loss function  $V_N(\theta, Z^N)$  decreases with increasing number of iterations. By changing  $R_N^i$  the search direction given by the gradient  $V_N'(\hat{\theta}^i, Z^N)$  is modified. Here, the choice called the Levenberg-Marquardt procedure [Nocedal and Wright, 2006] is used, for which

$$R_N^i = J^T J + \lambda_{LM}^2 I_{n_\theta \times n_\theta} \quad (2.33)$$

where  $J = \frac{1}{N} \frac{\partial \epsilon(\theta)}{\partial \theta}$  and  $\lambda_{LM}$  is used for regularization, i.e., to take care of numerical problems, typically when  $J^T J$  is close to singular. Putting  $\lambda_{LM} = 0$  gives the well-known Gauss-Newton approach.

No analysis of convergence or consistency concerning the PEM is given here, but these aspects can be found in Ljung [1978]. It should be noted that the nonlinear

versions of the Kalman filter [Kalman, 1960] use approximations that lead to convergence properties that are hard to analyze. A good starting guess of the solution will help the convergence. This aspect is investigated in the aircraft application in Chapter 8.

### 2.3.2 State and parameter estimation method

Another method, using prediction errors, is to augment the parameter vector with the states at each time step

$$\vartheta = [x_0^T \dots x_{N-1}^T \theta^T]^T. \quad (2.34)$$

Hence, the predictor becomes

$$\hat{y}_k(\vartheta) = h(u_k; \vartheta). \quad (2.35)$$

The dynamic equation for  $x_k$  is not needed here since the states are included in the parameter vector  $\vartheta$ . Then the prediction error in (2.23) is rewritten as

$$\epsilon_k(\vartheta) = y_k - \hat{y}_k(\vartheta). \quad (2.36)$$

This leads to a constrained optimization problem, described in Mulders et al. [2010] that can be written as

$$\begin{aligned} & \underset{\vartheta}{\text{minimize}} \quad \frac{1}{2} \epsilon_k(\vartheta)^T \epsilon_k(\vartheta) \\ & \text{subject to} \quad F(\vartheta) = 0 \end{aligned} \quad (2.37)$$

where  $\epsilon(\vartheta) = [\epsilon_1(\vartheta)^T \ \epsilon_2(\vartheta)^T \ \dots \ \epsilon_N(\vartheta)^T]^T$ . For this, (2.22) has been used to formulate the constraint with

$$F(\vartheta) = \begin{bmatrix} f(x_0, u_0, \theta) - x_1 \\ f(x_1, u_1, \theta) - x_2 \\ \vdots \\ f(x_{N-1}, u_{N-1}, \theta) - x_N \end{bmatrix} \quad (2.38)$$

It should be noted that this constraint does not take care of any process noise. If process noise is present, a noise model has to be included, otherwise the method can lead to biased results. The solution of the minimization is given by, as in (2.32), iteratively calculating the parameters

$$\vartheta^{i+1} = \vartheta^i + \delta\vartheta \quad (2.39)$$

until convergence. Here  $\delta\vartheta$  is calculated from a constrained version of the general search routine (2.32) using the Levenberg-Marquardt procedure (2.33), which gives

$$\begin{bmatrix} J_1^T J_1 + \lambda_{LM}^2 I_{n_\vartheta, n_\vartheta} & J_2^T \\ J_2 & 0 \end{bmatrix} \begin{bmatrix} \delta\vartheta \\ \lambda \end{bmatrix} = \begin{bmatrix} -J_1^T \epsilon \\ -F \end{bmatrix} \quad (2.40)$$

where  $J_1 = \frac{\partial \epsilon(\vartheta)}{\partial \vartheta}$  and  $J_2 = \frac{\partial F(\vartheta)}{\partial \vartheta}$ . The parameter  $\lambda_{LM}$  is used for regularization in the same way as in (2.33). The model parameter estimates  $\hat{\theta}$  is extracted from  $\hat{\vartheta}$ .

### 2.3.3 Instrumental variable method

If there is correlation between the regressors  $\phi_k$  and the noise  $v_k$  when using the Least-Squares approach to solve the linear regression problem, the solution can be biased. An alternative that can be used to give consistent solutions and that is a generalization of the Least-Squares method uses instrumental variables  $\zeta_k$ , which are independent of the noise but correlated with the regressors. The Instrumental-Variable (IV) method [Söderström and Stoica, 2002], which is not a PEM, gives the parameter estimate

$$\hat{\theta}^{IV} = \left( \frac{1}{N} \sum_{k=1}^N \zeta_k \phi_k^T \right)^{-1} \frac{1}{N} \sum_{k=1}^N \zeta_k y_k = (Z^T \Phi)^{-1} Z^T y \quad (2.41)$$

where  $Z = [\zeta_1 \ \zeta_2 \ \dots \ \zeta_N]^T$ . This will, as in the Least-Squares approach, give a solution if the inverse exists. As can be seen, the structures of the solution in the two approaches are similar. Optimal instruments in a variance sense are dependent on the true system, which is unknown since it is the goal of the identification. However, one way would be to use a prior estimate of the model to generate noise-free data, which would improve the identification [Ljung, 1999, Chapter 7, p. 225].

### 2.3.4 State estimation method

A common method in the navigation community when treating unknown parameters is to add them as static states in the model,

$$\bar{x}_k = \begin{pmatrix} x_k \\ \theta_k \end{pmatrix}. \quad (2.42)$$

This gives rise to the following state-space model

$$\begin{aligned} \bar{x}_{k+1}(\theta_k) &= \begin{pmatrix} x_{k+1}(\theta_k) \\ \theta_{k+1} \end{pmatrix} = \begin{pmatrix} f(x_k(\theta_k), u_k; \theta_k) + w_k \\ \theta_k + w_{\theta,k} \end{pmatrix} \\ y_k(\theta_k) &= h(\bar{x}_k(\theta_k), u_k) \end{aligned} \quad (2.43)$$

where  $w_{\theta,k}$  is a small artificial noise term that allows the parameters to vary during the identification. The identification problem can be solved by using a recursive filter to produce improved state estimates in a similar way as the Extended Kalman filter [Welch and Bishop, 2006] does when fusing state estimates with measurement data to minimize the state variance. Since, in the present case, the model parameters are a part of the states they will also be improved during the recursive filtering.

## 2.4 Testing

When designing an experiment, care has to be taken as to get enough information in the estimation and validation data. This has to be done so that a proper estimation can be performed. When the data has been collected, missing information

means that further experiments have to be performed. This can be a costly and time-consuming process. This makes the experiment design a crucial part of the system identification process.

The systems under consideration can be unstable and work in closed-loop. This means that the reference signal, i.e., the pilot input, has to be persistently exciting, meaning that it leads to an input that will excite the system so that the model parameters can be uniquely estimated.

## 2.5 Simple example

Here, a simple example is given to illustrate the identification process. Consider a F104-A Starfighter aircraft, as shown in Figure 2.7. The goal is to identify a model that can be used to describe a pure rolling maneuver at low speeds. This type of maneuver is controlled by the ailerons, which are a control surface pair that is deflected asymmetrically ( $\delta_a$ ), positioned at the trailing edge of the outer part of the wing. The response is a motion given by the roll rate ( $p$ ) around the length-axis of the aircraft. The system can be described by the model structure

$$\dot{p} = L_p p + L_{\delta_a} \delta_a, \quad (2.44)$$

which comes from prior knowledge of flight mechanics. Here  $L_{\delta_a}$  and  $L_p$  are the model parameters to be estimated. They are called aileron effectiveness and roll damping respectively.

Assume that two datasets,  $Z_e^N$  and  $Z_v^N$ , at low speed and low altitude are available. These datasets usually come from flight tests, but are here given by simulations. The true parameters,  $L_p = -1.3$  and  $L_{\delta_a} = 4.66$ , used come from Nelson [1998]. The dataset  $Z_e^N$ , an aileron step input shown in Figure 2.8, is used for the estimation. White noise with zero mean and a standard deviation of 0.1 deg/s has been added to the measurements, which can be seen in the figure.

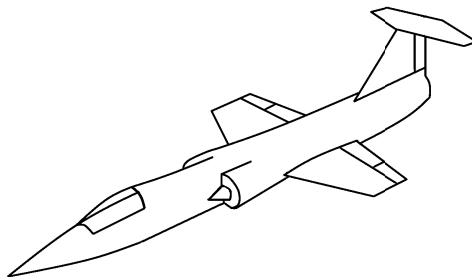


**Figure 2.7:** F104A Starfighter.

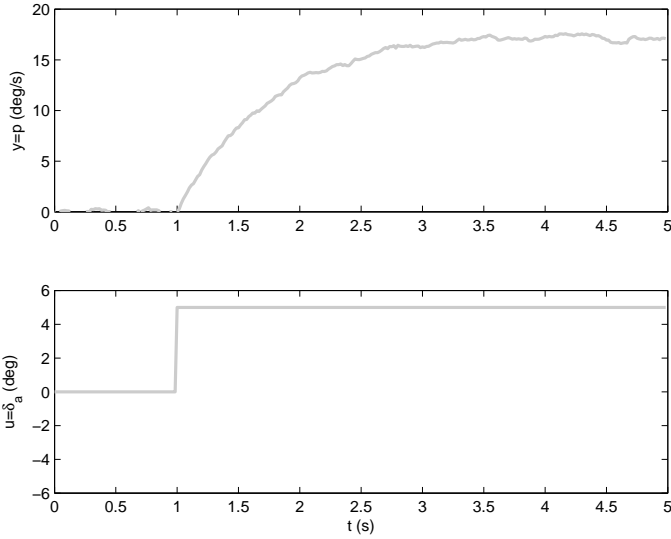


**Figure 2.8:** Dataset  $Z_e^N$ : an aileron step input and the roll response.

The identification is done in discrete time since data are sampled. For this a simple Euler forward discretization of (2.44) with sample time  $T_s = (1/60)$  s has been used, which resulted in the model

$$p_k = (1 + T_s L_p)p_{k-1} + T_s L_{\delta_a} \delta_{a, k-1}. \quad (2.45)$$

By looking at this equation it is possible to define the regression  $\hat{y}_k(\theta) = \phi_k^T \theta$  with the regressors

$$\phi_k = [p_{k-1} \quad \delta_{a, k-1}]^T \quad (2.46)$$

and the parameters

$$\theta = [\theta_1 \quad \theta_2]^T = [(1 + T_s L_p) \quad (T_s L_{\delta_a})]^T \quad (2.47)$$

Here the Least-Squares approach, described by (2.27), can be used to estimate  $\hat{\theta}_1$  and  $\hat{\theta}_2$ . These are then used to calculate the estimate of  $\hat{L}_p$  and  $\hat{L}_{\delta_a}$ , which are the model parameters of interest in the continuous-time equation (2.44). In this case the Least-Squares estimate based on the estimation data is  $\hat{L}_p = -1.2941$  and  $\hat{L}_{\delta_a} = 4.6116$ .

To see if the estimated model is useful, a validation is performed on the second dataset  $Z_v^N$ , an aileron doublet shown as the solid line in Figure 2.9. White noise with zero mean and a standard deviation of 0.1 deg/s has, also here, been added to the measurements. The model predicts the new data well as can be seen by the dashed line in the figure. In this example the model fit (2.21) is 96.87% and

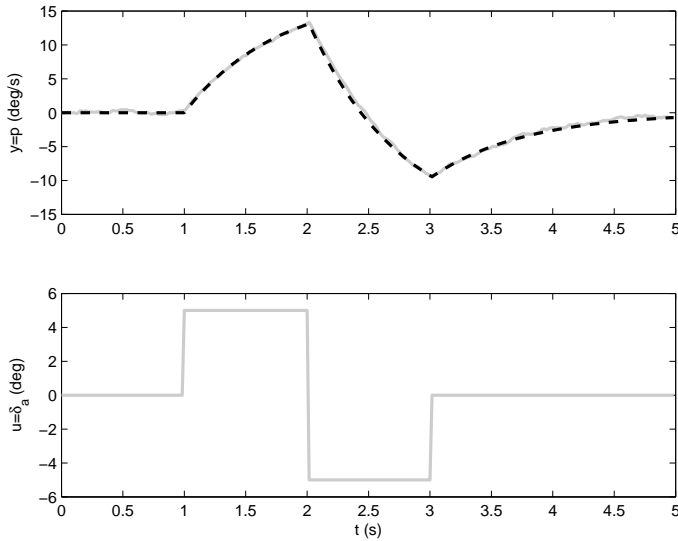


**Figure 2.9:** Dataset  $Z_v^N$ : an aileron doublet input and roll response for the true system (solid) and identified model (dashed).

one can conclude that the estimated model clearly is useful for describing roll maneuvers at low speed and low altitude. Comparing the estimated parameters  $\hat{L}_p = -1.2941$  and  $\hat{L}_{\delta_a} = 4.6116$  with  $L_p = -1.3$  and  $L_{\delta_a} = 4.66$  used to simulate the true system, one can see that they are very close.

This simple example was only used to illustrate the identification process. It was based on a simple system. The systems of interest in this thesis are more complex since they are unstable and/or nonlinear working under closed-loop conditions. All these aspects make the identification problem harder. The next chapter describes the aircraft system in more detail, mostly for those without an aeronautical background.



# 3

---

## Aeronautics

*“It is possible to fly without motors, but not without knowledge and skill”*  
- Wilbur Wright (1867 - 1912)

In the previous chapter, systems and modeling of systems were described in a general sense. Here the flight mechanical system characteristics of an aircraft and the corresponding modeling are going to be described in some detail to prepare for the theory and results in the coming chapters. The aircraft flight mechanics are given as the stability and control properties during maneuvering. To get the whole picture of this subject, the reader is recommended to look into Etkin [1972], Stevens and Lewis [1992] and Nelson [1998], which are considered as standard references.

### 3.1 Definitions

To be able to describe the flight mechanical system there are two coordinate systems that have to be considered. First an Earth-fixed system  $S_E$  ( $O_E x_E y_E z_E$ ) is defined, as shown in Figure 3.1, with the origin at a fixed point on the Earth's surface and the axes pointing north, east and down. For all practical purposes concerning aircraft maneuvering the Earth rotation is ignored and a “Flat Earth” assumption is made, i.e., the local surface curvature is assumed to be zero.  $S_E$  can then be used as an inertial reference system. The second coordinate system is a Body-fixed system  $S_B$  ( $O_B x_B y_B z_B$ ) with the origin fixed in the aircraft center of gravity and the axes pointing forward (roll axis), to the right (pitch axis) and down (yaw axis), all from the pilot's point of view. Traditionally, the axes of  $S_B$  are given as ( $Oxyz$ ) as in Figure 3.2. The Euler angles  $[\Phi \ \Theta \ \Psi]^T$  that describe the rotation between  $S_E$  and  $S_B$  are called the roll, pitch and yaw angles, respectively.



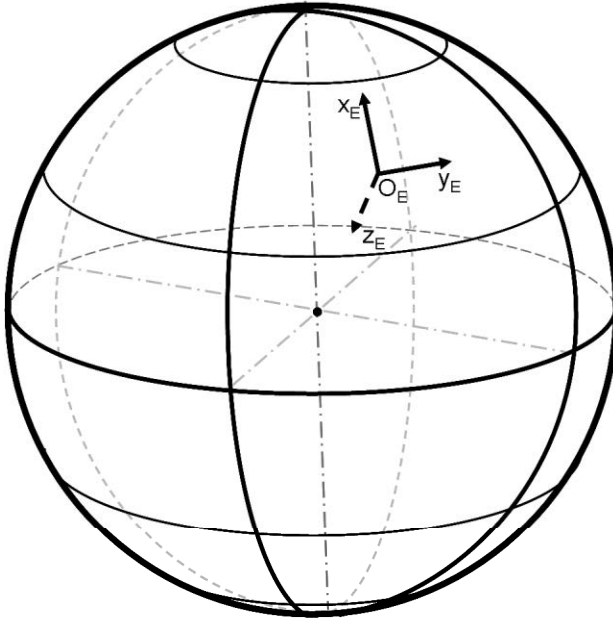


**Figure 3.1:** Earth system: Used as inertial system.

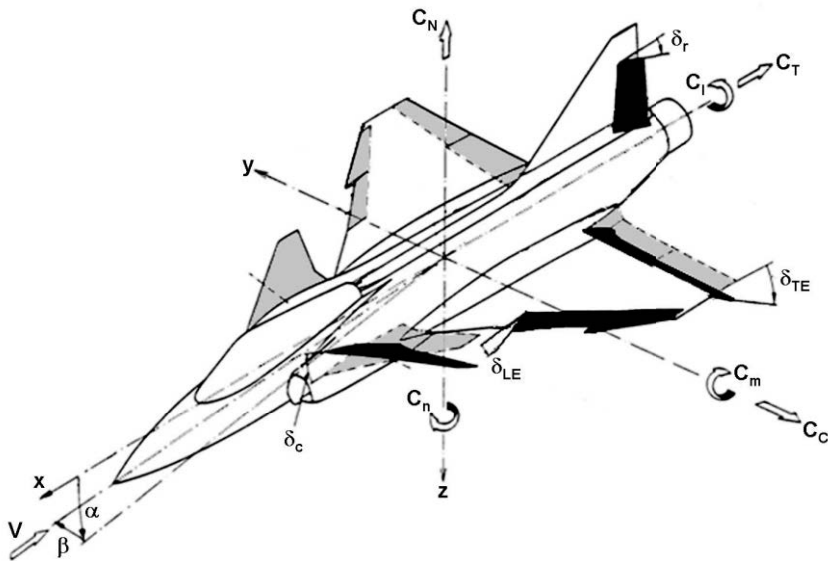


**Figure 3.2:** Body System: Used to define stability and control parameters.

The kinematic equations describe the motion of the aircraft. For this, parameters concerning the translation and rotation of the aircraft have to be defined. The translation is given by the velocity  $\mathbf{V} = [u \ v \ w]^T$ , which is the aircraft velocity relative to the air. Here  $u$ ,  $v$  and  $w$  are the components in the  $S_B$  system. The velocity is often given in spherical coordinates  $\mathbf{V} = [V \ \alpha \ \beta]^T$  shown in Figure 3.2. The components are defined as

$$\begin{aligned} V &= \sqrt{u^2 + v^2 + w^2} && \text{airspeed} \\ \alpha &= \tan^{-1}\left(\frac{w}{u}\right) && \text{angle-of-attack} \\ \beta &= \sin^{-1}\left(\frac{v}{V}\right). && \text{angle-of-sideslip} \end{aligned} \quad (3.1)$$

An often used alternative definition of airspeed is the Mach number,  $M$  or Mach, which is the ratio between the airspeed  $V$  and the speed of sound  $a$ ,  $M = \frac{V}{a}$ . It should be noted that the speed of sound changes with the altitude, meaning that the Mach number will change with altitude for a constant airspeed.

The rotation of the aircraft is given by the angular velocity  $\boldsymbol{\omega} = [p \ q \ r]^T$  around the axes of  $S_B$ . Here  $p$ ,  $q$  and  $r$  are called the roll, pitch and yaw angular velocity, respectively.

To be able to describe the dynamics, i.e., the forces and moments that generate the kinematic motion, the parameters that affect the forces and moments acting on the aircraft have to be defined. There are three major sources that contribute to the forces and moments. The first is the gravitational force ( $F_G = mg$ ) which acts on the aircraft mass  $m$  and gives rise to a force in the center of gravity. Here,  $g$  is the gravity vector pointing towards the center of the earth. In addition, due to the rotation of the aircraft, the mass in itself gives rise to inertial forces and moments. The corresponding part of the mass in the force equation is the moment of inertia  $I$  in the moment equation. This is defined as

$$I = \begin{bmatrix} I_{xx} & I_{xy} & I_{xz} \\ I_{xy} & I_{yy} & I_{yz} \\ I_{xz} & I_{yz} & I_{zz} \end{bmatrix} \quad (3.2)$$

where the components are given by

$$\begin{aligned} I_{xx} &= \int_m (y^2 + z^2) \, dm, & I_{yy} &= \int_m (x^2 + z^2) \, dm, & I_{zz} &= \int_m (x^2 + y^2) \, dm \\ I_{xy} &= \int_m (xy) \, dm, & I_{yz} &= \int_m (yz) \, dm, & I_{xz} &= \int_m (xz) \, dm. \end{aligned} \quad (3.3)$$

Here the coordinates  $(x, y, z)$  are viewed as functions of the mass distribution, i.e., they give the distance to every incremental mass  $dm$ . The second source is the propulsion, ( $F_P = T_e$ ) where  $T_e$  is the installed engine thrust vector. This depends on the propulsion system used. Gliders use gravity ( $F_P$  is then not used), some aircraft use the power from one or more engine driven propellers, other

aircraft use the thrust from one or several jet engines. The thrust depends on the throttle setting  $\delta_{PLA}$  (Power Leverage Angle), airspeed  $V$  defined above, atmospheric temperature  $T_a$  and pressure altitude  $H_p$  defined as the altitude in the ISA (International Standard Atmosphere, ISO 2533:1975) with the same pressure as measured by the aircraft. Generally, the propulsive force has its main component in the  $x$ -direction in the body system. For military aircraft with the engine embedded in the fuselage the thrust vector is often very closely aligned with the  $x$ -axis. For aircraft with the engines at an offset from the  $x$ -axis there will also be a pitching and/or yawing moment due to the thrust. The sizes of these contributions depend on the offset size. The third source is the aerodynamic forces ( $F_A$ ) and moments ( $M_A$ ), which in a flight mechanical perspective come from the interaction between the airflow and the geometrical surface shape of the aircraft. The components in  $S_B$ ,  $[T \ C \ N]^T$  are called Tangential, Side and Normal force,  $[\mathcal{L} \ \mathcal{M} \ \mathcal{N}]^T$  are called Rolling, Pitching and Yawing moment. These are defined as

$$\begin{aligned} T &= q_a S C_T, & C &= q_a S C_c, & N &= q_a S C_N \\ \mathcal{L} &= q_a S b C_l, & \mathcal{M} &= q_a S c C_m, & \mathcal{N} &= q_a S b C_n \end{aligned} \quad (3.4)$$

where  $q_a = \frac{1}{2}\rho V^2$  is the dynamic pressure,  $\rho$  is the air density,  $S$  is a reference area,  $c$  is the longitudinal reference length and  $b$  is the lateral/directional reference length. The reference entities are usually the wing area, wing mean aerodynamic chord and wingspan, of the main wing respectively. The coefficients  $C_x$ ,  $x = T, C, N, l, m, n$ , are commonly used in the field of aerodynamics. These are non-dimensional versions of the forces and moments. When describing the equilibrium condition of flight dynamics, lift  $L$  and drag  $D$  are used. The relation to the body fixed forces are defined as

$$\begin{aligned} L &= N \cos(\alpha) - T \sin(\alpha) \\ D &= T \cos(\alpha) + N \sin(\alpha). \end{aligned} \quad (3.5)$$

Note that the angle-of-sideslip is assumed to be zero and hence neglected. Lift and drag are also used for flight performance calculations, typically describing the aircraft range or take-off/landing properties.

The above definitions apply to all types of aircraft regardless of whether it is a canard configuration, as in Figure 3.2, or a conventional tail configuration or even a V-tail configuration. However, the way an aircraft is controlled is specific for each type. The most common way to control an aircraft is to deflect one or more control surfaces, thereby changing the aerodynamics, to rotate the aircraft around the different axes of  $S_B$ . The surface deflection is named by the Greek symbol  $\delta$  with a subscript to define its function. The deflection is defined positive as shown in Figure 3.2 for the  $\delta_{TE}$  (Trailing Edge),  $\delta_{LE}$  (Leading Edge) and the  $\delta_c$  (Canard). Note here that the  $\delta_r$  (Rudder) is a type of trailing edge surface.

## 3.2 Flight mechanics

The flight mechanical characteristics of an aircraft are about equilibrium, stability and control. Equilibrium in aeronautics is called trim. This is when all accelerations and angular accelerations are zero, i.e., when the sum of all forces and the sum of all moments are zero. This is the same definition as for a general system. Figures 3.3 and 3.4 show a typical longitudinal trim condition for an F16 aircraft flying at low altitude and low speed. The pitching moment is zero and the lift balances the gravitational force, i.e., the weight. This results in a drag that gives the required thrust. The aircraft has to meet this with the thrust available given by the installed engine. The balancing is here done by the elevator deflection and angle-of-attack for a fixed leading and trailing edge flap setting. In this specific case,  $\delta_e = -1.35^\circ$  and  $\alpha = 7.55^\circ$ .

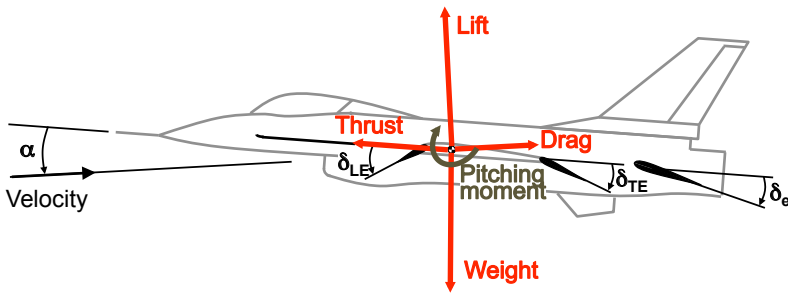


*Figure 3.3: Forces and moments on an F16 aircraft.*

In addition to the general stability definitions from Chapter 2, which can be used to characterize the aircraft motion, a specific definition called static stability is used in flight mechanics. This stability is often used to describe the static moment characteristics of the aircraft. The moments are evaluated around the body-fixed axes, which have their origin at the center of gravity. The mass distribution and thus the center of gravity will change with internal movement of mass such as fuel or passengers as well as mounting or dropping of external stores.

An aircraft is said to be pitch stable when its pitching moment derivative with respect to the angle-of-attack is negative ( $M_\alpha = \partial M / \partial \alpha < 0$ ). A disturbance that changes the angle-of-attack from the trim condition will in this case create a moment, leading to a motion, which will change the angle-of-attack back towards the trim condition. If the aircraft were unstable, then a motion would change the angle-of-attack away from the trim condition. In the same way stability in roll is defined to be when the rolling moment derivative is negative with respect to the angle-of-sideslip ( $\mathcal{L}_\beta = \partial \mathcal{L} / \partial \beta < 0$ ) and stability in yaw is defined to be when the yawing moment derivative is positive with respect to the angle-of-sideslip ( $\mathcal{N}_\beta = \partial \mathcal{N} / \partial \beta > 0$ ).

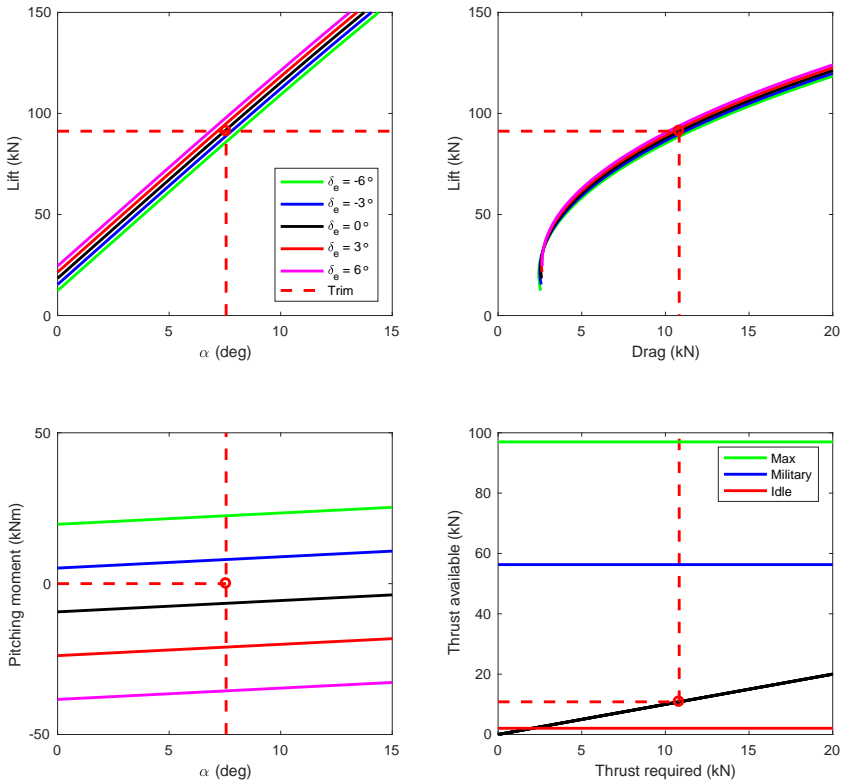


**Figure 3.4:** For the trim condition, the weight is balanced by the Lift and the pitching moment is zero. The condition gives a specific combination of the angle-of-attack and the elevator deflection resulting in a aerodynamic drag, which has to be balanced with the engine thrust. The red dashed lines give all these values. To the lower right the black line gives that thrust required equals thrust available.

The concept of static stability is shown in Figure 3.5, where a solid line is stable and a dashed line is unstable. The stability definition in Chapter 2 is closely related to what in aeronautics is called dynamic stability, which is about the damping characteristics of the aircraft motion. The size of the pitch and yaw damping is mainly dependent on the main stabilizing surfaces, i.e., the horizontal and vertical stabilizers. Roll damping on the other hand mainly depends on the wingspan.

For the description of control, focus in this thesis is on the JAS 39 Gripen multi-role aircraft. The primary control functions are called aileron ( $\delta_a$ ) for roll control, elevator ( $\delta_e$ ) for pitch control and rudder ( $\delta_r$ ) for yaw control. These control functions are made by deflecting one or more of the control surfaces as

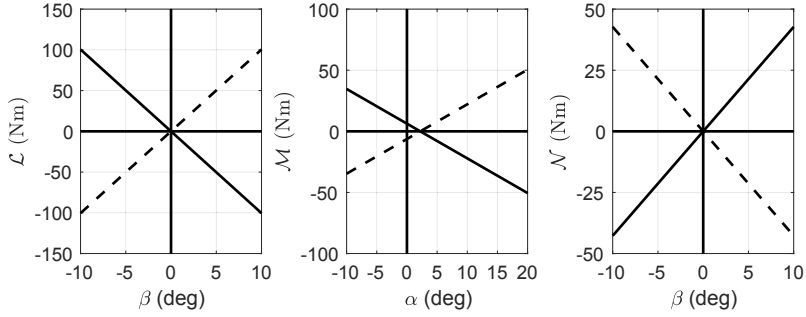


**Figure 3.5:** Static stability for roll, pitch and yaw (solid is stable, dashed is unstable).

$$\delta_a = \frac{\delta_{TE,Left} - \delta_{TE,Right}}{2} \quad (3.6)$$

and

$$\delta_e = \frac{\delta_{TE,Left} + \delta_{TE,Right}}{2}. \quad (3.7)$$

The rudder control is defined in Figure 3.2. For JAS 39 Gripen there is an additional control function mainly used for pitch control and that is the canard ( $\delta_c$ ). This function is similar to that for the elevator

$$\delta_c = \frac{\delta_{c,Left} + \delta_{c,Right}}{2}. \quad (3.8)$$

A positive elevator deflection gives a negative pitching moment and a positive canard deflection gives a positive pitching moment. The idea is to be able to use combinations of elevator and canard settings to improve the aircraft performance and maneuverability. Positive aileron and rudder deflections will give a positive rolling moment and negative yawing moment, respectively. These two last controls also have secondary effects. A positive rudder deflection will contribute to a positive rolling moment. The aileron deflection gives a contribution to the yawing moment that can be positive or negative depending on the speed and the elevator setting. To improve take-off and landing performance, flaps are used. For the JAS 39 Gripen, the trailing edge flaps coincide with the elevator. In addition, there are leading edge flaps ( $\delta_{LE}$ ). Flaps are used to increase the wing lift, which makes it possible to fly at lower speeds for a given weight. For a fighter aircraft the flaps are also used to improve turning performance. With the flaps deflected it is possible to make tighter turns. To illustrate the complexity of the flight mechanical characteristics of a fighter aircraft, an example showing the different sources, is given in Appendix A. This is taken from the Admire simulation environment described in Forssell and Nilsson [2005], which features an aircraft similar to Gripen.

The process noise  $w(t)$  comes, in a flight mechanical point of view, from atmospheric turbulence. This is a chaotic, irregular random motion of air due to convective heating and wind shear in the atmosphere. This leads to internal friction in the atmosphere as layers of air close together get different velocities. Consider for example a warm summer day. A paved asphalt road can then be about 40% hotter than the grass surfaces on either side of the road. Therefore the air above the asphalt will get warmer than the air above the grass and hence, due to convection, ascend faster. This difference in air speed gives rise to friction, which in turn will give rise to what is called *thermal turbulence*. Another source of friction is ground structures such as forests, hills, mountains and buildings. When air flows over and around these, there will be friction between the air and the surfaces, which will create turbulence. This type of turbulence is called *mechanical turbulence*. Together with the thermal turbulence, this low level turbulence can reach up to about two km if the turbulence is severe. At higher altitudes there is thermal turbulence due to instabilities in weather systems when hot air ascend. In the worst cases these instabilities lead to thunderstorms. There is also mechanical turbulence due to larger two-dimensional atmospheric eddies such as rotations around low or high-pressure centers or at cold or warm weather fronts. The larger eddies give energy to smaller eddies, which in turn give energy to even smaller eddies and when a critical scale is reached, the turbulence gets three-dimensional. The intensity of turbulence can vary from light to severe and the length scales can also change from centimeters up to kilometers. These effects vary both with space and time.

The other noise source is measurement noise  $v(t)$ . This comes from inaccuracies in the sensors used, but can also come from the positioning of and the environment around the sensor. As an example, turbulence can affect the angle-of-attack vane to give false measurements relative the effect on the aircraft as a whole.

### 3.3 Modeling

With the definitions and system description at hand it is now possible to look at the modeling of the flight mechanical motion of the aircraft.

#### 3.3.1 System modeling

The equations describing the dynamics of an aircraft in motion are based on Newton's second law. The force equation is given by

$$\mathbf{F} = m\dot{\mathbf{V}} + \boldsymbol{\omega} \times m\mathbf{V} \quad (3.9)$$

Here,  $\mathbf{F}$  on the left hand side is the sum of the forces acting on the aircraft that come from the engine propulsion, the aerodynamics and gravity. The right hand side represents the change in motion. The first term comes from the well-known momentum change, i.e., mass times change in velocity (often given as mass times acceleration), and the second term has to be added since the motion is described

in a system ( $S_B$ ) that in itself is in rotational movement relative to the inertia system, which in this case is the earth ( $S_E$ ). The equation can be written as

$$\begin{bmatrix} T_{e,x} \\ 0 \\ 0 \end{bmatrix} + \begin{bmatrix} -T \\ -C \\ -N \end{bmatrix} + \begin{bmatrix} -mg \sin(\Theta) \\ mg \cos(\Theta) \sin(\Phi) \\ mg \cos(\Theta) \cos(\Phi) \end{bmatrix} = m \begin{bmatrix} \dot{u} \\ \dot{v} \\ \dot{w} \end{bmatrix} + \begin{bmatrix} p \\ q \\ r \end{bmatrix} \times m \begin{bmatrix} u \\ v \\ w \end{bmatrix} \quad (3.10)$$

Note here that the gravity components depend on the orientation of the aircraft relative to the earth. Looking at the components in the aircraft body system ( $S_B$ ), the equations can be split up as

$$\begin{aligned} T_{e,x} - T - mg \sin(\Theta) &= m\dot{u} + [m(qw - rv)] \\ -C + mg \cos(\Theta) \sin(\Phi) &= m\dot{v} + [m(ru - pw)] \\ -N + mg \cos(\Theta) \cos(\Phi) &= m\dot{w} + [m(pv - qu)] \end{aligned} \quad (3.11)$$

which can be rewritten as

$$\begin{aligned} \dot{u} &= \frac{1}{m} T_{e,x} - \frac{1}{m} T - g \sin(\Theta) - qw + rv \\ \dot{v} &= -\frac{1}{m} C + g \cos(\Theta) \sin(\Phi) - ru + pw \\ \dot{w} &= -\frac{1}{m} N + g \cos(\Theta) \cos(\Phi) - pv + qu \end{aligned} \quad (3.12)$$

These give the change in velocity as a function of time. To get the time change for the angular rotation velocity, Newton's second law for the moment has to be used. This is given by

$$\mathbf{M} = I\dot{\omega} + \omega \times I\omega \quad (3.13)$$

where  $\mathbf{M}$  is the sum of all moments. The derivation follow the same principle as for the forces, but the engine propulsion and the gravity give no contribution. This is because the forces from these sources act in the center of gravity for the aircraft under consideration. The component equation can then be written as

$$\begin{aligned} \mathcal{L} &= I_{xx}\dot{p} + [-I_{xz}\dot{r} + (I_{zz} - I_{yy})qr - I_{xz}pq] \\ \mathcal{M} &= I_{yy}\dot{q} + [(I_{xx} - I_{zz})rq + I_{xz}(p^2 - r^2)] \\ \mathcal{N} &= I_{zz}\dot{r} + [-I_{xz}\dot{p} + (I_{yy} - I_{xx})pq + I_{xz}qr] \end{aligned} \quad (3.14)$$

which can be rewritten as

$$\begin{aligned} \dot{p} &= \frac{I_{zz}}{I_*^2} \mathcal{L} - \frac{I_{xz}}{I_*^2} \mathcal{N} + \frac{I_{xz}(I_{yy} - I_{xx} - I_{zz})}{I_*^2} pq + \frac{I_{xz}^2 + I_{zz}(I_{zz} - I_{yy})}{I_*^2} qr \\ \dot{q} &= \frac{1}{I_{yy}} \mathcal{M} - \frac{(I_{xx} - I_{zz})}{I_{yy}} rq - \frac{I_{xz}}{I_{yy}} (p^2 - r^2) \\ \dot{r} &= \frac{I_{xx}}{I_*^2} \mathcal{N} + \frac{I_{xz}}{I_*^2} \mathcal{L} + \frac{I_{xz}(I_{yy} - I_{xx} - I_{zz})}{I_*^2} qr + \frac{I_{xz}^2 + I_{xx}(I_{xx} - I_{yy})}{I_*^2} pq \end{aligned} \quad (3.15)$$



where  $I_*^2 = I_{xx}I_{zz} - I_{xz}^2$ . It is assumed that the aircraft under consideration is symmetric in such a way that  $I_{xy} = 0$  and  $I_{yz} = 0$ .

Since the gravity components are dependent on the orientation of the aircraft relative to the earth, kinematic equations that describe the change in orientation have to be used to get a system of equations that gives a unique solution. The change in orientation between the earth system  $S_E$  and the body system  $S_B$  is derived by three consecutive rotations in a specific order. To simplify the description, the origin of the two systems is taken to be the same. Then two systems,  $S_1$  and  $S_2$ , are used to help visualizing the three rotations. The order is first a yaw rotation about  $z_E$ , then a pitch rotation about  $y_1$  and finally a roll rotation about  $x_2$ . This is shown in Figures 3.6 and 3.7.  $S_E$  is used as a fixed inertia system, i.e., it has no angular velocity

$$\begin{aligned} p_E &= 0 \\ q_E &= 0 \\ r_E &= 0 \end{aligned} \tag{3.16}$$

To describe the motion of  $S_1$  relative to  $S_E$ , the angular velocity of  $S_E$  is projected

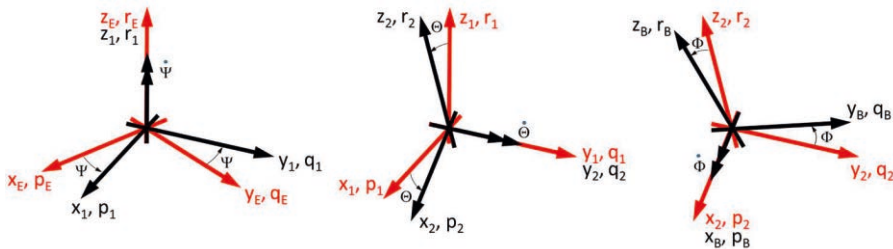


Figure 3.6: Euler rotations in order: yaw, pitch and roll.

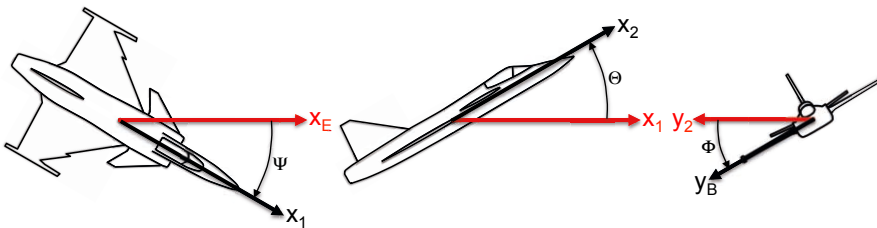


Figure 3.7: Euler rotations for an aircraft.

onto  $S_1$  and then the yaw angular velocity  $\dot{\Psi}$  is added to  $r_E$

$$\begin{aligned} p_1 &= p_E \cos(\Psi) + q_E \sin(\Psi) = 0 \\ q_1 &= q_E \cos(\Psi) - p_E \sin(\Psi) = 0 \\ r_1 &= r_E + \dot{\Psi} = \dot{\Psi} \end{aligned} \quad (3.17)$$

Then the angular velocity of  $S_1$  is projected onto  $S_2$  and the pitch rotation is added to  $q_1$

$$\begin{aligned} p_2 &= p_1 \cos(\Theta) - r_1 \sin(\Theta) = -\dot{\Psi} \sin(\Theta) \\ q_2 &= q_1 + \dot{\Theta} = \dot{\Theta} \\ r_2 &= r_1 \cos(\Theta) + p_1 \sin(\Theta) = \dot{\Psi} \cos(\Theta) \end{aligned} \quad (3.18)$$

Next the angular velocity of  $S_2$  is projected onto  $S_B$  and the roll rotation is added to  $p$

$$\begin{aligned} p &= p_2 + \dot{\Phi} = -\dot{\Psi} \sin(\Theta) + \dot{\Phi} \\ q &= q_2 \cos(\Phi) + r_2 \sin(\Phi) = \dot{\Theta} \cos(\Phi) + \dot{\Psi} \cos(\Theta) \sin(\Phi) \\ r &= r_2 \cos(\Phi) - q_2 \sin(\Phi) = \dot{\Psi} \cos(\Theta) \cos(\Phi) - \dot{\Theta} \sin(\Phi) \end{aligned} \quad (3.19)$$

Finally, this is solved for the Euler angular velocities, which gives

$$\begin{aligned} \dot{\Phi} &= p + q \sin(\Phi) \tan(\Theta) + r \cos(\Phi) \tan(\Theta) \\ \dot{\Theta} &= q \cos(\Phi) - r \sin(\Phi) \\ \dot{\Psi} &= q \sin(\Phi) \sec(\Theta) + r \cos(\Phi) \sec(\Theta) \end{aligned} \quad (3.20)$$

where  $\sec(\Theta) = 1/\cos(\Theta)$ . Equations (3.12), (3.15) and (3.20) make up the basic model structure for the flight mechanical motion.

### 3.3.2 Noise modeling

In addition to the system model, the modeling of realistic noise properties is needed to be able to simulate real flight test data. Both process noise  $w(t)$  and measurement noise  $v(t)$  will be used in the coming chapters. Here the mathematical descriptions of these are given.

For the process noise, the Dryden continuous turbulence model, described in U.S. military specification MIL-F-8785C (1980), has been used. Only turbulence above 610m (2000ft) is considered. Below this altitude the airflow and thus also the turbulence is affected by the ground topography such as trees, mountains and buildings as well as by the vertical air movement due to solar heating. Over 610m these effects are greatly reduced and the turbulence is said to be isotropic, meaning that the total energy content is equal in all directions. However, the Dryden model is described relative to the aircraft, which leads to different turbulence effects in different directions. The main idea is to let white noise, representing the isentropic energy, pass through shaping filters that are different depending on

the directions. The filters are given by

$$\begin{aligned}
 F_u(s) &= \frac{1}{1 + \frac{1}{V}s}, & F_v(s) &= \frac{1 + \frac{\sqrt{3}L}{V}s}{(1 + \frac{1}{V}s)^2}, & F_w(s) &= \frac{1 + \frac{\sqrt{3}L}{V}s}{(1 + \frac{1}{V}s)^2} \\
 F_p(s) &= \frac{(\frac{\pi}{4b})^{1/6}}{L^{1/3}(1 + \frac{4b}{\pi V}s)}, & F_q(s) &= \frac{\pm \frac{1}{V}s}{1 + \frac{4b}{\pi V}s} F_w(s), & F_r(s) &= \frac{\pm \frac{1}{V}s}{1 + \frac{3b}{\pi V}s} F_v(s)
 \end{aligned} \tag{3.21}$$

where  $L = 534\text{m}$  (1750ft) is a length scale,  $b$  is the wingspan and  $V$  is the aircraft velocity. The white noises have zero mean and standard deviations given by

$$\begin{aligned}
 \sigma_{wn,u} &= \sigma \sqrt{\frac{2L}{\pi V}}, & \sigma_{wn,v} &= \sigma \sqrt{\frac{L}{\pi V}}, & \sigma_{wn,w} &= \sigma \sqrt{\frac{L}{\pi V}} \\
 \sigma_{wn,p} &= \sigma \sqrt{\frac{4}{5V}}, & \sigma_{wn,q} &= \sigma_{wn,w}, & \sigma_{wn,r} &= \sigma_{wn,v}
 \end{aligned} \tag{3.22}$$

where  $\sigma$  is the standard deviation of the velocity fluctuations, representing the isentropic atmospheric turbulence energy, given in Figure 3.8.

The measurement noise used in the analyses has been assumed to be zero mean white noise. The standard deviation has been chosen with consideration to actual aircraft sensors.

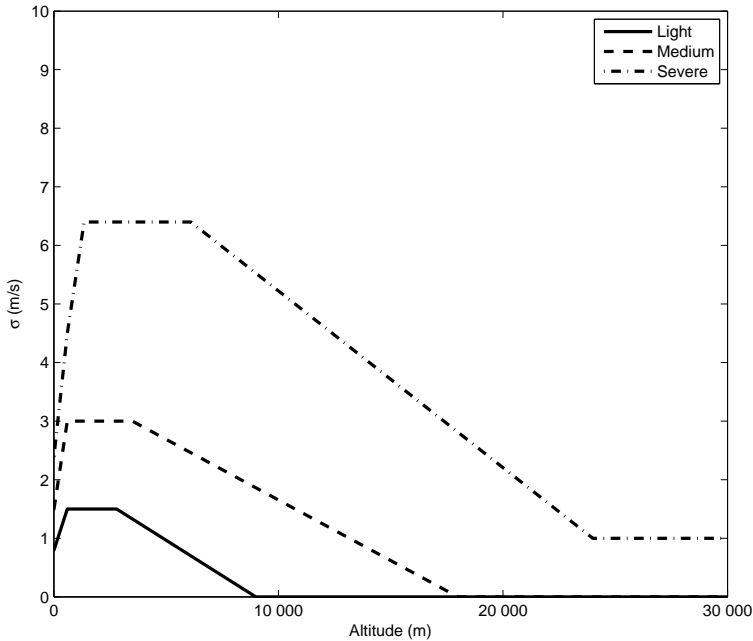


**Figure 3.8:** Standard deviation of the velocity fluctuations.

### 3.3.3 Total model

Equations (3.12), (3.15) and (3.20) make up the basic model structure for the flight mechanical motion. By putting these together the following model is given

$$\begin{aligned}
\dot{u} &= \frac{1}{m} T_e - \frac{1}{m} T - g \sin(\Theta) - qw + rv \\
\dot{v} &= -\frac{1}{m} C + g \cos(\Theta) \sin(\Phi) - ru + pw \\
\dot{w} &= -\frac{1}{m} N + g \cos(\Theta) \cos(\Phi) - pv + qu \\
\dot{p} &= \frac{I_{zz}}{I_*^2} \mathcal{L} - \frac{I_{xz}}{I_*^2} \mathcal{N} + \frac{I_{xz}(I_{yy} - I_{xx} - I_{zz})}{I_*^2} pq + \frac{I_{xz}^2 + I_{zz}(I_{zz} - I_{yy})}{I_*^2} qr \\
\dot{q} &= \frac{1}{I_{yy}} \mathcal{M} - \frac{(I_{xx} - I_{zz})}{I_{yy}} rq - \frac{I_{xz}}{I_{yy}} (p^2 - r^2) \\
\dot{r} &= \frac{I_{xx}}{I_*^2} \mathcal{N} + \frac{I_{xz}}{I_*^2} \mathcal{L} + \frac{I_{xz}(I_{yy} - I_{xx} - I_{zz})}{I_*^2} qr + \frac{I_{xz}^2 + I_{xx}(I_{xx} - I_{yy})}{I_*^2} pq \\
\dot{\Phi} &= p + q \sin(\Phi) \tan(\Theta) + r \cos(\Phi) \tan(\Theta) \\
\dot{\Theta} &= q \cos(\Phi) - r \sin(\Phi) \\
\dot{\Psi} &= q \sin(\Phi) \sec(\Theta) + r \cos(\Phi) \sec(\Theta)
\end{aligned} \tag{3.23}$$

where  $I_*^2 = I_{xx}I_{zz} - I_{xz}^2$  and  $\sec(\Theta) = 1/\cos(\Theta)$ . The engine thrust and aerodynamic contributions are given as

$$\begin{aligned}
&T_e(\delta_{PLA}, M, T_a, H_p) \\
&F_a(u, v, w, p, q, r, \delta_{cs}, H_p)
\end{aligned} \tag{3.24}$$

where  $T_a$  and  $H_p$  are going to be considered as constant parameters during the simulations used. Furthermore,  $\delta_{cs}$  is the control surface vector, which is dependent on aircraft configuration and can contain any of  $\delta_a, \delta_e, \delta_r, \delta_c, \delta_{LE}$ , or even more. This is a nonlinear model of the form

$$\begin{aligned}
\dot{x} &= f(x, u) + w_g \\
y &= x + v
\end{aligned} \tag{3.25}$$

where

$$u = [\delta_{PLA} \quad \delta_{cs}^T]^T \tag{3.26}$$

and

$$x = [u \quad v \quad w \quad p \quad q \quad r \quad \Phi \quad \Theta \quad \Psi]^T \tag{3.27}$$

or by using (3.1)

$$x = [M \quad \alpha \quad \beta \quad p \quad q \quad r \quad \Phi \quad \Theta \quad \Psi]^T \tag{3.28}$$

Note that  $w_g$  is the atmospheric turbulence that is based on (3.21) and (3.22). The nonlinear model will, in coming chapters, be simplified based on the assumptions made from case to case. Note also that it is assumed that all states are measured, which is the case for the flight test cases used in this thesis.

The nonlinear model (3.25) describes any kind of flight motion in the whole flight envelope. For small disturbance motions a linearized system description of the form

$$\begin{aligned}\dot{x} &= Ax + Bu + w_g \\ y &= x + v\end{aligned}\tag{3.29}$$

can be used. As an example, the classical flight mechanical stick fixed motion modes are shown in Figure 3.9 for a F-16 aircraft in subsonic flight. The Phugoid and Short period modes are longitudinal motions while the Roll, Yaw, Dutch roll and Spiral modes are lateral-directional motions.

As can be seen, the Phugoid is a relative slow loosely damped oscillative motion. This mode has a period  $P \approx 40$  s and a time to half amplitude  $t_{1/2} \approx 10$  s. In

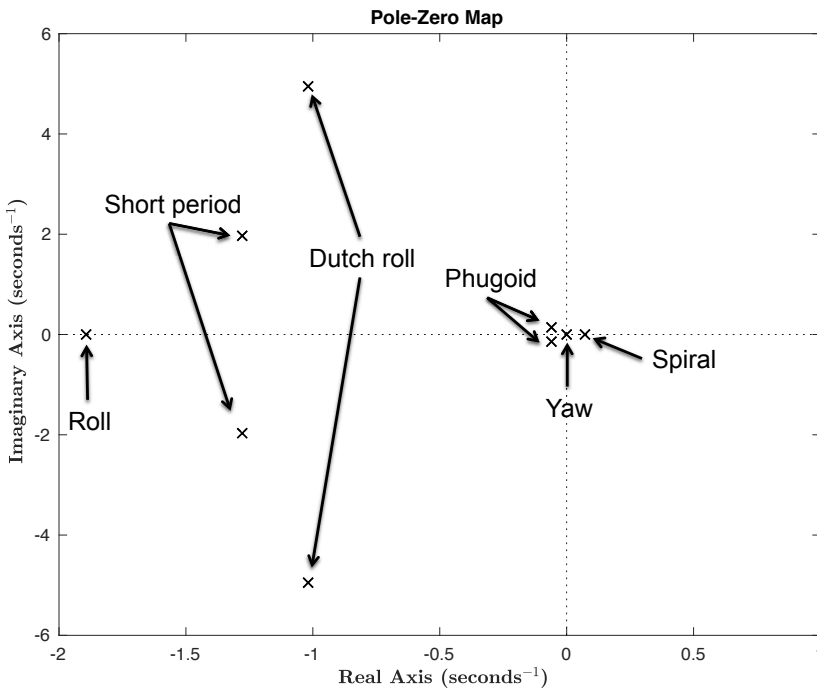


**Figure 3.9:** Pole-zero map for the F-16 aircraft describing the classical flight mechanical modes.

contrast, both the Short period and Dutch roll modes are usually hardly damped, fast oscillative motions. They have a period  $P \approx 2$  s and a time to half amplitude  $t_{1/2} \approx 0.5$  s. The Roll mode is a stable non-oscillative motion while the Yaw and Spiral modes can be neutral or even unstable motions. For the example given in Figure 3.9 the roll mode has a time to half amplitude  $t_{1/2} \approx 0.5$  s and the spiral mode, which is unstable, has a time to double amplitude  $t_2 \approx 10$  s. For more information about these classical modes see Nelson [1998].

For more aggressive flight maneuvers the whole 6 DOF model in (3.25) is needed to describe the motion. Examples of both small disturbance and more aggressive flight test maneuvers will be given in Chapter 4.



# 4

## Flight testing

*“If you can walk away from a landing, it’s a good landing. If you use the airplane the next day, it’s an outstanding landing.”*

- Chuck Yeager (1923 - )

There is a long journey in an aircraft project between the writing of the customer requirements and verifying these in a production aircraft. Flight testing is the aircraft company’s final verification of the aircraft characteristics in this process. Many of the early pioneers in aviation went directly to this testing stage, often with a fatal outcome. Today’s flight testing is more controlled. The process can, in a broad perspective, be presented as the verification and validation “V” shown in Figure 4.1.

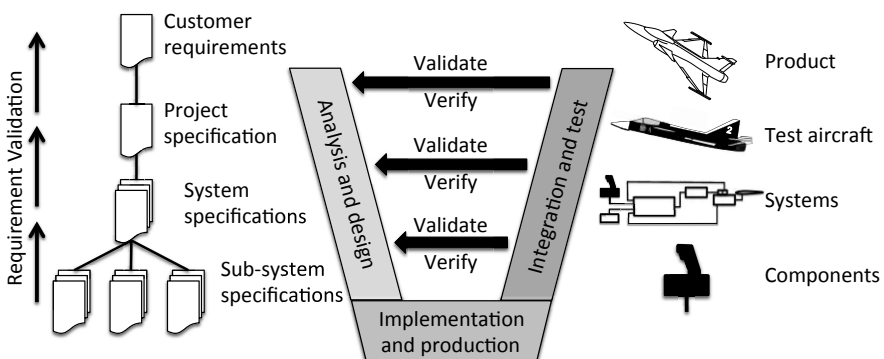


**Figure 4.1:** The verification and validation process from beginning to end.



In a first step the customer requirements, which can be as specific as “*the aircraft in a certain configuration shall have a maximum speed of Mach 2 at an altitude of 11 km*” or as vague as “*the aircraft shall be care-free in the normal flight envelope*”, are interpreted by the aircraft company. This interpretation is done by putting specific and testable requirements into a project specification. The customer and aircraft company have to agree on the content of this specification. This is the start of the analysis and design phase. The project specification is then successively taken apart into system specifications and sub-system specifications to be used as guiding documents during this phase. For every level of breakdown there has to be a validation of the requirements to see that they reflect the intended use in the level above in a correct way. During the design phase several models of systems and physical characteristics are developed. These are used for analysis and improvements of the design.

When the design is made, it is time to start to implement and produce the different sub-system components. These will, in the integration and test phase, be tested by themselves to verify the functionality specified by the sub-system specification requirements. A validation of the properties is also performed to see that the sub-system works as intended in a customer perspective. The sub-systems are then combined and tested on a system level to verify the system requirements. Once again a validation is performed with a customer’s view in mind. For this part simulation and rig testing of system characteristics are used extensively. When the systems are mature enough they are put together in one or more test aircraft. There are two main objectives for this level of testing. The first, and maybe the most obvious, is the testing of aircraft characteristics on the ground and in flight to see that the requirements given in the project specification are verified. Another, almost equally important, reason is the verification of the accuracy of the models used for simulation. If these models are found accurate enough, they can be used to reduce cost and time for the flight test period and possible future development of the aircraft. Methods for identifying flight mechanical characteristics are what this thesis is all about. The flight testing is the last verification that the aircraft company does before the customer tests a production aircraft. Then a validation of the aircraft characteristics as intended for use in a real situation is performed, reflected by the customer requirements documentation.

## 4.1 Pre-flight activities

Looking a bit closer on the above-described process, with focus on the flight mechanical characteristics of interest in this thesis, it can be divided into pre-flight activities and flight testing.

### 4.1.1 The analysis and design phase

This phase can be symbolized by Figure 4.2. There is, as can be seen, three stages in this phase.

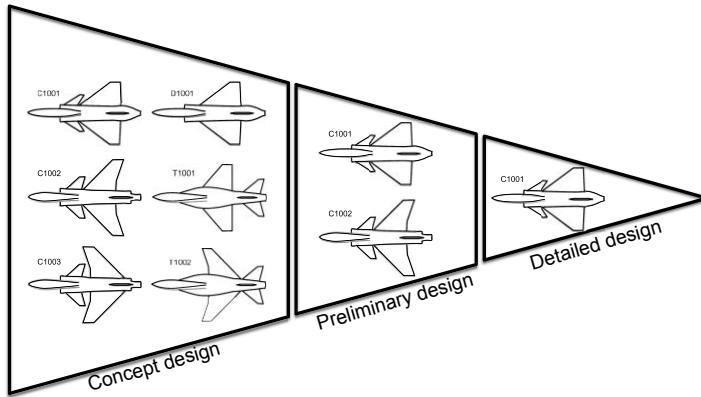


**Figure 4.2:** Overall design and down-selection.

*Conceptual design* is the stage in which many different concepts, based on the project specification, are analyzed. Design possibilities, such as number and placement of engines, wing shape and placement, tail plane or canard configuration choice, etc., are considered. For the analysis of these, “pen and paper”, statistics and simple computational tools, are used. As an example, panel methods are used for rough calculations of the aerodynamic properties. Some of the configurations will not fulfill the requirements or are judged to be too expensive. These are eliminated in the conceptual design phase.

In the *preliminary design* stage the remaining configurations are refined in terms of body, wing and empennage sizing and placement. Also, major systems, like landing gear, fuel system, control surfaces, etc., are sized and positioned. This is used to get a weight and balance estimate. More advanced methods are used during this stage. Computational fluid dynamics (CFD) and wind tunnel testing are used for the aerodynamic analysis. Structural analysis of major components and control solutions are studied in this stage. The configurations are compared to each other to find the best one. If this concept meets all requirements, then the go ahead for the next step is given. Otherwise an iteration back to the conceptual design stage is needed.

The *detailed design* is a stage where extensive development of the structure and systems are done. Drawings and blueprints are produced for the coming implementation and production. In this stage, detailed models of mass from CAD programs, engine thrust from the manufacturer and the aerodynamics from wind tunnel test are developed. Databases for these together with models of systems are put together in flight simulators.

Figure 4.3 shows the increasing complexity of the methods used for the aerodynamic modeling during the analysis and design phase.

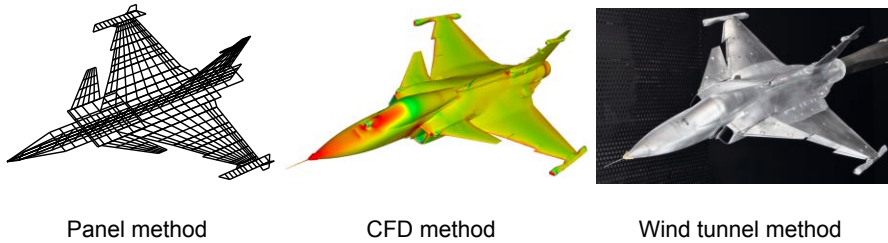


*Figure 4.3: Increase in method complexity during the design phase.*

### 4.1.2 The production and implementation phase

In this phase the hardware is realized from the drawings and blueprints developed in the previous phase and software solutions are implemented into computers. Some systems are bought from subcontractors and others are made in-house.

### 4.1.3 The integration and test phase

This phase starts with the different sub-systems. They are put together and tested by themselves to see that they are working as they were supposed to. Then the sub-systems are put together to perform integrated testing. Flight mechanical simulations are made to investigate the handling and flying characteristics. When the first prototype/test aircraft is assembled a test readiness review is performed. This will be the starting point for the ground and flight testing. During the ground testing, the vehicle characteristics are looked at during slow speed and high speed test runs. These are made to ensure that the aircraft will behave satisfactory during take-off and landing.

## 4.2 Flight testing

The maiden flight is truly a milestone in an aircraft development. Several test aircraft are built and equipped with many sensors for different types of testing. From the flight dynamic perspective this includes: accelerometers, gyros, sensors for altitude, velocity, control surface deflections and more. For a modern fighter aircraft, the amount of sensors leads to the positive effect that some properties can be derived in more than one way. It is therefore possible to make corrections to ensure that the best possible data is used for analysis of the flights.

During the testing engineers look at flight data in almost real-time. The flight mechanical model is run in parallel with the actual flight using pilot inputs. At Saab the tool ROMAC [Andersson et al., 2002] is used. This analysis is done to give a feeling for how well the simulations can predict the true flight. The comparison is used when judging the progress of the testing performed.

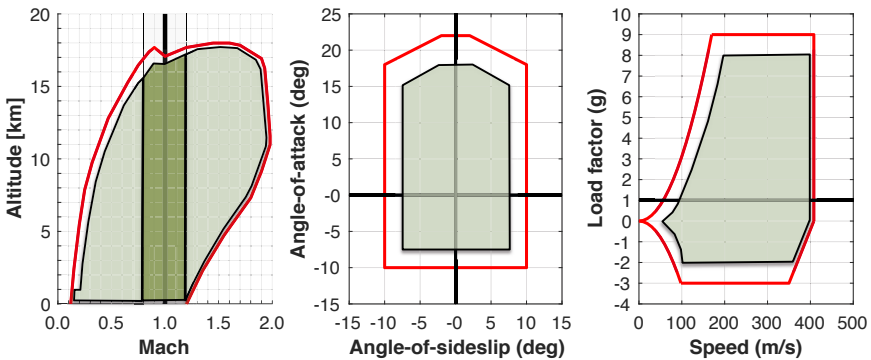


**Figure 4.4:** Normal flight envelope with a margin to the limits.

The testing of flight mechanical characteristics is performed in three phases.

*Envelope expansion* is a hectic period after the first flight. This is low risk flight testing with the main purpose to check handling and flying qualities as well as verifying engine thrust and aerodynamic models. Successively, the flight envelope, shown in Figure 4.4, is opened for system testing of different kind. First the subsonic envelope is opened, starting at medium speed and altitude. This state is then varied step-by-step, finally ending up at low altitude with take-off and landing speed. Typically small disturbance inputs, like steps and pulses, are performed. In addition one-axis excitations like large but clean roll and pitch maneuvers are also performed. Another maneuver used is the steady heading sideslip (SHSS), in which a combination of roll and yaw commands increase the angle-of-sideslip in a quasi-steady manner.

The next step is to open the supersonic envelope. The aircraft is tested up to maximum speed at different altitudes with similar maneuvers as in the subsonic case. The last part to be tested at this stage is transonic envelope. Nonlinearities and hysteresis effects due to aerodynamic shock wave transients can be encountered. To investigate the nature of these, accelerations and retardations are added to the previously mentioned test maneuvers.

To illustrate data from typical flight test maneuvers, the Vegas simulation model has been used. Data from a subsonic double pulse can be seen in Figure 4.5. A supersonic step is shown in Figure 4.6 and a retardation in Figure 4.7. Also, a steady heading sideslip maneuver is given in Figure 4.8.

Currently these types of test maneuvers are mostly analyzed using linear regression of the error between the flight test data and the aircraft model data.

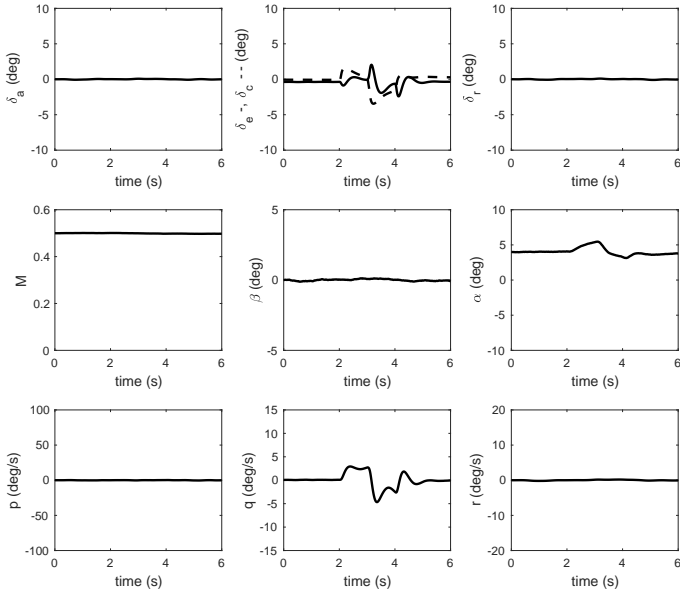


**Figure 4.5:** Pitch pulse at subsonic speed.

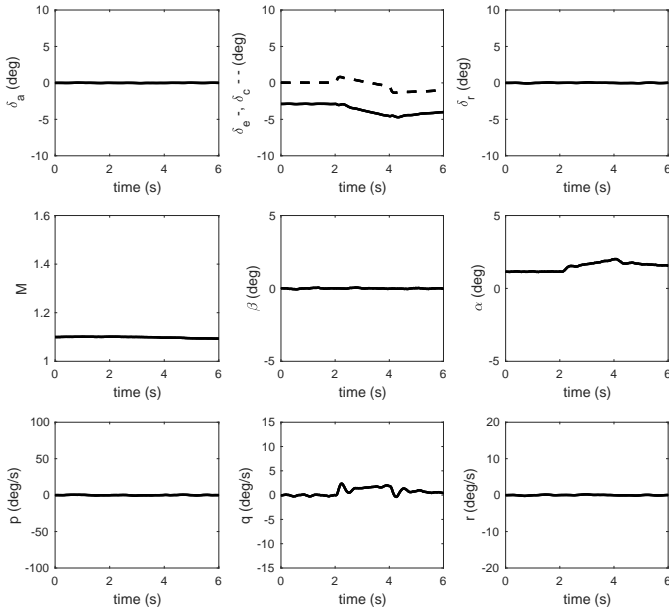


**Figure 4.6:** Pitch step at supersonic speed.

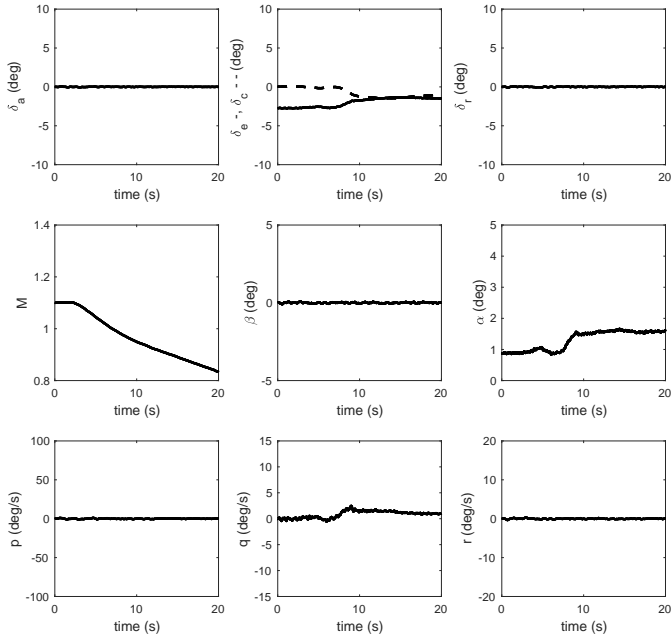


**Figure 4.7:** Retardation from supersonic to subsonic speed.

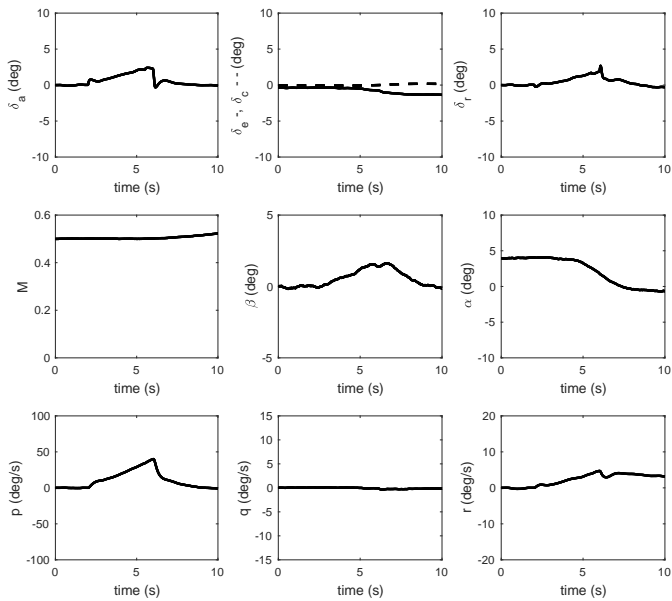


**Figure 4.8:** Steady heading sideslip at subsonic speed.

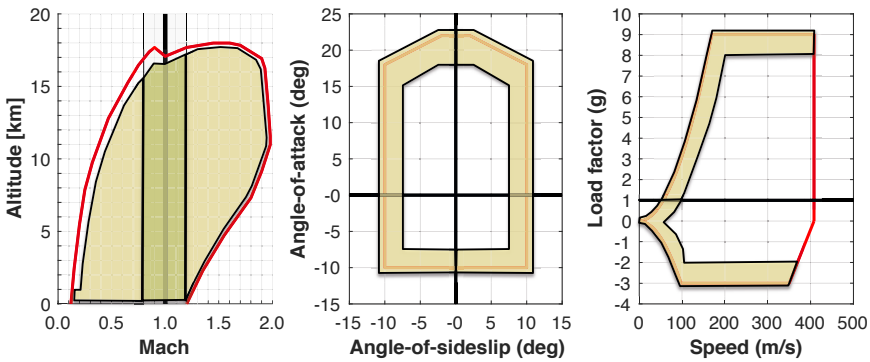


**Figure 4.9:** Maneuver Load Limit (MLL) test envelope.

*Maneuver Load Limit (MLL) flight test* is a verification of the MLL-functionality of the flight control system. This will give the pilot full access to the aircraft performance without having to worry about the aircraft leaving the operational envelope, which is a part of the care-free maneuvering concept. With this the pilot can concentrate more on the task at hand. To test the MLL-functionality means pushing the aircraft right to the boundary of the angle-of-attack, angle-of-sideslip and load factor limits, see Figure 4.9. The maneuvers are more aggressive and dynamic than in the envelope expansion phase, often ending up in nonlinear states. Typical maneuvers are Wind-Up-Turns (WUT) with constant speed, Bleed-Off-Turns (BOT) at constant altitude. They are performed as is or in combination with a full roll command. Other maneuvers are continuously alternating roll command and simultaneous full pitch, roll and yaw commands. These types of maneuvers are needed to reach the corners of the boundaries often using a build-up process starting within the envelope and successively increasing the amplitude up to the limit. Also, part of this testing is performed with the limits widened a bit to ensure that nothing bad happens if the dynamic maneuvers lead to smaller overshoots crossing the boundaries.

Figures 4.10 - 4.12 show three typical MLL-maneuvers for testing the limits of the angle-of-attack/angle-of-sideslip envelope shown in Figure 4.9. The first is a Bleed-Off-Turn with a roll command reaching the upper limits ( $\alpha = 22^\circ$ ,  $\beta = 6^\circ$ ), the second is a continuous alternating roll command which in this case is a build-up for testing the side limits reaching ( $\alpha = 15^\circ$ ,  $\beta = \pm 5^\circ$ ) and the last is a diagonal stick forward checking the lower limit ( $\alpha = -8^\circ$ ,  $\beta = 5^\circ$ ).

These types of testing are mostly analyzed with nonlinear regression and manual work by looking at the error between the flight test data and the aircraft model data. This is hard work leading to many working hours.

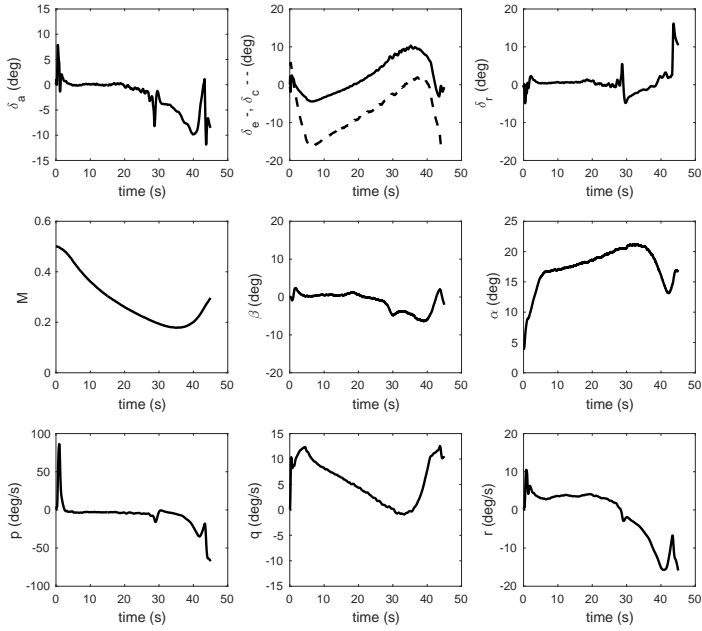


**Figure 4.10:** Bleed-Off-Turn with a roll.

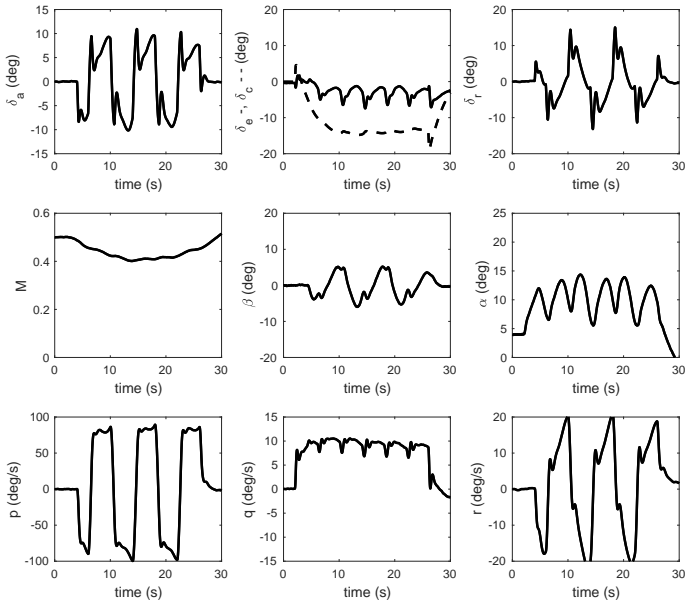


**Figure 4.11:** Continuously alternating roll input.



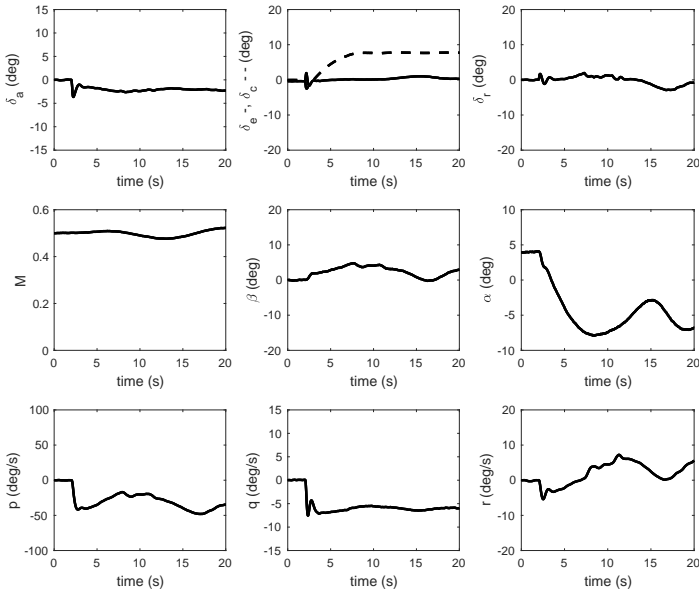


**Figure 4.12:** Diagonal stick forward input.

*Hazardous flight testing* is a special kind of high risk testing where the aircraft is taken beyond the boundary of the intended flight envelope, see Figure 4.13. Even though the MLL-function protects against leaving the operational envelope, some cases cannot be prevented, for example flight into the low energy cone where a steep climb at low speed is performed. If the pilot ignores the low speed warning the excess energy of the engine will eventually decrease to zero resulting in a stall. The transient through the boundary is too fast for the flight control system to handle. This is the first step beyond this boundary, where the airflow over the aircraft starts to separate leading to a decrease in lift. Going further in to post-stall flight can lead to "deep stall", which is a trimmed condition at extreme angle-of-attack, or spin, which is a yaw rotational state during a deep stall. Both of these conditions are dangerous since altitude is lost fairly fast and correct actions are needed to brake the fall and return into controlled flight. Figure 4.14 shows three different post stall maneuvers for this kind of testing. It should be mentioned that the entry could be inverted so that the aircraft tips over on its back leading to similar problems for returning to normal flight. Also, the entry could be over one of the wings. This leads to another kind of dynamics where relative fast transitions between extreme angles-of-sideslip and angles-of-attack can occur.

It is hard to find entries of this type of maneuvering in Vegas so no time histories are given here.

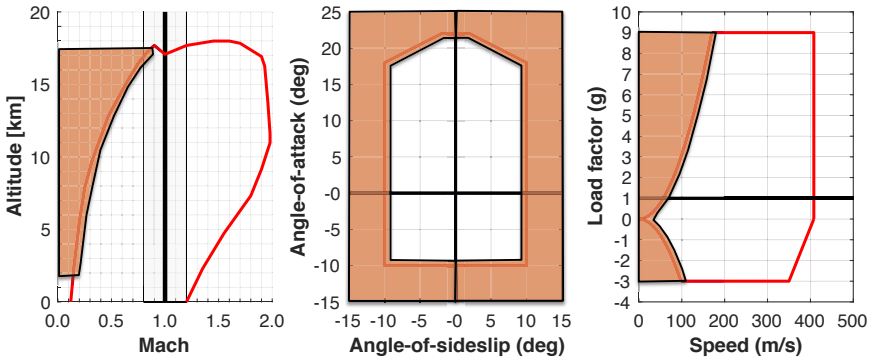


Figure 4.13: Low energy envelop near the stall limit.

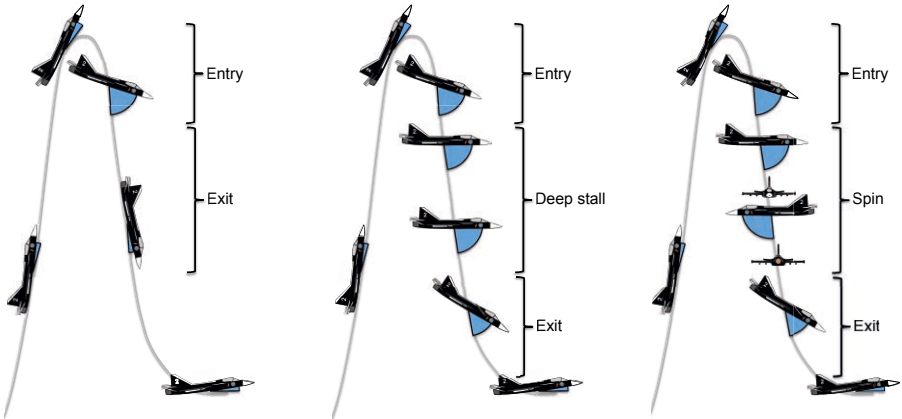
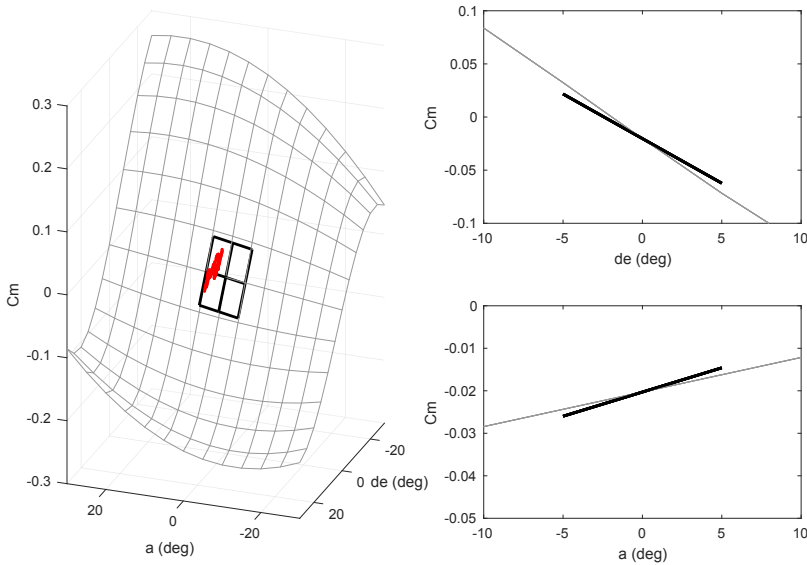


Figure 4.14: Hazardous flight testing outside the operational flight envelope. Left: Stall, Middle: Deep stall, Right: Spin. The angle-of-attack is shown in blue.

## 4.3 System identification

System identification of the flight mechanical characteristics of the three different flight test phases has different requirements on the methods needed. During the *envelope expansion* using the small disturbance testing, linear regression is often the main tool. From this derivatives around a trimmed state are esti-



**Figure 4.15:** Aerodynamic derivative update given in black due to flight test data from small disturbance maneuvering shown as a red line.

mated. Since this only gives a limited coverage of the flight envelope, care has to be taken when incorporating the results into the existing nonlinear model, otherwise non-physical effects can be introduced and simulations can give strange behaviors. As an example, a suggested local update to the aerodynamic pitching coefficient is given in Figure 4.15. The question is whether the entire surface should be changed or if the effect is local, i.e., there is some nonlinearity in the physics. Since the model describes the total system, which is multidimensional, strange effects can spread in several state space directions. Therefore, more data are needed. This can come from the *MLL flight testing*, which usually includes nonlinear dynamic behavior. Good tools for estimating this type of effects are needed. This is a much harder task than identifying linear effects, but it gives more information in a sense. It should be noted that this still only gives a trace in the state space, see Figure 4.16. Therefore, it is good to make several types of maneuvers in the same state space area to excite the system in different ways. Even harder is the identification for the *Hazardous flight testing* because the flow over the aircraft is chaotic with separated flow over a large part of the aircraft. This leads to a large aerodynamic wake of often oscillating flow. There are also hysteresis effects, adding extra complexity, during the transition phases in and out of the post-stall envelope. An example of this is shown in Figure 4.17.

In the next four chapters, a sequential method for online estimation of derivatives and one method for post flight evaluation of nonlinear characteristics are proposed and evaluated.

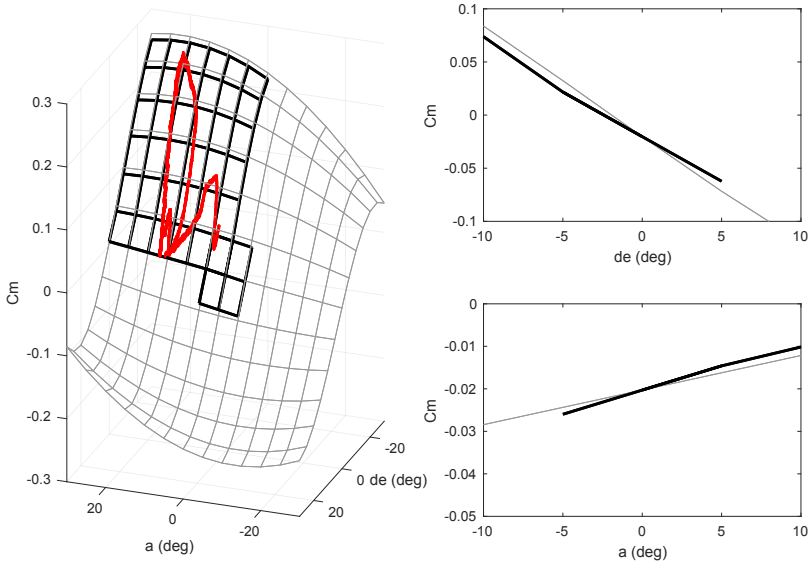


**Figure 4.16:** Aerodynamic derivative update given in black due to flight test data from aggressive maneuvering shown as a red line.

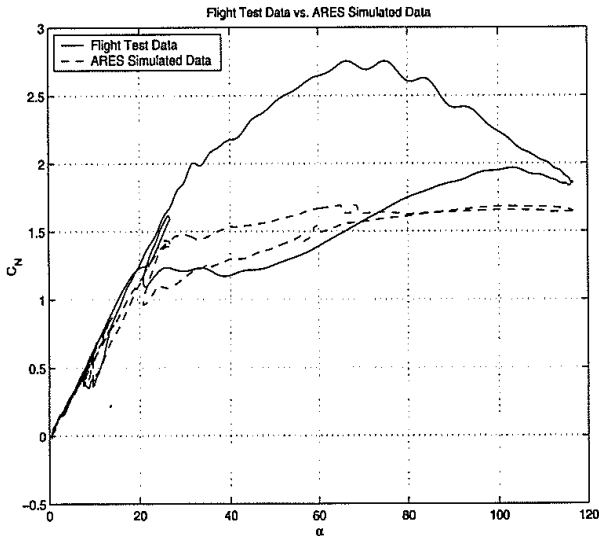


**Figure 4.17:** Example of the normal force coefficient  $C_N$  for a deep stall maneuver showing flight test data compared to a simulation based on quasi-steady data. The picture is taken from [Kristiansson, 2006].



# 5

---

## Sequential identification

"Time is an illusion."  
- Albert Einstein (1879 - 1955)

Flight testing involves many hours of planning and preparation as described in the previous chapter. To have a good model that describes the true aircraft behavior well can significantly help in this process by using a model based system engineering way of working. To get as much out of every test as possible, analysis of flight mechanical characteristics is today done during testing.

For estimation of linear flight mechanical parameters, Morelli [1999] and Klein and Morelli [2016] present a real-time method, for aircraft system identification. This is based on a frequency domain approach. Having a tool for this kind of analysis can be used to make decisions about continuation or abortion of the testing and also to see that enough information is available in the test data to make good post-flight analysis possible and thereby increasing model quality. This can make the flight testing more effective. The method has been used in a number of aerospace applications. For example, DeBusk et al. [2010] have used it in a framework of on-board estimation of flight characteristics for adaptive control. In Basappa and Jategaonkar [2004] the method has been compared to Recursive Least-Squares (RLS) and Extended Kalman Filter (EKF) time domain methods, and it is commented that the frequency domain method is preferable since it is computationally simpler and has no tuning parameter to be set by the engineers.

Here, analysis of this frequency domain real-time method is performed and some improvements to the method are suggested. The improved method is applied to real flight test data.

## 5.1 Problem formulation

The methods described in this chapter are made for identification, during flight testing, of a continuous-time linear system. A block diagram of a general linear system with a controller is shown in Figure 5.1. Mathematically the linear system

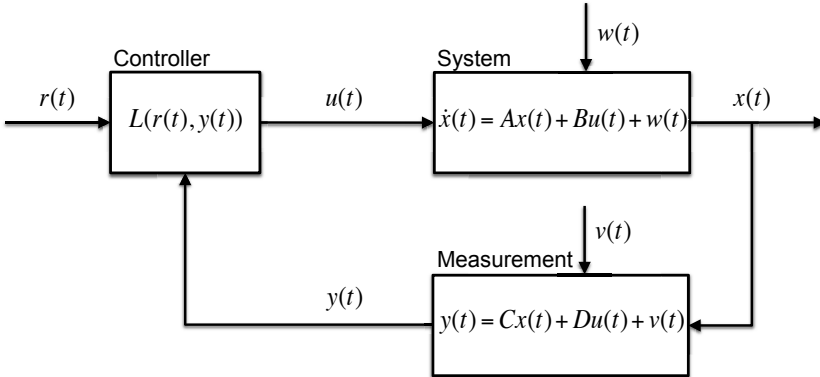


**Figure 5.1:** Block diagram for a general linear continuous-time closed loop linear system.

and measurement part can be described as

$$\dot{x}(t) = A x(t) + B u(t) + w(t) \quad (5.1a)$$

$$y(t) = C x(t) + D u(t) + v(t) \quad (5.1b)$$

where  $x(t)$  is an  $n_x \times 1$  state vector,  $u(t)$  is an  $n_u \times 1$  input vector and  $w(t)$  is the process noise, which in the application corresponds to atmospheric turbulence.  $A$  and  $B$  are the state and input matrices of the system. For the measurement  $y(t)$  is an  $n_y \times 1$  output vector, and  $v(t)$  is white measurement noise. Here,  $C$  and  $D$  are called the output and feedthrough matrices, respectively.

There are three assumptions used in the application. First,  $C$  is the identity matrix, i.e., all states are measured. Secondly,  $u(t)$  is, not directly, influencing  $y(t)$  resulting in  $D$  being a zero matrix. Thirdly, the measurement noise is white and is therefore denoted  $e(t)$  instead of  $v(t)$ . This gives the formulation

$$\dot{x}(t) = A x(t) + B u(t) + w(t) \quad (5.2a)$$

$$y(t) = x(t) + e(t) \quad (5.2b)$$

A linear parameterized model of the form

$$\dot{x}(t, \theta) = A(\theta) x(t, \theta) + B(\theta) u(t) + w(t) \quad (5.3a)$$

$$y(t, \theta) = x(t, \theta) + e(t) \quad (5.3b)$$

is used for the identification, where  $\theta$  is a vector containing the unknown parameters to be identified. If  $C$  in (5.1b) is not the identity matrix an observer is needed which depends on the model and then the estimation problem gets more complex.

The idea is to use (5.3a) in an equation-error framework where the inputs  $u(t)$  and the outputs  $y(t, \theta)$ , approximating the state  $x(t, \theta)$  through (5.3b), are used to estimate the parameters in  $A(\theta)$  and  $B(\theta)$ . The method should also, sequentially, present the estimates of the parameters as well as an uncertainty estimate to the user. This should be done so that the user can judge how accurate the estimates are.

With a slight abuse of notation, the  $\theta$  in the states  $x(t, \theta)$  and the outputs  $y(t, \theta)$  will be dropped to increase the readability of the equations.

## 5.2 Methods

Here, the existing sequential frequency domain method, presented in Klein and Morelli [2016], is described. It is compared to a recursive time domain method and some improvements are suggested.

### 5.2.1 Sequential frequency domain method

There are two main parts that build up the sequential frequency domain method, one using a recursive Fourier transformation of the input and output data and the other solving a regression problem with a complex least squares approach in the frequency domain. These parts will be described below.

**The Recursive Fourier Transform** uses a finite Fourier transform of a general function  $f(t)$ , which has to be piece-wise differentiable on the interval  $[0, T]$ . The continuous-time transform, for a frequency  $\omega_i$ , is defined by

$$\tilde{f}_{c,T}(\omega_i) = \int_0^T f(t) e^{-j\omega_i t} dt \quad (5.4)$$

where the  $\tilde{\cdot}$  is used to denote the transformed entities and the index  $c$  marks that the transform is for the continuous-time case.

When data are sampled, a rectangle approximation of the integral of the finite Fourier transform with a sampling time  $T_s$  can be used

$$\tilde{f}_{c,T}(\omega_i) \approx T_s \sum_{k=0}^{N-1} f_k e^{-j\omega_i k T_s} \quad (5.5)$$

where  $f_k \equiv f(kT_s)$ . This will give a reasonable approximation if the sample time  $T_s$  is short relative to changes in  $f(t)$ . This is the case for the aircraft application



in this thesis since the frequency interval of interest is [0.01 2] Hz and the sample frequency is 60 Hz. Otherwise other approximations, like for example trapezoids, can be used. The approximation (5.5) can be written as

$$\tilde{f}_{c,T}(\omega_i) \approx T_s \tilde{F}_N(\omega_i) \quad (5.6)$$

where

$$\tilde{F}_N(\omega_i) \equiv \sum_{k=0}^{N-1} f_k e^{-j\omega_i k T_s} \quad (5.7)$$

is a discrete-time finite Fourier transform.

To make the method useful for a real-time application, the transform has to be calculated at every time step. This can be done sequentially since

$$\begin{aligned} \tilde{F}_N(\omega_i) &\equiv \sum_{k=0}^{N-1} f_k e^{-j\omega_i k T_s} = \left( \sum_{k=0}^{N-2} f_k e^{-j\omega_i k T_s} \right) + f_{N-1} e^{-j\omega_i (N-1) T_s} \\ &= \tilde{F}_{N-1}(\omega_i) + f_{N-1} e^{-j\omega_i (N-1) T_s} \end{aligned} \quad (5.8)$$

That is, the transform at the current time is made up of the transform from the previous time step plus the function value from the previous time step. This means that all information in the transform from earlier time steps is stored in  $\tilde{F}_{N-1}(\omega_i)$  much like the states in a state-space model.

**The Complex Least-Squares Regression** is obtained by rewriting (5.3a) in the frequency domain using (5.7). This gives the following formulation

$$\tilde{X}_N(\omega_i) = A(\theta) \tilde{X}_N(\omega_i) + B(\theta) \tilde{U}_N(\omega_i) + \tilde{W}_N(\omega_i) \quad (5.9)$$

where  $\tilde{X}_N(\omega_i)$ ,  $\tilde{U}_N(\omega_i)$  and  $\tilde{W}_N(\omega_i)$  are the discrete-time finite Fourier transforms of the states, inputs and process noise, respectively. These are given for frequencies  $\omega_i$ ,  $i = 1, \dots, M$ , at times  $t = NT_s$ . The following approximation has been used by Klein and Morelli [2016] for the transform of the time derivative

$$\tilde{F}_N(\omega_i) \equiv \sum_{k=0}^{N-1} \dot{f}_k e^{-j\omega k T_s} \approx j\omega_i \tilde{F}_N(\omega_i) \quad (5.10)$$

With (5.10), (5.9) can be rewritten as

$$j\omega_i \tilde{X}_N^T(\omega_i) = \left[ \tilde{X}_N^T(\omega_i) \quad \tilde{U}_N^T(\omega_i) \right] \begin{bmatrix} A(\theta) & B(\theta) \end{bmatrix}^T + \tilde{W}_N^T(\omega_i) \quad (5.11)$$

where the parameters to be estimated in  $A(\theta)$  and  $B(\theta)$  have been collected in a separate matrix. This formulation cannot be used directly because the states are not available, but the transformed outputs can be used as approximations in (5.11), since all states are assumed to be measured. This gives

$$j\omega_i \tilde{Y}_N^T(\omega_i) = \left[ \tilde{Y}_N^T(\omega_i) \quad \tilde{U}_N^T(\omega_i) \right] \begin{bmatrix} A(\theta) & B(\theta) \end{bmatrix}^T + \tilde{V}_N^T(\omega_i) \quad (5.12)$$

where  $\tilde{V}_N^T(\omega_i)$  has a different structure than  $\tilde{W}_N^T(\omega_i)$  including both process and measurement noise. However, both the color and structure of the noise are ignored here since no noise model is to be identified in this approach.

The expression (5.12) is a complex regression of the form

$$\tilde{z}_N(\omega_i) = \tilde{\phi}_N(\omega_i) \Theta + \tilde{V}_N^T(\omega_i) \quad (5.13)$$

where  $\Theta = [A(\theta) B(\theta)]^T$ . The parameter estimation in the linear regression (5.13) can be solved with a Complex Least-Squares (CLS) method where the prediction error is given by

$$\tilde{\varepsilon}(\omega_i, \theta) = \begin{bmatrix} \Re(\tilde{z}_N(\omega_i)) \\ \Im(\tilde{z}_N(\omega_i)) \end{bmatrix} - \begin{bmatrix} \Re(\tilde{\phi}_N(\omega_i)) \\ \Im(\tilde{\phi}_N(\omega_i)) \end{bmatrix} \Theta \quad (5.14)$$

The least-squares criterion becomes

$$V_M(\theta, Z^M) = \frac{1}{M} \sum_{i=1}^M \frac{1}{2} |\tilde{\varepsilon}(\omega_i, \theta)|^2 \quad (5.15)$$

which gives the parameter estimator

$$\hat{\Theta} = (\tilde{\Phi}_N^{aT} \tilde{\Phi}_N^a)^{-1} (\tilde{\Phi}_N^{aT} \tilde{Z}_N^a) \quad (5.16)$$

Here, the real and imaginary parts have been separated such that

$$\tilde{\Phi}_N^a = \begin{bmatrix} \Re(\tilde{\Phi}_N) \\ \Im(\tilde{\Phi}_N) \end{bmatrix} \quad \text{and} \quad \tilde{Z}_N^a = \begin{bmatrix} \Re(\tilde{Z}_N) \\ \Im(\tilde{Z}_N) \end{bmatrix} \quad (5.17)$$

where

$$\tilde{\Phi}_N = \begin{bmatrix} \tilde{\phi}_N(\omega_1) \\ \vdots \\ \tilde{\phi}_N(\omega_M) \end{bmatrix} \quad \text{and} \quad \tilde{Z}_N = \begin{bmatrix} \tilde{z}_N(\omega_1) \\ \vdots \\ \tilde{z}_N(\omega_M) \end{bmatrix} \quad (5.18)$$

Now, (5.16) can be written as

$$\hat{\Theta} = (\Re(\tilde{\Phi}_N^* \tilde{\Phi}_N))^{-1} \Re(\tilde{\Phi}_N^* \tilde{Z}_N) \quad (5.19)$$

where  $*$  is the complex conjugate transpose. This expression is used by Klein and Morelli [2016]. To show that (5.16) can be written as (5.19) consider two complex matrices  $\tilde{A}$  and  $\tilde{B}$  where  $\tilde{A} = \tilde{\Phi}_N$  and  $\tilde{B} = \tilde{\Phi}_N$  or  $\tilde{B} = \tilde{Z}_N$ . Then

$$\begin{aligned} \Re(\tilde{A}^* \tilde{B}) &= \Re\left( (\Re(\tilde{A})^T - i \Im(\tilde{A})^T) (\Re(\tilde{B}) + i \Im(\tilde{B})) \right) \\ &= \Re\left( \Re(\tilde{A})^T \Re(\tilde{B}) + \Im(\tilde{A})^T \Im(\tilde{B}) + i (\Re(\tilde{A})^T \Im(\tilde{B}) - \Im(\tilde{A})^T \Re(\tilde{B})) \right) \\ &= \Re(\tilde{A})^T \Re(\tilde{B}) + \Im(\tilde{A})^T \Im(\tilde{B}) \\ &= \begin{bmatrix} \Re(\tilde{A})^T & \Im(\tilde{A})^T \end{bmatrix} \begin{bmatrix} \Re(\tilde{B}) \\ \Im(\tilde{B}) \end{bmatrix} \\ &= (\tilde{A}^a)^T \tilde{B}^a \end{aligned} \quad (5.20)$$

An important property of (5.19) is that it makes sure that the parameter vector is real, which is the case for the aircraft application. The error variance estimator used is given by

$$\hat{\sigma}_k^2 = \frac{1}{M - n_p} ((\tilde{Z}_{N,k} - \tilde{\Phi}_N \hat{\Theta}_k)^* (\tilde{Z}_{N,k} - \tilde{\Phi}_N \hat{\Theta}_k)) \quad (5.21)$$

where  $n_p$  is the number of parameters to be estimated for each column in  $\hat{\Theta}$  and  $k$  is a column index. The covariance  $\text{Cov}(\hat{\Theta}) \equiv E\{(\hat{\Theta} - E(\hat{\Theta}))(\hat{\Theta} - E(\hat{\Theta}))^T\}$  is estimated as

$$\hat{P}_k(\hat{\Theta}) = \hat{\sigma}_k^2 (\Re(\tilde{\Phi}_N^* \tilde{\Phi}_N))^{-1} \quad (5.22)$$

where (5.20) has been used once more. The predicted parameter standard deviations can then be calculated as the square root of the diagonal elements of  $\hat{P}(\hat{\Theta})$  as

$$s_{k,i} = \sqrt{\hat{P}_{k,ii}(\hat{\Theta})}, i = 1, \dots, n_p \quad (5.23)$$

The above-described method is given as Algorithm 0. For the method to give unbiased results,  $\tilde{V}_N(\omega_i)$  has to be zero mean white noise and uncorrelated with the regressors in  $\tilde{\phi}_N(\omega_i)$ . Improvements to the method will be suggested in a later section.

To investigate the properties of Algorithm 0, simulations of an American F-16 fighter aircraft (Figure 5.2) flying at an altitude of 10,000 ft (3048 m) with a speed of  $M=0.37$  will be used.

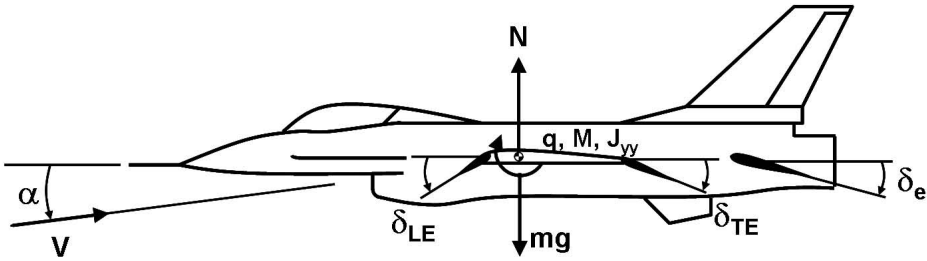


Figure 5.2: Definition of the variables for the F-16.

Excitation of the flight mechanical short period, a highly damped motion in angle-of-attack ( $\alpha$ ) and pitch angular velocity ( $q$ ) where the aircraft nose moves up and down in the pitch (symmetry) plane at almost constant altitude and speed, is performed. The aircraft model, taken from Morelli [1999], is stable and runs in an open-loop configuration. The problem formulation is given by

$$\begin{aligned} \begin{bmatrix} \dot{\alpha}(t) \\ \dot{q}(t) \end{bmatrix} &= \begin{bmatrix} Z_\alpha & Z_q \\ M_\alpha & M_q \end{bmatrix} \begin{bmatrix} \alpha(t) \\ q(t) \end{bmatrix} + \begin{bmatrix} Z_{\delta_e} \\ M_{\delta_e} \end{bmatrix} [\delta_e(t)] + w(t) \\ \begin{bmatrix} \alpha_m(t) \\ q_m(t) \end{bmatrix} &= \begin{bmatrix} \alpha(t) \\ q(t) \end{bmatrix} + e(t) \end{aligned} \quad (5.24)$$

where  $\alpha_m$  and  $q_m$  are the measurements of the angle-of-attack and pitch angular velocity, respectively, and  $\delta_e$  is the elevator input. The true model parameters taken from Morelli [1999] are

$$\begin{aligned} Z_\alpha &= -0.6, Z_q = 0.95, Z_{\delta_e} = -0.115, \\ M_\alpha &= -4.3, M_q = -1.2 \text{ and } M_{\delta_e} = -5.157. \end{aligned}$$

It should be noted that the vertical force  $Z$  is the same as the normal force  $N$  (shown in Figure 5.2) but with the opposite sign, i.e.,  $Z = -N$ . The flight characteristics for this stable open-loop system are given by the pole-zero map and elevator step response shown in Figure 5.3. As can be seen the system has a damping, which results in an overshoot of about 25 % in the angle-of-attack.

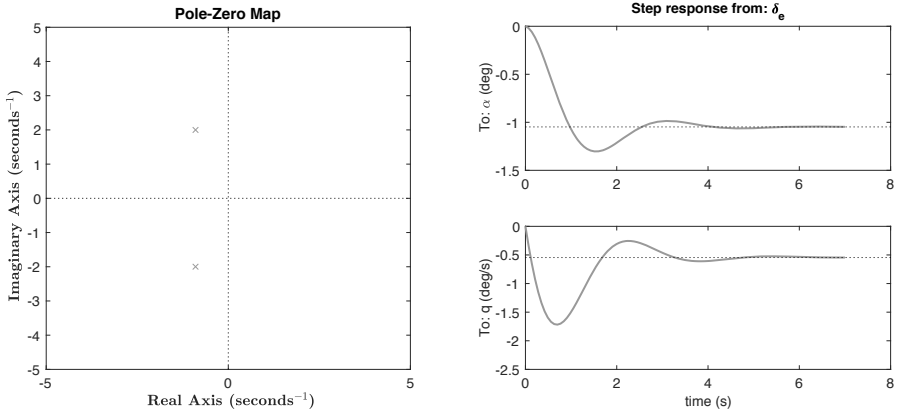


**Figure 5.3:** Pole-Zero map and elevator step response for the F-16.

The main frequency content of the short period rigid-body aircraft dynamics is, according to Klein and Morelli [2016], in the range of  $[0.01 \ 2.0]$  Hz. In this example, a frequency band of  $[0.1 \ 2.0]$  Hz is used and this should be adequate according to Morelli [1999]. A frequency resolution of 0.04 Hz is recommended, which gives the number of frequencies,  $M = 48$ . For the investigations, the simulation tool Simulink® has been used to generate the data. This has been done with a sample time of  $T_s = (1/60)$  s.

For this problem, the parameter estimation of the sequential frequency domain method (5.19) is written as

$$\hat{\Theta} = (\Re\epsilon(\tilde{\Phi}_N^* \tilde{\Phi}_N))^{-1} \Re\epsilon(\tilde{\Phi}_N^* \tilde{Z}_N) \quad (5.25)$$

where

$$\tilde{Z}_N = \begin{bmatrix} j\omega_1 \tilde{\alpha}_m(\omega_1) & j\omega_1 \tilde{q}_m(\omega_1) \\ j\omega_2 \tilde{\alpha}_m(\omega_2) & j\omega_2 \tilde{q}_m(\omega_2) \\ \vdots & \vdots \\ j\omega_M \tilde{\alpha}_m(\omega_M) & j\omega_M \tilde{q}_m(\omega_M) \end{bmatrix} \quad (5.26)$$

$$\tilde{\Phi}_N = \begin{bmatrix} \tilde{\alpha}_m(\omega_1) & \tilde{q}_m(\omega_1) & \tilde{\delta}_e(\omega_1) \\ \tilde{\alpha}_m(\omega_2) & \tilde{q}_m(\omega_2) & \tilde{\delta}_e(\omega_2) \\ \vdots & \vdots & \vdots \\ \tilde{\alpha}_m(\omega_M) & \tilde{q}_m(\omega_M) & \tilde{\delta}_e(\omega_M) \end{bmatrix} \quad (5.27)$$

and

$$\Theta = \begin{bmatrix} Z_\alpha & M_\alpha \\ Z_q & M_q \\ Z_{\delta_e} & M_{\delta_e} \end{bmatrix} \quad (5.28)$$

The  $\tilde{Z}_N$  and  $\tilde{\Phi}_N$  matrices are updated every time step ( $t = NT_s$ ) using the sequential discrete finite Fourier transform (5.8).

A typical estimation result using the algorithm with low measurement noise can look like Figure 5.4 where the regression and presentation of results are done every second. At the top the input, i.e., the elevator ( $\delta_e$ ) double-pulse as well as the outputs' response in angle-of-attack ( $\alpha$ ) and pitch angular velocity ( $q$ ), are shown. This type of input is commonly used when investigating short-period aircraft behavior. The estimates of the parameters are shown in row two and three in the figure. Here the dashed line gives the true value. The estimates are given as squares and the estimated uncertainties of two standard deviations are given as vertical bars. The values at time  $t = 10$  s are shown in Table 5.1. As can be seen the results are fairly accurate at the end of the simulation. There is a larger bias effect during the excitation, especially at time  $t = 2 - 3$  s. The bias due to excitation comes from the fact that the Fourier transform of the time derivative used, i.e., the step from (5.9) to (5.11), is only an approximation.

When calculating the finite Fourier transform of a time derivative,  $\dot{f}(t)$ , integration by parts has to be used, which gives

$$\begin{aligned} \tilde{f}_c(\omega) &= \int_{t_0}^{t_1} \dot{f}(t) e^{-j\omega t} dt = j\omega \int_{t_0}^{t_1} f(t) e^{-j\omega t} dt + [f(t) e^{-j\omega t}]_{t_0}^{t_1} \\ &= j\omega \tilde{f}_c(\omega) - f(t_0) e^{-j\omega t_0} + f(t_1) e^{-j\omega t_1} \end{aligned} \quad (5.29)$$

If  $t_0 \rightarrow -\infty$  and  $t_1 \rightarrow +\infty$  the ordinary Fourier transform is obtained, and then

$$\tilde{f}_c(\omega) = j\omega \tilde{f}_c(\omega) \quad (5.30)$$

because  $f(t)$  has to be absolutely integrable on the interval  $-\infty < t < +\infty$  leading to the fact that  $f(t) \rightarrow 0$  as  $t \rightarrow -\infty$  or  $t \rightarrow +\infty$ . However, this is not the case for

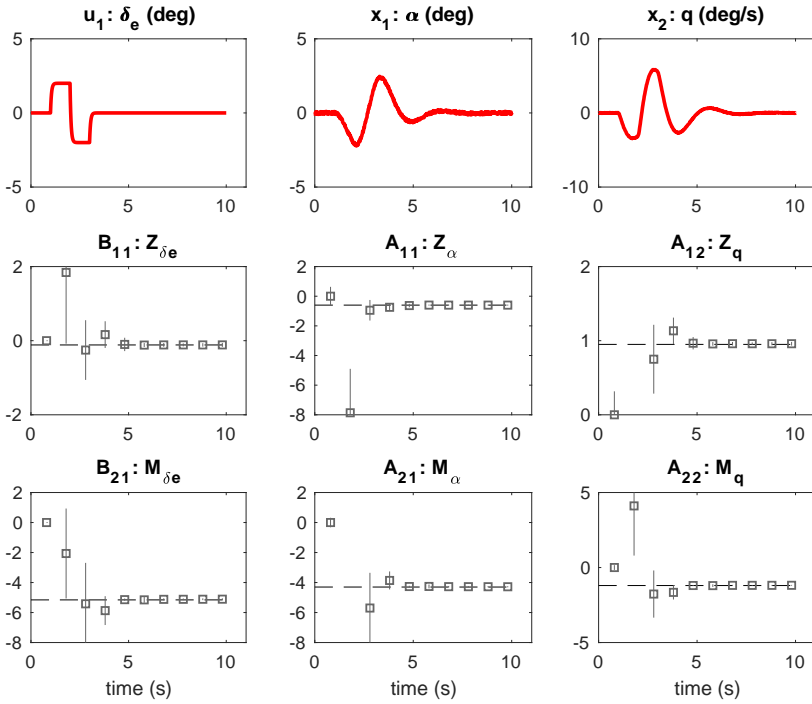


**Figure 5.4:** Estimation of parameters based on simulated data for the F-16. The dashed lines are the true parameters, the squares are the estimated parameters and the vertical lines are the estimated uncertainties of two standard deviations.

**Table 5.1:** True and estimated parameters including two standard deviations for the F-16 model at time  $t = 10$  s.

	True	Algorithm 0
$Z_\alpha$	-0.600	$-0.600 \pm 0.036$
$Z_q$	0.950	$0.959 \pm 0.025$
$Z_{\delta_e}$	-0.115	$-0.113 \pm 0.054$
$M_\alpha$	-4.300	$-4.280 \pm 0.039$
$M_q$	-1.200	$-1.185 \pm 0.027$
$M_{\delta_e}$	-5.157	$-5.110 \pm 0.058$

the finite Fourier transform where the interval is  $0 \leq t \leq T$ . Then

$$\tilde{f}_c(\omega) = j\omega \tilde{f}_c(\omega) - f(0) + f(T)e^{-j\omega T} \quad (5.31)$$

which leads to the discrete Fourier transform of the time derivative

$$\tilde{F}(\omega) \equiv \sum_{k=0}^{N-1} \dot{f}_k e^{-j\omega k T_s} \approx j\omega \tilde{F}(\omega) - \frac{1}{T_s}(f_0 - f_N e^{-j\omega N T_s}) \quad (5.32)$$

This was mentioned in Morelli [2010] and the effect was analyzed in Larsson and Enqvist [2012a]. The principle is similar to what is done in Pintelon et al. [1997] where system identification of arbitrary signals in the frequency domain using correction terms is described. With this (5.12) can be rewritten as

$$j\omega_i \tilde{Y}_N^T(\omega_i) + \frac{1}{T_s} \underline{(y_N e^{-j\omega_i N T_s} - y_0)} = \left[ \tilde{Y}_N^T(\omega_i) \quad \tilde{U}_N^T(\omega_i) \right] \left[ A(\theta) \quad B(\theta) \right]^T + \tilde{V}_N(\omega_i)^T \quad (5.33)$$

where the noise  $\tilde{V}_N(\omega_i)^T$  has a different structure compared to (5.12) due to the added correction. Here, the changes have been underlined.

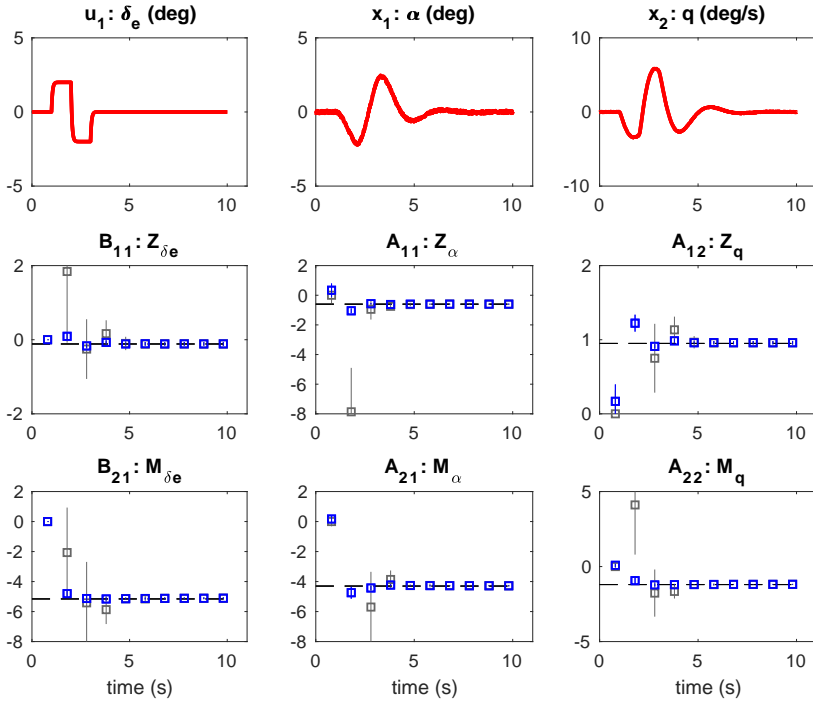
Putting the theory together ends up in **Algorithm 1**, which can be found in Appendix C. This algorithm will hereinafter be called the **Method A**.

Figure 5.5 and Table 5.2 show a comparison between Algorithm 0 and Method A for the same simulated data as shown in Figure 5.4. As can be seen, the addition of the boundary terms underlined in (5.33) improves the estimates during the excitation at time  $t = 2 - 3$  s.

Method A is easy to implement and has no explicit tuning parameters, like the Kalman filter, that the user has to adjust. This is a big advantage in an industrial application where many employees use the same method. What has to be done is to specify the frequencies that should be used, which depend on the application. This can be looked on as a kind of tuning, but for the application used here the settings mentioned earlier from Morelli [1999] can be used. The elements in the variables  $\tilde{z}_N(\omega_i)$ ,  $\tilde{\phi}_N(\omega_i)$  and  $\tilde{Y}_N(\omega_i)$  can initially be put to zero without any problem. A parameter ( $t_{pres}$ ), representing the time-step for when to start solving the regression and present the results, has also to be specified.

Running a noise-free simulation based on the estimated model for Method A given in Table 5.2 and comparing it to a new realization of simulated noisy data using the true system is not a true validation, but it gives a hint of what response one could expect from Method A for this type of maneuver. The result is shown in Figure 5.6. The model fit of this comparison is 97.0%, which reflects the low noise case and the accurate estimation.

Having a tool like this, running during a flight test where data from the prior model is used as the reference, given as the dashed line instead of the true simulated value in the Figure 5.5, can help the flight test engineers. Analysis of the



**Figure 5.5:** Estimation of parameters for the F-16 using Algorithm 0 in gray and Method A in blue. The dashed lines are the true parameters, the squares are the estimated parameters and the vertical lines are the estimated uncertainties of two standard deviations.

**Table 5.2:** Comparison of Algorithm 0, Method A and the true parameters, showing the estimated parameters including two standard deviations at time  $t = 10$  s for the F-16 model.

	True	Algorithm 0	Method A
$Z_\alpha$	-0.600	$-0.600 \pm 0.036$	$-0.601 \pm 0.035$
$Z_q$	0.950	$0.959 \pm 0.025$	$0.959 \pm 0.024$
$Z_{\delta_e}$	-0.115	$-0.113 \pm 0.054$	$-0.113 \pm 0.052$
$M_\alpha$	-4.300	$-4.280 \pm 0.039$	$-4.281 \pm 0.038$
$M_q$	-1.200	$-1.185 \pm 0.027$	$-1.184 \pm 0.026$
$M_{\delta_e}$	-5.157	$-5.110 \pm 0.058$	$-5.109 \pm 0.058$



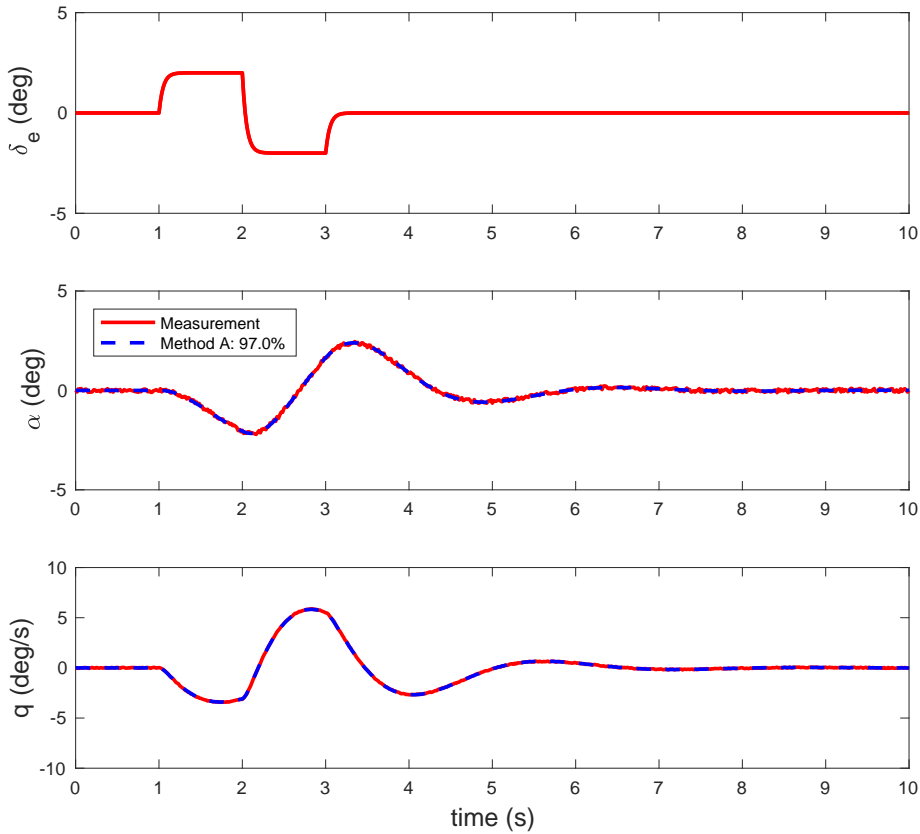


**Figure 5.6:** Validation of the estimated F-16 model. The blue dashed lines are the responses using estimated parameters from Method A and the red lines are the true simulated data.

stability and control characteristics can be done on-line and used to guide the progress of the test in an effective way.

Before continuing, a short analysis of the use of the Fourier transform is given. In Figure 5.7 the time signals and their Fourier transforms are shown for one realization. Above a frequency of about 2 Hz most of the output amplitude spectrum, where the absolute value has been used, contain only noise as can be seen in the lower row. This can cause a problem if a full Fourier transform is used. Method A uses only data up to 2 Hz, which can be a benefit in this case. It should be mentioned that other applications may have other limits. Figure 5.8 shows the difference between Method A and the use of the fast Fourier transform (FFT) when estimating the parameter  $M_\alpha$ . For this open loop case with low and white

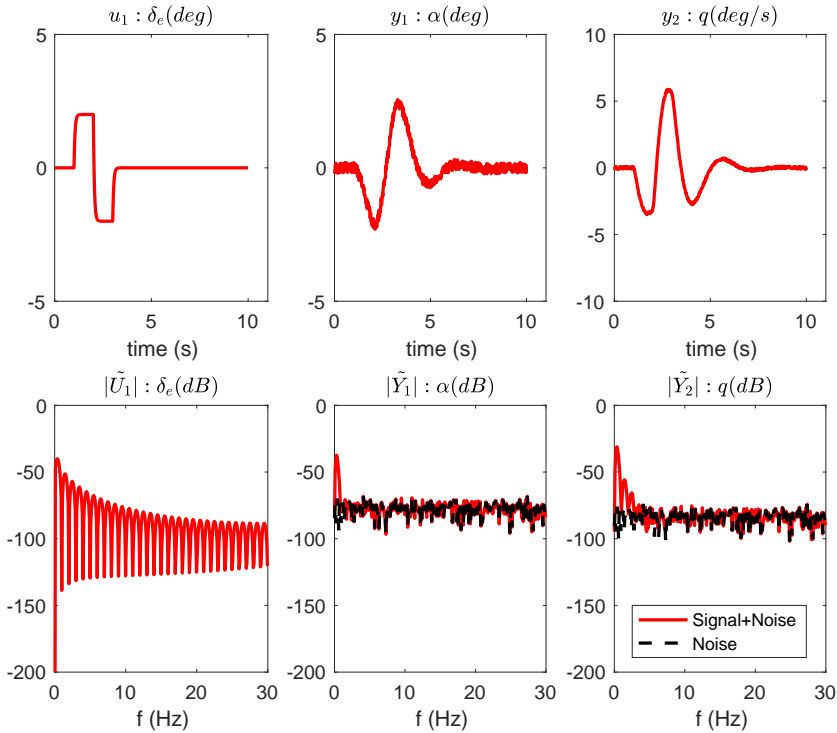


**Figure 5.7:** Input and output data together with their discrete Fourier transforms.

measurement noise, the estimates are fairly accurate and similar, but the estimated uncertainties are larger when using the full FFT instead of a FFT when only frequencies below 2 Hz are used. One reason for this is the estimation error  $(\tilde{z} - \tilde{\phi} \hat{\Theta})$  used in (5.21) for calculating the uncertainty estimates. Above 2 Hz these errors grow when using the full FFT and are so many that they out-weight the increase in the number of frequencies used. The growth can be seen in Figure 5.9. This effect is probably due to the fact that even though the measurement noise in itself is white, it is colored by the way it enters the model (5.12) since the measurements are used as a substitute for the state.

Another important point is that both the input and the output signals are used as regressors. Since these are noisy the problem to solve is not really on the ordinary least squares form, which can lead to biased estimates (see Appendix B for a simple example). The problem to solve is rather on an errors-in-variables form. This can be treated in different ways and one of them will be used later in this chapter.

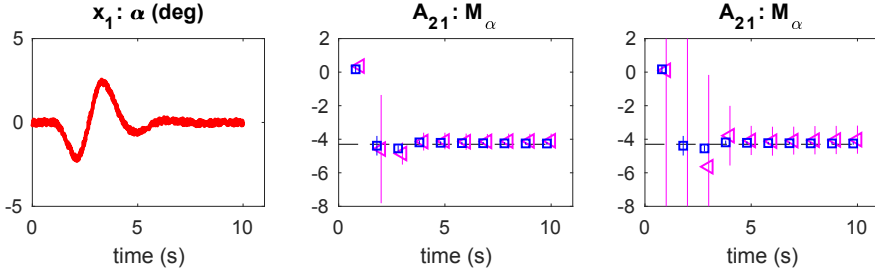


**Figure 5.8:** Difference between Method A (blue squares), FFT [0 – 2] Hz (magenta in the middle) and the full FFT (magenta to the right) when estimating the  $M_\alpha$  parameter.

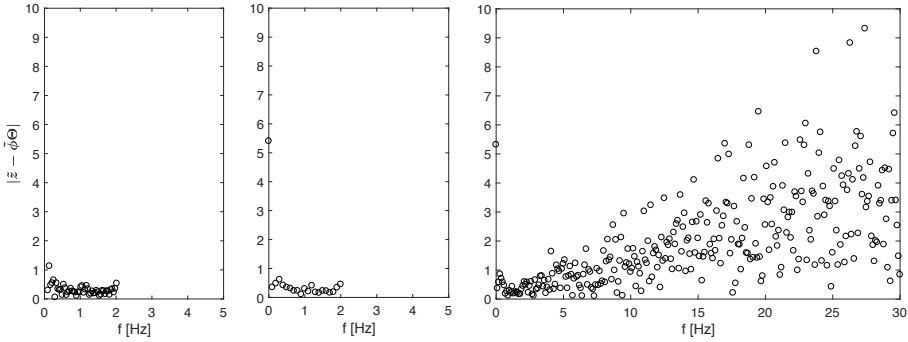


**Figure 5.9:** The absolute value of the frequency content of  $(\tilde{z} - \tilde{\phi} \hat{\Theta})$  used in (5.21) for calculating the uncertainty estimates. The figure shows Method A (left), FFT [0 – 2] Hz (middle) and the full FFT (right)  $M_\alpha$  parameter.

## 5.2.2 Recursive time-domain method

A natural question concerning the described identification method is, why go to the frequency domain? Here a recursive least-squares time domain method, as a comparison to the described sequential frequency domain methods, is given. It is taken from Klein and Morelli [2016], but a similar description can also be found in Ljung [1999].

To get similar expressions for the time-domain method as for Method A, (5.2a) can, with the use of (5.2b), be rewritten as

$$\frac{1}{T_s}(y_N^T - y_{N-1}^T) = [y_N^T \quad u_N^T] \begin{bmatrix} A(\theta) & B(\theta) \end{bmatrix}^T + v_N^T \quad (5.34)$$

where the approximation  $\dot{y}(T) \approx \frac{1}{T_s}(y_N - y_{N-1})$  for the time derivative is used. The noise term  $v_N^T$  is also here colored, similar to (5.12), but in the time domain.

Now, (5.34) can be written as

$$z_N = \phi_N \Theta + v_N^T \quad (5.35)$$

The recursion is based on the following four equations:

$$K_{N,k} = P_{N-1,k} \phi_N^T (\hat{\sigma}_{N-1,k}^2 + \phi_N P_{N-1,k} \phi_N^T)^{-1} \quad (5.36)$$

$$P_{N,k} = P_{N-1,k} - K_{N,k} \phi_N P_{N-1,k} \quad (5.37)$$

$$\hat{\Theta}_{N,k} = \hat{\Theta}_{N-1,k} + K_{N,k} (z_{N,k} - \phi_N \hat{\Theta}_{N-1,k}) \quad (5.38)$$

$$\hat{\sigma}_{N,k}^2 = \begin{cases} \left(\frac{1}{N}\right) \left( (N-1) \hat{\sigma}_{N-1,k}^2 + (z_{N,k} - \phi_N \hat{\Theta}_{N,k})^2 \right) & N < 5n_p + 1 \\ \left(\frac{1}{N-n_p}\right) \left( (N-1) \hat{\sigma}_{N-1,k}^2 + (z_{N,k} - \phi_N \hat{\Theta}_{N,k})^2 \right) & N = 5n_p + 1 \\ \left(\frac{1}{N-n_p}\right) \left( (N-1-n_p) \hat{\sigma}_{N-1,k}^2 + (z_{N,k} - \phi_N \hat{\Theta}_{N,k})^2 \right) & N > 5n_p + 1 \end{cases} \quad (5.39)$$

Here  $k$  is the column index in  $z_N$  and  $\Theta$ , i.e., the problem is solved separately for each column. The matrix  $K_{N,k}$  is a time varying gain working much like the gain in the Kalman filter and  $P_{N,k}$  is the covariance matrix. In fact the equations are very similar to the Kalman filter [Kalman, 1960] equations. The expression for the predicted error variance  $\hat{\sigma}_{N,k}^2$  changes appearance depending how many iterations that have passed. This can give a bias in the early predictions but has to be done to make the method stable in the beginning. The value of  $5n_p$  has been taken from Klein and Morelli [2016] and might not be optimal but seems to work well. The algorithm that has been implemented is given in **Algorithm 2**, which can be found in Appendix C. This will from now on be called the **Method B**.

A comparison of Method A and Method B is shown in Figure 5.10 and Table 5.3. In the figure the estimates from Method B are given as brown squares and for Method A as blue squares shifted to the left. The estimates are similar for the two methods during the whole time sequence, but the estimated uncertainties in the beginning are larger for Method B. This is better than for Method A that underpredicts the uncertainty.

A validation similar to the one given for Method A has been run for Method B. The result is shown in Figure 5.11. The model fit is 95.5%, which is close to the result for Method A.

Method B has approximately the same complexity as Method A. Instead of the sequential Fourier transform, used in Method A, the data have been run through a low-pass-filter to get the selected frequency content of the signal before using the recursion described by (5.36) - (5.39). This has been done to get the same frequency content for all the studied methods.

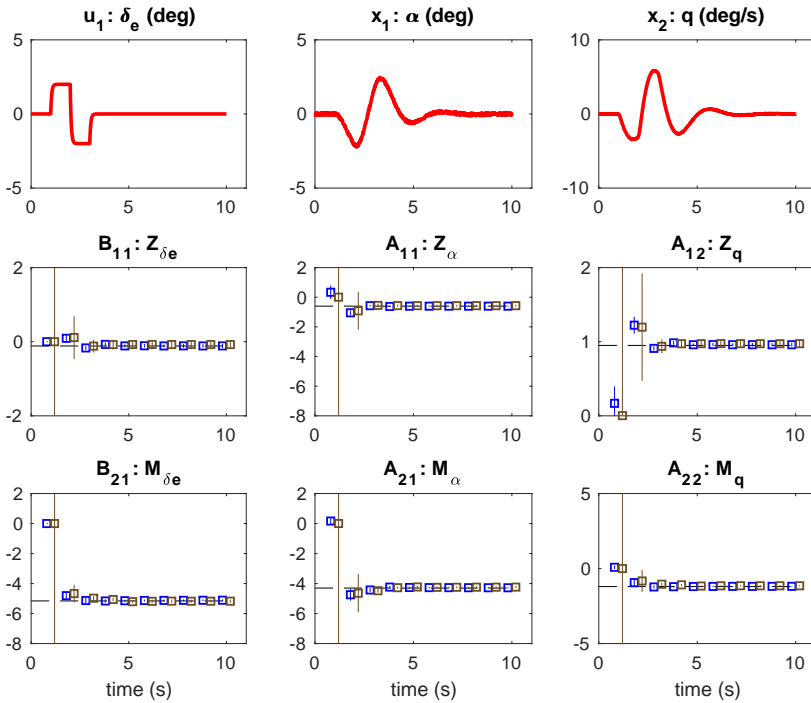


**Figure 5.10:** Estimation of parameters for the F-16 using Method A in blue and Method B in brown. The dashed lines are the true parameters, the squares are the estimated parameters and the vertical lines are the estimated uncertainties of two standard deviations.

**Table 5.3:** Comparison of Method A, Method B and the true parameters, showing the estimated parameters including two standard deviations at time  $t = 10$  s for the F-16 model.

	True	Method A	Method B
$Z_\alpha$	-0.600	$-0.601 \pm 0.035$	$-0.569 \pm 0.061$
$Z_q$	0.950	$0.959 \pm 0.024$	$0.973 \pm 0.042$
$Z_{\delta_e}$	-0.115	$-0.113 \pm 0.052$	$-0.077 \pm 0.104$
$M_\alpha$	-4.300	$-4.281 \pm 0.038$	$-4.236 \pm 0.061$
$M_q$	-1.200	$-1.184 \pm 0.026$	$-1.147 \pm 0.042$
$M_{\delta_e}$	-5.157	$-5.110 \pm 0.058$	$-5.174 \pm 0.104$

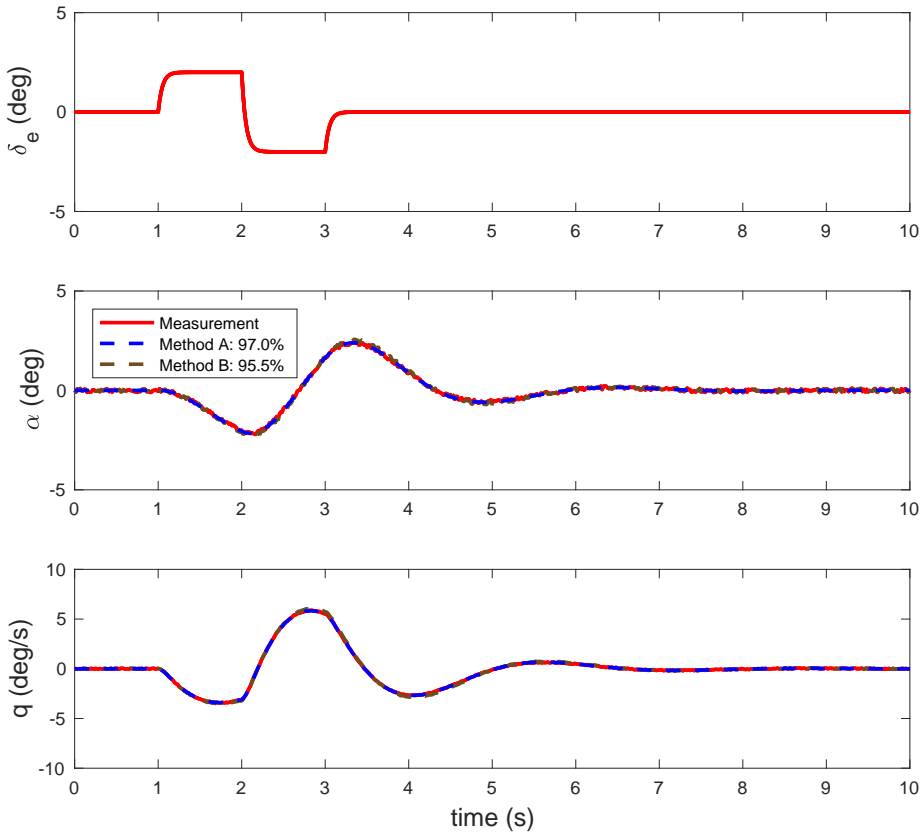


**Figure 5.11:** Validation of the estimated F-16 model. The brown dashed lines are the responses using estimated parameters from Method B and the red lines are the true simulated data.

So far the estimations have been done for low noise conditions. Even though this might sometimes be the case during real flight-testing, it is not true all the time. Therefore the robustness against both measurement and process noise are of interest. For this, two simulation study cases are used. The first is *the measurement noise case* in which only measurement noise is added to disturb the simulations. The noise amplitude is higher than expected in a real flight test of a full-scale aircraft where very accurate sensors are used. This has been chosen to challenge the methods. The second case, *the process noise case*, uses atmospheric turbulence. For this, the Dryden continuous turbulence model, described in U.S. military specification MIL-F-8785C, has been used (see Section 3.3.2 for some details). All four turbulence levels, No, Light, Medium and Severe have been used

in study cases. To be more realistic, measurement noise with a low amplitude is added to this case. To check how the estimates from Method A and Method B are affected by noise, 200 Monte Carlo (MC) runs for different noise conditions have been used.

For *the measurement noise case*, the results are shown in Figure 5.12. Here the mean of the estimated parameter values are given as squares, for Method A in blue and Method B in brown. The bars represent a mean of two estimated standard deviations based on the mean of the estimated variance over the 200 MC runs. In addition, the value of two standard deviations of the estimated parameters based on the MC simulations is given as dashed-dotted lines. This is done to see if the estimated uncertainties are close to the actual standard deviation. The estimated values at time  $t = 9$  s are shown in Table 5.4, and a similar validation as before is shown in Figure 5.13.

As can be seen in the figures and in the table, the effect of the measurement noise on the estimated model parameters is, for this open loop and stable aircraft case, not so large. The two methods appear to behave in a similar way. The model fit has decreased from around 96.0% for the noise-free validation to about 81.0%. This is to be expected, otherwise noise would most probably have entered into the estimates.

As stated before, *the process noise case* uses the Dryden model, which has four levels, no, light, medium and severe turbulence. Identification of flight mechanical characteristics is seldom done for the two higher levels, but all levels will be included in this analysis. This is done to see the robustness of the methods. Figure 5.14 shows a condensed result, displaying the input signal, the response of the angle-of-attack and the estimation of the model parameter  $M_\alpha$ , which has been chosen since it is one of the most important parameters in the model. The figure gives an overview of how the process noise affects the identification results. The estimated parameters at time  $t = 10$  s are shown in Table 5.5. More detailed figures, showing all estimated parameters, can be found in Appendix D.

As expected, the identification gets harder for increasing levels of process noise. For no and light turbulence the validation gives indications that the estimates are accurate enough to be used. Estimation for medium turbulence conditions is on the boundary of being rejected. For severe turbulence the biases in the estimates are too big to give a reasonable accurate validation.

It should also be noted that the estimated uncertainties are much lower than the standard deviation based on the MC simulations. This is not good since this implies that the estimates are more accurate than they really are.

In conclusion Method A and Method B behave in a very similar way for the studied case. There are however some practical differences in the implementation and use of the two methods. The time domain method is a recursive method, mean-

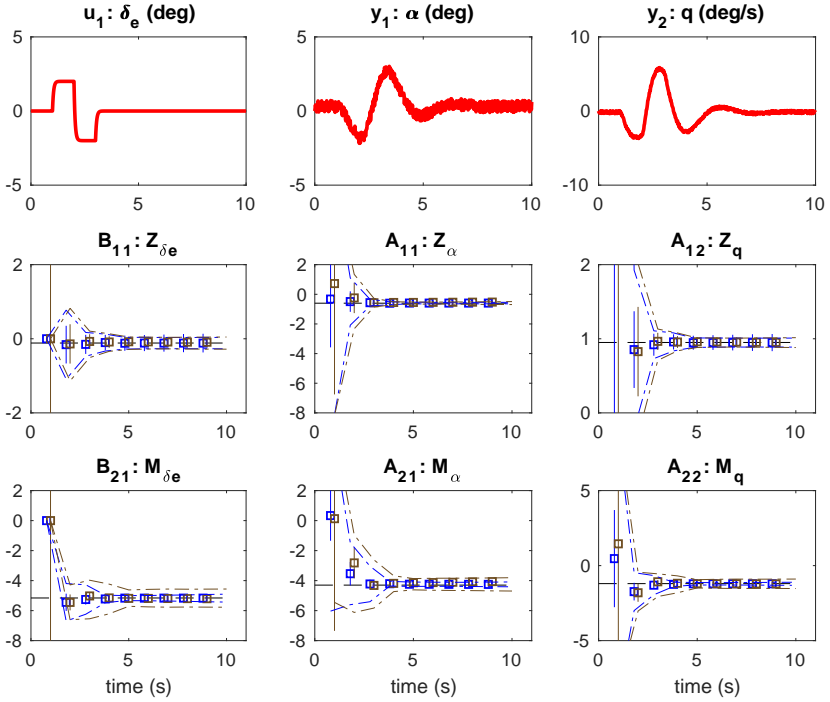


**Figure 5.12:** Comparison of estimation using Method A (blue squares) and Method B (brown squares) for the F-16 fighter. The true parameters are given by the black horizontal dashed line. The dash-dotted lines are the uncertainty of two standard deviations based on the parameter estimates, which should be compared to the vertical lines based on the mean of the estimated two standard deviations.

**Table 5.4:** Estimated parameters including two standard deviations, i.e., the vertical bars in Figure 5.12, using Method A, Method B and the true parameters, at time  $t = 9$  s for the F-16 model.

	True	Method A	Method B
$Z_\alpha$	-0.600	$-0.592 \pm 0.176$	$-0.519 \pm 0.087$
$Z_q$	0.950	$0.948 \pm 0.123$	$0.949 \pm 0.063$
$Z_{\delta_e}$	-0.115	$-0.117 \pm 0.267$	$-0.096 \pm 0.134$
$M_\alpha$	-4.300	$-4.250 \pm 0.161$	$-4.044 \pm 0.087$
$M_q$	-1.200	$-1.211 \pm 0.112$	$-1.226 \pm 0.063$
$M_{\delta_e}$	-5.157	$-5.167 \pm 0.245$	$-5.211 \pm 0.134$



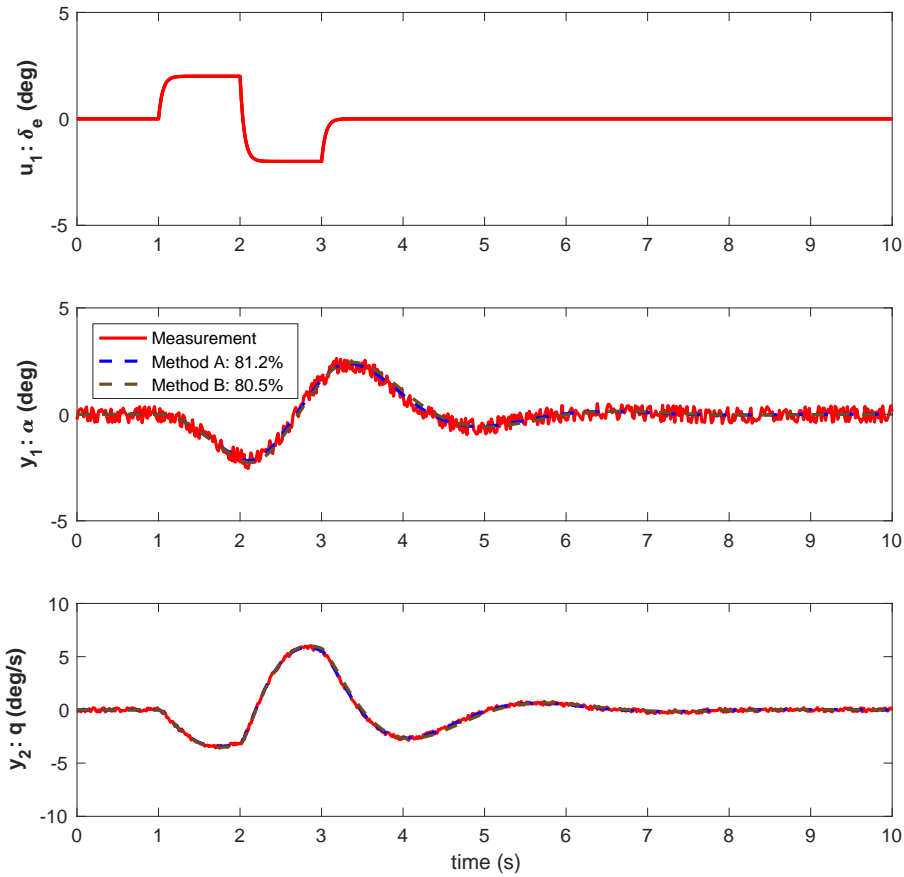


**Figure 5.13:** Validation of the estimated F-16 model. The dashed lines are the responses using estimated parameters from Method A in blue and Method B in brown. The red lines are the true simulated data.

ing that the evaluation at one time instant is dependent on the previous one. This can pose a problem if the data sent from the aircraft to the ground station is of varying length. The estimates can then be delayed when longer time sequences are transmitted. This problem, described in Andersson [2010], will not be as severe for Method A since it is sequential and the Fourier transform in (5.8) can be done in vector form.

### 5.2.3 Instrumental variables

Here some improvements to Method A will be suggested and analyzed. The focus will be on improving the bias that occurs for identification using noisy data.

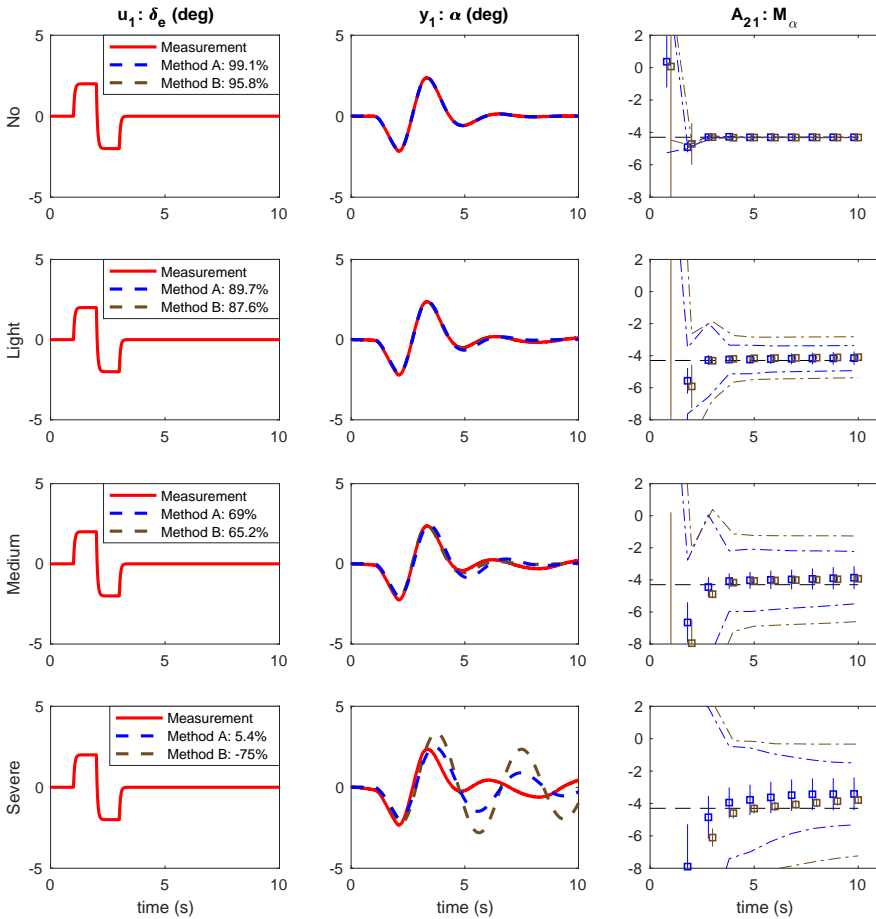


**Figure 5.14:** Estimation and validation of the estimated F-16 model for different levels of process noise. To the left the input and model fit is given. The middle column shows the response of the angle-of-attack. To the right the estimates of the model parameter  $M_\alpha$  are given.

**Table 5.5:** Comparison of Method A and Method B, showing the estimated parameter  $M_\alpha$  including two standard deviations at time  $t = 10$  s for the F-16 model. The true parameter  $M_\alpha = -4.300$ .

Turbulence	Method A	Method B
No	$-4.302 \pm 0.008$	$-4.317 \pm 0.059$
Light	$-4.153 \pm 0.415$	$-4.096 \pm 0.097$
Medium	$-3.864 \pm 0.721$	$-3.931 \pm 0.158$
Severe	$-3.410 \pm 1.011$	$-3.786 \pm 0.257$

The problem with bias due to process noise comes from the way that the noise affects the least-squares solution. Assume that the true system can be written as

$$\tilde{Z}_N = \tilde{\phi}_N \Theta_0 + \tilde{V}_0^T \quad (5.40)$$

where  $\Theta_0$  and  $\tilde{V}_0$  are the true model parameters and the transform of the true noise, including the color and structure used in (5.33), respectively. Then under fairly general assumptions [see Ljung, 1999]

$$\lim_{M \rightarrow \infty} \hat{\Theta} - \Theta_0 = \bar{E}\{(\Re(\tilde{\Phi}_N^* \tilde{\Phi}_N))^{-1}\} \bar{E}\{\Re(\tilde{\Phi}_N^* \tilde{V}_0)\} \quad (5.41)$$

This means that there has to be enough excitation so that the term  $\Re(\tilde{\Phi}_N^* \tilde{\Phi}_N)$  is invertible and the noise  $\tilde{V}_0$  has to be uncorrelated with the regressors in  $\tilde{\Phi}_N^*$  for the method to be consistent. In the applications studied here the process noise comes from atmospheric turbulence, which is not white. The measurement noise is assumed to be white, but gives rise to a noise contribution to  $\tilde{V}_0$  since the measurements are used to approximate the states. All this might lead to biased estimates of the ordinary least squares approach used in Method A. Furthermore, an aircraft with a closed-loop system will respond to the noise adding to the correlation between the noise and the output. To improve the consistency, the use of a complex Instrumental Variable (IV) approach is suggested. Instruments  $\tilde{\zeta}_N$  which are uncorrelated with the noise  $\tilde{V}_0$  but correlated with the regressors have to be chosen. This will, according to Ljung [1999], give the following estimator for parameters and their covariance

$$\hat{\Theta} = (\Re(\tilde{\zeta}_N^* \tilde{\Phi}_N))^{-1} \Re(\tilde{\zeta}_N^* \tilde{Z}_N) \quad (5.42)$$

$$\hat{C}_k(\hat{\Theta}) = \hat{\sigma}_k^2 (\Re(\tilde{\zeta}_N^* \tilde{\Phi}_N))^{-1} \Re(\tilde{\zeta}_N^* \tilde{\zeta}_N) (\Re(\tilde{\Phi}_N^* \tilde{\zeta}_N))^{-1} \quad (5.43)$$

where the real part has been used in the same way as was done for (5.19). The choice of the instruments can be made more or less optimal. One choice is to use an existing simulation model, which produces noise-free data  $(u_{N,sim}, y_{N,sim})$ . In practice, this means that the signals  $\tilde{\alpha}_m$ ,  $\tilde{q}_m$  and  $\tilde{\delta}_e$  used for  $\tilde{\Phi}_N$  in (5.27) are changed to  $\tilde{\alpha}_{sim}$ ,  $\tilde{q}_{sim}$  and  $\tilde{\delta}_{e,sim}$  used for  $\tilde{\zeta}_N$  in (5.42) and (5.43). This can be done for the intended application during a flight test, where the simulation model is run in parallel to the test (almost in real-time) using the true pilot command. The model does not have to produce the exact truth as long as the simulated data is a close approximation to the truth and correlated to the flight test data [Gilson and Van den Hof, 2005]. The described improvement will be called **Method IV**.

Running 200 Monte Carlo simulations for Method IV, for *the measurement noise case*, as for Method B, gives the results shown in Figure 5.15 and Table 5.6. It is hard to see any big differences in the resulting models between the Method A and Method IV. As a matter of fact, by looking at the validation in Figure 5.16 it can be seen that the model fit is about 81% for both cases.

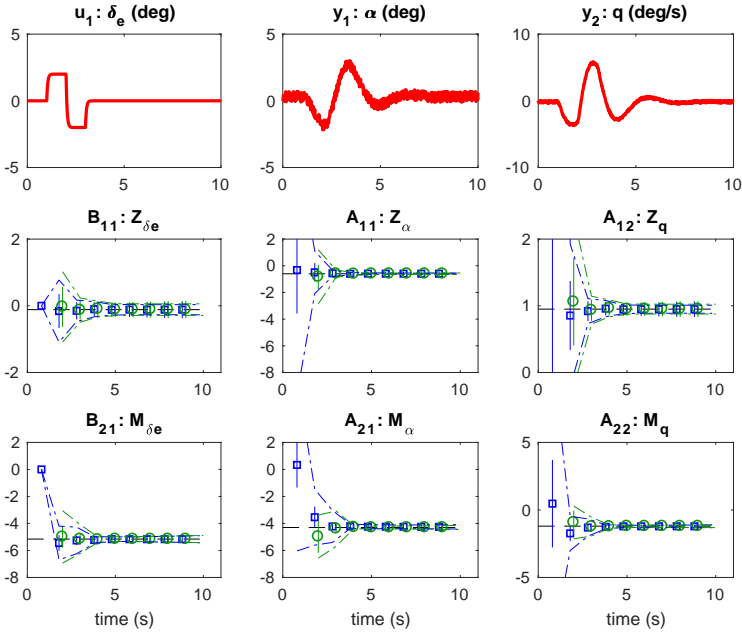


**Figure 5.15:** Comparison of estimation using the Method A (blue squares) and Method IV (green circles) for the F-16 fighter. The true parameters are given by the black horizontal dashed line. The dash-dotted lines are the uncertainty of two standard deviations based on the parameter estimates, which should be compared to the vertical lines based on the mean of the estimated two standard deviations.

**Table 5.6:** Estimated parameters including two standard deviations using Method A, Method IV and the true parameters, at time  $t = 9$  s for the F-16 model.

	True	Method A	Method IV
$Z_\alpha$	-0.600	$-0.592 \pm 0.176$	$-0.598 \pm 0.178$
$Z_q$	0.950	$0.948 \pm 0.123$	$0.950 \pm 0.127$
$Z_{\delta_e}$	-0.115	$-0.117 \pm 0.267$	$-0.115 \pm 0.279$
$M_\alpha$	-4.300	$-4.250 \pm 0.161$	$-4.300 \pm 0.163$
$M_q$	-1.200	$-1.211 \pm 0.112$	$-1.203 \pm 0.117$
$M_{\delta_e}$	-5.157	$-5.167 \pm 0.245$	$-5.160 \pm 0.256$

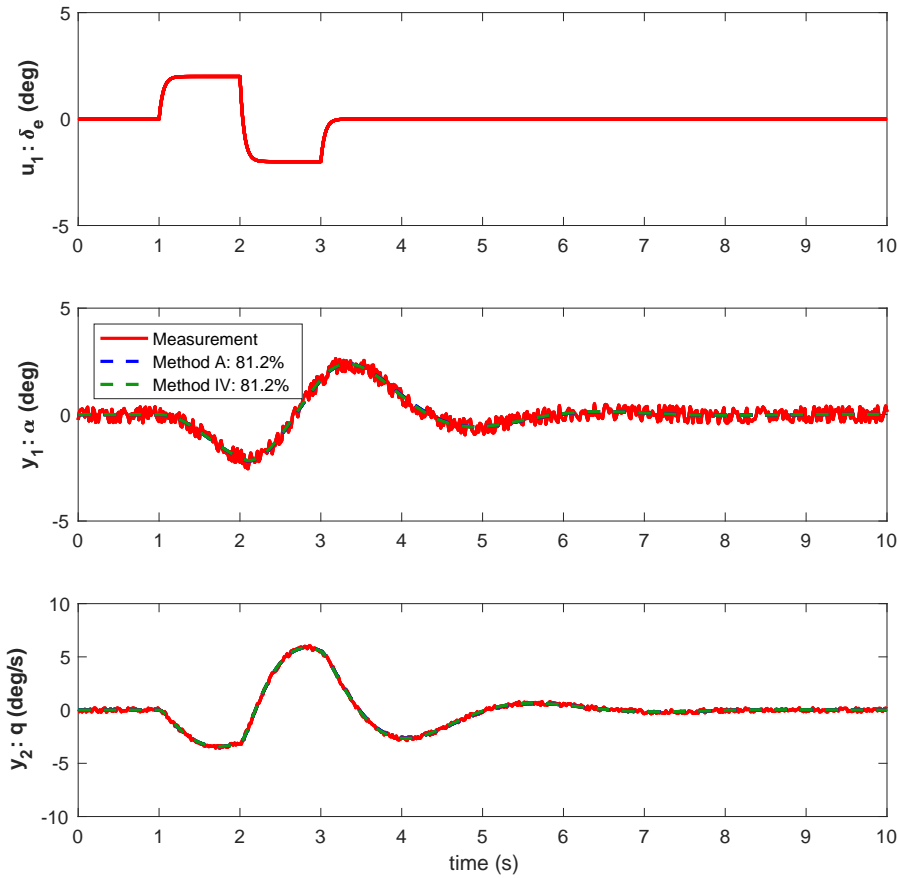


**Figure 5.16:** Validation of the estimated F-16 model. The lines are the responses using estimated data parameters from Method A in blue and Method IV in green. The red lines are the true simulated data.

The effect of Method IV is clearer when looking at the results for *the process noise* case. This is shown in Figure 5.17 and Table 5.7. The results for Method IV are much closer to the true model than for Method A. Already at light turbulence improvements, by using instruments from pre-model simulations, can be seen. However, the estimated uncertainties of two standard deviations are larger. This is, to some extent, expected since the pre-model is not the same as the true model (system). One problem is that these uncertainties keep growing with time, which is clearly seen for the medium and severe turbulence cases in Figure 5.17.

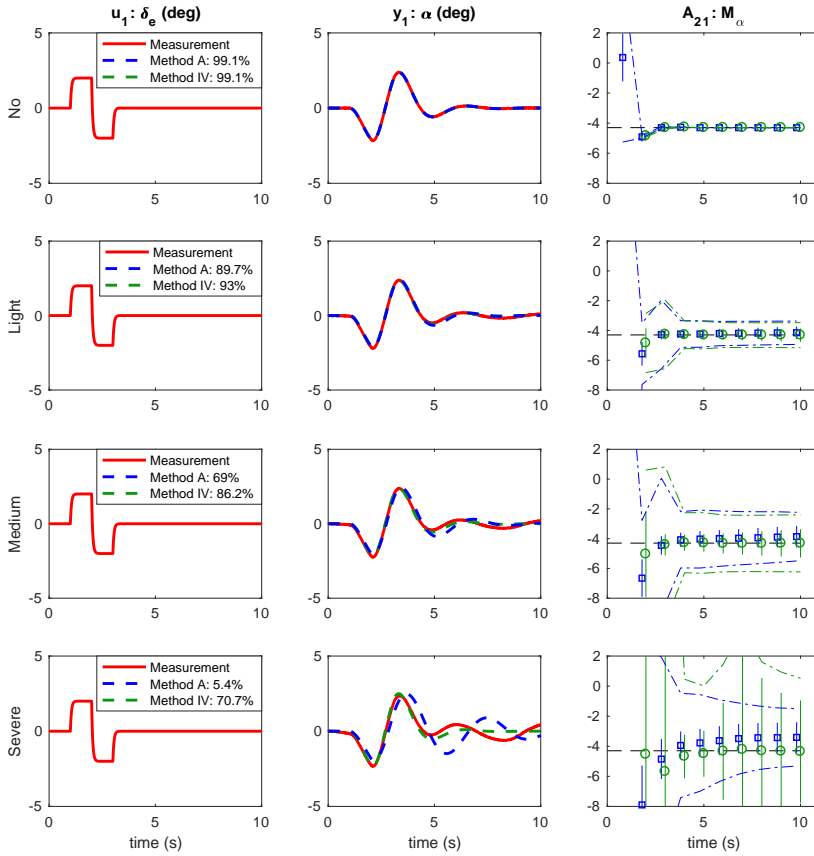


**Figure 5.17:** Estimation and validation of the estimated F-16 model for different levels of process noise. From the top, no, light, medium to severe turbulence at the bottom. To the left the input and model fit is given. The middle column shows the response of the angle-of-attack, both measurement and the models based on Method A and Method IV. To the right the estimates of the model parameter  $M_\alpha$  are given.

**Table 5.7:** Comparison of Method A and Method IV, showing the estimated parameter  $M_\alpha$  including two standard deviations at time  $t = 10$  s for the F-16 model. The true parameter  $M_\alpha = -4.300$ .

Turbulence	Method A	Method IV
No	$-4.302 \pm 0.008$	$-4.302 \pm 0.009$
Light	$-4.153 \pm 0.415$	$-4.315 \pm 0.447$
Medium	$-3.864 \pm 0.721$	$-4.316 \pm 0.950$
Severe	$-3.410 \pm 1.011$	$-4.356 \pm 3.406$

For the open-loop case Method IV works well. What will happen if the system is working under closed-loop conditions? For this, a feedback loop, based on an LQ-regulator using Bryson's rule, has been added to the stable F16 simulation model. Bryson's rule is a simple way of choosing the  $Q$  and  $R$  matrices when designing the LQ-regulator [Hespanha, 2018, Lecture 21, p. 285]. The changes of the flight characteristics from an open loop to a closed-loop system are given by the pole-zero map and elevator step response shown in Figure 5.18. As can be seen the system get a little bit faster and more damped.

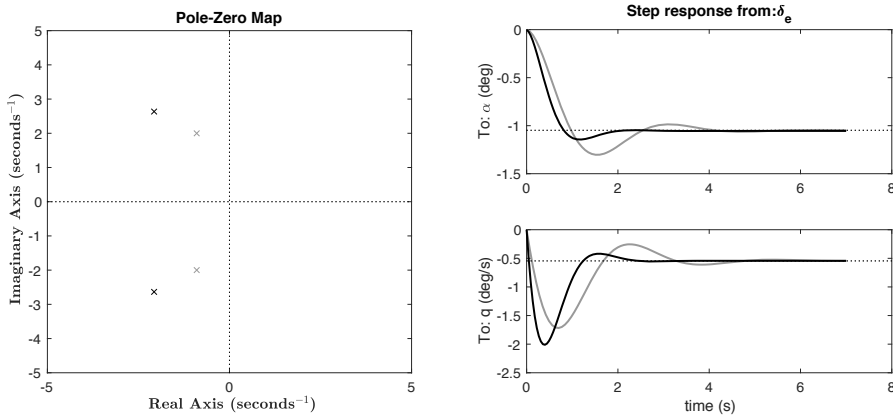


**Figure 5.18:** Pole-Zero map and elevator step response for the F-16. Gray is used for the open-loop system and black is used for the closed loop system.

The results for *the measurement noise case* are shown in Figure 5.19 and Table 5.8. The differences between Method A and Method IV are still small. This can also be seen in Figure 5.20, which shows the validation. It is interesting to see that the model fit has been reduced from 81% for the open loop case to 60% for the closed loop case since the level of measurement noise is of the same level. This means that the estimation is affected by the system feedback.

The effect on the system identification for *the process noise case* is shown in Figure 5.21 and Table 5.9. The closed-loop feedback makes it harder to get accurate estimates of the parameters, but Method IV still works well, which can be seen when looking at the model fit in the validation. It is harder to see why when looking at the estimation. This however, only shows the estimates for the pitch stability. To get the details, see Appendix D.

Method IV seems to give accurate enough results for the estimation of parameters for the stable cases using open and closed-loop systems up to medium turbulence. Many of today's fighter aircraft are unstable, working under feedback control. To investigate how well Method IV works in these conditions a model of

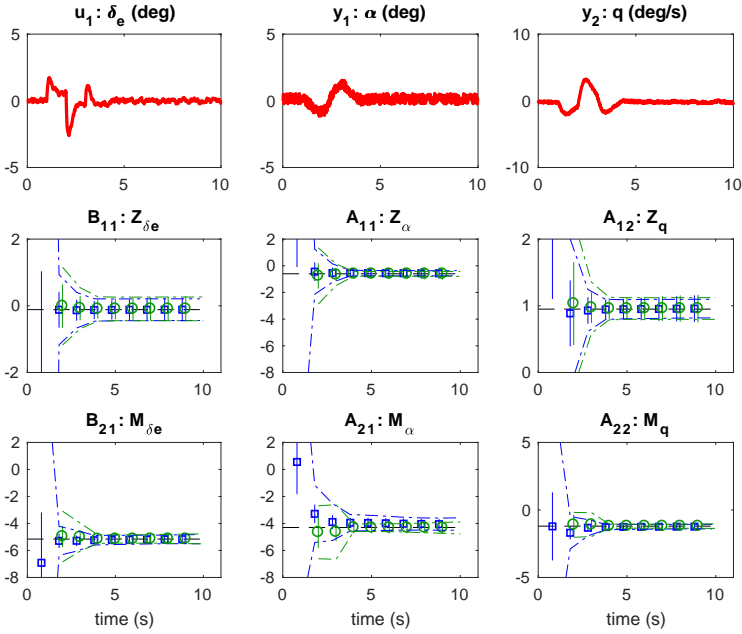


**Figure 5.19:** Comparison of estimation using Method A (blue squares) and Method IV (green circles) for the F-16 fighter in closed loop. The true parameters are given by the black horizontal dashed line. The dash-dotted lines are the uncertainty of two standard deviations based on the parameter estimates, which should be compared to the vertical lines based on the mean of the estimated two standard deviations.

**Table 5.8:** Estimated parameters including two standard deviations using Method A, Method IV and the true parameters, at time  $t = 9$  s for the F-16 model in closed loop.

	True	Method A	Method IV
$Z_\alpha$	-0.600	$-0.556 \pm 0.429$	$-0.608 \pm 0.450$
$Z_q$	0.950	$0.958 \pm 0.206$	$0.959 \pm 0.215$
$Z_{\delta_e}$	-0.115	$-0.116 \pm 0.375$	$-0.092 \pm 0.403$
$M_\alpha$	-4.300	$-4.045 \pm 0.396$	$-4.330 \pm 0.427$
$M_q$	-1.200	$-1.233 \pm 0.190$	$-1.197 \pm 0.204$
$M_{\delta_e}$	-5.157	$-5.164 \pm 0.346$	$-5.138 \pm 0.382$



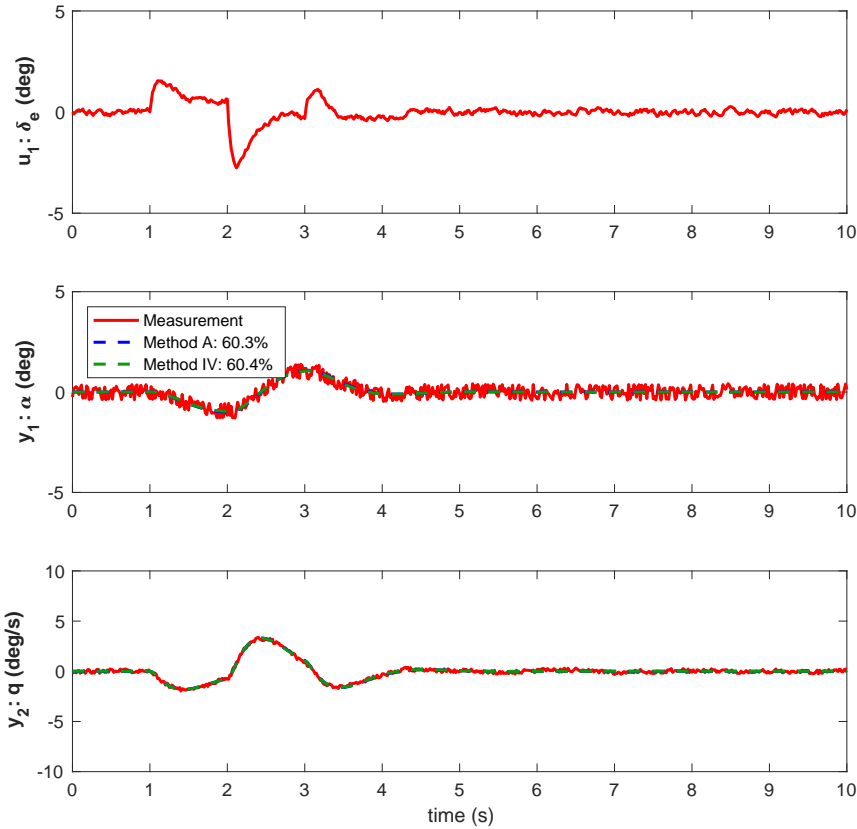


**Figure 5.20:** Validation of the estimated F-16 model. The dashed lines are the responses using estimated parameters from Method A in blue and Method IV in green. The red lines are the true simulated data.

the Swedish JAS 39 Gripen multi-role aircraft is used. The JAS 39 Gripen, shown in Figure 5.22, is open-loop unstable in the subsonic flight envelope. As for the previous F-16 case, a double pulse is used to excite the motion. However, this is done both for the elevator and the canard with a small time delay in between to avoid correlation between the input signals.

The model to estimate in this example is given by

$$\begin{aligned}
 \begin{bmatrix} \dot{\alpha}(t) \\ \dot{q}(t) \end{bmatrix} &= \begin{bmatrix} Z_\alpha & Z_q \\ M_\alpha & M_q \end{bmatrix} \begin{bmatrix} \alpha(t) \\ q(t) \end{bmatrix} + \begin{bmatrix} Z_{\delta_e} & Z_{\delta_c} \\ M_{\delta_e} & M_{\delta_c} \end{bmatrix} \begin{bmatrix} \delta_e(t) \\ \delta_c(t) \end{bmatrix} + w(t) \\
 \begin{bmatrix} \alpha_m(t) \\ q_m(t) \end{bmatrix} &= \begin{bmatrix} \alpha(t) \\ q(t) \end{bmatrix} + e(t)
 \end{aligned} \tag{5.44}$$

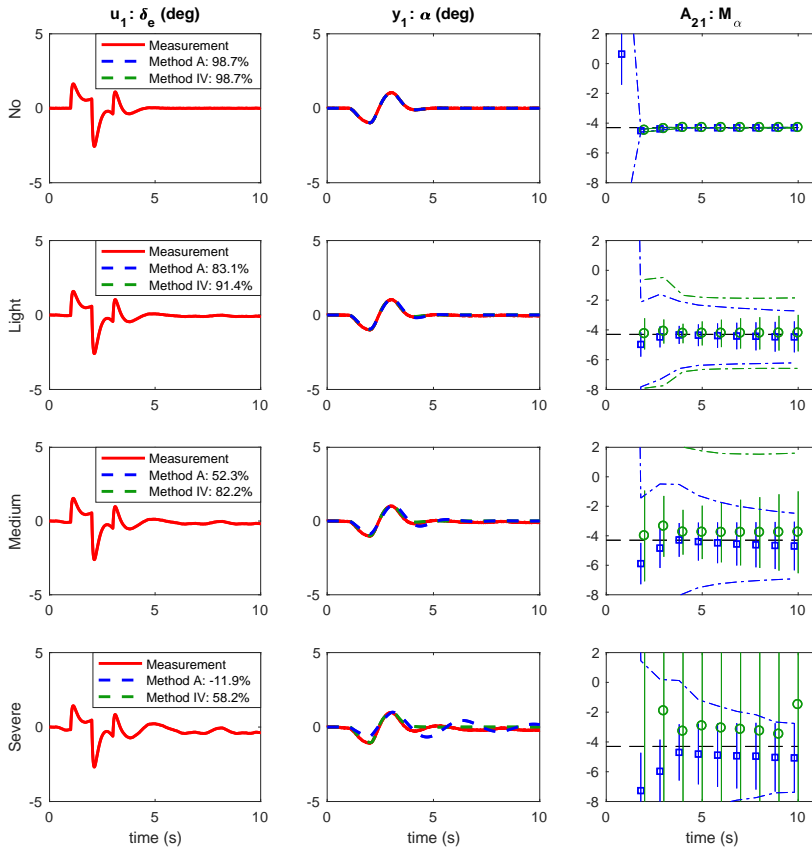


**Figure 5.21:** Estimation and validation of the estimated F-16 model, in closed loop, for different levels of process noise. From the top, no, light, medium to severe turbulence at the bottom. To the left the input and model fit is given. The middle column shows the response of the angle-of-attack, both measurement and the models based on Method A and Method IV. To the right the estimates of the model parameter  $M_\alpha$  are given.

**Table 5.9:** Comparison of Method A and Method IV, showing the estimated parameter  $M_\alpha$  including two standard deviations at time  $t = 10$  s for the F-16 model, in closed loop. The true parameter  $M_\alpha = -4.300$ .

Turbulence	Method A	Method IV
No	$-4.307 \pm 0.021$	$-4.306 \pm 0.022$
Light	$-4.467 \pm 1.040$	$-4.216 \pm 1.225$
Medium	$-4.694 \pm 1.649$	$-3.764 \pm 2.775$
Severe	$-5.066 \pm 2.336$	$-1.502 \pm 233.3$

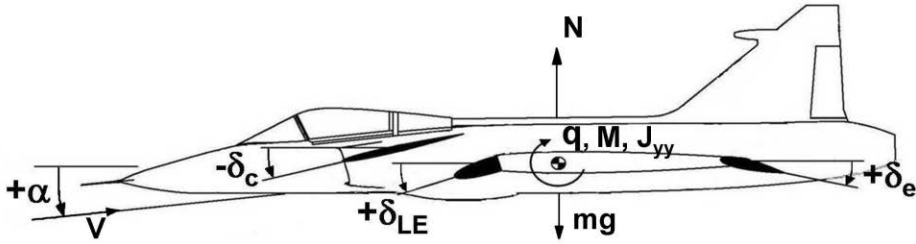


Figure 5.22: Definition of the variables of JAS 39 Gripen.

The model structure is about the same as for the simulated F-16 case, but the JAS 39 Gripen aircraft has a close-coupled wing-canard configuration compared to the more conventional configuration of the F-16. The canard input  $\delta_c(t)$  has been added in this case.

The true model parameters are

$$Z_\alpha = -0.679, Z_q = 0.992, Z_{\delta_e} = -0.220, Z_{\delta_c} = -0.012, \\ M_\alpha = 1.399, M_q = -0.537, M_{\delta_e} = -10.330 \text{ and } M_{\delta_c} = 4.324.$$

The open loop and closed-loop system characteristics are given by the pole-zero map and elevator step response shown in Figure 5.23. Here, there is an unstable pole for the open-loop system, making the step response go to infinity.

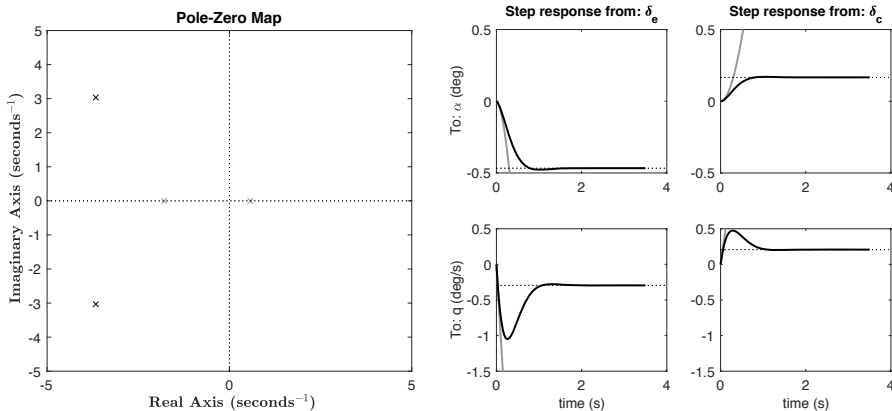


Figure 5.23: Pole-Zero map and elevator and canard step response for the JAS 39 Gripen. Gray is used for the open-loop system and black is used for the closed system.

For the identification, the definition (5.26) for  $\tilde{Z}$  stays the same as before, but (5.27) and (5.28) have to be modified to take the canard data into account. The result is

$$\tilde{\Phi} = \begin{bmatrix} \tilde{\alpha}_m(\omega_1) & \tilde{q}_m(\omega_1) & \tilde{\delta}_e(\omega_1) & \tilde{\delta}_c(\omega_1) \\ \tilde{\alpha}_m(\omega_2) & \tilde{q}_m(\omega_2) & \tilde{\delta}_e(\omega_2) & \tilde{\delta}_c(\omega_2) \\ \vdots & \vdots & \vdots & \vdots \\ \tilde{\alpha}_m(\omega_M) & \tilde{q}_m(\omega_M) & \tilde{\delta}_e(\omega_M) & \tilde{\delta}_c(\omega_M) \end{bmatrix} \quad (5.45)$$

and

$$\Theta = \begin{bmatrix} Z_\alpha & M_\alpha \\ Z_q & M_q \\ Z_{\delta_e} & M_{\delta_e} \\ Z_{\delta_c} & M_{\delta_c} \end{bmatrix} \quad (5.46)$$

Making 200 Monte Carlo simulations, as for the F16 cases, for *the measurement noise case* gives the results shown in Figure 5.24 and Table 5.10, for Method A and Method IV. As before, the results are still similar even for this case. As can be seen by the validation in Figure 5.25 the model fit is about 54% for both cases. However, there is a tendency for Method A to develop a bias over time. The phenomenon is easiest seen for the  $B_{11} : Z_{\delta_e}$  parameter. This is an effect of the continuously added noise after the end of the excitation at  $t = 7$  s. More details about this phenomenon will be given later in the convergence and consistency analysis in Section 5.3.

For *the process noise case*, the results are a bit different. Figure 5.27 and Table 5.11 show acceptable estimates for no and light turbulence. For medium turbulence Method IV performs better than Method A, even if the accuracy is not acceptable. For severe turbulence this is reversed. In fact Method IV gives very poor results. One reason for this is given by Figure 5.26, which shows the condition number for the matrix  $\Re(\tilde{C}_N^* \tilde{\Phi}_N)$  from (5.42) that should be inverted. As can be seen this condition number is very high for the JAS 39 Gripen case, leading to poor estimates. The signal-to-noise ratio is however very low so good results are not expected.

In conclusion, Method A and Method IV seem to be fairly robust towards measurement noise for the length of excitation used and instrument used here. For non-white process noise Method IV adds to the accuracy of the estimation for the F-16 cases. This is even true for the JAS 39 Gripen case up to the medium noise level. For severe turbulence the results are varying between the three studied aircraft system configurations, but system identification is not normally used for this type of data. The use of other instruments could possible mitigate this, but a study of this has not been included in this thesis. Method IV presented here seems useful for identification purposes of the application used. One remaining problem is however the tendency of the predicted uncertainty to grow over time.

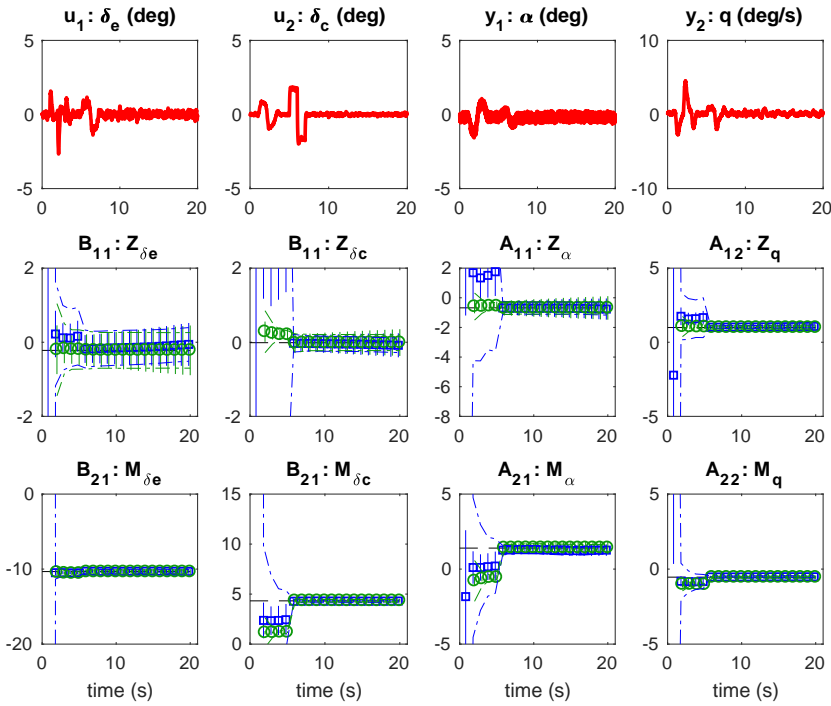


**Figure 5.24:** Comparison of estimation using Method A (blue squares) and Method IV (green circles) for the JAS 39 Gripen fighter. The true parameters are given by the black horizontal dashed line. The dash-dotted lines are the uncertainty of two standard deviations based on the parameter estimates, which should be compared to the vertical lines based on the mean of the estimated two standard deviations.

**Table 5.10:** Estimated parameters including two standard deviations using Method A, Method IV and the true parameters, at time  $t = 20$  s for the JAS 39 Gripen model.

	True	Method A	Method IV
$Z_\alpha$	-0.679	$-0.761 \pm 0.715$	$-0.686 \pm 0.793$
$Z_q$	0.992	$1.068 \pm 0.198$	$0.994 \pm 0.213$
$Z_{\delta_e}$	-0.220	$-0.059 \pm 0.579$	$-0.219 \pm 0.671$
$Z_{\delta_c}$	-0.012	$-0.082 \pm 0.324$	$-0.009 \pm 0.361$
$M_\alpha$	1.399	$1.265 \pm 0.381$	$1.420 \pm 0.424$
$M_q$	-0.537	$-0.511 \pm 0.106$	$-0.544 \pm 0.114$
$M_{\delta_e}$	-10.330	$-10.311 \pm 0.309$	$-10.370 \pm 0.359$
$M_{\delta_c}$	4.324	$4.311 \pm 0.173$	$4.338 \pm 0.193$

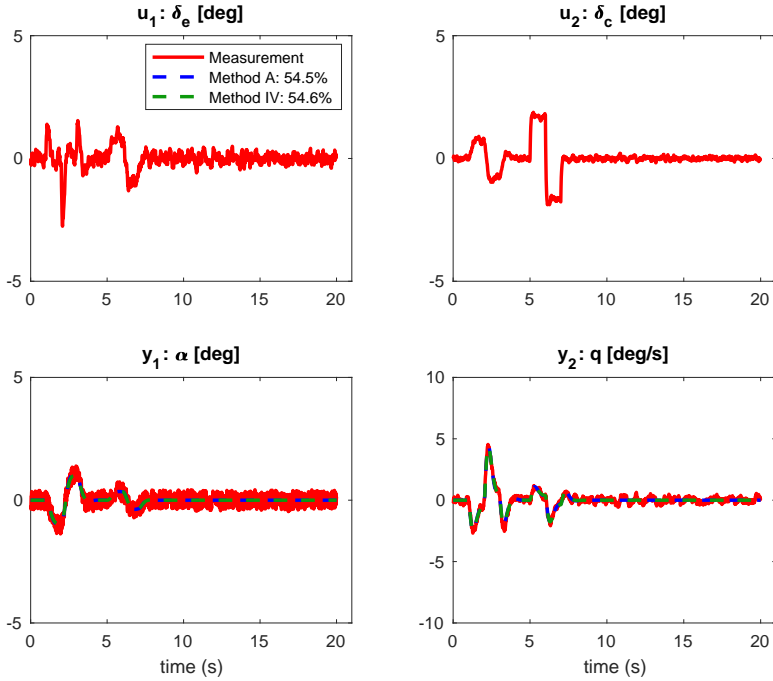


**Figure 5.25:** Validation of the estimated JAS 39 Gripen model. The lines are the responses using estimated parameters from Method A in blue and Method IV in green. The red lines are the true simulated data.

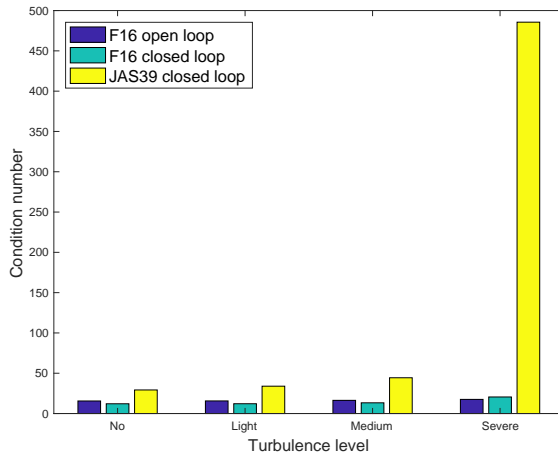


**Figure 5.26:** Condition number for the  $\Re(\tilde{C}_N^* \tilde{\Phi}_N)$ -matrix used in the suggested Method IV.

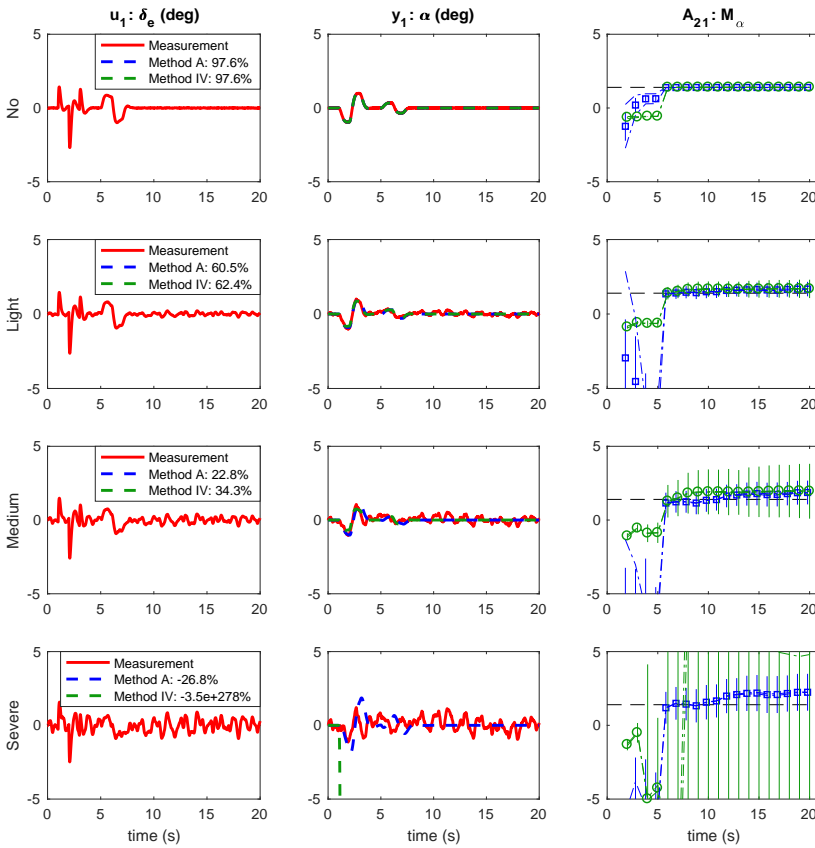


**Figure 5.27:** Estimation and validation of the estimated JAS 39 Gripen model for different levels of process noise. From the top, no, light, medium to severe turbulence at the bottom. To the left the input and model fit is given. The middle column shows the response of the angle-of-attack, both measurement and the models based on Method A and Method IV. To the right the estimates of the model parameter  $M_\alpha$  are given.

**Table 5.11:** Comparison of Method A and Method IV, showing the estimated parameter  $M_\alpha$  including two standard deviations at time  $t = 20$  s for the JAS39 model, in closed loop. The true parameter  $M_\alpha = 1.399$ .

Turbulence	Method A	Method IV
No	$1.391 \pm 0.024$	$1.403 \pm 0.026$
Light	$1.674 \pm 0.486$	$1.687 \pm 0.616$
Medium	$1.867 \pm 0.806$	$1.952 \pm 1.859$
Severe	$2.242 \pm 1.251$	$5.464 \pm 96.37$

### 5.2.4 Data fusion

A suggestion to improve the behavior of growing uncertainty estimations, which seems to be an effect of the excitation and the estimation method rather than the system, is to separate the data into time batches as in Figure 5.28 and to use data fusion, like the sensor fusion given in Gustafsson [2012, Chapter 2, p. 31], based on the information content in each batch. This could also improve estimations during longer time sequences that are without any excitation.

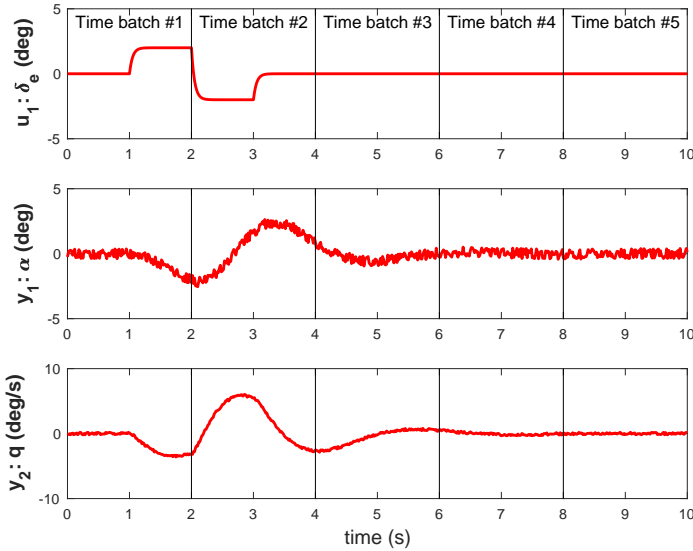


**Figure 5.28:** Data set divided into time batches to be used for data fusion.

An example of the effect of growing uncertainties for estimation during times with no excitation using least squares is illustrated in Example 5.1 below.

---

#### Example 5.1: Simple LS estimator

---

Consider a simple scalar system

$$y_k = b_0 u_k + v_k, \quad k = 1, \dots, N \quad (5.47)$$

where  $v_k$  is zero mean white noise with variance  $\sigma_v^2$  and let the excitation be as in Figure 5.29. The ordinary Least-Squares method in the time domain would then be given by

$$\hat{b}_0 = \frac{\Phi_N^T y_N}{\Phi_N^T \Phi_N} \quad (5.48)$$

with  $\Phi_N = u_N$ . Here  $u_N$  and  $y_N$  are vectors containing the  $N$  samples.



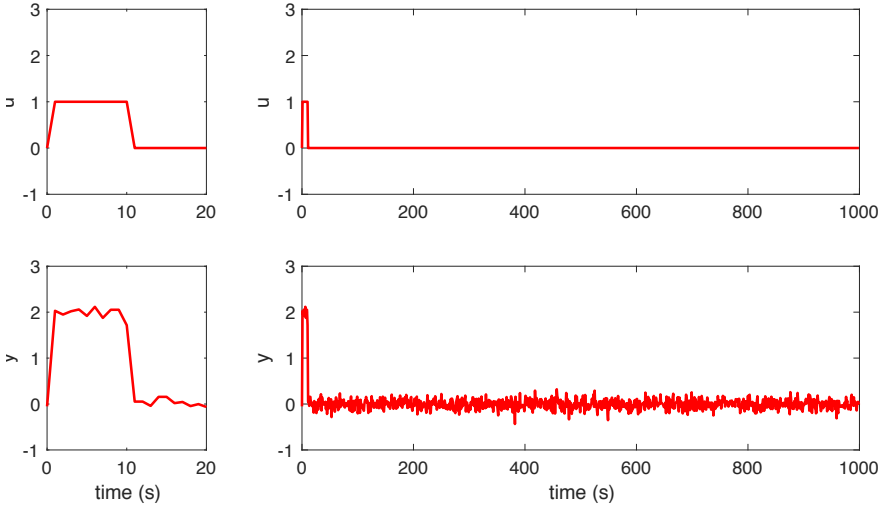


**Figure 5.29:** Data for an excitation using a single pulse as a input  $u$  giving the response  $y$ . To the left a zoom of the time interval of  $[0 - 20]$  s is given.

By taking the sample mean of (5.47), the expression becomes

$$\bar{y}_N = b_0 \bar{u}_N + \bar{v}_N \quad (5.49)$$

where

$$\bar{y}_N = \frac{1}{N} \sum_{k=1}^N y_k, \bar{u}_N = \frac{1}{N} \sum_{k=1}^N u_k \text{ and } \bar{v}_N = \frac{1}{N} \sum_{k=1}^N v_k. \quad (5.50)$$

This is similar to the discrete-time finite Fourier transform given by (5.7) by using a single frequency of  $\omega = 0$ . This new expression has a Least-Squares form

$$\hat{b}_{0,N} = \frac{\Phi_N^T \bar{y}_N}{\Phi_N^T \Phi_N} = \frac{\bar{y}_N}{\bar{u}_N} = b_0 + \frac{\bar{v}_N}{\bar{u}_N} \quad (5.51)$$

with  $\Phi_N = \bar{u}_N$ , since  $\bar{u}_N$  and  $\bar{y}_N$  are a scalars. Here (5.49) has been used in the third equality. Note also that using the IV approach does not change the estimator in (5.51).

Let the true system parameter be  $b_0 = 2$ . Then, for time  $t = 10$  s

$$\bar{y}_{10} = 2 + \bar{v}_{10} \text{ and } \bar{u}_{10} = 1 \quad (5.52)$$

which gives

$$\hat{b}_{0,10} = 2 + \bar{v}_{10} \quad (5.53)$$

At time  $t = 1000$  s

$$\bar{y}_{1000} = 0.02 + \bar{v}_{1000} \text{ and } \bar{u}_{1000} = 0.01 \quad (5.54)$$

which gives

$$\hat{b}_{0,1000} = 2 + 100\bar{v}_{1000} \quad (5.55)$$

This will give a growing variance with time as

$$\text{var}(\hat{b}_{0,10}) = \frac{1}{10}\sigma_v^2 \text{ increase to } \text{var}(\hat{b}_{0,1000}) = \frac{10000}{1000}\sigma_v^2 \quad (5.56)$$

In Figure 5.30 a time history of  $\hat{b}_0$  is given together with  $\text{var}(\hat{b}_0)$ .

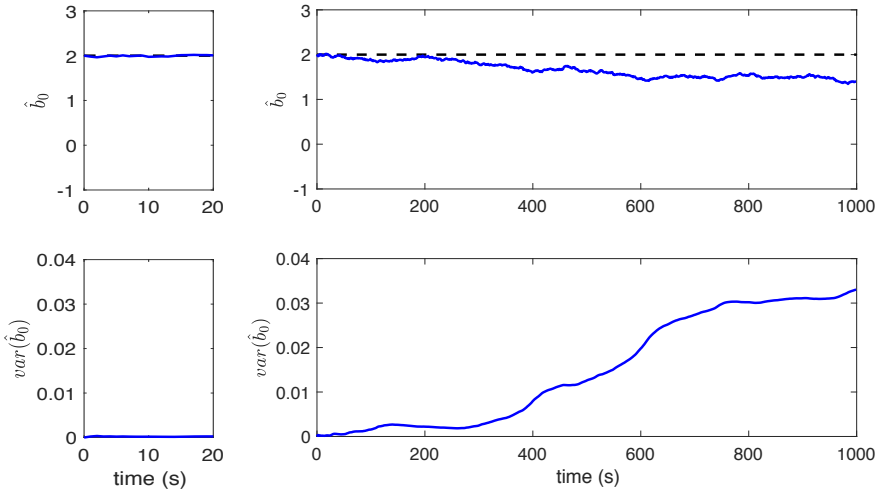


**Figure 5.30:** The top figure shows a comparison of the estimate of  $\hat{b}_0$ , using Method A (blue), with the true  $b_0 = 2$ . In the lower figure the growing  $\text{var}(\hat{b}_0)$  is shown. To the left a zoom of the time interval of  $[0 - 20]$  s is given.

This simple example shows that both the estimate and the uncertainties are affected by the noise when the excitation is active only during a limited period of time relative to the whole time sequence, which makes  $\bar{u}_N \rightarrow 0$  as  $N \rightarrow \infty$ .

Data fusion is a weighted average of two estimates  $\hat{\theta}_1$  and  $\hat{\theta}_2$  from different sources measuring the same system. In this case the sources are two different time sequences, which gives the fusion

$$\begin{aligned} \hat{I} &= \hat{I}_1 + \hat{I}_2 \\ \hat{\theta} &= \hat{I}^{-1}(\hat{I}_1\hat{\theta}_1 + \hat{I}_2\hat{\theta}_2) \end{aligned} \quad (5.57)$$

Here  $\hat{I}_i = \hat{P}_i^{-1}$  is an estimate of the Fisher information matrix. Information can be added from several time batches and to get an algorithm that runs sequentially it is possible to store the old information in  $\hat{I}_k$  and  $\hat{\theta}_k$ ,  $k = 1, \dots, B - 1$  and let the

new information from the latest batch be  $\hat{I}_B$  and  $\hat{\theta}_B$ . This gives

$$\begin{aligned}\hat{I}_{[1,B]} &= \hat{I}_{[1,B-1]} + \hat{I}_{[B]} \\ \hat{\theta}_{[1,B]} &= \hat{I}_{[1,B]}^{-1}(\hat{I}_{[1,B-1]}\hat{\theta}_{[1,B-1]} + \hat{I}_{[B]}\hat{\theta}_{[B]})\end{aligned}\quad (5.58)$$

At the start of each batch a new estimation is begun from scratch. If estimates are to be presented more than one time in each batch, say every second in Figure 5.28, then fusion is done between the old information,  $\hat{I}_{[1,B-1]}$ , and the part of the new information in  $k = B$  that exist at those times. This means that at time  $t = 5$  s in Figure 5.28, the fusion is done between  $\hat{I}_{[1,2]}$ , and the information that exist in time interval  $t = 4 - 5$  s.

$$\begin{aligned}\hat{I}_{t=0-5} &= \hat{I}_{[1,2]} + \hat{I}_{t=4-5} \\ \hat{\theta}_{t=0-5} &= \hat{I}_{t=0-5}^{-1}(\hat{I}_{[1,2]}\hat{\theta}_{[1,2]} + \hat{I}_{t=4-5}\hat{\theta}_{t=4-5})\end{aligned}\quad (5.59)$$

At  $t = 6$  s the fusion of whole batches are done like

$$\begin{aligned}\hat{I}_{[1,3]} &= \hat{I}_{[1,2]} + \hat{I}_{[3]} \\ \hat{\theta}_{[1,3]} &= \hat{I}_{[1,3]}^{-1}(\hat{I}_{[1,2]}\hat{\theta}_{[1,2]} + \hat{I}_{[3]}\hat{\theta}_{[3]})\end{aligned}\quad (5.60)$$

---

**Example 5.2: Simple LS estimator cont.**

---

Here, a continuation of Example 5.1 using the data fusion approach is presented.

The formulation (5.49) can, for the excitation given in Figure 5.29, be rewritten as

$$\bar{y}_N = \begin{cases} b_0 \bar{u}_N + \bar{v}_N & \text{if } t \leq 10 \text{ s} \\ \bar{v}_N & \text{otherwise} \end{cases}\quad (5.61)$$

So, there is only noise in this system for  $t > 10$  s. Therefore, the information is zero for times larger than ten seconds.

For simplicity the batch length is set to 10 s, leading to 100 batches. Then, for time  $t = 10$  s

$$\bar{v}_{10} = 2 + \bar{v}_{10} \text{ and } \bar{u}_{10} = 1\quad (5.62)$$

which gives

$$\begin{aligned}\hat{b}_{0,10} &= 2 + \bar{v}_{10} \\ \text{var}(\hat{b}_{0,10}) &= \frac{1}{10} \sigma_v^2\end{aligned}\quad (5.63)$$

as before. The information will at this time be

$$\hat{I}_{[1]} = \frac{1}{\text{var}(\hat{b}_{0,10})} = \frac{10}{\sigma_v^2}\quad (5.64)$$

At time  $t = 1000$  s the data fusion will give

$$\hat{I}_{[1,100]} = \hat{I}_{[1]} + \sum_{k=2}^{100} \hat{I}_{[k]} \quad (5.65)$$

$$\hat{b}_{0,[100]} = \hat{I}_{[1,100]}^{-1} (\hat{I}_{[1]} \hat{b}_{0,[1]} + \sum_{k=2}^{100} \hat{I}_{[k]} \hat{b}_{0,[k]})$$

Since  $\hat{I}_{[k]} = 0, \forall k > 1$  this becomes

$$\begin{aligned} \hat{I}_{[1,100]} &= \hat{I}_{[1]} \\ \hat{b}_{0,[100]} &= \hat{b}_{0,[1]} \end{aligned} \quad (5.66)$$

Therefore, the resulting estimate and variance becomes

$$\begin{aligned} \hat{b}_{0,1000} &= 2 + \bar{v}_{10} \\ \text{var}(\hat{b}_{0,1000}) &= \frac{1}{10} \sigma_v^2 \end{aligned} \quad (5.67)$$

which is the same as for  $t = 10$  s, i.e., both the estimate and the variance are unaffected by the noise as time increases. Figure 5.31 shows  $\hat{b}_0$  together with  $\text{var}(\hat{b}_0)$  for the data fusion approach compared to Method A.

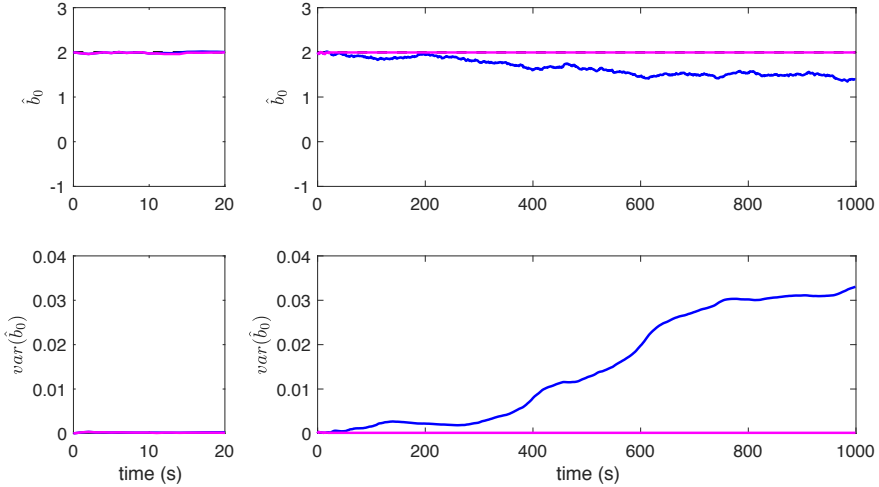


**Figure 5.31:** The top figure shows a comparison of the estimate of  $\hat{b}_0$ , using Method A (blue) and using data fusion (magenta), with the true  $b_0 = 2$ . In the lower figure the growing  $\text{var}(\hat{b}_0)$  is shown. To the left a zoom of the time interval of [0 – 20] s is given.

Adding the fusion part to Method IV gives **Method C**. The length of the time batches can be adjusted to fit the problem at hand. This means that if there is much noise in the data, longer batches can be used. By choosing a batch time that is the whole test time, Method IV is regained. This might be the best choice for short tests with much noise.

When running the Monte Carlo simulations for Method C, only the case of the JAS 39 Gripen is presented since the results are very similar when compared to Method IV. The differences are mainly in the estimates of the uncertainties. The results for the F16 cases can be found in Appendix D.

The results for *the measurement noise case* are shown in Figure 5.32 and Table 5.12. As for the earlier analysis of Method IV, it is hard to see any big differences in the resulting models between the Method A and Method C. In fact, by looking at the validation in Figure 5.33 it can be seen that the model fit is about 54% for both methods.

It should be pointed out that the uncertainty bounds using the Monte Carlo simulations, shown as dash-dotted lines in Figure 5.32, are much wider than the estimated ones, shown as the vertical bars, for this case. This is in contrast to Method IV for which the two ways of estimating the uncertainty are closer together. The reason for these wider uncertainty bounds is that there is a spread in the estimate as shown in Figure 5.34. As can be seen, most estimates are close to the true value, but there are some outliers that really affect the MC boundaries.

The results from *the process noise case* for Method C follow closely Method IV results as can be seen in Figure 5.35 and Table 5.13. Acceptable results are received from the no and light turbulence data. At the medium level the results are not so accurate and for severe turbulence the estimates give an unusable model. Compared to Method IV, Method C does not have the problem of growing uncertainties. Here, the Monte Carlo simulated uncertainty bounds are much smaller than the estimated ones. This is the opposite from *the measurement noise case* analysis.

### 5.3 Convergence and consistency analysis

Here the convergence and consistency of the three frequency domain methods will be analyzed. As will be seen this also gives a reason to discuss how the input affects the outcome of the identification using these methods.

As a first step in this analysis a noise free case for a double pulse input on the elevator and canard is applied. The sequence is, first an elevator double pulse with a period time of two seconds followed by a delay of one second before a similar double pulse for the canard is executed. This is the same input as the one

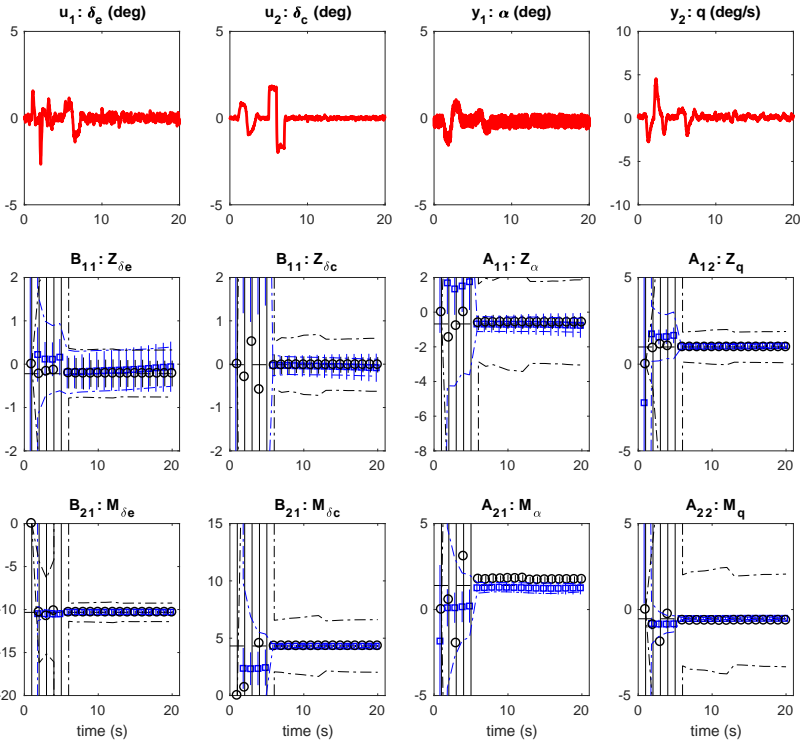


**Figure 5.32:** Comparison of estimation using Method A (blue squares) and Method C (black circles) for the JAS39 fighter. The true parameters are given by the black horizontal dashed line. The dash-dotted lines are the uncertainty of two standard deviations based on the parameter estimates, which should be compared to the vertical lines based on the mean of the estimated two standard deviations.

**Table 5.12:** Estimated parameters including two standard deviations using Method A, Method C and the true parameters, at time  $t = 20$  s for the JAS39 model.

	True	Method A	Method C
$Z_\alpha$	-0.679	$-0.762 \pm 0.715$	$-0.592 \pm 0.353$
$Z_q$	0.992	$1.068 \pm 0.198$	$0.984 \pm 0.094$
$Z_{\delta_e}$	-0.220	$-0.059 \pm 0.579$	$-0.215 \pm 0.297$
$Z_{\delta_c}$	-0.012	$-0.082 \pm 0.324$	$-0.014 \pm 0.177$
$M_\alpha$	1.399	$1.265 \pm 0.381$	$1.751 \pm 0.188$
$M_q$	-0.537	$-0.511 \pm 0.106$	$-0.633 \pm 0.050$
$M_{\delta_e}$	-10.330	$-10.311 \pm 0.309$	$-10.328 \pm 0.158$
$M_{\delta_c}$	4.324	$4.311 \pm 0.173$	$4.324 \pm 0.096$

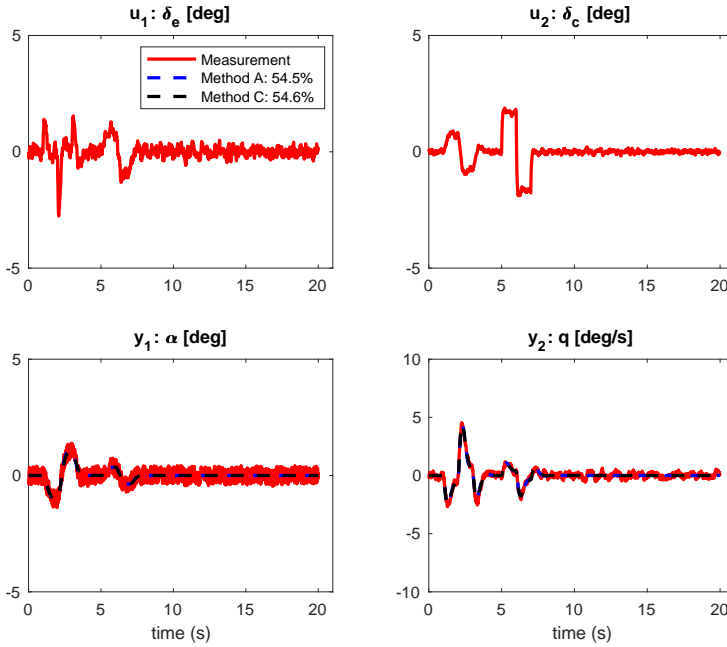


**Figure 5.33:** Validation of the estimated JAS39 model. The dashed lines are the responses using estimated parameters from the Method A in blue and Method C in black. The red lines are the true simulated data.

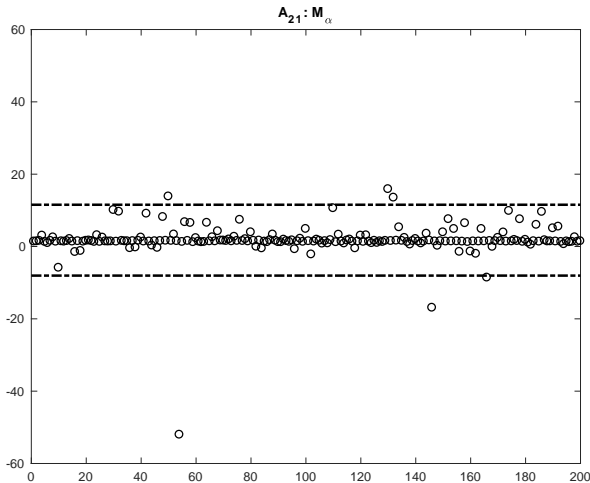


**Figure 5.34:** The 200 estimates of  $M_\alpha$  at time  $t = 20$  s for Method C, which have been used for the Monte Carlo bounds in Figure 5.32.

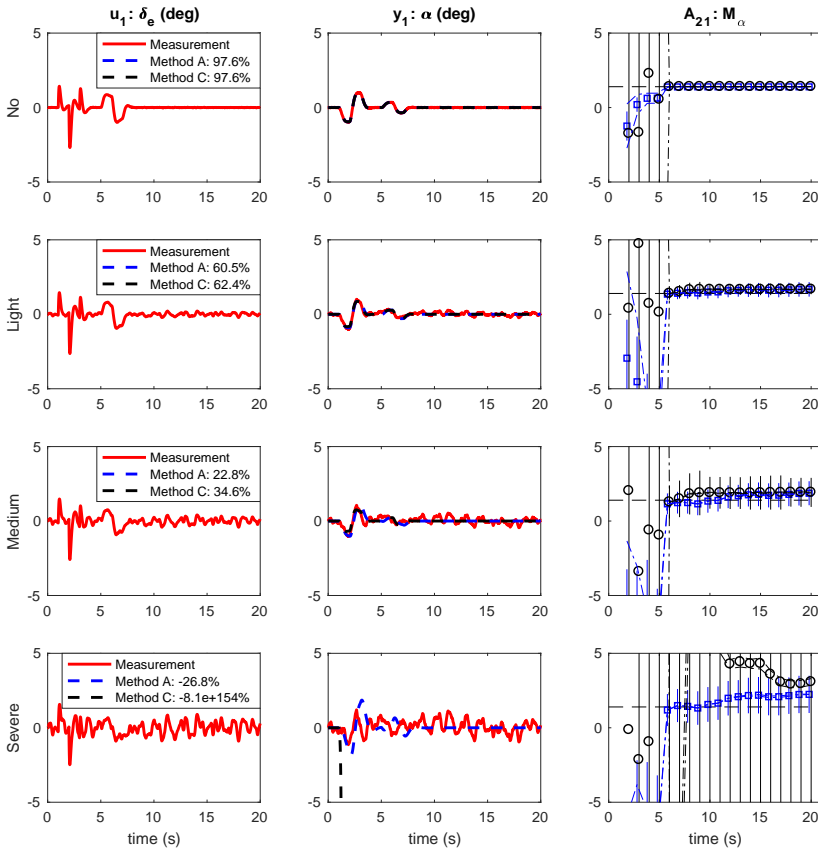


**Figure 5.35:** Estimation and validation of the JAS39 model for different levels of process noise, from the top, no, light, moderate to severe turbulence at the bottom. To the left the input and model fit is given. The middle column shows the response of the angle-of-attack, both measurement and the models based on Method A and Method C. To the right the estimates of the model parameter  $M_\alpha$  are given.

**Table 5.13:** Comparison of Method A and Method C, showing the estimated parameter  $M_\alpha$  including two standard deviations at time  $t = 20$  s for the JAS39 model. The true parameter  $M_\alpha = 1.399$ .

Turbulence	Method A	Method C
No	$1.391 \pm 0.024$	$1.403 \pm 0.014$
Light	$1.674 \pm 0.486$	$1.679 \pm 0.328$
Medium	$1.867 \pm 0.806$	$1.924 \pm 0.975$
Severe	$2.242 \pm 1.251$	$3.083 \pm 46.64$



previously used in this chapter for the JAS 39 Gripen configuration. Here however, the simulation is run for a longer time. The result is shown in Figure 5.36. Only the elevator input is shown to give a feeling for the excitation. In the same way only the response in the angle-of-attack is shown. Both the measurements and the simulated instruments are given. The parameter  $A_{21} : M_\alpha = 1.399$  from Table 5.13 has been chosen to represent the model estimates. The input used has enough information for the estimates to be consistent, i.e., to converge to the true parameter value.

When noise is added the results are very different. A case with both measurement noise and severe turbulence is shown in Figure 5.37. As can be seen Method A and Method IV both have large errors in the estimates and do not seem to converge at all. Method C converges, but also with a bias. Clearly a single double pulse is not enough to get consistency for a noisy case like this. The reason for the convergence of Method C is that the data fusion part do not use so much of the non-informative part after the end of the input. This can be seen in Figure 5.38, which shows the saved and the new estimates as well as how they are weighted together to get the fused estimate.

In Figure 5.39 continuously input varying for the elevator and canard have been used. When looking at the results both Method A and Method IV do not converge, at least not based on the uncertainty estimates. Also, even though the estimates are close to the true system parameter, there seem to be some problems. This can for example be seen close to time  $t = 150$  s and  $t = 300$  s. The gray lines in the subfigures show the condition number for the matrix to be inverted in the estimation process. This condition number gets really big close to the mentioned times. This will affect the estimates in a bad way. Therefore the consistency can also be questioned. For Method A this behavior is expected since there is noise in the regressors, but Method IV should be able to handle this phenomenon.

In contrast to the above behavior, Method C seems to converge as well as being consistent. The reason is the same as before and can be seen in Figure 5.40. As the fused information  $\hat{I}_{[1,B-1]}$  grows larger, it gets dominant over the information of the new estimates  $\hat{I}_{[B]}$  in (5.58). This means that new estimates are scaled down. This also occurs before the condition number problem, and therefore improves the consistency properties.

The problem with the condition number comes from the fact that the input and the evaluation frequencies coincide with a full period at a rate of 150 s. Looking at the input, it has a period of  $T_u = 6$  s or a frequency of  $T_u = 1/6$  Hz. When setting up the identification the frequency vector used for the evaluation is  $f = 0.10 : 0.04 : 2.0$  Hz. This can be written as  $f = 0.10, 0.14, 0.18, \dots = 5 * 0.02, 7 * 0.02, 9 * 0.02, \dots$ , which gives a period time of  $T = 50$  s or a frequency of  $f = 1/50$  Hz. The common denominator of the two frequencies is 150. To show that this frequency coupling really is the trigger to the problem a test to change the frequency for evaluation to  $f = 1/100$  Hz is done, which gives the common

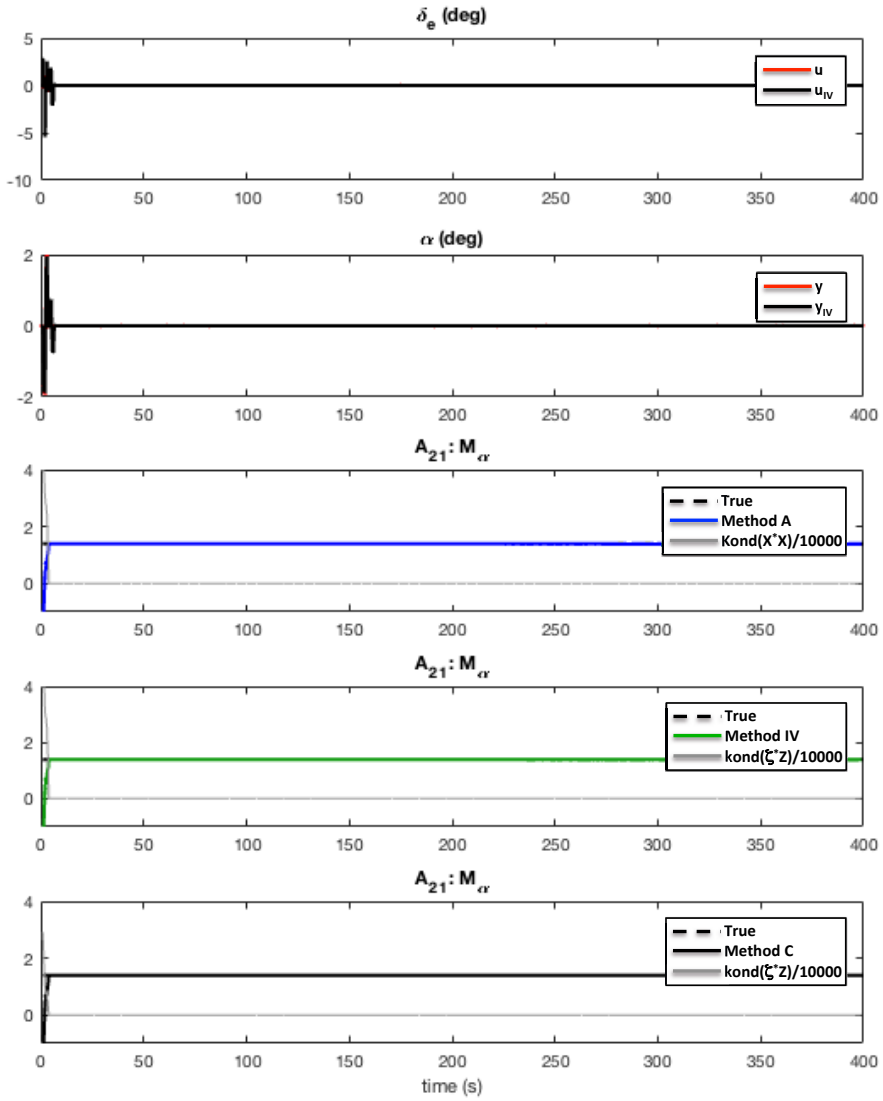


**Figure 5.36:** Comparison of the different frequency domain methods for a single input noise-free excitation for convergence and consistency analysis. The elevator double-pulse input and angle-of-attack output are shown together with the JAS 39 model parameter  $M_\alpha = 1.399$ .

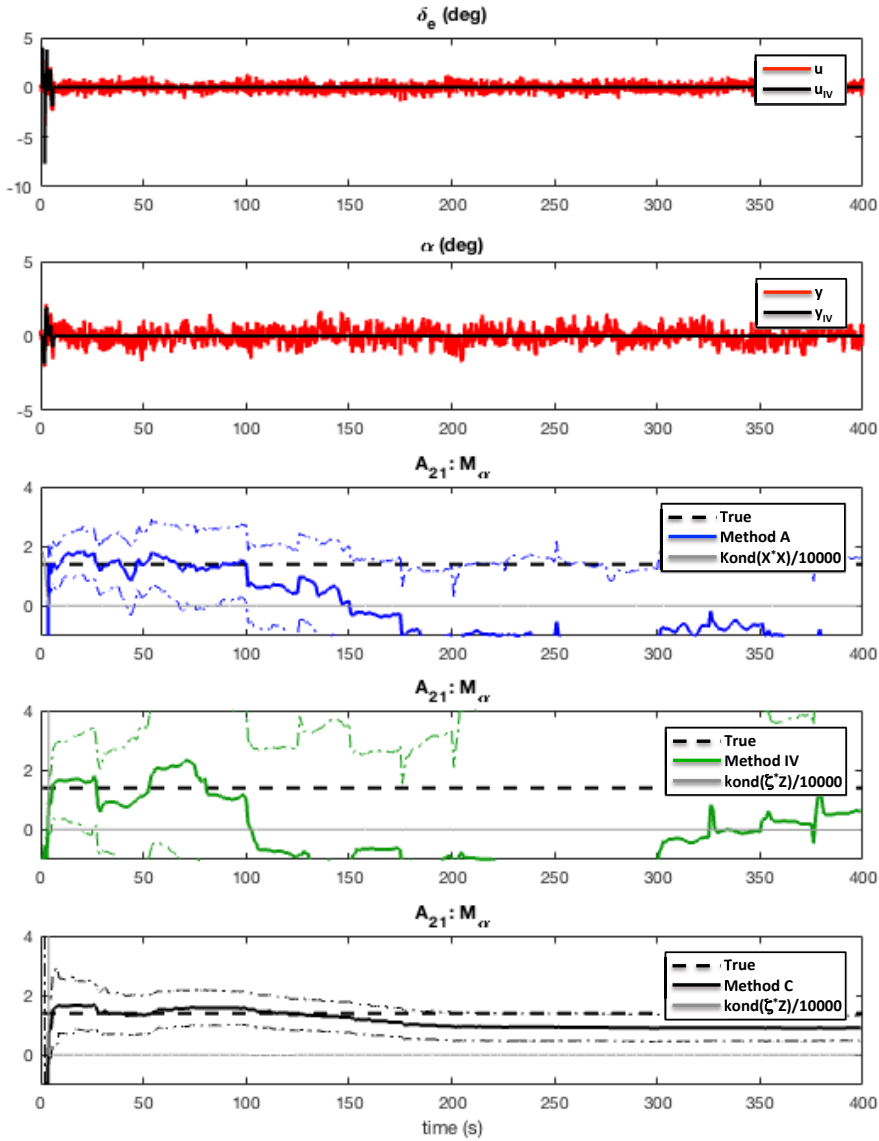


**Figure 5.37:** Comparison of the different frequency domain methods for a single input noisy excitation for convergence and consistency analysis. The elevator double-pulse input and angle-of-attack output are shown together with the JAS 39 model parameter  $M_{\alpha} = 1.399$ .

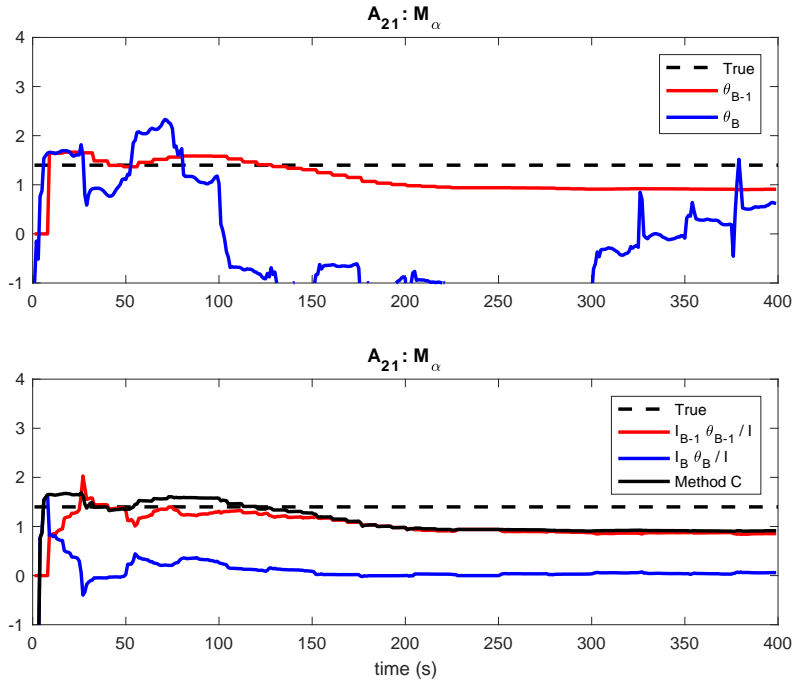


**Figure 5.38:** Display of the parts of the data fusion for the JAS 39 model parameter  $M_\alpha = 1.399$ . At the top are the estimated parameters from the old fused data in red and the new data in blue. At the bottom are the fused estimate in black and the weighted parts in red and blue.

denominator of the frequencies of 300. This is shown in Figure 5.41. The problem is then shifted to a time interval of  $T_u = 300$  s, which supports the statement of coinciding frequencies.

Another suggestion to get away from the problem is to use a more random input to break the coupling. An example is shown in Figure 5.42. The condition number problem has vanished, but a bias problem occurs instead for Method A and Method IV. It is interesting to note that Method C is fairly insensitive to all these changes made in the convergence and consistency analysis.

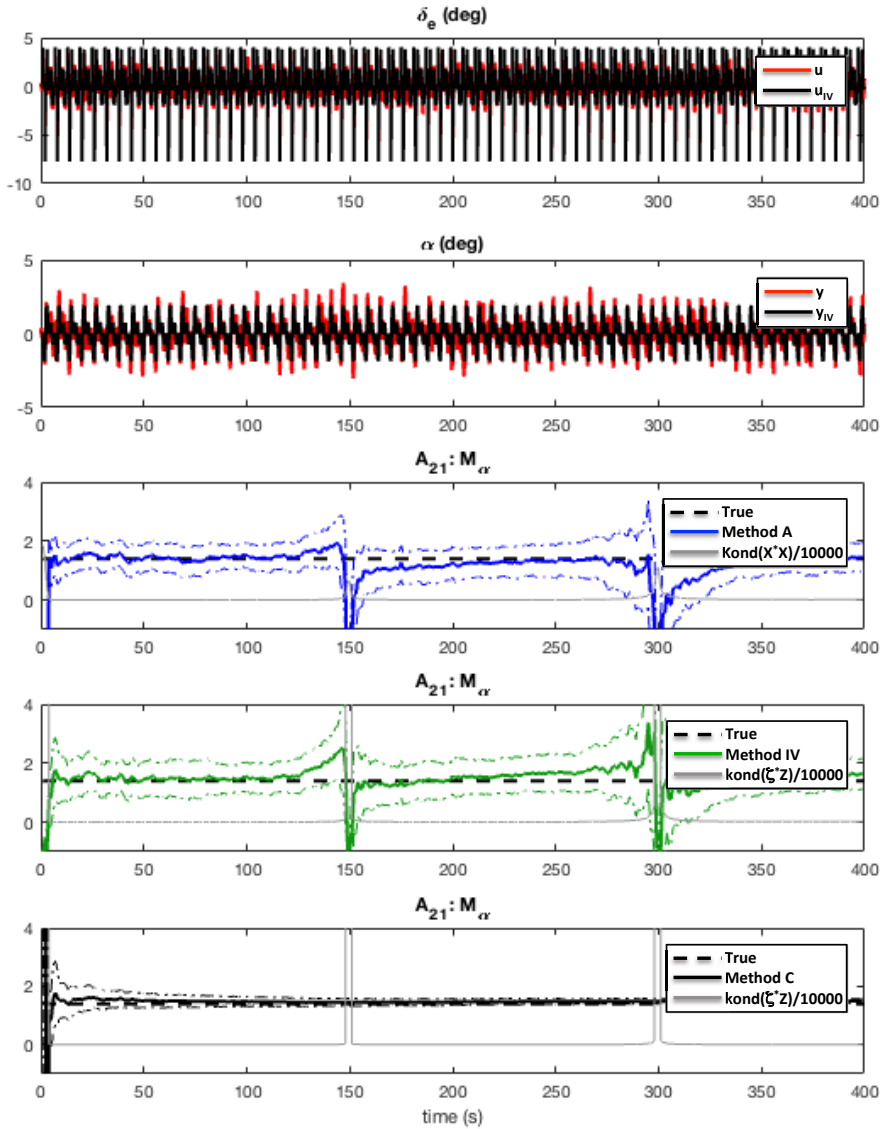


**Figure 5.39:** Comparison of the different frequency domain methods for a continuously varying noisy excitation for convergence and consistency analysis. The elevator double-pulse input and angle-of-attack output are shown together with the JAS 39 model parameter  $M_\alpha = 1.399$ .

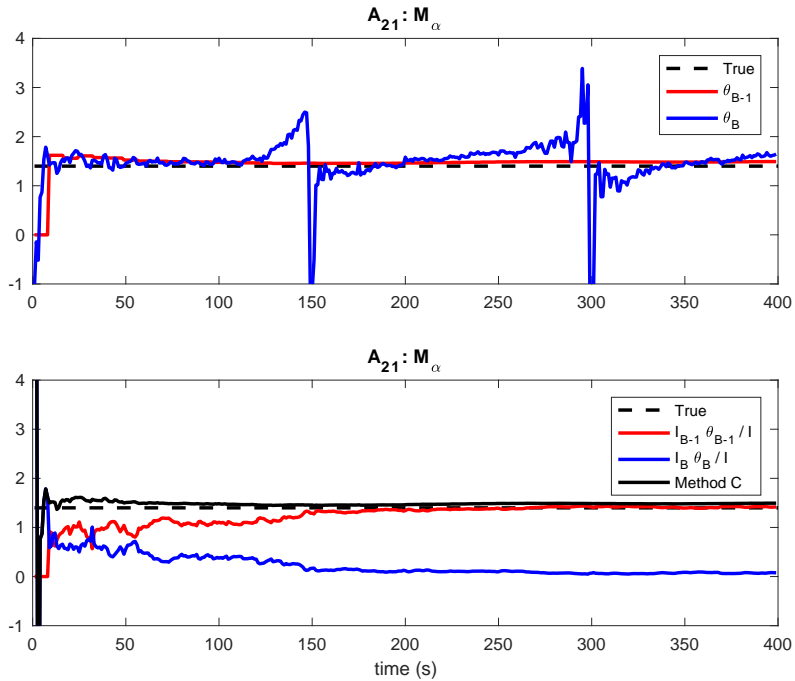


**Figure 5.40:** Display of the parts of the data fusion of the JAS 39 model parameter  $M_\alpha = 1.399$  is given. At the top are the estimated parameters from the old fused data in red and the new data in blue. At the bottom are the fused estimate in black and the weighted parts in red and blue.

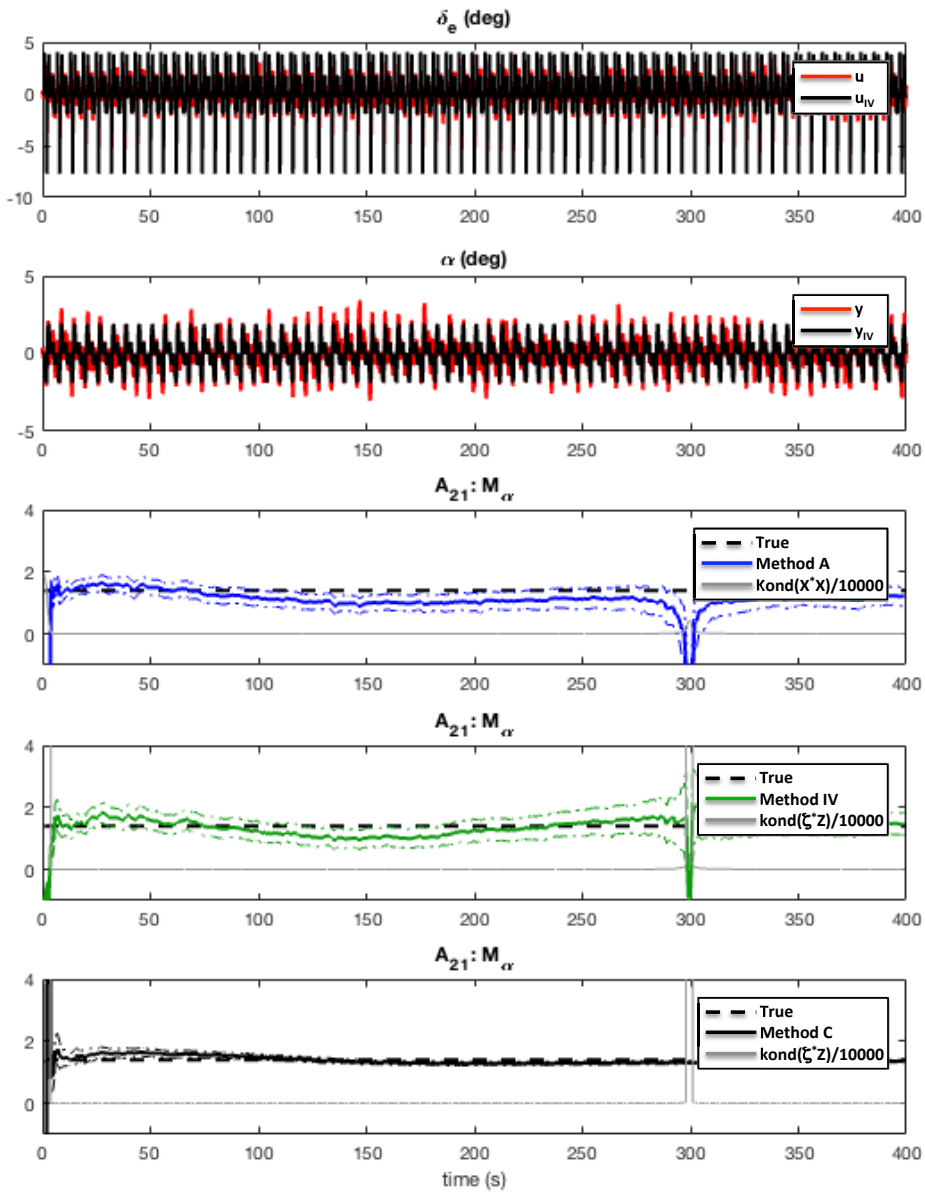


**Figure 5.41:** Comparison of the different frequency domain methods for a continuously varying noisy excitation for convergence and consistency analysis with a changes evaluation frequency span. The elevator double-pulse input and angle-of-attack output are shown together with the JAS 39 model parameter  $M_{\alpha} = 1.399$ .

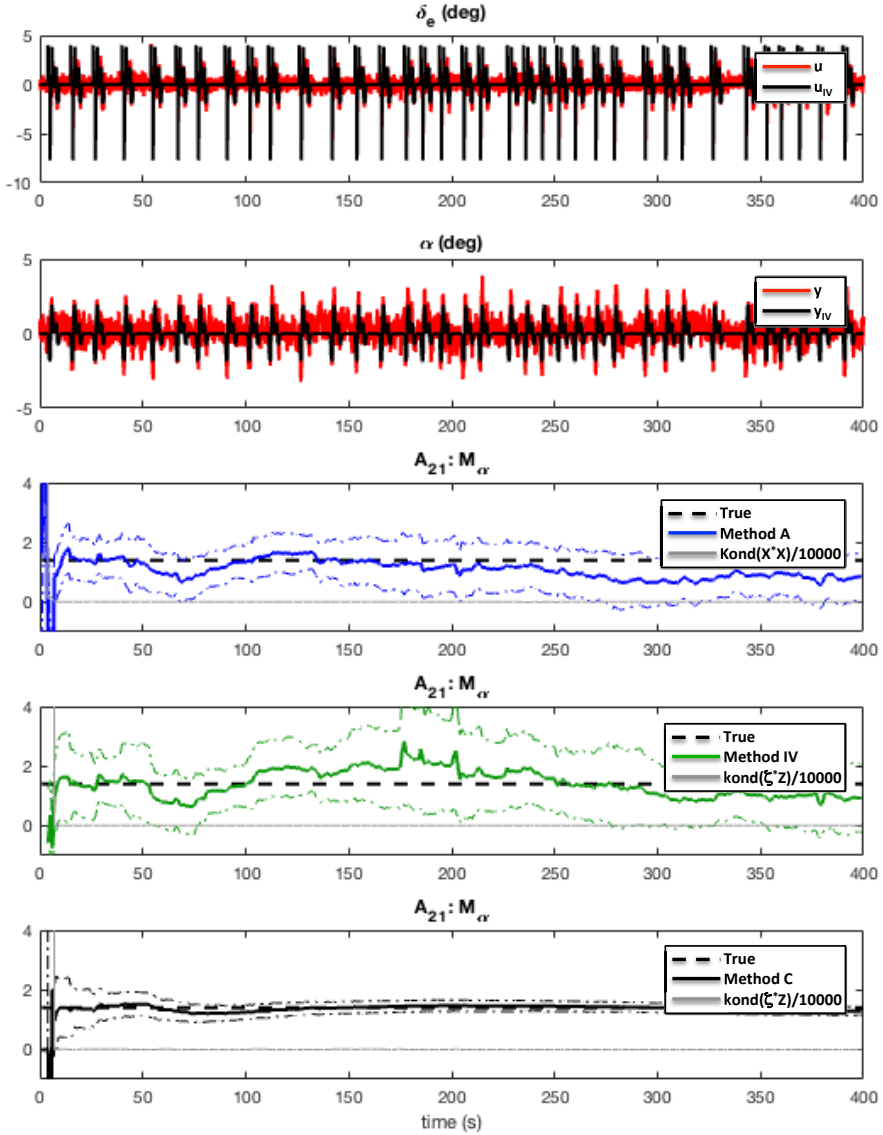


**Figure 5.42:** Comparison of the different frequency domain methods for a continuously varying noisy excitation for convergence and consistency analysis. The random elevator double-pulse input and angle-of-attack output are shown together with the JAS 39 model parameter  $M_\alpha = 1.399$ .



## 5.4 Estimation on real data

In this section, Method C has been applied to real data from a flight test with the JAS 39 Gripen fighter aircraft. The model structure is the same as for the JAS 39 Gripen model used for the estimation on simulated data, and can be written as

$$\begin{aligned} \begin{bmatrix} \dot{\alpha}(t) \\ \dot{q}(t) \end{bmatrix} &= \begin{bmatrix} Z_\alpha & Z_q \\ M_\alpha & M_q \end{bmatrix} \begin{bmatrix} \alpha(t) \\ q(t) \end{bmatrix} + \begin{bmatrix} Z_{\delta_e} & Z_{\delta_c} \\ M_{\delta_e} & M_{\delta_c} \end{bmatrix} \begin{bmatrix} \delta_e(t) \\ \delta_c(t) \end{bmatrix} + w(t) \\ \begin{bmatrix} \alpha_m(t) \\ q_m(t) \end{bmatrix} &= \begin{bmatrix} \alpha(t) \\ q(t) \end{bmatrix} + e(t) \end{aligned} \quad (5.68)$$

There is no known true model when looking at a real flight test, but one can use the values from the current simulator model for the aircraft as a reference. Here, a dataset has been selected from an old test that excites the short-period motion. For this case the existing model parameters are

$$\begin{aligned} Z_\alpha &= -0.679, Z_q = 0.992, Z_{\delta_e} = -0.220, Z_{\delta_c} = -0.012, \\ M_\alpha &= 0.472, M_q = -0.551, M_{\delta_e} = -10.490 \text{ and } M_{\delta_c} = 4.247. \end{aligned}$$

During a real flight test, excitation is usually done for all types of control surfaces. For the model given in (5.68) 2 DOF excitation is enough. Figure 5.43 shows the input and response data as well as the estimates of the parameters.

The input in this maneuver is very close to the double-pulses of the elevator and canard that were used in the simulation examples given earlier, but the flight control system is of an older version so it is not the same as the simple LQ-controller used for the simulations. The estimates at the end of the maneuver are given in Table 5.14. The results are fairly close to the data from the existing simulator model in most cases. One concern is the change of the sign of the elevator ( $\delta_e$ ) influence on the vertical force component. Otherwise, the conclusion based on test data would be that the aircraft is a little more pitch stable and that the canard efficiency on the vertical force is a bit larger than what the simulator model suggests. Information like this could have been used to make a decision to abort or go ahead with the test, either for safety reasons or amount of data content.

During a flight test, the JAS 39 Gripen flight simulator is run in parallel with the actual test. Data is transmitted to the ground station and the true pilot commands are used to drive the simulation. This makes it easy to use the simulated noise-free input and response as instrumental variables in Method C. These will probably be well correlated to the tested values making them a logical choice. It should be noted that the instrumental variables used in the current identification was based on a Simulink model with the values given by the model values in Table 5.14. This was done since the older version of the FCS was not implemented in the current version of the ARES simulator that otherwise would have been used. However, it is believed that the result would not have changed too much if ARES data had been used since the noise level is very low for the investigated case.

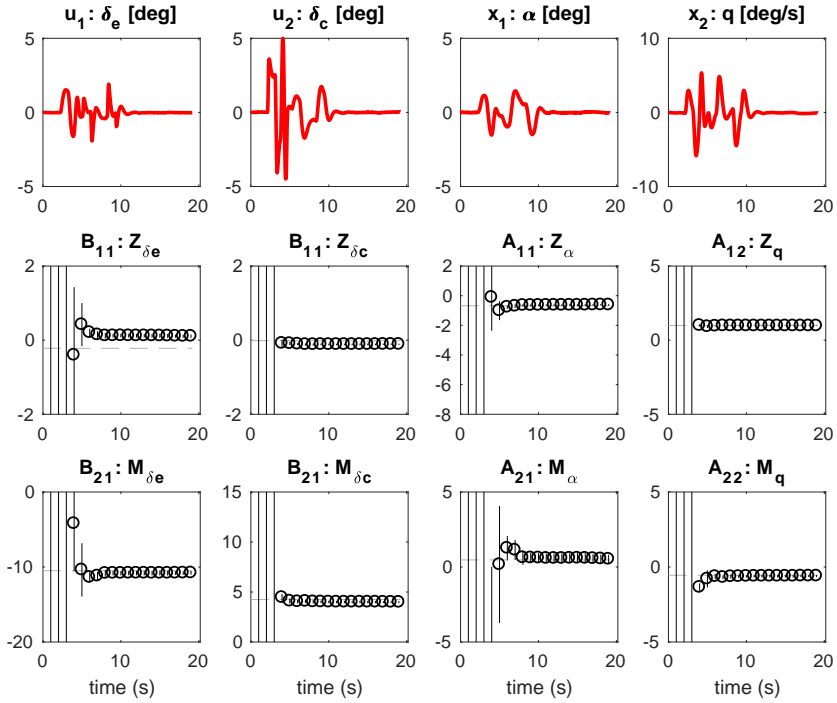


**Figure 5.43:** Estimation of parameters for the JAS 39 Gripen using Method C. The dashed lines are values from the Saab simulation model, the circles are the estimated values and the vertical lines are the estimated two standard deviations.

**Table 5.14:** Comparison of the estimated parameters including two standard deviations using Method C with the parameters for the JAS 39 Gripen model.

	Model	Method C
$Z_\alpha$	-0.679	$-0.619 \pm 0.025$
$Z_q$	0.992	$0.965 \pm 0.006$
$Z_{\delta_e}$	-0.220	$0.108 \pm 0.022$
$Z_{\delta_c}$	-0.012	$-0.111 \pm 0.009$
$M_\alpha$	0.472	$0.525 \pm 0.145$
$M_q$	-0.551	$-0.597 \pm 0.033$
$M_{\delta_e}$	-10.490	$-10.780 \pm 0.124$
$M_{\delta_c}$	4.247	$3.982 \pm 0.050$

## 5.5 A six degrees-of-freedom model

Up to now a two degrees-of-freedom model has been used to describe the system. This simplification has been done to be able to better understand the underlying mechanisms of the methods under investigation. During an actual flight test, a full six degrees-of-freedom model is usually needed. Therefore, a model of a F-16 aircraft taken from Stevens and Lewis [1992] will be used in this section to mimic a real flight test. The linear state-space system is given as

$$\begin{aligned}\dot{x}(t) &= Ax(t) + Bu(t) \\ y(t) &= Cx(t) + Du(t)\end{aligned}\quad (5.69)$$

Here the states include the velocity vector  $[V(t) \alpha(t) \beta(t)]^T$ , the Euler rotational angles  $[\Phi(t) \Theta(t) \Psi(t)]^T$  and the rotational angle velocities  $[p(t) q(t) r(t)]^T$ . Furthermore, as input vector the aileron, elevator and rudder,  $[\delta_a(t) \delta_e(t) \delta_r(t)]^T$ , are used to control the aircraft around the three roll, pitch and yaw axes. Three things should be noted about the model. First, the speed  $V(t)$  is given in (ft/sec). This has not been changed, but the presentation in the figures shows this in (m/s). Second, the input values in the model have been converted from (deg) to (rad). Third, the  $C$  and  $D$  matrices have been put to the identity and null matrices respectively. This was not the case for the original model. With this the system components are given by

$$\begin{aligned}x(t) &= [V(t) \quad \alpha(t) \quad \beta(t) \quad \Phi(t) \quad \Theta(t) \quad \Psi(t) \quad p(t) \quad q(t) \quad r(t)]^T \\ u(t) &= [\delta_a(t) \quad \delta_e(t) \quad \delta_r(t)]^T \\ A &= \begin{bmatrix} -0.127 & -235 & -0.0028 & 0.00126 & -32.2 & 0 & 5e-5 & -9.51 & 2e-4 \\ -7e-4 & -0.969 & 1.5e-5 & 0 & 0 & 0 & -4e-5 & 0.908 & -1e-5 \\ 1e-8 & 2e-5 & -0.322 & 0.0612 & 3e-6 & -1e-8 & 0.298 & 8e-7 & -0.948 \\ 0 & 0 & 0 & 0.0930 & 0 & 0 & 1 & 0 & 0.310 \\ 0 & 0 & 0 & 0 & 0 & 0 & 0 & 1 & 0 \\ 0 & 0 & 0 & 0 & 0 & 0 & 0 & 0 & 1 \\ -3e-7 & -0.00248 & -62.5 & 0 & 0 & 0 & -3.00 & 3e-4 & 1.99 \\ 9e-4 & -4.56 & 9.2e-5 & 0 & 0 & 0 & 0 & -1.58 & -0.00287 \\ -3e-6 & -0.00188 & 7.67 & 0 & 0 & 0 & -0.262 & 0.00254 & -0.629 \end{bmatrix} \\ B &= \begin{bmatrix} 0.0003 & -13.9802 & 0.0011 \\ 0 & -0.1197 & 0 \\ 0.0172 & 0 & 0.0458 \\ 0 & 0 & 0 \\ 0 & 0 & 0 \\ 0 & 0 & 0 \\ -36.9558 & 0 & 7.2193 \\ 0 & -11.4019 & 0 \\ -0.9167 & 0 & -3.7643 \end{bmatrix} \\ C &= I_{9 \times 9} \\ D &= 0_{9 \times 3}\end{aligned}$$

As can be seen, the 6th state  $\Psi(t)$  is a pure integration of the yaw rotation velocity  $r(t)$  and it only affects the angle-of-sideslip in a weak manner. To avoid unnecessary numerical problems during the identification this is removed from the model used. Therefore, there will be 88 parameters to be estimated.

The previously used two degrees-of-motion systems only covered the dynamics for the short period motion. When completing the six degrees-of-freedom sys-

tem, the additional four classical flight mechanical stick fixed motion modes, described in Chapter 3, appear. The lower bound of the frequency vector used for evaluation has to be reduced to match the Phugoid model, which has a frequency of about 0.03 Hz. Therefore, a lower bound of 0.02 Hz will be used. The upper bound of 2 Hz used for the Short period mode is enough to handle both the Roll and Dutch roll modes. To mimic a realistic flight test some measurement noise and light atmospheric turbulence is added. In addition, a prior model with a difference to the true system of up to  $\pm 10\%$  is used to create the instruments.

For the analysis a closed-loop system is used. A simple LQ-feedback loop, using Bryson's rule is applied. To simulate a realistic flight test, a maneuver block of three double pulses, one in each channel (roll, pitch and yaw), is performed. The resulting response can be seen in Figure 5.44. During flight the most interesting parameters to monitor are the ones for the input, main static stability and damping. Estimation of these parameters, for the maneuver block, is shown in Figure 5.45. Since the simulation is a low noise case, two things can be noted. The first is that the uncertainty estimation for  $M_\alpha$  is larger than expected based on the previous simulations. The second is that some parameters do not converge to the correct parameter value.

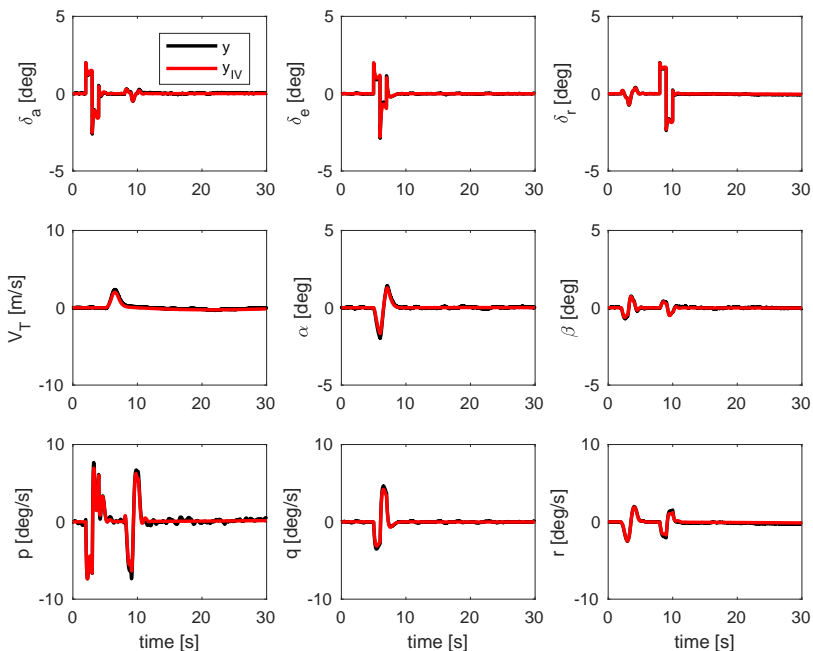


**Figure 5.44:** Realistic block of double-pulses in roll, pitch and yaw to excite small disturbances responses around all axes. This is a low noise case.

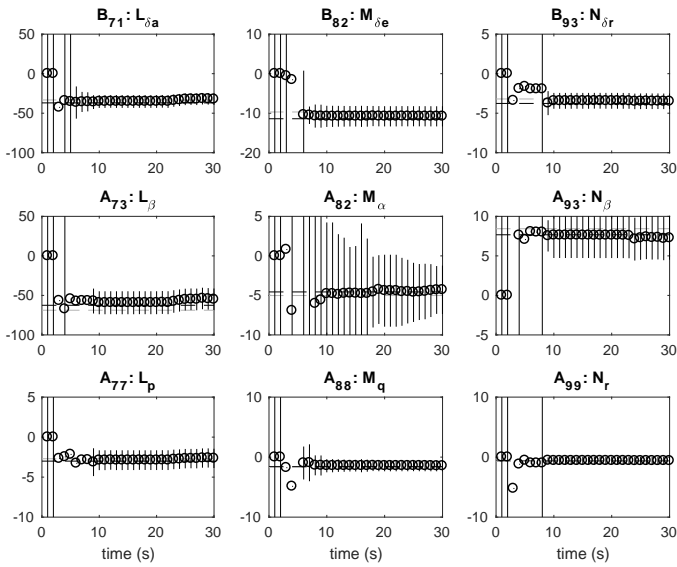


**Figure 5.45:** Estimation of the most interesting parameters with the original settings.

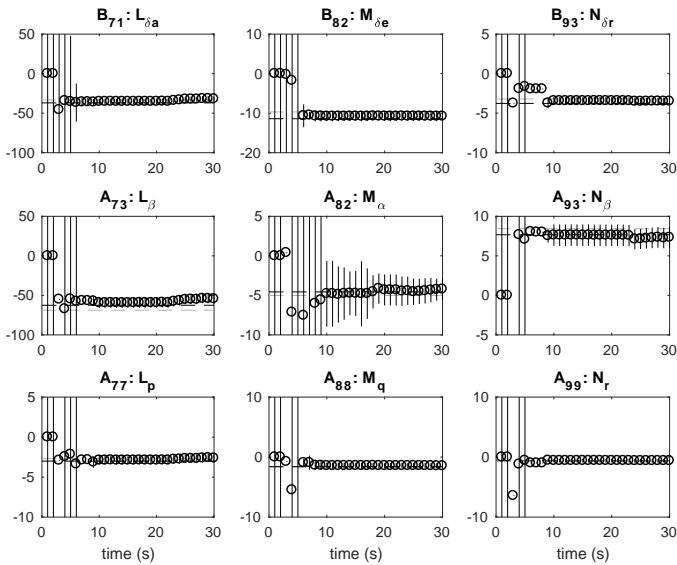


**Figure 5.46:** Estimation of the most interesting parameters with higher frequency resolution (0.01 Hz) settings.

To investigate these effects the estimation frequency vector was given a finer resolution from 0.04 Hz to 0.01 Hz. The result is shown in Figure 5.46. As can be seen this makes the uncertainty estimates smaller. It does not, however, improve the accuracy of the estimated parameters. A possible source for this accuracy problem could be that the data fusion uses the information matrices for weighting. If measurements of different sizes are used to estimate the information content there could be a numerical problem affecting the accuracy. To investigate this a threshold concept has been used. If the information is lower than a certain value it is set to a very low value so that it cannot corrupt the identification process. The result from this is shown in Figure 5.47. The estimates now converge to a value that is very close to the real system.

A more noisy case with severe turbulence for the same maneuver block is shown in Figure 5.48. The estimation without any threshold is shown in Figure 5.49. Here the resolution of the frequency vector used for the estimation had to be reduced to 0.02 Hz. By applying the threshold much better estimates of the parameters can be achieved. This is shown in Figure 5.50. For this case the uncertainty estimate is again large for  $M_\alpha$ . In this situation it would be possible to ask for more excitation in the pitch plane.

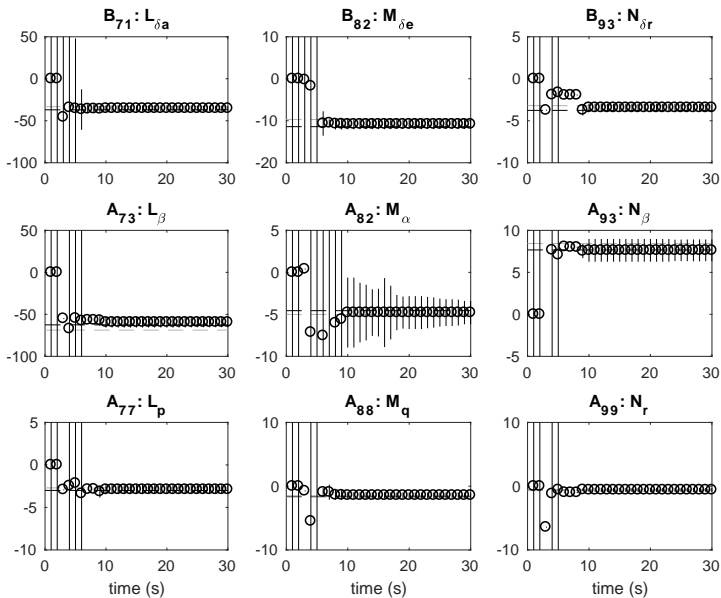


**Figure 5.47:** Estimation of the most interesting parameters with higher frequency resolution (0.01 Hz) settings and a threshold function on the information matrix.

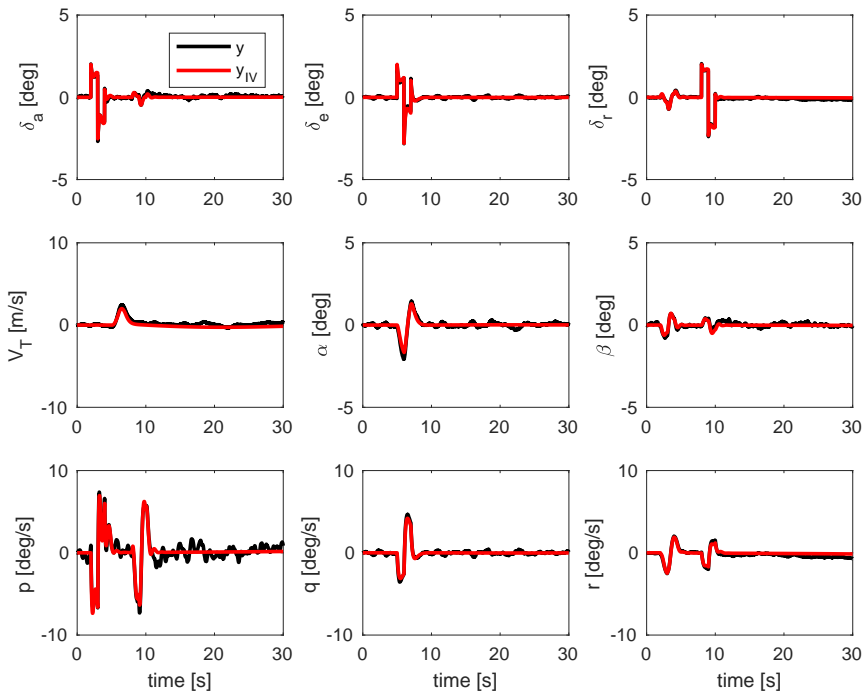


*Figure 5.48: Maneuver block in severe turbulence.*

A request of this kind could be to excite a 3-2-1-1 pulse, with a broader frequency content than the double pulse input. The result can look like in Figures 5.51 and 5.52. As can be seen the uncertainty in  $M_\alpha$  decreases substantially with the additional information, giving once again a usable estimate. One of the benefits of using an online method is that decisions like this can be made while the aircraft is still in the air. This will save time and reduce cost relative to have to get the extra needed information during another flight.

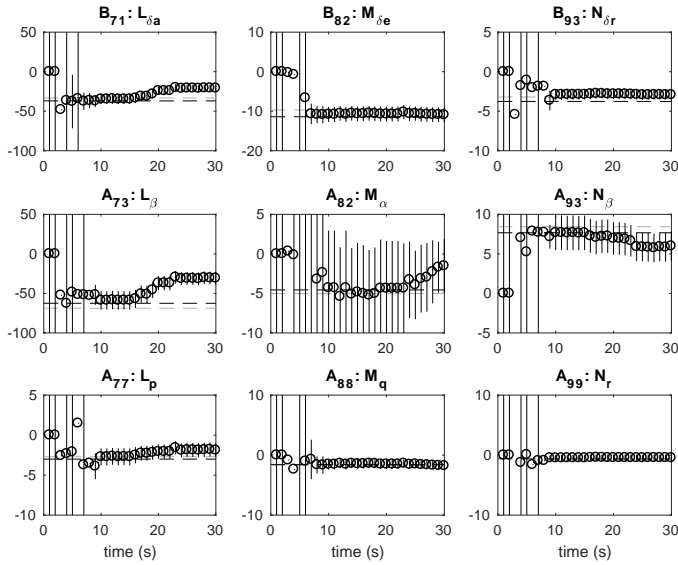


**Figure 5.49:** Estimation, without a threshold, of the most interesting parameters for a maneuver in severe turbulence.

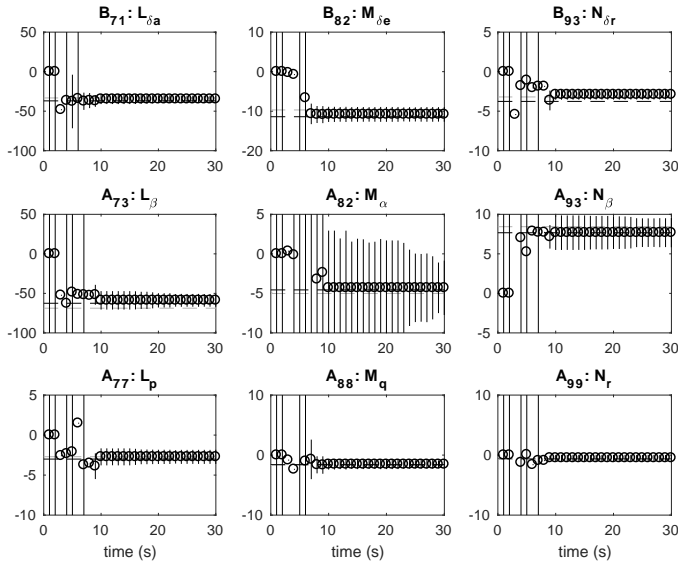


**Figure 5.50:** Estimation, with a threshold, of the most interesting parameters for a maneuver in severe turbulence.



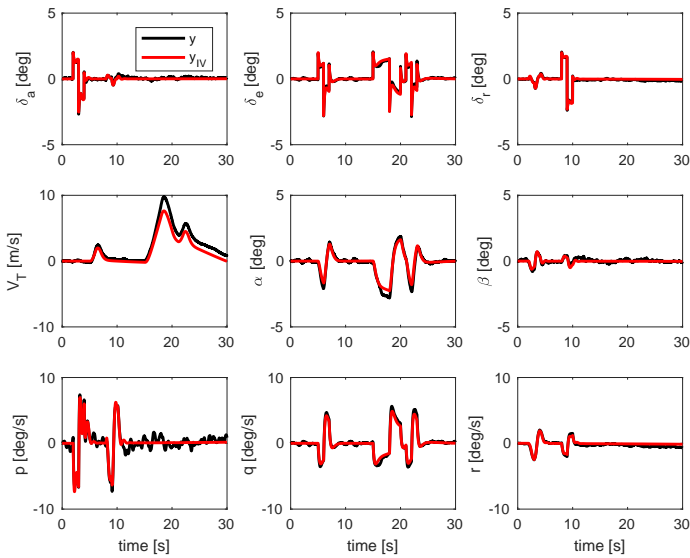


*Figure 5.51: Maneuver block in severe turbulence with extra excitation.*

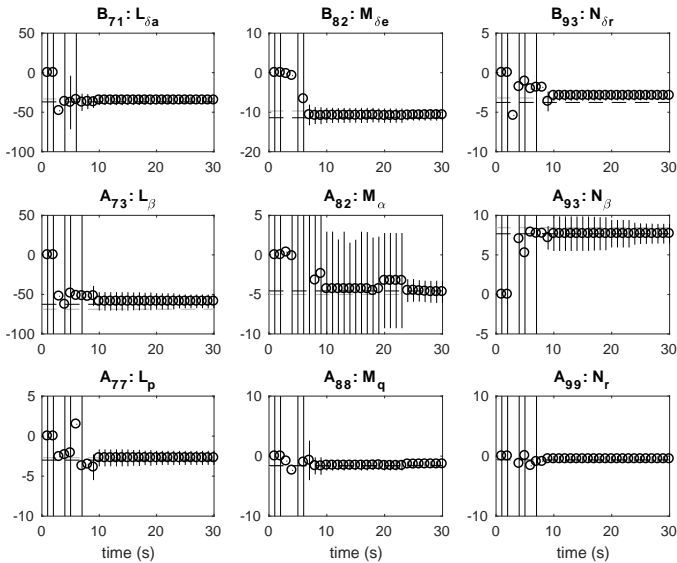


*Figure 5.52: Estimation, with a threshold, of the most interesting parameters with severe turbulence and with extra excitation.*

## 5.6 Conclusions

When looking at the results in this chapter it is clear that the Method C, consisting of the Method IV together with data fusion, improves the performance of Method A taken from Klein and Morelli [2016] for system identification when noise is present. The differences are small for measurement noise, but when process noise is present the benefits of using an instrumental variables method together with data fusion can be seen. This is due to the fact that Method A uses an ordinary least squares approach, which can give biased results for the errors-in-variables problem that arises in the studied cases. For severe turbulence Method C runs into problems with the condition number for matrices to be inverted. This is not a critical problem for the application studied since this is not a flight condition where system identification is used. It can be seen from the convergence and consistency analysis that Method C has better properties when the data fusion part is added. It has also been shown that a 6 DOF problem can be handled by Method C and that there is a benefit of having a method for online decision during flight.



# 6

---

## Generic future fighter

"To invent an airplane is nothing. To build one is something.  
But to fly is everything."  
- Otto Lilienthal (1848 - 1896)

The complexity and large cost associated with modern aircraft design makes subscale model testing an interesting idea for risk and cost reduction. If a model is dynamically scaled in a correct way, concerning geometry, mass, aerodynamics, engine thrust, etc., so that the dynamics of the subscale model represents the full-scale aircraft, there are ways to assess stability and control characteristics of the real aircraft [Chambers, 2009]. Using remotely piloted vehicles (RPVs) requires robust and reliable ground support for the pilot and the test team as described in Bailey et al. [2005]. A more cost effective option is to use a radio-controlled demonstrator to test the implementation of new technologies and also to support choices early in the design process [Lundström, 2012, Sobron, 2018].

In this chapter an experimental flight test with a genetic future fighter (GFF), using the methods developed in the previous chapter, will be presented. The methods are as stated suitable for real-time applications, which is beneficial when conducting radio-controlled flight with a subscale aircraft. The reason for this is that in the early phase of an aircraft design only basic knowledge of the flight characteristics exist. Hence, being able to support the test with information in real-time can reduce risks and uncertainties and thereby increase the test performance.

## 6.1 Introduction

Historically, wind tunnel testing has been the main source used to build up knowledge of aircraft concepts. With the continuous increase of computational power in modern computers together with the advancement of computational fluid dynamic (CFD) methods, it is nowadays easier to evaluate the static aircraft characteristics earlier in the design phases. Subscale flight-testing is more concentrated on dynamic behavior. To get the full picture, both the static and dynamic characteristics of the aircraft are needed.

A good example of subscale model testing is the early development of the Saab J35 Draken, featuring a double-delta wing configuration. A step from transonic speed up to two times the speed of sound was taken, thereby braking new unexplored physical ground in aeronautical technology. To investigate the low speed stability characteristics, several 10% scale, swingline control models were built and flown. Figure 6.1 show the principle of swingline model testing together with a picture of one of these models. In the next step the Saab 210, a manned double-delta demonstrator aircraft of about half scale, was built and several air intakes were tested. Together with wind tunnel tests, these subscale demonstrators added enough knowledge to develop the full scale Saab J35 Draken aircraft [Dorr et al., 1987].



**Figure 6.1:** *Draken 10% swingline model aircraft.*

The subscale aircraft named GFF (Generic Future Fighter), shown in Figure 6.2, uses today's technology level for radio-controlled flight and is thereby much more advanced than the 10% scale model of the Saab J35 Draken.

The GFF model aircraft is described in Jouannet et al. [2012]. Earlier existing test data have been used for input design and results are given for new tests with these inputs.



Figure 6.2: GFF, Subscale model aircraft.

## 6.2 Input design using simulated data

In this section, the design of input signals will be described. For the design a linear state-space model on the form (6.1), based on previous flight test data, was created. The definitions of the variables are shown in Figure 6.3.

$$\begin{aligned} \begin{bmatrix} \dot{\alpha}(t) \\ \dot{q}(t) \end{bmatrix} &= \begin{bmatrix} Z_{\alpha} & Z_q \\ M_{\alpha} & M_q \end{bmatrix} \begin{bmatrix} \alpha(t) \\ q(t) \end{bmatrix} + \begin{bmatrix} Z_{\delta_e} & Z_{\delta_c} \\ M_{\delta_e} & M_{\delta_c} \end{bmatrix} \begin{bmatrix} \delta_e(t) \\ \delta_c(t) \end{bmatrix} \\ \begin{bmatrix} \alpha_m(t) \\ q_m(t) \end{bmatrix} &= \begin{bmatrix} 1 & 0 \\ 0 & 1 \end{bmatrix} \begin{bmatrix} \alpha(t) \\ q(t) \end{bmatrix} \end{aligned} \quad (6.1)$$

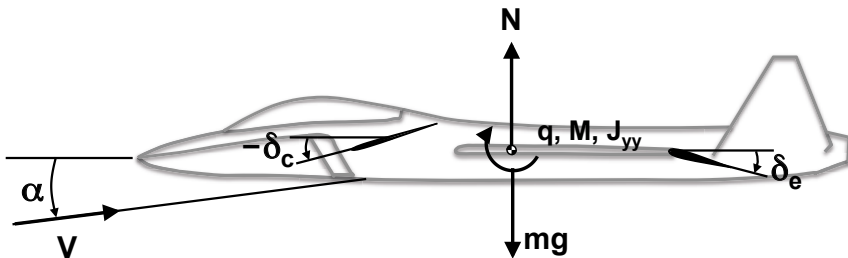
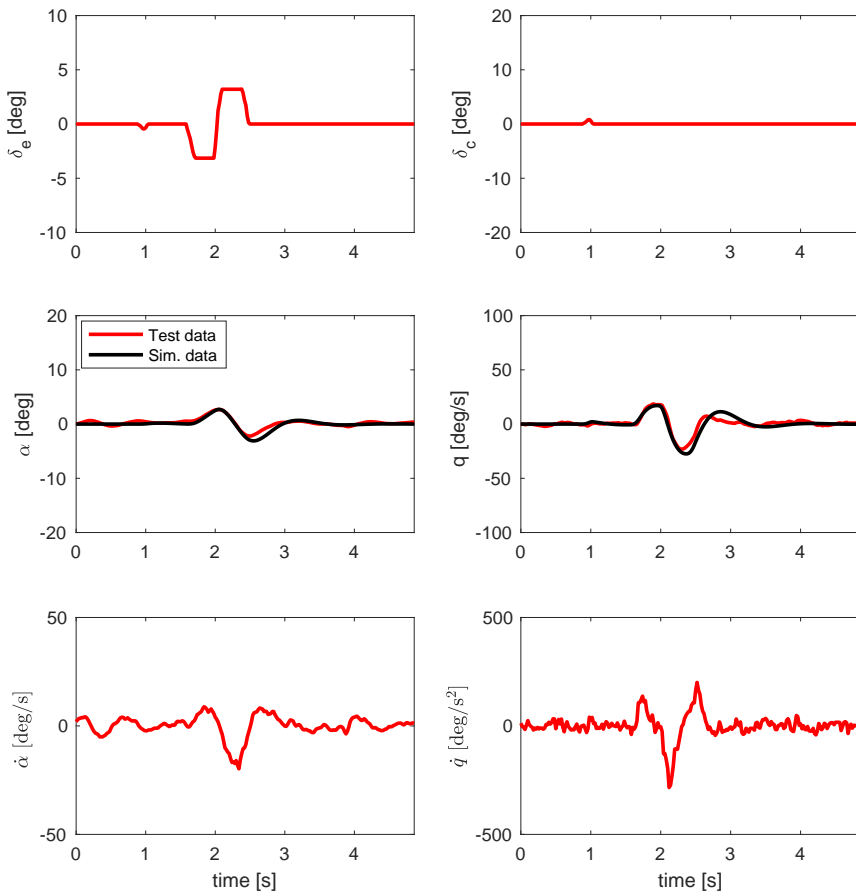


Figure 6.3: Definition of the variables of the GFF. Note that  $Z$  in (6.1) is the same as  $-N$  in the figure.

The states  $x(t) = [\alpha(t) \ q(t)]^T$  are the angle-of-attack and the pitch rotation velocity, and the input  $u(t) = [\delta_e(t) \ \delta_c(t)]^T$  are the elevator and canard deflections. All states are measured. Making an estimation of the model parameters  $Z$  and  $M$  in (6.1) using an ordinary least-squares (OLS) time domain method [Ljung, 1999] on the existing data shown in Figure 6.4 leads to the following continuous-time model

$$\begin{aligned} \dot{x}(t) &= \begin{bmatrix} -1.88 & 0.65 \\ -36.39 & -2.77 \end{bmatrix} x(t) + \begin{bmatrix} -0.33 & -0.37 \\ -39.04 & 17.49 \end{bmatrix} u(t) \\ y(t) &= \begin{bmatrix} 1.00 & 0.00 \\ 0.00 & 1.00 \end{bmatrix} x(t) \end{aligned} \quad (6.2)$$



**Figure 6.4:** Estimation data from earlier flight tests. Test data (red) and simulated model data (black) are shown.

The OLS in time domain has been used here in a batch mode since the whole data set is available and it is a quick and easy way to get a model to use. The model (6.2) has been validated on other data sets. One of these is shown in Figure 6.5. Even though the match is not perfect, the model is deemed accurate enough to be used for the experimental design.

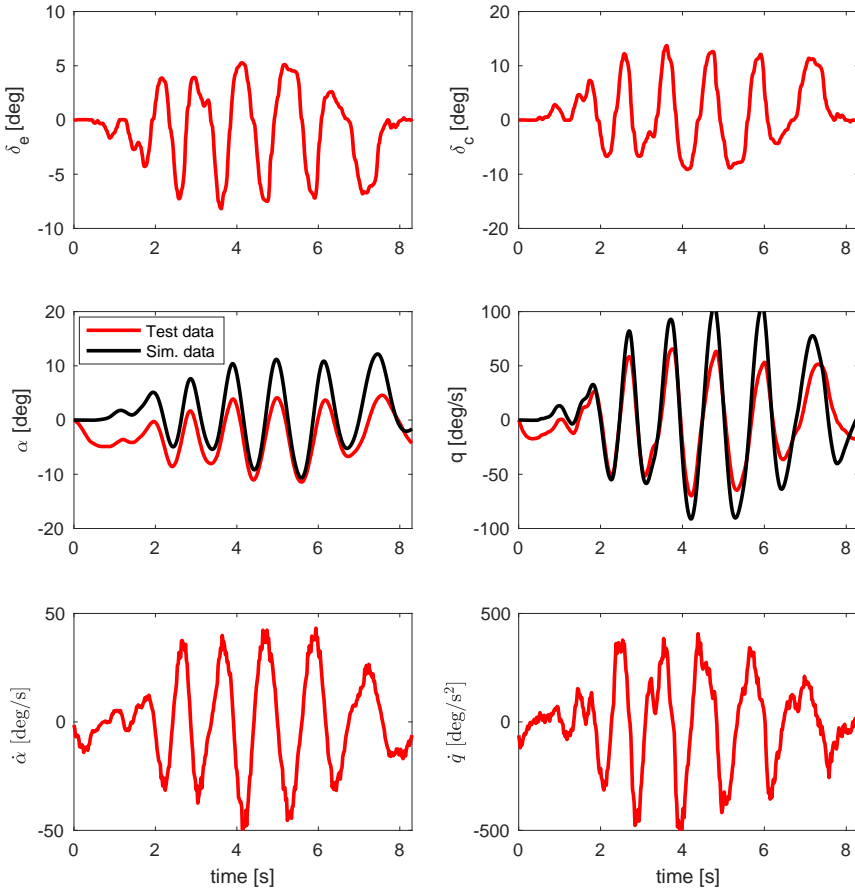


**Figure 6.5:** Validation data from earlier flight tests. Test data (red) and simulated model data (black) are shown.

Two types of signals are evaluated (see Figure 6.6). The first one is a double pulse, commonly used for estimating aerodynamic derivatives from flight test data. The second one is a multisine signal

$$u(t) = \sum_{r=1}^{N_u} A_r \cos(\omega_0 r t + \varphi_r) \quad (6.3)$$



where  $A_r$  and  $\varphi_r$  are the amplitudes and phases for the signal components respectively. One reason for using a multisine is that it is possible to achieve weakly correlated, simultaneously excited input signals by using different frequencies for the different control surfaces, a method described in Morelli [2011]. This will save time and reduce cost since it reduces the time spent in the air for the same amount of information gathered.

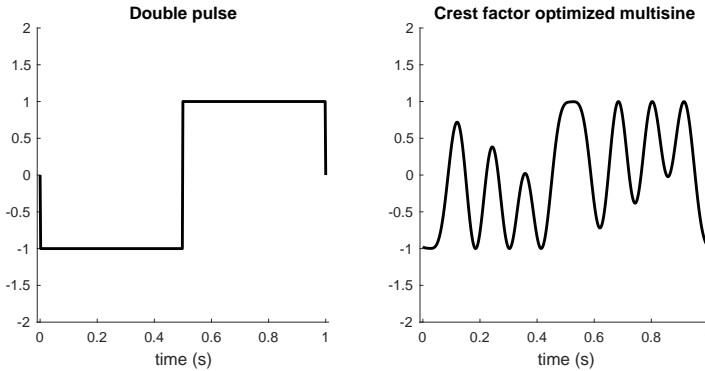


**Figure 6.6:** A double pulse (DP) input (left) and a crest factor optimized multisine (CR) input (right).

Nine different crest factor optimized multisine input signals have been created with a sample frequency of 100 Hz and a period of 1 s. To generate the crest factor optimized input signals the toolbox described in Kollár et al. [2006] has been used. An example of the amplitudes and the phases for the separated input signals is shown in Figure 6.7.

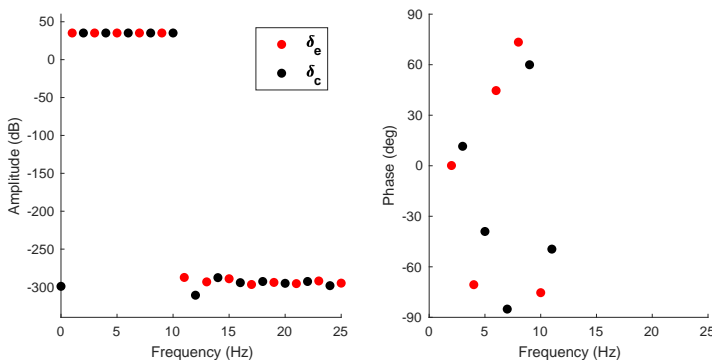


**Figure 6.7:** Amplitudes (left) and phases (right) of the multisine frequency separated elevator and canard input signals. The excitation has odd frequencies for the elevator (red) and even for the canard (black).

To get good input signals three periods of excitation have been used, one to take care of the transient in the beginning and two steady-state periods. This type of signal is described in Schoukens et al. [2016], where it is used to detect nonlinearities.

Note that the frequency span of 1 – 10 Hz has been chosen to excite the short period flight mechanical model for this subscale GFF aircraft. This is higher than the 0.1 – 2 Hz for full-sized aircraft, stated in Klein and Morelli [2016]. It is a well-known fact that small-scale aircraft have this short period characteristic. The phenomena can be seen in the Bode plot in Figure 6.8, where the model of the full scale Saab JAS 39 Gripen used in Larsson and Enqvist [2012a] has been compared to the subscale GFF model from (6.2).

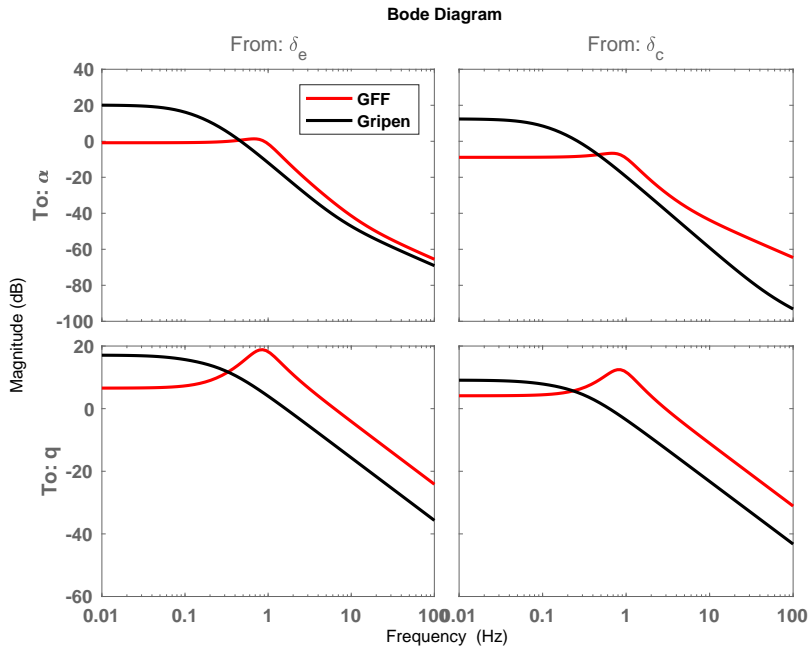


**Figure 6.8:** Bode plot of GFF (red) and Gripen (black).

For the investigation of possible benefits of the multisine signals, the inputs for the elevator and the canard have been run both separated and in parallel. They have also been compared to the double pulse input when separated and with a small time delay to mimic the parallel input without causing too much correlation between the different control surfaces. Examples of input signals from simulations, with a process noise of about ten percent of the input amplitude are shown in Figure 6.9. The total excitation time is here 10 s, which is the time window available in the real flight test.

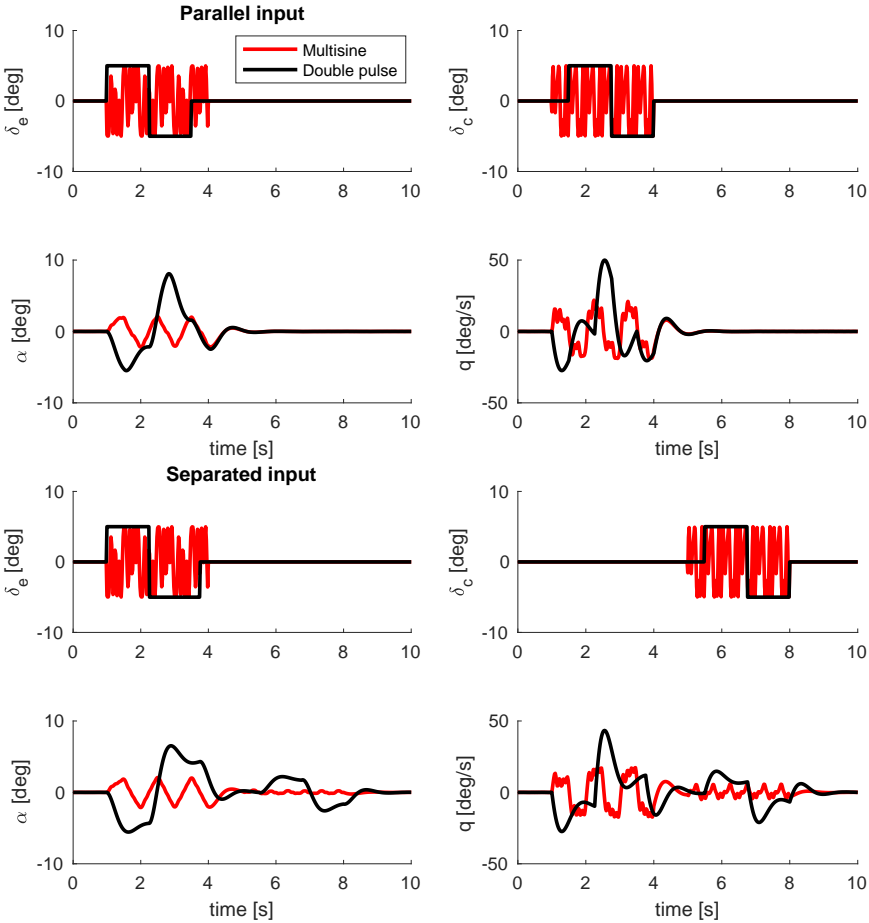


**Figure 6.9:** Simulations with different input signals. Crest factor optimized multisine (red) vs. Double pulse (black).

Making simulations with the estimated models for nine realizations of input signals and comparing the double pulse (DP) and the crest factor optimized (CR) multisine results to the true model using the relative error

$$\varepsilon = 100 \left| \frac{\theta_{model} - \theta_{true}}{\theta_{true}} \right| \quad (6.4)$$

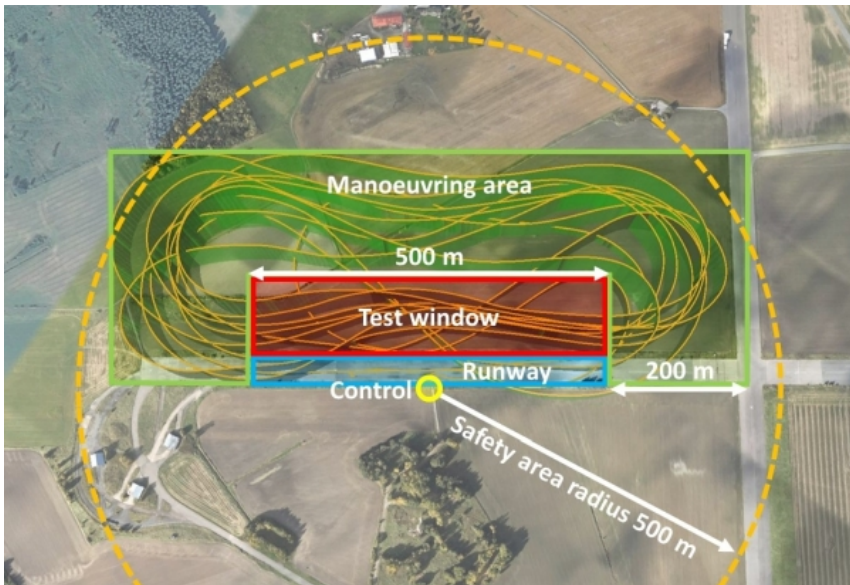
as a measure, gives the results in Table 6.1. It is clear that the crest factor optimized input gives more accurate estimates for this type of testing.

**Table 6.1:** The relative error (6.4) when using the double pulse (DP) and the crest factor optimized multisine (CR) input signals. The true model (6.2) is given as a reference.

	True Model	$\varepsilon_{DP}$	$\varepsilon_{CR}$
$Z_\alpha$	-1.880	1.601	0.997
$Z_q$	0.651	0.868	0.386
$Z_{\delta_e}$	-0.332	3.703	2.871
$Z_{\delta_c}$	-0.367	10.430	0.619
$M_\alpha$	-36.395	0.829	0.514
$M_q$	-2.772	2.037	0.908
$M_{\delta_e}$	-39.044	0.317	0.244
$M_{\delta_c}$	17.488	2.184	0.130

### 6.3 Experimental setup

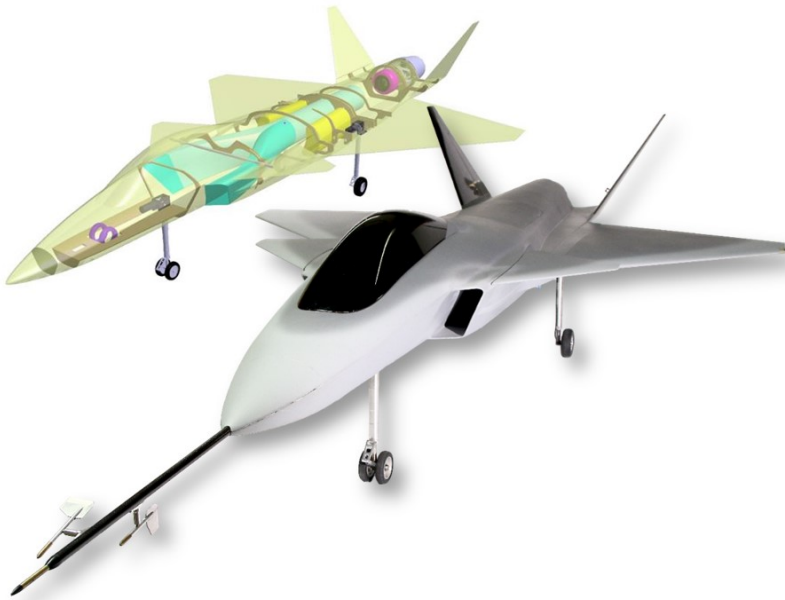
A flight test has been carried out at Bråvalla, a disused military airfield on the outskirts of the city of Norrköping, Sweden. Due to regulations, the rc-aircraft has to remain within visual line-of-sight at all times. Such a limited available airspace requires a precise management of the test area. An illustration is given in Figure 6.10, which shows the test area and aircraft trajectory during one of the flight tests of the campaign.



**Figure 6.10:** Test area at Bråvalla airfield and aircraft trajectory during a flight test.

The test was performed by a team of three persons: one test conductor, responsible for controlling the test execution; one pilot, flying the aircraft from the ground control; and one test monitor, evaluating the test results between the flights and supervising the safety area. Test cards were used to predefine the maneuvers to be performed. One of these test cards can be seen in Appendix E. The corresponding commands and excitation signals were pre-programmed and automatically executed from the radio-control transmitter by means of a novel flight-test application developed at Linköping University [Sobron et al., 2018]. This application, based on *Lua* scripts, also allowed the team to easily reconfigure the test sequences between flights, improving efficiency as fast decisions could be taken during the test.

The test object was the radio-controlled subscale demonstrator aircraft GFF, which is shown in Figure 6.2. The demonstrator was designed and produced within the NFFP4 Swedish National Aeronautical Research Program and it made its first flight in 2009 [Jouannet et al., 2012]. The aircraft is a jet-powered fighter with close-coupled delta-wing canard configuration that reproduces the full-scale design at a 13 % scale, using the Froude number as similarity parameter. An overview of the airframe is presented in Figure 6.11 and its main characteristics are given in Table 6.2. Although it originated from a conceptual study at Saab, it is a generic design and it has no couplings to any current or future Saab products.

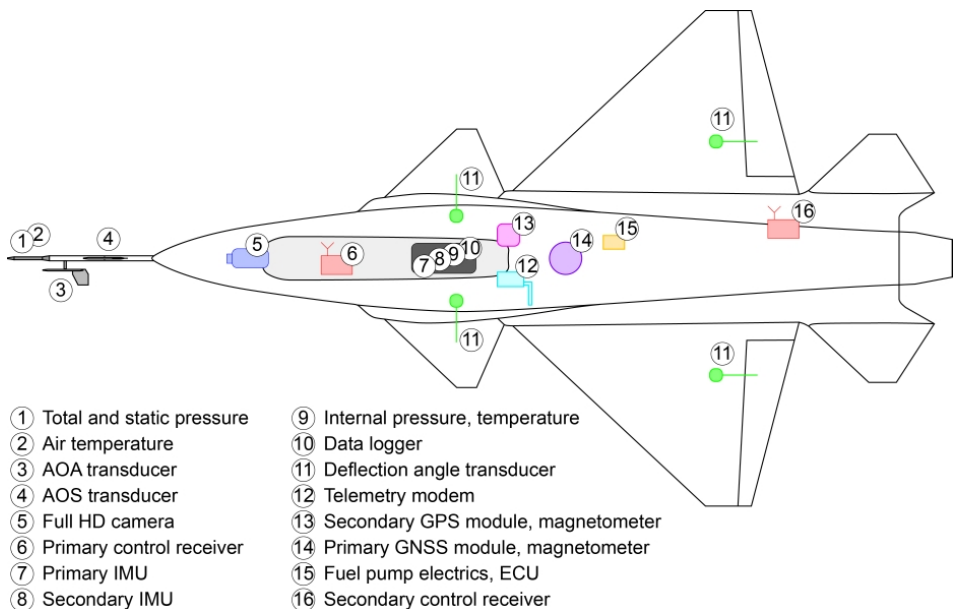


**Figure 6.11:** Overview of the GFF subscale demonstrator.

**Table 6.2:** Main characteristics of the GFF subscale demonstrator.

Length	2.4 m
Wing span	1.5 m
Typical take-off weight	19 kg
Typical fuel weight	3 kg
Engine	Jetcat P160
Maximum static thrust	160 N

The GFF aircraft is one of the platforms used in the MSDEMO research program for investigating the potential of subscale flight testing within aircraft conceptual design [Lundström et al., 2016]. It is equipped with a data acquisition system and several sensors. Two inertial measurement units (IMU) provide accelerations and angular velocities. Furthermore, the IMUs together with GPS receivers, magnetometers, and air-pressure transducers are used to estimate the position, orientation and altitude. A custom-made nose-boom provides airspeed, angle-of-attack and angle-of-sideslip. The system also registers the incoming pilot commands as well as the deflection of each control surface. These signals are logged on-board at an average sampling frequency of 100 Hz and are also sent to a ground station in real-time via a separate telemetry link. Figure 6.12 shows the layout of the data acquisition system.

**Figure 6.12:** Layout of the data acquisition system on the GFF platform.

On the test day three flights were made. The first one was for checking and the calibration of instruments. The two other were made to collect identification data. The first two of the nine multisine input signals, mentioned earlier in Section 6.2, were used both for parallel and separate excitation of the elevator and canard. The test program can be seen in Table 6.3. The test setup was used to get repetitions of excitation for different fuel weights. The fuel weight is about 16 % of the take-off weight and can therefore have an effect on the outcome of the results. It should be noted that Method C was run in IV-mode, i.e., the whole test sequence was used for the identification since each excitation was only 10 s long.

**Table 6.3:** Test program for identification.

Flight FT. #2	Flight FT. #3
Take-off	Take-off
Multisine 1 separated, MSs1	Multisine 1 parallel, MSp1
Multisine 1 separated, MSs1	Multisine 1 parallel, MSp1
Multisine 2 separated, MSs2	Multisine 2 parallel, MSp2
Multisine 1 parallel, MSp1	Multisine 1 separated, MSs1
Multisine 1 parallel, MSp1	Multisine 1 separated, MSs1
Multisine 2 parallel, MSp2	Multisine 2 separated, MSs2
Double pulse parallel, DPP	Double pulse separated, DPs
Landing	Landing

## 6.4 Results using real flight test data

Some examples of estimation results from the four different types of maneuvers, (MSs, MSp, DPP, DPs) defined in Table 6.3, are shown in Figures 6.13 - 6.16. The test with the separated double-pulse (DPs) had to be repeated during flight FT. #3 since the first one was aborted due to ground proximity. This gave two realizations DPs1 (aborted) and DPs2 (repeated). The figures show the flight test data in red and the model (6.2), based on earlier flight test data, is shown as the black dashed line. Estimated parameters are given as blue squares for Method A and as black circles for method C. The estimated uncertainty measures of two standard deviations are shown as vertical bars. It should be noted that the model (6.2) is not the true system, but rather a reference. If the differences are big, when comparing the test result with the model, then a decision has to be made if the test can be continued or if it should be aborted and a more thorough analysis is needed.

When comparing the results in Figures 6.13 and 6.14 for the separated and parallel multisine inputs, the methods give quite similar estimates in the end of the two inputs. This can be seen in Table 6.4. The difference is during the test maneuvers where the estimated canard effectiveness  $Z_{\delta_c}$  and  $M_{\delta_c}$  are quite uncertain before the excitation for the separated maneuvers, as should be expected.

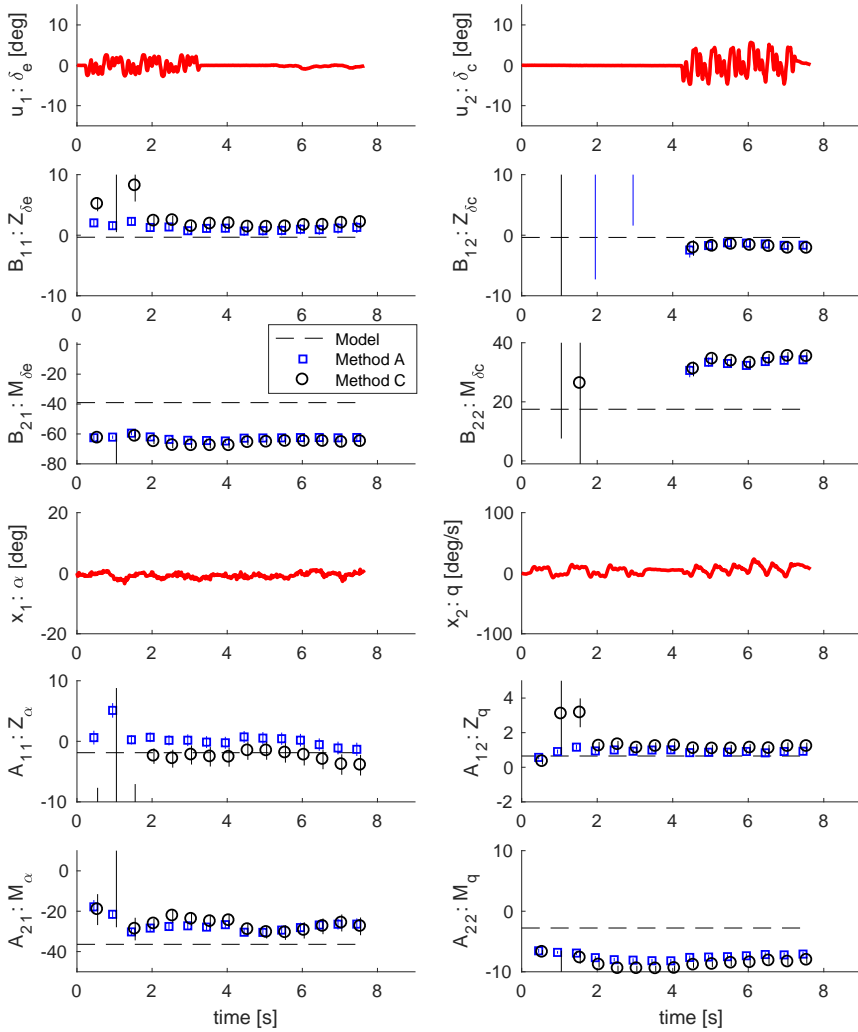


**Figure 6.13:** Results from flight FT. #2 with maneuver MSs1. The flight test data is shown in red, the results from Method A as blue squares and the results from Method C as black circles. The uncertainties are given as vertical bars.



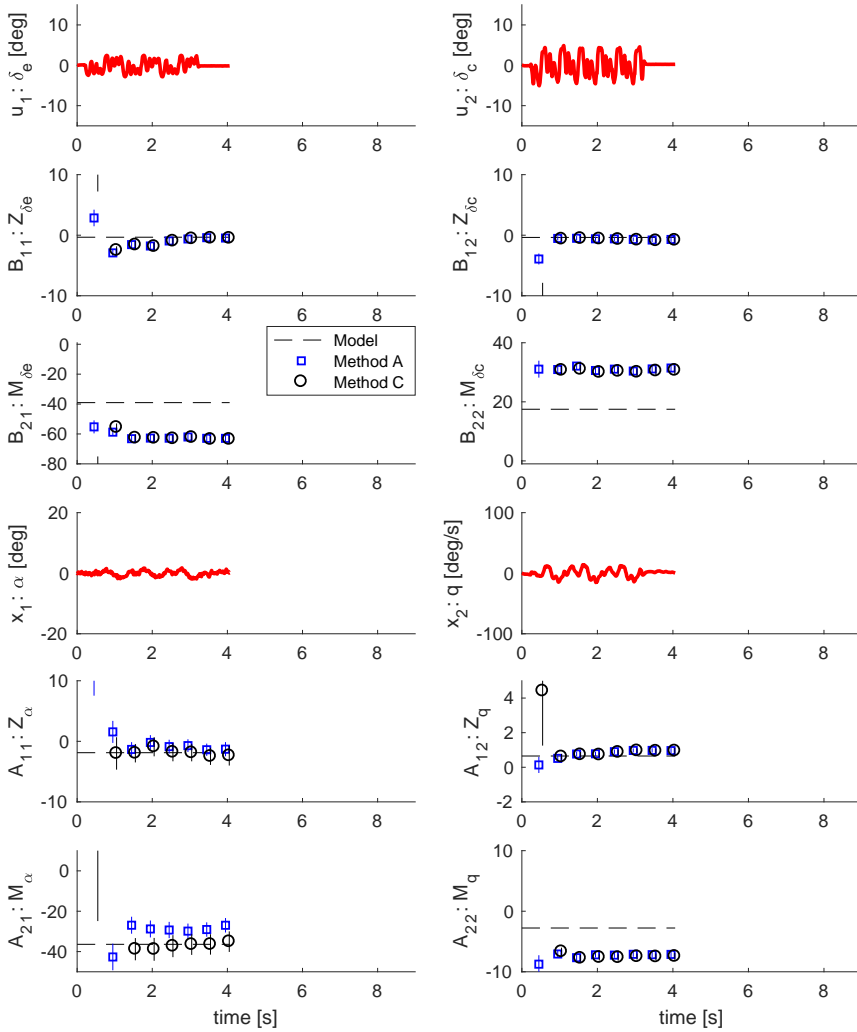


**Figure 6.14:** Results from flight FT. #2 with maneuver MSp1. The flight test data is shown in red, the results from Method A as blue squares and the results from Method C as black circles. The uncertainties are given as vertical bars.

**Table 6.4:** Comparison of estimates for the crest factor optimized multisine (CR) input signal run separated and in parallel. The model (6.2) is given as a reference.

	Model	Method A		Method C	
		MSs1	MSp1	MSs1	MSp1
$Z_\alpha$	-1.880	-1.322	-1.296	-3.939	-2.376
$Z_q$	0.651	0.926	0.962	1.205	0.945
$Z_{\delta_e}$	-0.332	1.288	-0.468	2.131	-0.499
$Z_{\delta_c}$	-0.367	-1.643	-0.703	-2.161	-0.821
$M_\alpha$	-36.395	-26.387	-26.959	-27.502	-35.076
$M_q$	-2.772	-7.078	-7.131	-8.080	-7.449
$M_{\delta_e}$	-39.044	-62.373	-62.951	-65.082	-63.570
$M_{\delta_c}$	17.488	34.231	31.444	35.329	30.688

The differences are bigger when comparing the parallel multisine and double pulse in Figures 6.14 and 6.15. This difference is mostly in the pitching moment. The biggest difference is in the canard effectiveness  $M_{\delta_c}$  where the estimated effectiveness is much lower for the double pulse input. A similar result can be seen when comparing the two double pulse inputs in Figures 6.15 and 6.16. This can also be seen in Table 6.5.

The results from the repeated separated double pulse (DPs2) are shown in Figure 6.16. It gives not exact, but similar results as the separated multisine in Figure 6.13 when using method C. It can also be seen that Method A and Method C give the biggest difference in the estimates for this maneuver.

**Table 6.5:** Comparison of estimates for the classic double pulse (DP) input signal run separated and in parallel. The model (6.2) is given as a reference.

	Model	Method A		Method C	
		DPp	DPs	DPp	DPs
$Z_\alpha$	-1.880	-1.684	-1.938	-2.397	-2.600
$Z_q$	0.651	0.851	0.645	1.072	1.000
$Z_{\delta_e}$	-0.332	0.306	0.078	0.767	1.061
$Z_{\delta_c}$	-0.367	0.450	-0.613	-0.730	-1.306
$M_\alpha$	-36.395	-27.740	-26.251	-30.032	-28.269
$M_q$	-2.772	-3.431	-4.664	-4.408	-8.804
$M_{\delta_e}$	-39.044	-31.932	-40.702	-36.745	-58.807
$M_{\delta_c}$	17.488	3.048	22.343	3.933	33.533

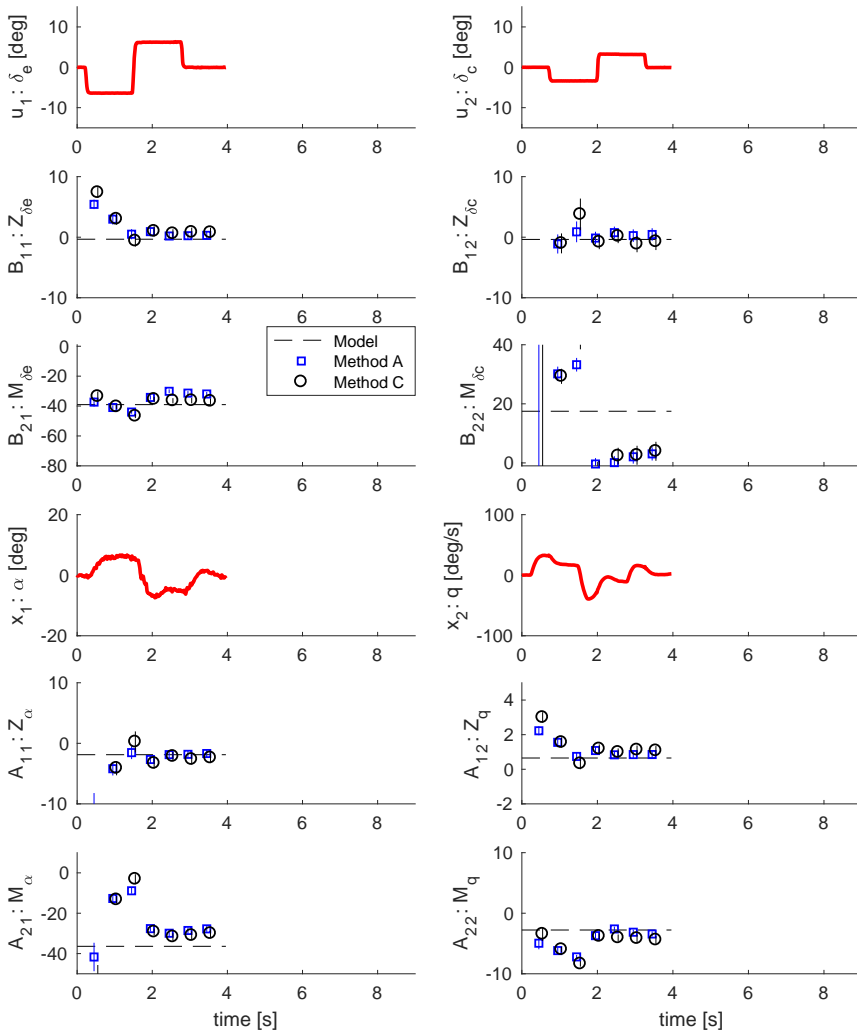


**Figure 6.15:** Results from flight FT. #2 with maneuver DPp. The flight test data is shown in red, the results from Method A as blue squares and the results from Method C as black circles. The uncertainties are given as vertical bars.

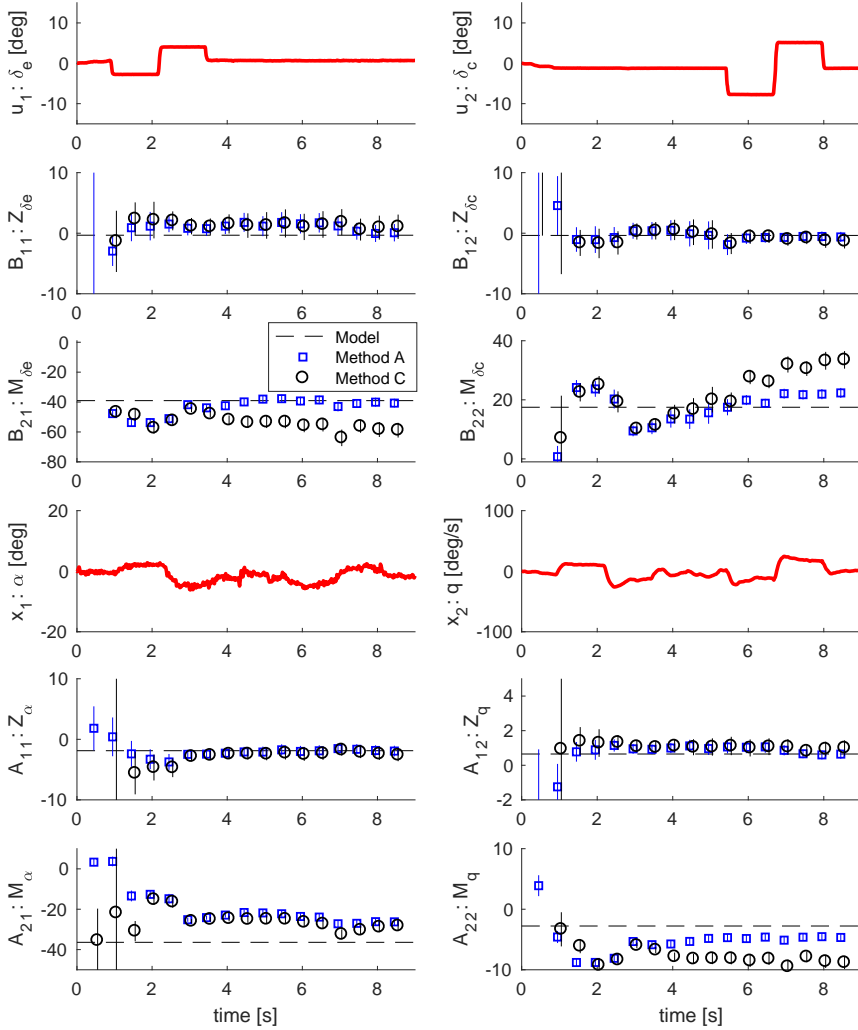


**Figure 6.16:** Results from flight FT. #3 with maneuver DPs. The flight test data is shown in red, the results from Method A as blue squares and the results from Method C as black circles. The uncertainties are given as vertical bars.

In Table 6.6, the absolute values of the correlation between the real parts of the regressors are given. The multisine input signals have much lower correlation than the double pulses. The parallel double pulse, DPp, has the highest correlation of 0.86. This might reduce the resulting estimation accuracy.

**Table 6.6:** Absolute value of correlation between the real parts of the regressors.

MSs1					MSp1			
	$\delta_e$	$\delta_c$	$\alpha$	$q$	$\delta_e$	$\delta_c$	$\alpha$	$q$
$\delta_e$	1.00	0.07	0.04	0.18	1.00	0.08	0.02	0.35
$\delta_c$		1.00	0.42	0.34		1.00	0.40	0.22
$\alpha$			1.00	0.06			1.00	0.06
$q$				1.00				1.00
DPp					DPs rep			
	$\delta_e$	$\delta_c$	$\alpha$	$q$	$\delta_e$	$\delta_c$	$\alpha$	$q$
$\delta_e$	1.00	0.61	0.78	0.72	1.00	0.68	0.54	0.49
$\delta_c$		1.00	0.86	0.03		1.00	0.58	0.70
$\alpha$			1.00	0.42			1.00	0.04
$q$				1.00				1.00

The validation of the estimated models is an important part of system identification [Ljung, 1999, Morelli and Klein, 2005]. The test flight FT. #3, DPs1, that was aborted due to ground proximity, has been used as the test data set to validate the different estimated models. A common measure for judging how well a model,  $m$ , can explain the information in the validation data set,  $Z$ , is the model fit criterion defined as

$$F(m, Z) = 100(1 - \frac{\|y - \hat{y}(\theta)\|_2}{\|y - \bar{y}\|_2}) \quad (6.5)$$

This has been used to compare Method A and Method C. The results are shown in Table 6.7 and Figure 6.17. Two things can be noted. First, Method C gives in general a better model fit than Method A. This means that the addition of instrumental variables contribute in a positive way. Second, the double pulse excitation gives a lower model fit than the multisine input with one exception. This means that it is often beneficial to use multisine inputs for this type of testing with an rc-aircraft.

## 6.5 Post flight analysis

For post flight analysis all test maneuvers are available and should be used together. This will improve the estimation result since the information content available is much larger than for each maneuver separately. The aborted test

**Table 6.7:** Comparison of Method A and Method C using the aborted test flight DPs1 as validation data and the model fit criterion (6.5) as a measure.

Flight	FT. #2		Flight	FT. #3	
Pos.	Method A	Method C	Pos.	Method A	Method C
MSs1	62.5 %	66.7 %	MSP1	50.3 %	47.0 %
MSs1	50.2 %	63.0 %	MSP1	50.5 %	47.6 %
MSs2	-12.4 %	39.8 %	MSP2	68.3 %	68.9 %
MSP1	54.5 %	60.8 %	MSs1	62.5 %	68.1 %
MSP1	57.5 %	67.7 %	MSs1	54.9 %	62.0 %
MSP2	66.3 %	67.7 %	MSs2	55.2 %	64.3 %
DPP	26.1 %	41.9 %	DPs	69.9 %	70.5 %

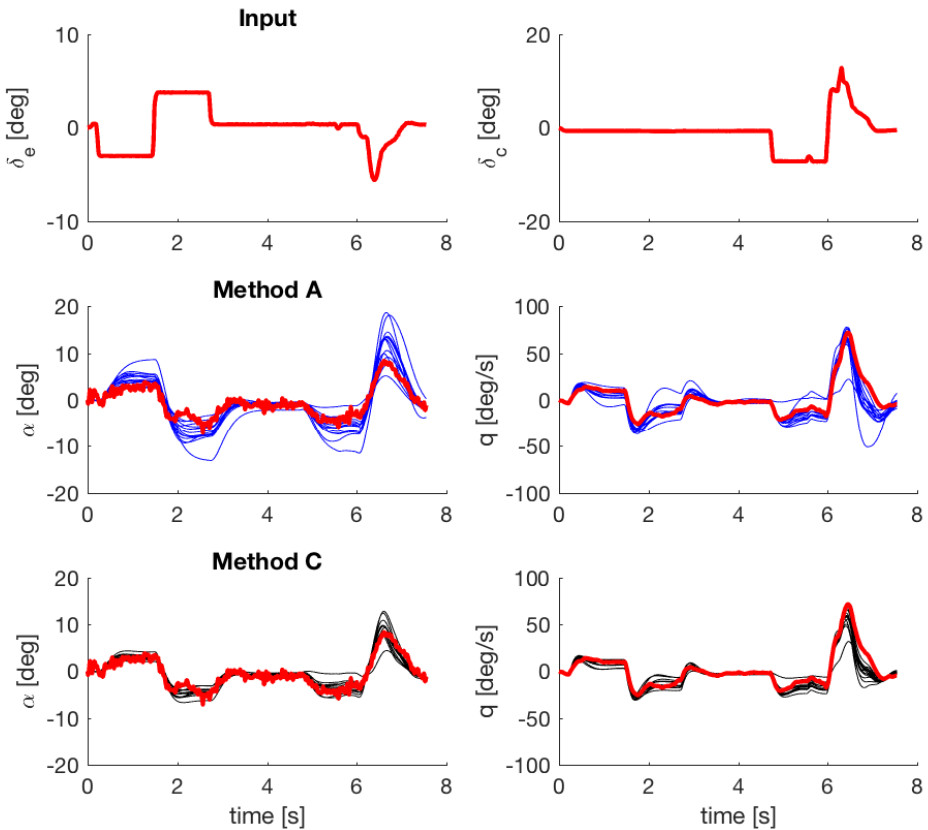


**Figure 6.17:** Validation with flight test data in red. Upper: Input, middle: Output from Method A and bottom: Output from Method C.

flight DPs1 has again been used as test data for validation purposes and the remaining  $K=14$  maneuvers (including DPs2) given in Table 6.3 are used for model construction. A data fusion approach, like the one given in Gustafsson [2012], has been used to combine the models from the different maneuvers into one single model. The model fusion is a weighted average of estimates  $\hat{\theta}_i$ ,  $i = 1 \dots K$ , where the weights are the information matrices  $\hat{I}_i = \hat{P}_i^{-1}$  from different time sequences. The model fusion is given as

$$\begin{aligned}\hat{I} &= \sum_{i=1}^K \hat{I}_i \\ \hat{\theta} &= \hat{I}^{-1} \sum_{i=1}^K \hat{I}_i \hat{\theta}_i\end{aligned}\tag{6.6}$$

The resulting model, based on Method A, is given by

$$\begin{aligned}\dot{x}(t) &= \begin{bmatrix} -1.90 & 1.03 \\ -24.52 & -7.11 \end{bmatrix} x(t) + \begin{bmatrix} 0.90 & -1.27 \\ -51.25 & 29.43 \end{bmatrix} u(t) \\ y(t) &= \begin{bmatrix} 1.00 & 0.00 \\ 0.00 & 1.00 \end{bmatrix} x(t)\end{aligned}\tag{6.7}$$

and for Method C by

$$\begin{aligned}\dot{x}(t) &= \begin{bmatrix} -2.74 & 1.14 \\ -26.29 & -8.30 \end{bmatrix} x(t) + \begin{bmatrix} 0.90 & -1.46 \\ -55.61 & 30.70 \end{bmatrix} u(t) \\ y(t) &= \begin{bmatrix} 1.00 & 0.00 \\ 0.00 & 1.00 \end{bmatrix} x(t).\end{aligned}\tag{6.8}$$

Validating these models on the DPs1 data set give a result shown in Figure 6.18. Here, the pre-flight model (6.2) has also been incorporated. As can be seen, the resulting models for Method A and Method C are almost on top of each other and they give a good model fit of 68.4% and 67.9% respectively. The pre-flight model (6.2) has a little more undamped behavior, which also is shown in a model fit of 54.0%.

It should be noted that since Method A and Method C give such similar results, this could be due to an averaging effect since the estimates are based on more data than what is available during one GFF flight test maneuver.

## 6.6 Conclusions

This chapter describes a cost effective way to perform flight tests with radio-controlled aircraft for system identification of flight mechanical characteristics. Multisine input signals have been designed based on old flight test data. It is

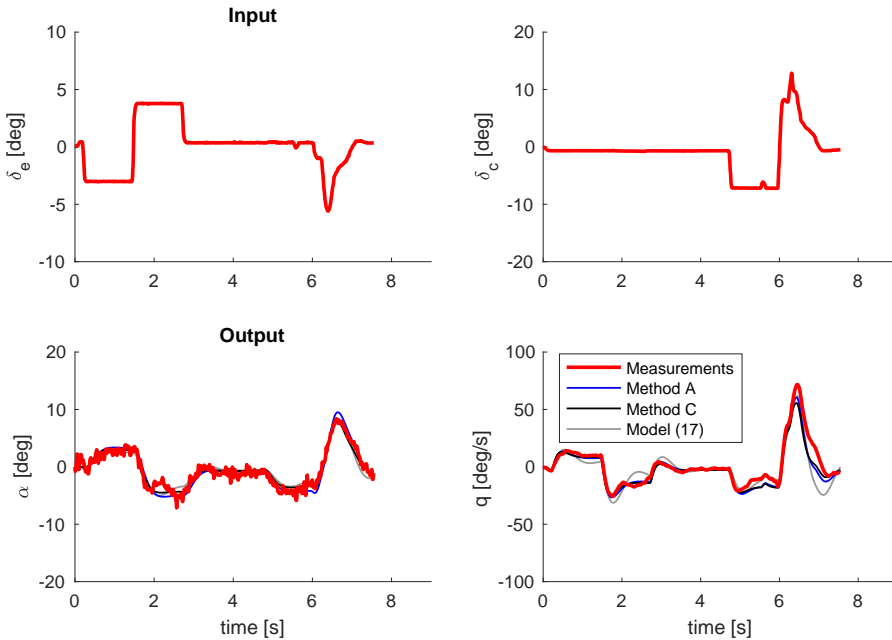


**Figure 6.18:** Validation simulations with flight test data in red.

shown how the use of these signals can reduce the time needed for excitation. This is important due to the requirements for rc-aircraft to be held within visual line-of-sight. The difference between exciting the control surfaces in parallel or separated is not so large, when using the multisine signals. However, when compared to traditional double pulses the multisine signals give a better result. For the analysis of flight test data, two methods have been used. The first uses an existing real-time frequency domain approach, Method A. The second is Method C where the full time sequence has been used so that only the instrumental variables are added compared to Method A. The result shows that Method C improves the accuracy for flights in turbulent conditions. A post flight analysis using both methods has been done. The differences between the methods are here small and this could be an averaging effect since the estimates are here based on more data.





# 7

---

## The parameterized observer method

"If you can't explain it simply, you don't understand it well enough."  
- Albert Einstein (1879 - 1955)

A complex system can have properties that vary from stable to unstable, from linear to nonlinear and thereby need a closed-loop control system that can deal with all combinations of these characteristics. The noise properties can add even more complexity when performing system identification of such a system. Flight mechanical characteristics of a modern fighter aircraft are typically a system where these kinds of problems can occur during system identification. Also, the process noise for this application comes from atmospheric turbulence, which is noise that is colored. This can be a problem in itself for some identification methods.

Engineers often look for simple ways to solve problems. One way is to use Occam's razor, a philosophical principle named after friar William of Ockham (1287-1347), that states that, "Of two competing theories, the simpler explanation of an entity is to be preferred" [Duignan, 2018]. User friendliness is another important aspect that can affect the choice of method to be used. This is especially true in industry since potential users can be inexperienced engineers.

In this chapter the properties of a relatively simple and robust prediction error method [Larsson et al., 2009], which requires a minimum of input from the engineer, is investigated. A direct identification approach is used to identify the system without any knowledge of the control system. This makes the methods more general and easier to apply to different aircraft. Methods like this need to have a stable predictor and also be to robust against different noise properties. The question is whether or not the mentioned method is a suitable candidate to be used for identification of complex systems working in feedback control.

## 7.1 Problem formulation

A block diagram describing a nonlinear continuous-time, closed-loop system is shown in Figure 7.1.

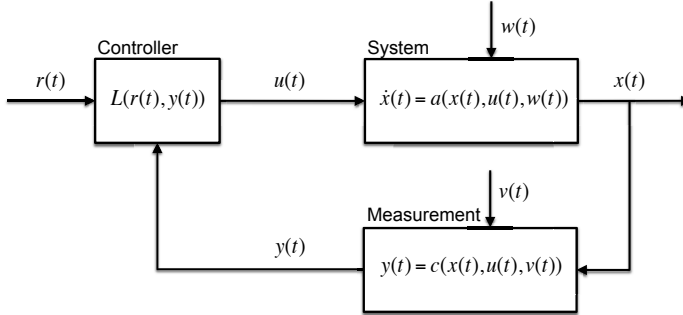


**Figure 7.1:** Block diagram of a general continuous-time, closed-loop system.

Mathematically the closed-loop system can be described as

$$\begin{aligned} \dot{x}(t) &= a_S(x(t), u(t), w(t)) \\ y(t) &= c_S(x(t), u(t), v(t)) \\ u(t) &= L_S(r(t), y(t)) \end{aligned} \quad (7.1)$$

where  $x$  is a  $n_x \times 1$  state vector,  $u$  is a  $n_u \times 1$  input vector,  $w$  is the process noise and  $a_S$  describes the dynamics of the system, which can have combinations of both stable and unstable parts. Furthermore,  $y$  is a  $n_y \times 1$  output vector,  $v$  is the measurement noise and  $c_S$  describes the measurement system. The controller  $L_S$  is based on a reference signal  $r$  and the measurements  $y$ .

It is assumed that no direct influence from the input to the output exists. It is also assumed that the process noise as well as the measurement noise are additive. Furthermore, the measurement noise is white. This simplifies the system description (7.1) to

$$\begin{aligned} \dot{x}(t) &= a_S(x(t), u(t)) + w(t) \\ y(t) &= c_S(x(t)) + e(t) \\ u(t) &= L_S(r(t), y(t)). \end{aligned} \quad (7.2)$$

For the identification, a discrete-time nonlinear model structure of (7.2) is used

$$\begin{aligned} x_{k+1} &= f(x_k, u_k; \theta) + w_k \\ y_k &= h(x_k; \theta) + e_k \end{aligned} \quad (7.3)$$

where  $x_k \equiv x(kT_s)$  is the state vector with sample time  $T_s$  and  $\theta$  is a model parameter vector.

The problem is to estimate the unknown parameters in  $\theta$  so that the model (7.3) represents the system (7.2) well enough to be used for accurate enough simulations of the system properties.

## 7.2 Method

The problem described in the previous section can be solved in different ways. Here a relatively simple and robust system identification method called the Parameterized Observer (PO) method will be described. This method is based on a prediction-error method (PEM) approach [Ljung, 1999, Chapter 7, p. 199].

A prediction-error method uses a predictor of the output in (7.3). One such class of predictors is given by

$$\begin{aligned}\hat{x}_{k+1}(\theta) &= f(\hat{x}_k(\theta), u_k; \theta) + K_k(\theta)\varepsilon_k(\theta) \\ \hat{y}_k(\theta) &= C\hat{x}_k(\theta) \\ \varepsilon_k(\theta) &= y_k - \hat{y}_k(\theta)\end{aligned}\tag{7.4}$$

Here it is assumed that the measurements are linearly dependent of the states. The prediction error  $\varepsilon_k(\theta)$  is used to define a scalar cost function

$$V_N(\theta, Z^N) = \frac{1}{N} \sum_{k=1}^N \frac{1}{2} \varepsilon_k(\theta)^T \varepsilon_k(\theta),\tag{7.5}$$

where  $Z^N$  represents the  $N$  input-output measurements. To obtain a parameter estimate  $\hat{\theta}$ , an unconstrained optimization problem has to be solved

$$\hat{\theta} = \arg \min_{\theta \in D_M} V_N(\theta, Z^N)\tag{7.6}$$

The minimization problem is in this thesis solved using the iterative Levenberg-Marquardt approach described in Chapter 2. Traditionally, an optimal predictor is sought, but sub-optimal predictors can also work. It is however required that  $K_k(\theta)$  in (7.4) gives a stable predictor. This leads to an implicit constraint on the optimization problem since the parameters  $\theta$  are limited under this requirement. If the system dynamics are linear, stable and working under open loop conditions, then it is possible to use a predictor with  $K_k(\theta) = 0$ . A particular choice of a nonzero  $K_k(\theta)$  can be used when the system is linear but unstable [Forsell and Ljung, 2000]. However, the choice of the predictor is not obvious if the system is nonlinear and unstable. The closed-loop part of the system makes the identification extra hard in this case. For example, in Schön et al. [2011] a particle filter approach is tested on nonlinear systems, but in open loop.

In the PO method, it is assumed that the stabilization of the predictor can be achieved by using a time-invariant observer gain  $K_k = K$ . It is not obvious that

such a gain exists, but if it does, a PEM using the predictor (7.4) with

$$\theta = \begin{bmatrix} \theta_f \\ \theta_K \end{bmatrix} \quad (7.7)$$

can be used. Here  $\theta_f$  are the parameters that appear in  $f$  and  $\theta_K = \text{vec}(K)$  is a vector containing the observer gain parameters. It is however unclear what performance can be expected from this predictor.

The PO is a simple approach and if the performance is good enough it will be attractive since the calculation of a time-varying  $K_k$  in (7.4) is generally a fairly complicated process, as is described in Ljung [1999] or as can be seen for a EKF or UKF approach where the  $K_k$  is updated recursively over time. Here an analysis of the properties of the PO method will be given and in Chapter 8 it will be compared to other identification methods.

### 7.3 Noise

The observer gain,  $K_k(\theta)$  in (7.4), does not only have to be stabilizing, it also needs to take care of different noise characteristics, i.e., the term  $K_k(\theta)\varepsilon_k(\theta)$  in (7.4) has to act as a noise model. As stated in Chapter 2, no consistency analysis of the PEM will be given, but to get a feeling for the PO method in this context, a short comparison with another method is given here. The PO method works in a similar way as the non-stationary linear predictor method described in Abdalmoaty [2017], which states that given a nonlinear model on the form

$$y_k = f_A(\varphi_{k-1}, w_{k-1}, \theta) + v_k \text{ with } \varphi_{k-1} = (u_{k-1}, u_{k-2}, \dots, u_{k-n_b}) \quad (7.8)$$

where  $v$  and  $w$  represents the measure and process noise, it is possible to rewrite (7.8) as

$$y_k = \hat{f}_A(\varphi_{k-1}; \theta) + \tilde{v}_k \quad (7.9)$$

where

$$\hat{f}_A(\varphi_{k-1}; \theta) = E(y_k | \varphi_{k-1}) = E(f_A(\varphi_{k-1}, w_{k-1}; \theta) | \varphi_{k-1}) \quad (7.10)$$

and

$$\tilde{v}_k = v_k + f_A(\varphi_{k-1}, w_{k-1}; \theta) - \hat{f}_A(\varphi_{k-1}; \theta) \text{ with } E(\tilde{v}_k | \varphi_{k-1}) = 0. \quad (7.11)$$

If it is assumed that  $\tilde{v}_k$  can be described as filtered white noise

$$\tilde{v}_k = H(q)e_k, \quad (7.12)$$

then a predictor can be defined as

$$\hat{y}_k = H^{-1}(q)\hat{f}_A(\varphi_k; \theta) + (1 - H^{-1}(q))y_k \quad (7.13)$$

This predictor is only nonlinear in the known regressors  $\varphi$  and parameters  $\theta$ . It has been shown in Abdalmoaty [2017] that the choice (7.10) makes the predictor

consistent. The key is the conditional expectation, which in many cases can be quite hard to calculate.

To get the feeling for the consistency of the predictor (7.4), consider the simple scalar FIR problem

$$\begin{aligned} x_{k+1} &= \left[ f([1 \ 0]x_k, u_k; \theta_f) \right] + w_k \\ y_k &= [0 \ 1]x_k + e_k \end{aligned} \quad (7.14)$$

which is of the form (7.3). It can be written as

$$y_k = f(u_{k-2} + [1 \ 0]w_{k-2}, u_{k-1}; \theta_f) + [0 \ 1]w_{k-1} + e_k, \quad (7.15)$$

This expression looks like (7.8) with

$$f_A(\varphi_{k-1}, w_{k-1}, \theta) = f(u_{k-2} + [1 \ 0]w_{k-2}, u_{k-1}; \theta_f) + [0 \ 1]w_{k-1}. \quad (7.16)$$

The similarities between (7.13) and (7.4) can be seen if (7.4) is rewritten as

$$\hat{y}_k(\theta) = C(f(\hat{x}_{k-1}(\theta), u_{k-1}; \theta_f) - \theta_K \hat{y}_{k-1}(\theta)) + C\theta_K y_k \quad (7.17)$$

where the filter  $H(q)$  is chosen as

$$H(q) = \frac{1}{1 - dq^{-1}} \quad (7.18)$$

and  $d = C\theta_K$ . With  $\varphi_k = (u_k, u_{k-1})$  and this specific choice of the filter  $H(q)$ , the predictor (7.17) is on the form (7.13) which will give a consistent estimator. This means that there exist simple problems on the state-space form that are consistent. In the general case this cannot be guaranteed, but the PO method has at least the potential to be consistent for the problems under consideration.

## 7.4 Stability of nonlinear systems

To be able to say something about the stability of the predictor (7.4), some basics of stability for nonlinear systems is needed. For a linear state-space system

$$x_{k+1} = Ax_k + Bu_k \quad (7.19)$$

the stability is analyzed by looking at the eigenvalues of the system matrix  $A$ . For a nonlinear system

$$x_{k+1} = f(x_k, u_k) \quad (7.20)$$

the Lyapunov stability theory [Lyapunov, 1892] can be used. Since a nonlinear system can have multiple equilibria, the stability is referred to an equilibrium point  $x^*$  and not to the system. There are different levels of stability for both linear and nonlinear systems as stated in Chapter 2. These are shown in Figure 7.2. The system can be (1) asymptotically stable, (2) stable or (3) unstable. In addition,

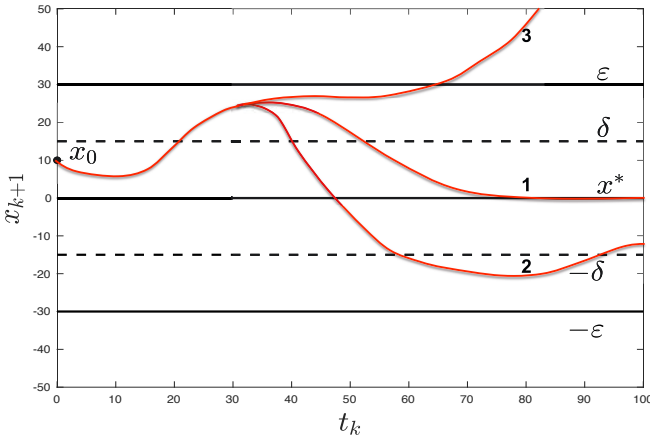


**Figure 7.2:** Different stability levels. The red curve show trajectories for a, (1) asymptotically stable, (2) stable or (3) unstable, nonlinear system.

input-to-state stability (ISS) is of interest to see that the input does not drive the states away. For nonlinear systems, the stability is also divided into two cases, either local around one or more of the equilibrium points or it can be globally stable. In the later case there can be only one equilibrium and hence the system can be said to be stable.

Mathematically the stability can be formulated as

$$|x_k| \leq \beta(|x_0|, k), \quad \forall x_0 \text{ and } k \geq 0 \quad (7.21)$$

and for the ISS

$$|x_k| \leq \beta(|x_0|, k) + \gamma(\|u\|_\infty), \quad \forall x_0, \forall u \text{ and } k \geq 0 \quad (7.22)$$

Here  $\beta(r, s)$  is a function for which  $\beta(0, s) = 0 \forall s$ . For a fixed  $s = s_f$ ,  $\beta(r, s_f)$  is strictly increasing and for a fixed  $r = r_f$ ,  $\beta(r_f, s)$  is decreasing and  $\beta(r_f, s) \rightarrow 0$  as  $s \rightarrow \infty$ . Also,  $\gamma(s)$  is a function for which  $\gamma(0) = 0$  and  $\gamma(s)$  is strictly increasing as  $s$  increases.

In Khalil [2002], stability theory for continuous systems is given. For discrete-time systems the theory is given in Bof et al. [2018] and it can be summarized as

$$\begin{aligned} V(x^*) &= 0, & x^* \text{ is an equilibrium point} \\ V(x) &> 0, & \forall x \in \Omega, x \neq x^*, \Omega \subset \mathbb{R} \\ V(x) &\rightarrow \infty \text{ as } \|x\| \rightarrow \infty \\ V(x_{k+1}) - V(x_k) &\leq 0 \end{aligned} \quad (7.23)$$

Here  $V(x)$  is a Lyapunov function that increases with the distance from the equilibrium  $x^*$ , but decreases with time. If there exist a Lyapunov function then the system is stable.

## 7.5 Piecewise affine systems

In this thesis, the nonlinear system in (7.3) is assumed to be piecewise affine. An example of a model for such a system is shown in Figure 7.3. Since affine systems are non-smooth, finding Lyapunov functions to prove stability requires some special attention. For example, in Johansson [1999] it is stated that not only the dynamics in each segment, but also the geometry of the segment has to be taken into account when looking at the stability. Techniques like solving a set of linear matrix inequalities [Feng, 2002] or applying linear programming, semi-definite programming and sum-of-squares [Biswas et al., 2005] can be used.

The conditions for global input-to-state stability of discrete-time piecewise affine systems are given in Lazar and Heemels [2008]. In this article the stability is analyzed from a control design point of view. In the present thesis it is the predictor that is under consideration. This means that there are not the same limitations as for a physical system since the predictor is a mathematical construction used in system identification.

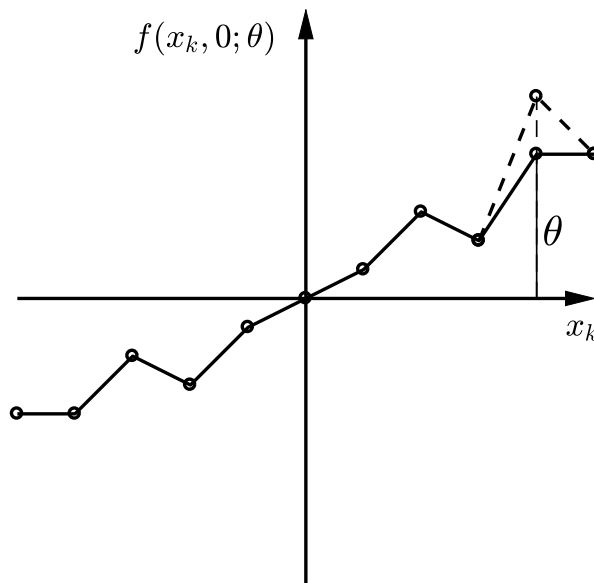


*Figure 7.3: Piecewise affine function with ten segments.*



In the following, a simple example of a scalar piecewise affine system is analyzed. This is done to give a feeling for the problems and possibilities of the PO method and further how a predictor with a constant  $K_k(\theta) = K$  affects the system identification.

## 7.6 Simple example

Here, the piecewise affine system is given by

$$\begin{aligned} x_{k+1} &= f_S(x_k, u_k) + w_k \\ y_k &= x_k + e_k \end{aligned} \quad (7.24)$$

with

$$f_S(x_k, 0) = \begin{cases} -2A_b a_b + A_a x_k & \text{if } x_k < -a_b, & m = 1 \\ (A_a + 2A_b)x_k & \text{if } |x_k| \leq a_b, & m = 2 \\ 2A_b a_b + A_a x_k & \text{if } x_k > a_b, & m = 3 \end{cases} \quad (7.25)$$

is used. Figure 7.4 shows the piecewise affine function  $f_S(x_k, 0)$ . This can also be written as

$$\begin{aligned} x_{k+1} &= A_{0,m} + A_m x_k + B u_k + w_k, \quad m = 1, 2, 3 \\ y_k &= x_k + e_k. \end{aligned} \quad (7.26)$$

Here, a predictor for (7.26), using (7.4) is

$$\begin{aligned} \hat{x}_{k+1}(\theta) &= A_{0,m} + A_m \hat{x}_k(\theta) + B u_k + K(y_k - \hat{y}_k(\theta)) \\ \hat{y}_k(\theta) &= \hat{x}_k(\theta). \end{aligned} \quad (7.27)$$

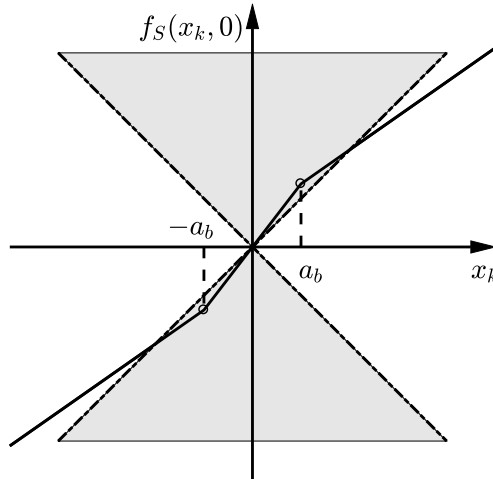


**Figure 7.4:** Piecewise affine function with three segments divided by the break points  $\pm a_b$ . The white area shows the stability region for an equilibrium point at the origin.

This can be reformulated as

$$\begin{aligned}\hat{x}_{k+1}(\theta) &= A_{0,m} + (A_m - K)\hat{x}_k(\theta) + \begin{bmatrix} B & K \end{bmatrix} \begin{bmatrix} u_k \\ y_k \end{bmatrix} \\ &= \tilde{A}_{0,m} + \tilde{A}_m \hat{x}_k(\theta) + \tilde{B} \tilde{u}_k\end{aligned}\quad (7.28)$$

where  $\tilde{A}_{0,m} = \text{sign}(m-2)2A_b a_b(1-\delta(m-2))$  and  $\tilde{A}_m = A_a + 2A_b\delta(m-2) - K$ . Note that both  $u_k$  and  $y_k$  acts as inputs to the predictor.

In this example the parameters  $A_b = 0.3$ ,  $a_b = 0.2$  and  $B = -0.115$  are assumed to be known. This means that  $\tilde{A}_{0,m}$  is known while  $\tilde{A}_m$  and  $\tilde{B}$  include the unknown parameters  $A_a$  and  $K$ . This simplification makes it easier to show the results.

To make the stability analysis of (7.28), using the Lyapunov stability theory the predictor can be looked upon as

$$\hat{x}_{k+1}(\theta) = f_m(\hat{x}_k(\theta), u_k; \theta) \quad (7.29)$$

with

$$\theta = \begin{bmatrix} A_a \\ K \end{bmatrix} \quad (7.30)$$

**Unperturbed analysis,**  $\tilde{u}_k = [0 \ 0]^T$ : For  $K = 0$  there are three equilibrium points  $(0, \pm 0.4)$  in this example, one in each segment. These can be seen in Figure 7.4. Here, the point  $x_k = 0$  is chosen for the stability analysis. This is done since it is independent of  $K$  and therefore will not change during the identification. A similar analysis can be done for the other two equilibrium points by coordinate changes.

By using the numerical values for  $A_b$ ,  $a_b$  and  $B$  in (7.25) the following nonlinear function is received

$$f(\hat{x}_k, 0) = \begin{cases} -0.12 + (A_a - K)\hat{x}_k & \text{if } \hat{x}_k < -0.2, \quad m = 1 \\ (A_a - K + 0.6)\hat{x}_k & \text{if } |\hat{x}_k| \leq 0.2, \quad m = 2 \\ 0.12 + (A_a - K)\hat{x}_k & \text{if } \hat{x}_k > 0.2, \quad m = 3 \end{cases} \quad (7.31)$$

A common quadratic Lyapunov function used is

$$V_m(x) = x^T P x \quad (7.32)$$

which satisfies the first three conditions of (7.23) for a symmetric positive definite matrix  $P$ . To prove stability  $V(x_{k+1}) - V(x_k) \leq 0$  is needed. With a choice of  $P = 1$  and since  $x_{k+1} = f(\hat{x}_k, 0)$ , this requirement becomes

$$f(\hat{x}_k, 0)^2 - x_k^2 \leq 0 \quad (7.33)$$

Putting in (7.31) into (7.33) and making the calculations gives the following conditions for stability

$$\begin{aligned} 1 + (0.12/\hat{x}_k) &\leq (A_a - K) \leq -1 + (0.12/\hat{x}_k) && \text{if } \hat{x}_k < -0.2, \quad m = 1 \\ -1.6 &\leq (A_a - K) \leq 0.4 && \text{if } |\hat{x}_k| \leq 0.2, \quad m = 2 \\ -1 - (0.12/\hat{x}_k) &\leq (A_a - K) \leq 1 - (0.12/\hat{x}_k) && \text{if } \hat{x}_k > 0.2, \quad m = 3 \end{aligned} \quad (7.34)$$

These stability requirements are given by red lines in the left part of Figure 7.5. As can be seen, the range of stability for a constant observer gain  $K$  over the whole state region is  $-1 \leq A_a - K \leq 0.4$ . This is given by the black dashed line in the figure.

To make the simulations easier the structure of the predictor is changed to a structure that is switching between two linear parts. This is done by setting the parameter  $a_b = 0$ . This turns (7.31) into

$$f(\hat{x}_k, 0) = \begin{cases} (A_a - K)\hat{x}_k & \text{if } \hat{x}_k < -0.2, \quad m = 1 \\ (A_a - K + 0.6)\hat{x}_k & \text{if } |\hat{x}_k| \leq 0.2, \quad m = 2 \\ (A_a - K)\hat{x}_k & \text{if } \hat{x}_k > 0.2, \quad m = 3 \end{cases} \quad (7.35)$$

From a stability point of view there is not a big difference between the two structures. The stability condition is changed so that it looks like the graph to the right in Figure 7.5. The requirement for a stable predictor with a constant  $K$  is actually the same as before, i.e.,  $-1 \leq A_a - K \leq 0.4$  as is shown by the black dashed lines.

**Perturbed analysis,  $\tilde{u}_k \neq [0 \ 0]^T$ :** When the input is taken into account in the stability analysis, an analysis of the input-to-state stability [Jiang et al., 1999] is

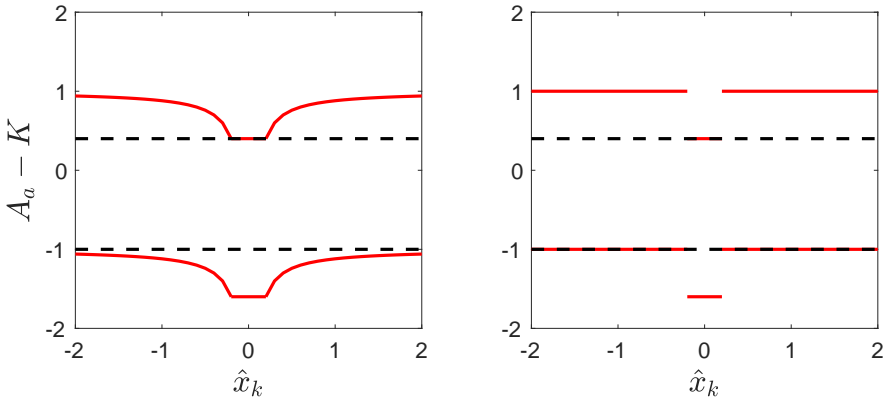


**Figure 7.5:** To the left the stability requirements for the piecewise affine function given by (7.34) is shown. The black dashed lines are the boundaries for a constant  $(A_a - K)$  over all segments. Similar boundaries are given for the switched system to the right.

needed. For this the first three conditions of (7.23) is the same, but the fourth criterion is changed to

$$V(x_{k+1}) - V(x_k) \leq -\alpha(|x_k|) + \sigma(|u_k|) \quad (7.36)$$

which needs to be fulfilled. Here, the functions  $\alpha(s)$  and  $\sigma(s)$  are strictly increasing with increasing  $s$ .

The switching predictor (7.34) with the input included will look like

$$f(\hat{x}_k, u) = \begin{cases} (A_a - K)\hat{x}_k + \tilde{B}\tilde{u}_k & \text{if } \hat{x}_k < -0.2, \quad m = 1 \\ (A_a - K + 0.6)\hat{x}_k + \tilde{B}\tilde{u}_k & \text{if } |\hat{x}_k| \leq 0.2, \quad m = 2 \\ (A_a - K)\hat{x}_k + \tilde{B}\tilde{u}_k & \text{if } \hat{x}_k > 0.2, \quad m = 3 \end{cases} \quad (7.37)$$

where  $\tilde{B} = [B \quad K]$  and  $\tilde{u}_k = [u_k \quad y_k]^T$ . This predictor can then be written as

$$\hat{x}_{k+1} = \tilde{A}_m \hat{x}_k + \tilde{B}\tilde{u}_k, \quad m = 1, 2, 3 \quad (7.38)$$

If the Lyapunov function

$$V_m(x) = x^2 \quad (7.39)$$

is applied to (7.38) the following analysis can be made

$$\begin{aligned} V(\hat{x}_{k+1}) - V(\hat{x}_k) &= (\tilde{A}_m \hat{x}_k + \tilde{B}\tilde{u}_k)^2 - \hat{x}_k^2 = \tilde{A}_m^2 \hat{x}_k^2 + 2\tilde{A}_m \hat{x}_k \tilde{B}\tilde{u}_k + (\tilde{B}\tilde{u}_k)^2 - \hat{x}_k^2 \\ &= -(1 - \tilde{A}_m^2) \hat{x}_k^2 + 2\tilde{A}_m \hat{x}_k \tilde{B}\tilde{u}_k + (\tilde{B}\tilde{u}_k)^2 \\ &\leq -(1 - \tilde{A}_m^2) |\hat{x}_k|^2 + 2\left(\frac{|\tilde{A}_m \hat{x}_k|^2}{2} + \frac{|\tilde{B}\tilde{u}_k|^2}{2}\right) + |\tilde{B}\tilde{u}_k|^2 \\ &= -(1 - 2\tilde{A}_m^2) |\hat{x}_k|^2 + 2|\tilde{B}\tilde{u}_k|^2 \leq -(1 - 2\tilde{A}_m^2) |\hat{x}_k|^2 + 2|\tilde{B}|^2 |\tilde{u}_k|^2 \end{aligned} \quad (7.40)$$

where Young's inequality of products [Young, 1912] has been used for the product  $\tilde{A}_m \hat{x}_k \tilde{B}\tilde{u}_k$ . Furthermore, since  $\tilde{A}_m$  and  $\hat{x}_k$  are scalars  $|\tilde{A}_m \hat{x}_k| = |\tilde{A}_m| |\hat{x}_k|$ . In the last step, Cauchy-Schwarz inequality  $|\tilde{B}\tilde{u}_k| \leq |\tilde{B}| |\tilde{u}_k|$  has been used. The expression (7.40) is on the form (7.36) with  $\alpha(s) = (1 - 2\tilde{A}_m^2)s^2$  and  $\sigma(s) = 2|\tilde{B}|^2 s^2$  if it holds that  $(1 - 2\tilde{A}_m^2) > 0$ , which means that  $1/\sqrt{2} > |\tilde{A}_m|$ . The system is therefore ISS stable in the different segments with the boundaries  $-0.71 \leq A_a - K \leq 0.11$ , which has been derived in the same way for a constant  $K$  as the analysis made for (7.35). This bound is more restrictive than the one given by the unperturbed analysis, but none of these two cases might give a tight bound for the largest possible stability boundary of the predictor since there might be other Lyapunov functions than the one used here that can be used for this. Finding such a maximum bound is beyond the scope of the current analysis, but optimization will probably have to be used like in Biswas et al. [2005].

## 7.7 Simulation study

A simulation study of different noise properties has been performed using the switching predictor (7.37). This has been done to illustrate the robustness of the

PO method. The system has been switched between the inner unstable segment ( $\tilde{A}_m = 1.3$ ) and the outer stable segment ( $\tilde{A}_m = 0.7$ ). A switching feedback loop with the poles placed in 0.5 has been used.

The simulations have been done so that the amount of data in the inner segment, i.e., for  $|\hat{x}_k| \leq 0.2$ , has been varied as [0 3 10 25 50 75 90 100] %. As an example, Figure 7.6 shows a dataset for medium noise. This specific data set has 50 % of the data in each segment. The first part of the data is in the unstable segment where ( $\tilde{A}_m = 1.3$ ). This can be seen as  $u$  works with a larger amplitude.

In Figures 7.7, identification using four different start guesses of  $A_a$  and  $K$  are shown. The identification result is shown as a red dot. Also, the stability bound are plotted as dashed lines. The red line gives the minimum value of  $A_a$  for each predictor gain  $K$ . In Figure 7.8 the prediction error surface for  $V_N(\theta, Z^N)$  is shown in the left part of the figure and to the right in the figure, contour lines are shown. The identification result for 100 % of data in the inner segment is shown as a blue dot and for 100 % of data in the outer segment as a violet dot. These are given as references. The result for this case is  $\hat{A}_a = 0.69$ , which is close to the true value of  $A_a = 0.70$ . The observer gain is predicted as  $K = 0.74$  for this case.

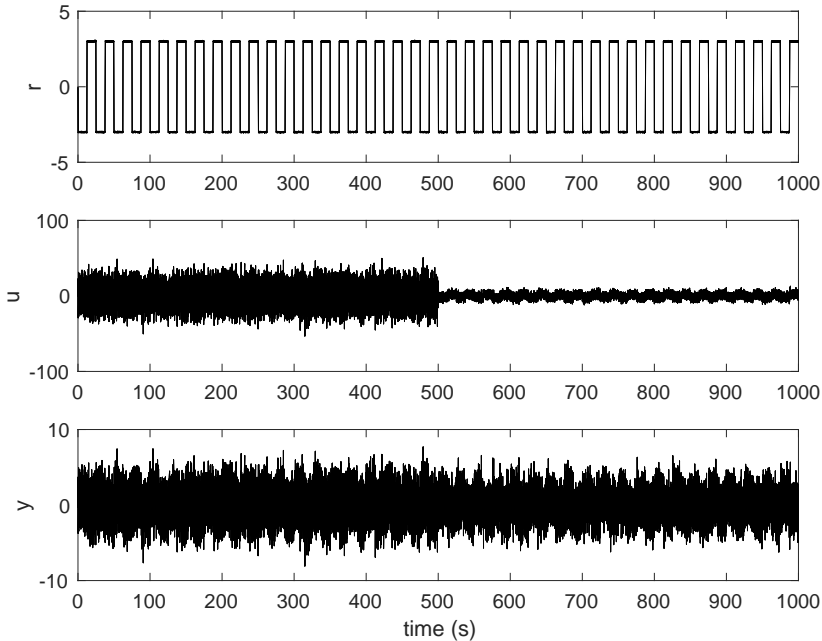


**Figure 7.6:** Simulation data for medium sized noise including the reference, input and output signals. Here a shift from the unstable to the stable segment is done at time  $t = 500$  s.

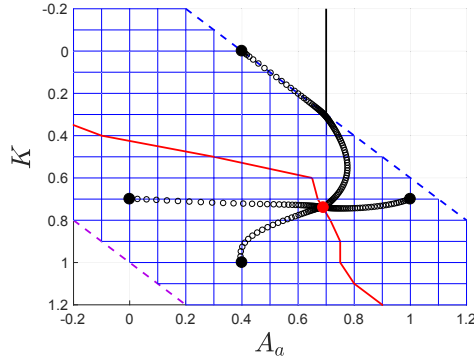


**Figure 7.7:** Identification using four different start guesses of  $A_a$  and  $K$ . Here a shift, which gives 50 % of data from the inner segment ( $\tilde{A}_m = 1.3$ ) and 50 % of data from the outer segment ( $\tilde{A}_m = 0.7$ ) is used. All start guesses end up in the point  $A_a = 0.69$  and  $K = 0.74$ .

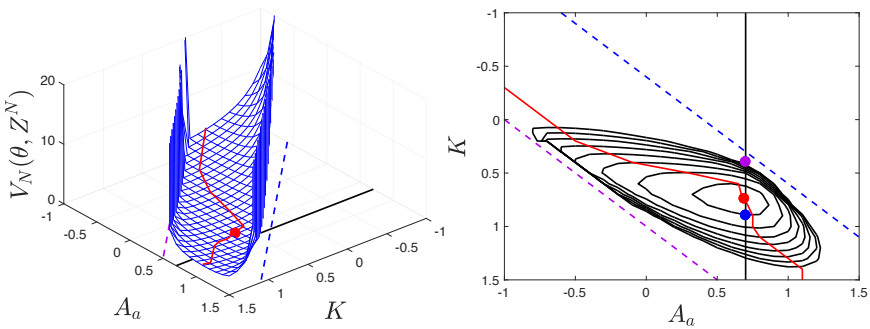


**Figure 7.8:** A surface (left) and a contour plot (right) of  $V_N(\theta, Z^N)$  for medium sized noise together with the stability requirements from Figure 7.5. Here the shift from the unstable to the stable segment is done at time  $t = 500$  s as in Figure 7.7.

The whole result from this simulation study is shown in Figure 7.9. Four different noise properties have been investigated. Low white noise ( $SNR = 4$ ), medium white noise ( $SNR = 4e-4$ ), high white noise ( $SNR = 1e-4$ ) and medium colored noise. As can be seen the results for the white noise with 100 % of data in one of the segments give accurate results. For the colored noise there is a slight bias for this case. For low white noise the result is accurate regardless of the distribution of data between the two segments. As the noise level increases the result depends on the data distribution. Furthermore, colored noise makes things worse. It is interesting to note that the red dots appear to be situated in the tangent between the level curves of the two segments regardless of the noise properties.

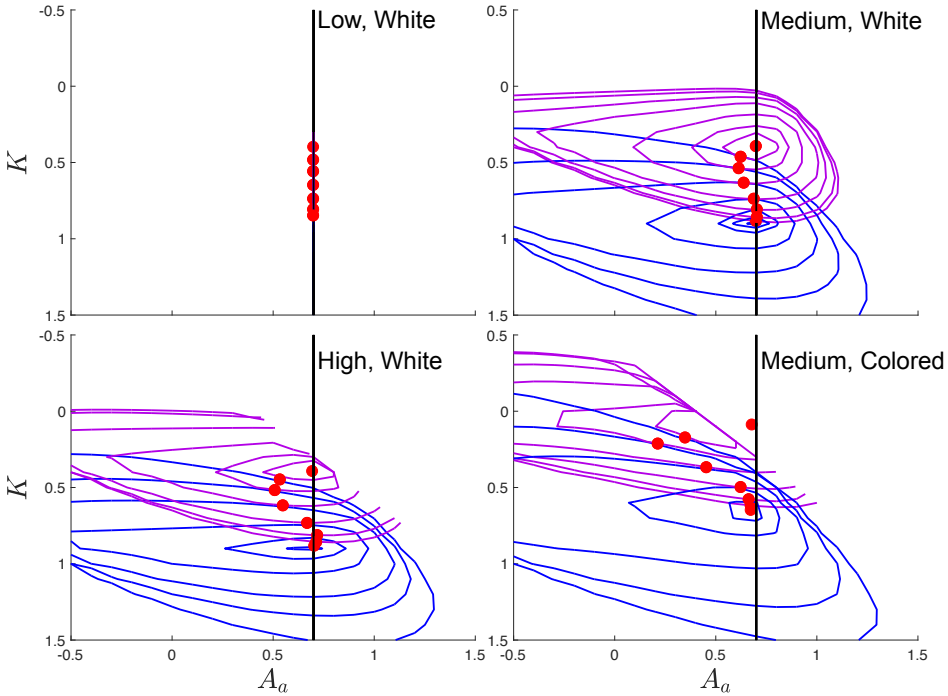


**Figure 7.9:** Visualization of the effect of noise level and color on the estimation. The results are given as red dots for  $[0 \ 3 \ 10 \ 25 \ 50 \ 75 \ 90 \ 100]$  % of data in the inner segment, i.e., for  $|\hat{x}_k| \leq 0.2$ . The black line is the true system parameter for  $A_a = 0.7$ . Blue level curves are from the inner segment ( $\tilde{A}_m = 1.3$ ) and violet level curves are from the outer segment ( $\tilde{A}_m = 0.7$ ).

## 7.8 Conclusions

The Parameterized Observer (PO) method has been analyzed in this chapter with respect to noise properties and stability characteristics. The method is relative simple to implement and has no tuning parameters to be set by the user. A simulation study of a scalar problem has been performed to give some intuitive results. It has been shown that the identification result is dependent on the data distribution between the segments and that increasing noise levels can give a biased result if this distribution is unfavorable. Colored noise seems to add to this problem. There is also a small bias regardless of the distribution in this case. All in all, the PO method seems to be an interesting approach to use for identification of nonlinear systems. In the next chapter the PO method will be compared to four other methods.

# 8

---

## Identification of unstable nonlinear systems

"Simplicity is the ultimate sophistication."  
- Leonardo da Vinci (1452 - 1519)

In this chapter, the Parameterized Observer (PO) method is compared to four other methods. This has been done for a piece-wise affine system with mixed characteristics (stable-unstable) working under feedback control. The comparison includes a robustness analysis against both measurement and process noise. Since iterative optimization methods are used, a study of initial parameter settings has also been performed. The question is whether or not the PO method is a suitable candidate to be used for identification of complex systems and how well it performs against other methods of equal complexity. Most of the analyses have been done by using a simulation example where the true system is known, but the methods are also tested on real flight test data.

Some of the descriptions from the previous chapter are repeated here for the convenience of the reader.

### 8.1 The identification methods

Here, the five identification methods, for which the basics are described in Chapter 2, are presented. The first three are prediction-error methods including an observer gain based on the parameterized observer (PO) from Chapter 7, the extended (EKF) and unscented Kalman filter (UKF). Furthermore, one state estimation method, using augmented states (AUG) is analyzed as well as one parameter and state estimation method featuring a constrained Levenberg-Marquardt (CLM) optimization.



There are other possible methods that could have been included in this analysis, like the maximum likelihood method with an estimation-maximization (ML-EM) approach or a particle filter (PF) method. The ML-EM approach is described in Moon [1996], Schön et al. [2006] and Hagenblad et al. [2008] and the particle filter theory can be found in Gordon et al. [1993], Moral [1996], Gustafsson [2010] and Schön et al. [2011]. These two methods rely on detailed knowledge about the probability distributions of the measurement and process noise. However, the true noise distributions can be time consuming and hard to find for the aircraft application studied here. The real distribution can also possibly change with time and position since the atmospheric turbulence can be different from day to day and also for example over sea compared to over land. Using an incorrect distribution can lead to decreasing accuracy of the ML and PF estimators. This is one aspect why the PO method is interesting since no such assumptions have to be made. In addition, for the particle filter method the number of particles that has to be used can also have an effect on the identification result. For large dimensional problems the number of particles grows rapidly and even if parallel computing can be used this can lead to costly computations.

It is also possible to use a different model structure than a state-space formulation, for example neural networks (NN) [Narendra and Parthasarathy, 1990, Ljung and Sjöberg, 1992]. Neural networks are very flexible and can thereby model complex systems. From an engineering point of view however, it is hard to interpret the resulting model. There has to be a step after the identification that brings the NN-model into an simplified model that the engineer can understand.

### 8.1.1 Prediction-error methods

The three different prediction-error methods use the predictor formulation of (7.3)

$$\begin{aligned}\hat{x}_{k+1}(\theta) &= f(\hat{x}_k(\theta), u_k; \theta) + K_k(\theta)\varepsilon_k(\theta) \\ \hat{y}_k(\theta) &= H(\theta)\hat{x}_k(\theta) \\ \varepsilon_k(\theta) &= y_k - \hat{y}_k(\theta).\end{aligned}\tag{8.1}$$

The methods can be used for general measurement equations, but here the partial derivative  $H(\theta) = \partial h(x_k, \theta)/\partial x_k$ , making  $h$  a linear approximation in  $x$ , is used. The prediction error  $\varepsilon_k(\theta)$  is used to define a scalar cost function

$$V_N(\theta, Z^N) = \frac{1}{N} \sum_{k=1}^N \frac{1}{2} \varepsilon_k(\theta)^T \varepsilon_k(\theta)\tag{8.2}$$

where  $Z^N$  represents the  $N$  input-output measurements. To obtain an estimate of  $\theta$ , the following unconstrained optimization problem has to be solved

$$\underset{\theta}{\text{minimize}} V_N(\theta, Z^N).\tag{8.3}$$

This is in Ljung [1999] called a prediction-error method (PEM). In order to use PEM, a stable predictor is required. Since the system can be unstable the term  $K_k(\theta)\varepsilon_k(\theta)$  in (8.1) will act as a stabilization as well as an indirect noise model for the predictor. This stability requirement on the predictor will work as an implicit constraint on the optimization problem since the parameters  $\theta$  are limited under this requirement. The choice of the predictor is not obvious if the system is unstable and nonlinear. In the current work, three approaches for calculating the observer gain  $K_k(\theta)$  in (8.1) are suggested.

**Parameterized observer (PO) approach:** This approach was described in Chapter 7 and is a simple approach, commonly used for linear cases, where the observer gain  $K_k$  is added to the parameters to be estimated.

$$\theta = \begin{bmatrix} \theta_f \\ \theta_K \end{bmatrix} \quad (8.4)$$

where  $\theta_f$  are the parameters that appear in  $f$  and  $\theta_K = \text{vec}(K_k)$  is a vector containing the observer gain parameters. By applying this approach, the optimization method used for solving (8.3) will find a time-invariant  $K_k$  that minimizes the cost function (8.2). The PO approach is attractive since the calculation of a time-varying  $K_k$  in (8.1) is general a fairly complicated problem, as is described in Ljung [1999] or as can be seen in the EKF and UKF approaches below.

**Extended Kalman Filter (EKF) approach:** The EKF is an extension of the Kalman filter [Kalman, 1960] to nonlinear systems. If the system would have been linear and all noise signals Gaussian distributed then the Kalman Filter would minimize the mean square error of the estimated states ( $\hat{x}_k$ ) giving optimal predictions. One of the first papers to discuss the ideas of the EKF is Smith et al. [1962]. The main idea is to compute  $K_k(\theta)$  at each time step using a linearized model based on a Taylor expansion. This linearization is performed by computing the partial derivatives of  $f$  with respect to  $x$  and  $u$  evaluated for  $\hat{x}_k$  and  $u_k$ , giving the matrices  $A_k(\theta)$  and  $B_k(\theta)$ , respectively. This gives the following gain recursion

$$\begin{aligned} S_k(\theta) &= [H(\theta) P_{k|k-1}^{xx}(\theta) H^T(\theta) + R] \\ K_k(\theta) &= P_{k|k-1}^{xx}(\theta) H^T(\theta) S_k^{-1}(\theta) \\ P_{k|k}^{xx}(\theta) &= (I - K_k(\theta) H(\theta)) P_{k|k-1}^{xx}(\theta) \\ P_{k|k-1}^{xx}(\theta) &= A_k(\theta) P_{k-1|k-1}^{xx}(\theta) A_k^T(\theta) + Q \end{aligned} \quad (8.5)$$

where the predicted covariance matrix  $P_{k|k}^{xx}(\theta)$  represents the uncertainty of the state prediction. A description of the EKF recursion is given in Appendix F.1 and a more detailed theory of the EKF can be found in Kailath et al. [2000].

**Unscented Kalman Filter (UKF) approach:** The EKF is sometimes said to have problems with highly nonlinear functions because only the predicted mean is propagated through the nonlinearity. An alternative is to use the Unscented

Kalman filter [Julier et al., 1995], which is another approximate method for propagating both the predicted mean and a representation of the covariance through the nonlinearity. This is done by using an unscented transformation where deterministically chosen points, sigma points, are used to represent both the mean and covariance. In this case, the gain recursion is

$$\begin{aligned} K_k(\theta) &= P_{k|k-1}^{xy}(\theta) (P_{k|k-1}^{yy}(\theta))^{-1} \\ P_{k|k}^{xx}(\theta) &= P_{k|k-1}^{xx}(\theta) - K_k(\theta) P_{k|k-1}^{yy}(\theta) K_k^T(\theta) \end{aligned} \quad (8.6)$$

where the covariance matrices  $P_{k|k-1}^{yy}(\theta)$ ,  $P_{k|k-1}^{xx}(\theta)$  and  $P_{k|k-1}^{xy}(\theta)$  are calculated using the sigma points. The full UKF recursion is given in Appendix F.2.

**Tuning parameters:** Unlike the PO approach, the two Kalman filter approaches include tuning parameters that have to be set by the user. This is undesirable since some prior knowledge of how to set these parameters is required leading to a subjective part of the identification. The parameters are the covariance  $Q$  of the process noise, the covariance  $R$  of the measurement noise and the initial state covariance  $P_0$ . The matrices  $Q$  and  $R$  work in pairs so when  $Q$  is larger than  $R$  the method relies more on the measurements. For the linear case the choice of the initial state covariance  $P_0$  is not critical because the convergence properties are well understood and it is not difficult to get the filter to converge. There is no general proof of a similar property for the nonlinear case. Here, one can only hope that the filter will converge. For the application presented in this thesis,  $P_0$  is chosen as the identity matrix. It is possible to use cross-validation to estimate the tuning parameters. For this a dataset that has not been used during the parameter estimation has to be used.

Other subjective inputs that apply to all PEM approaches are the initial values of the states  $x_0$  and parameters  $\theta_0$ . It is possible to make an estimation of  $x_0$ , but in our case one can use the initial measurements  $y_0$  which should not be too far from the true value. This can be done since it is assumed that all states are measured. The initial parameter vector  $\theta_0$  is an initialization of the PEM optimization routine and will affect how good the initial estimates using the different approaches are.

### 8.1.2 State estimation method

The fourth method includes the unknown parameters as additional states, which are estimated together with the real states.

**Augmented state (AUG) approach:** This approach is commonly used in the navigation community when treating uncertain parameters. These parameters are added to the model as static states, i.e., states that do not vary with time. The augmented state vector can be written as

$$\bar{x}_k = \begin{bmatrix} x_k \\ \theta_k \end{bmatrix}. \quad (8.7)$$

This gives rise to the following augmented state-space equation that should be used instead of (7.3)

$$\begin{aligned}\bar{x}_{k+1} &= \begin{bmatrix} x_{k+1} \\ \theta_{k+1} \end{bmatrix} = \begin{bmatrix} f(x_k, u_k; \theta_k) + w_k \\ \theta_k + w_{\theta,k} \end{bmatrix} \\ y_k &= \bar{H} \bar{x}_k + v_k\end{aligned}\quad (8.8)$$

where  $w_{\theta,k}$  is a zero mean artificial noise term with a covariance matrix that can be used to tune the estimator and  $\bar{H} = [H \ 0_{1 \times n_p}]$ . Here, the same method to estimate the observer gain  $K_k(\theta)$  as in the EKF approach is used, but for the model (8.8) instead of (7.3). The theory for this approach can be found in Simon [2006], Haessig and Friedland [1997] and Rangegowda et al. [2018]. For this approach the augmented system is filtered only once and the parameter estimate is then taken from the last estimate of  $\bar{x}$ .

**Tuning parameters:** Since the EKF is used, the same tuning strategy for  $Q$  and  $R$  as described earlier applies. The same goes for  $x_0$  and  $P_0$ . The covariance of the artificial noise term  $w_{\theta,k}$  can, as mentioned above, also be used as a tuning parameter. This adds to the user's burden when trying to solve the identification problem.

### 8.1.3 Parameter and state optimization method

The fifth method differs from the previous four in the way that it does not depend on prediction of the system at all. Therefore the system instability is not an issue.

**Constrained Levenberg-Marquardt (CLM) approach:** This approach uses a Levenberg-Marquardt optimization procedure of a Lagrangian function. Instead of augmenting the states  $x_k$  with the unknown parameters, as in the AUG approach, the unknown parameter vector  $\theta$  is augmented with all time samples of the state vector

$$\vartheta = [x_0^T \ \dots \ x_{N-1}^T \ \theta^T]^T. \quad (8.9)$$

The scalar cost function is then given by

$$V_N(\vartheta, Z^N) = \frac{1}{N} \sum_{k=1}^N \frac{1}{2} \varepsilon_k(\vartheta)^T \varepsilon_k(\vartheta) \quad (8.10)$$

and the estimate of  $\vartheta$  is found by solving the constrained optimization problem

$$\begin{aligned}\underset{\vartheta}{\text{minimize}} \quad & V_N(\vartheta, Z^N) \\ \text{subject to} \quad & F(\vartheta) = 0\end{aligned}\quad (8.11)$$

where

$$F(\vartheta) = \begin{bmatrix} f(x_0, u_0; \theta) - x_1 \\ f(x_1, u_1; \theta) - x_2 \\ \vdots \\ f(x_{N-1}, u_{N-1}; \theta) - x_N \end{bmatrix} \quad (8.12)$$

which comes from using the motion model in (7.3).

The constrained optimization problem can be formulated as iteratively solving the linear system [Nocedal and Wright, 2006]

$$\begin{bmatrix} J_1^T J_1 + \lambda_{LM}^2 I_{n_\vartheta, n_\vartheta} & J_2^T \\ J_2 & 0 \end{bmatrix} \begin{bmatrix} \delta\vartheta \\ \lambda \end{bmatrix} = \begin{bmatrix} -J_1^T \epsilon \\ -F \end{bmatrix} \quad (8.13)$$

where  $\epsilon = [\epsilon_1(\vartheta)^T \ \epsilon_2(\vartheta)^T \ \dots \ \epsilon_N(\vartheta)^T]^T$  and

$$J_1 = \frac{\partial \epsilon}{\partial \vartheta}, \quad J_2 = \frac{\partial F}{\partial \vartheta} \quad (8.14)$$

Here, the vector  $\delta\vartheta$  contains additive increments to the augmented parameter vector (8.9) and  $\lambda$  is a vector containing the Lagrangian multipliers.

A drawback with this method is that the Karush-Kuhn-Tucker matrix, containing  $J_1$  and  $J_2$ , in (8.13) to be inverted grows with the number of time samples used. This matrix is however sparse so efficient inversion methods can be used. Another problem with this method is that the constraint (8.12) cannot deal with process noise. Therefore, there is no noise model for this and if process noise is present in the signals a bias is likely to occur in the solution. The CLM method is described in Mulders et al. [2010].

**Tuning parameter:** Also this method has a tuning parameter, the Levenberg-Marquardt regularization parameter  $\lambda_{LM}$ . This is used to improve the rank properties of the KKT matrix and it thus affects the possibility to solve the system. This parameter has to be chosen carefully.

## 8.2 Estimation on simulated data

In this section, the five different methods will be analyzed based on simulated data. For this a Simulink<sup>®</sup> model has been developed as a benchmark problem. This model is based on the present aerodynamic model for JAS 39 Gripen. The simulations feature pitch maneuvers, with two degrees of freedom only. The variables used in the simulations are given in Figure 8.1. The definitions of these can be found in Chapter 3.

A simplification has been made in that the implemented control law moves the leading edge flap in full correlation with the angle-of-attack. Therefore the leading edge parameters have been incorporated into the angle-of-attack parameters. Furthermore, it is assumed that only the pitch stability, i.e., the pitching moment as a function of the angle-of-attack, is nonlinear and that all other relations are linear. In addition to this all states are measured. This is true for the JAS 39 Gripen aircraft used in this example, but might not be true for other aircraft.

This gives the following simplified continuous-time system

$$\begin{aligned}\dot{x}(t) &= a(x(t)) + Bu(t) + w(t) \\ y(t) &= x(t) + e(t)\end{aligned}\quad (8.15)$$

Here, the state and input vectors are  $x(t) = [\alpha(t) \ q(t)]^T$  and  $u(t) = [\delta_e(t) \ \delta_c(t)]^T$  respectively,  $e(t)$  is white noise and the system matrices are given as

$$\begin{aligned}a(x(t)) &= \begin{bmatrix} Z_\alpha \alpha(t) + Z_q q(t) \\ f(\alpha(t)) + M_q q(t) \end{bmatrix} \\ B &= \begin{bmatrix} Z_{\delta_e} & Z_{\delta_c} \\ M_{\delta_e} & M_{\delta_c} \end{bmatrix}\end{aligned}\quad (8.16)$$

which makes (8.15) a nonlinear version of the model (5.44) used in Chapter 5. Note that  $Z = -N$  as defined in Figure 8.1. The  $Z$ s and  $M$ s are scaled aerodynamic forces and moments. The scaling includes data from several parts. These are the used speed-altitude envelop point in the form of the speed  $V$  and dynamic pressure  $q_a$ , the mass-inertia properties  $m$  and  $I_{yy}$  and also the geometrical reference wing area  $S$  and mean aerodynamic chord  $\bar{c}$ .

The nonlinear function  $f(\alpha(t))$  is built up as a piecewise affine function, similarly to the structure of the present aerodynamic model for JAS 39 Gripen, with break-points positioned at  $\alpha_i = \alpha_{min}, \alpha_{min} + \Delta\alpha, \dots, \alpha_{max}$ . In general the piecewise function for  $\alpha_i < \alpha(t) < \alpha_{i+1}$  looks like

$$f(\alpha(t)) = \frac{f(\alpha_{i+1}) - f(\alpha_i)}{\alpha_{i+1} - \alpha_i} \cdot (\alpha(t) - \alpha_i) + f(\alpha_i) \quad (8.17)$$

An example of a piecewise affine function with  $\alpha_{min} = 5$  and  $\alpha_{max} = 11$  is shown in Figure 8.2. A value of  $\Delta\alpha = 1^\circ$  is used in the example as well as in implementation. In general, this choice has to reflect the problem to be solved and it could very well change in different parts of the angle-of-attack envelop. The current value has been chosen for simplicity.

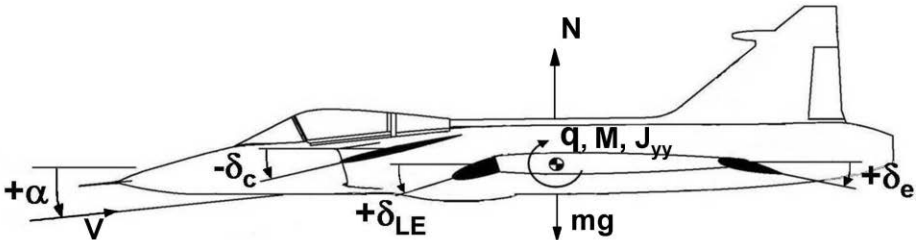


Figure 8.1: Variables used in simulation.

All  $Z_s$ ,  $M_s$  and break-points in  $f(\alpha_i)$  in (8.16) are put into the parameter vector. For the simulation model, there are 18 break-points from  $\alpha = -1^\circ$  to  $16^\circ$ . All the true parameters used to generate the simulated data are given in Table 8.1.

**Table 8.1:** True continuous-time model parameters.

$Z_\alpha$	$Z_q$	$M_q$	$Z_{\delta_e}$	$Z_{\delta_c}$	$M_{\delta_e}$	$M_{\delta_c}$
-0.9759	1.1740	-1.2616	0.3043	0.0289	-31.0898	8.2557
$f(-1^\circ)$	$f(0^\circ)$	$f(1^\circ)$	$f(2^\circ)$	$f(3^\circ)$	$f(4^\circ)$	$f(5^\circ)$
-0.2923	-0.2577	-0.2221	-0.1787	-0.1294	-0.0837	-0.0695
$f(6^\circ)$	$f(7^\circ)$	$f(8^\circ)$	$f(9^\circ)$	$f(10^\circ)$	$f(11^\circ)$	$f(12^\circ)$
-0.0645	-0.0798	0.0102	0.1833	0.3731	0.5011	0.6187
$f(13^\circ)$	$f(14^\circ)$	$f(15^\circ)$	$f(16^\circ)$			
0.7343	0.8076	0.8540	0.9133			

To generate data, a simple linear quadratic (LQ) regulator for a servo problem has been implemented in the simulation model. This will take care of the fact that the system is unstable for pitch motions. An algorithm in Skogestad and Postlethwaite [2005] has been used for the LQ design. The regulator is given by

$$\begin{aligned} \dot{\xi}(t) &= r(t) - Fy(t) \\ u(t) &= -K_r \begin{bmatrix} \xi(t) \\ y(t) \end{bmatrix} \end{aligned} \quad (8.18)$$

where  $r(t) = \alpha_{ref}(t)$ ,  $F = \begin{bmatrix} 1 & 0 \end{bmatrix}$  and  $K_r = \begin{bmatrix} -0.2339 & 0.1575 & 0.0483 \\ 0.9723 & -0.7610 & -0.0643 \end{bmatrix}$ .

A block diagram of the benchmark system is shown in Figure 8.3.

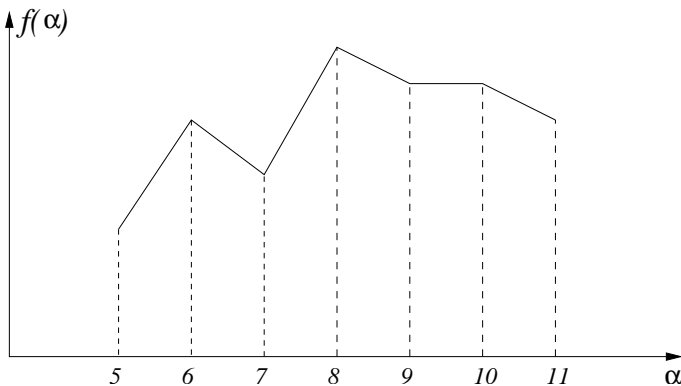


**Figure 8.2:** Example of a piecewise affine function with  $\alpha_{min} = 5^\circ$  and  $\alpha_{max} = 11^\circ$ .

The parameter estimation is done on sampled data and therefore the model is described in discrete time using Euler's method for the time derivatives. Thus, the total parameterized model is given by

$$\begin{aligned} \begin{bmatrix} \alpha_{k+1} \\ q_{k+1} \end{bmatrix} &= \begin{bmatrix} \theta_1 \alpha_k + \theta_2 q_k \\ f(\theta_8, \dots, \theta_{25}, \alpha_k) + \theta_3 q_k \end{bmatrix} + \begin{bmatrix} \theta_4 & \theta_5 \\ \theta_6 & \theta_7 \end{bmatrix} \begin{bmatrix} \delta_{ek} \\ \delta_{ck} \end{bmatrix} \\ \begin{bmatrix} \alpha_{k,m} \\ q_{k,m} \end{bmatrix} &= \begin{bmatrix} \alpha_k \\ q_k \end{bmatrix} \end{aligned} \quad (8.19)$$

where the index  $m$  separates the measurements from the states.

Investigations of sensitivity to measurement noise, biased initial parameters ( $\theta_0$ ) and process noise have been made. The first test of the methods is to run them on noise-free data with the true parameters as initial parameters. This is done to see if there are some basic deficiencies in the methods.

**Noise-free simulation:** The data used for estimation is based on a maneuver that starts from zero and is set to reach a reference angle-of-attack  $r = 15^\circ$ . To check how good an estimated model is, a validation has to be run on a separate dataset. This is based on a different maneuver which starts off like the one used for estimation but after one second changes to try to reach a reference angle-of-attack  $r = 3^\circ$ , so that the maneuver is exposed to the nonlinearity twice. Example data for estimation and validation is shown in Figure 8.4.

The true parameters of the discrete-time formulation, used as initial values for the estimation, can be seen as a black line in Figure 8.5 and as the left-most column in Table 8.2. The estimates using the different methods can also be seen in this figure and table. Since the PO method is the subject for comparison this is given in all sub-figures. All methods give estimates that are close to the true

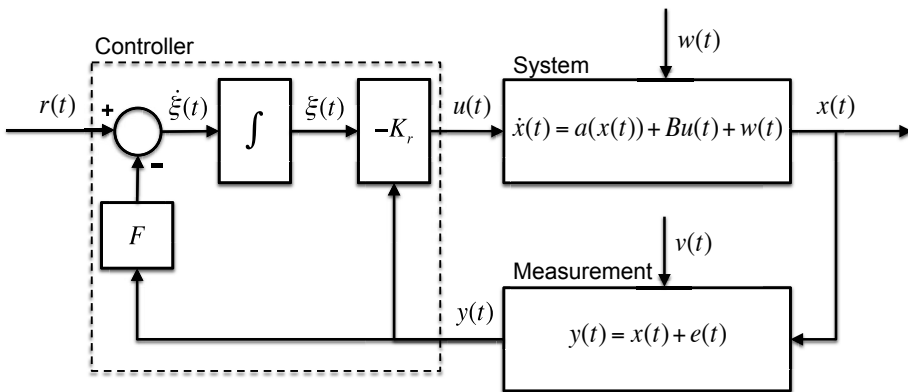
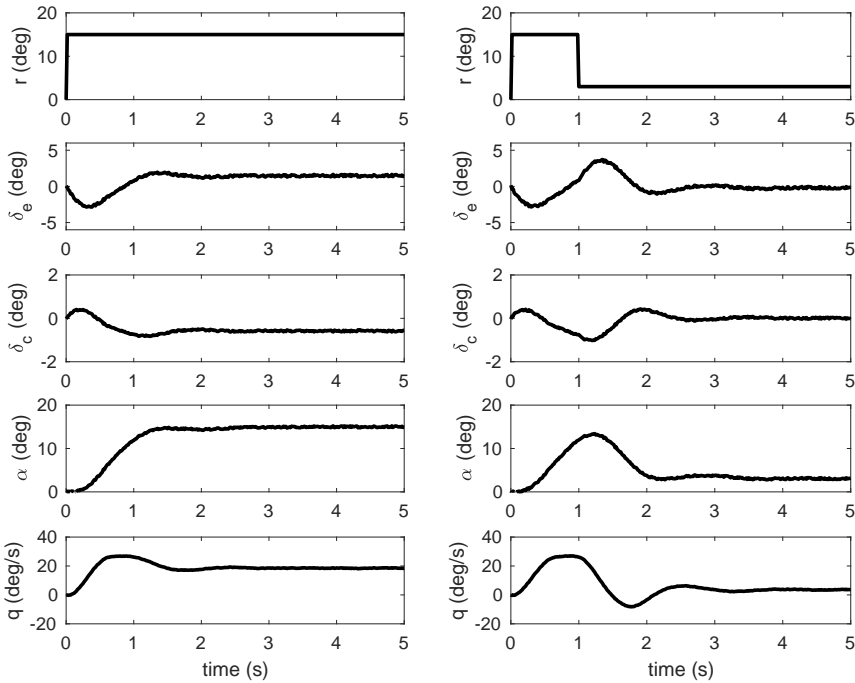


Figure 8.3: Block diagram for the benchmark system.





**Figure 8.4:** Example of simulations with measurement noise. Estimation data is shown to the left and validation data to the right. At the top is the reference signal. Below this, the two inputs elevator and canard deflection are shown. The two bottom figures give the two outputs, angle-of-attack and pitch angular velocity respectively.

parameters. There is a slight bias at the lower end of the angle-of-attack for the nonlinearity. This is most probably due to the low number of samples in this part of the envelope. The outcome of the validation can be seen in Figure 8.6. The conclusion is that all methods give usable model estimates for this noise-free case.

**Measurement noise simulation:** To investigate the noise sensitivity, 100 Monte-Carlo (MC) runs have been made with five different signal-to-noise ratios (SNRs), ( $10^k$ ,  $k = 7, 6, 5, 4, 3$ ). The test case SNR  $10^4$  represents the lowest SNR expected in real flight test data for this type of maneuver. Real flight test data will be run through a post-processing procedure, which will increase the SNR further and thereby improving the possibility to make more accurate estimations. The setting  $10^3$  has been used to get a test of a lower SNR, which can be relevant for other types of maneuvers or other applications.

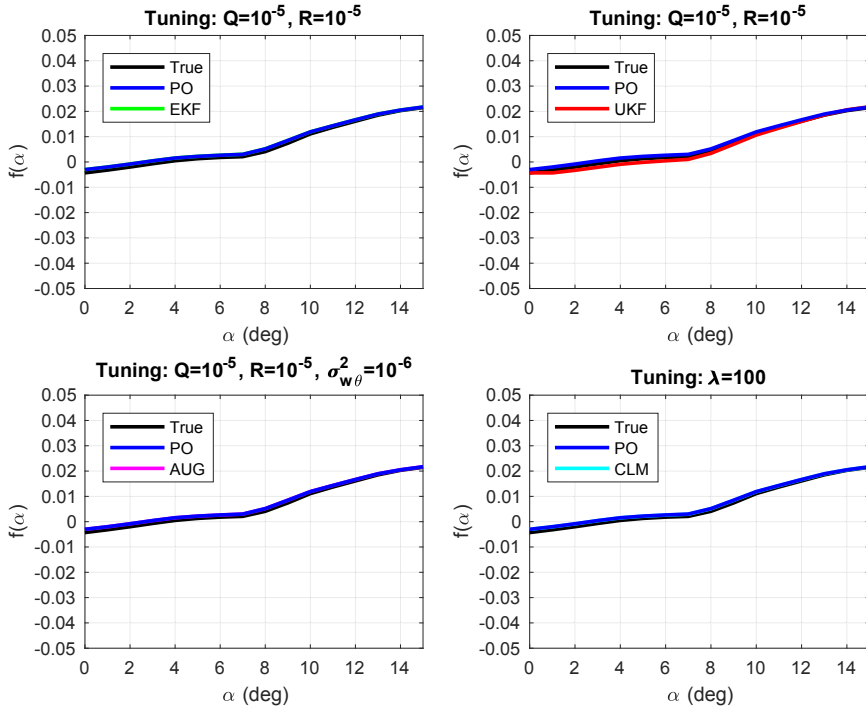


**Figure 8.5:** True and estimated nonlinear model parameters for the noise-free case.

**Table 8.2:** True and estimated linear model parameters for the noise-free case.

	True	PO	EKF	UKF	AUG	CLM
$Z_\alpha$	0.9804	0.9813	0.9813	0.9814	0.9813	0.9813
$Z_q$	0.0163	0.0159	0.0159	0.0159	0.0159	0.0159
$M_q$	0.9790	0.9769	0.9767	0.9897	0.9769	0.9770
$Z_{\delta_e}$	-0.0051	-0.0084	-0.0085	-0.0085	-0.0085	-0.0084
$Z_{\delta_c}$	-0.0005	0.0013	0.0014	0.0014	0.0013	0.0013
$M_{\delta_e}$	-0.5182	-0.5010	-0.5009	-0.5368	-0.5013	-0.5014
$M_{\delta_c}$	0.1376	0.1335	0.1335	0.1423	0.1336	0.1336

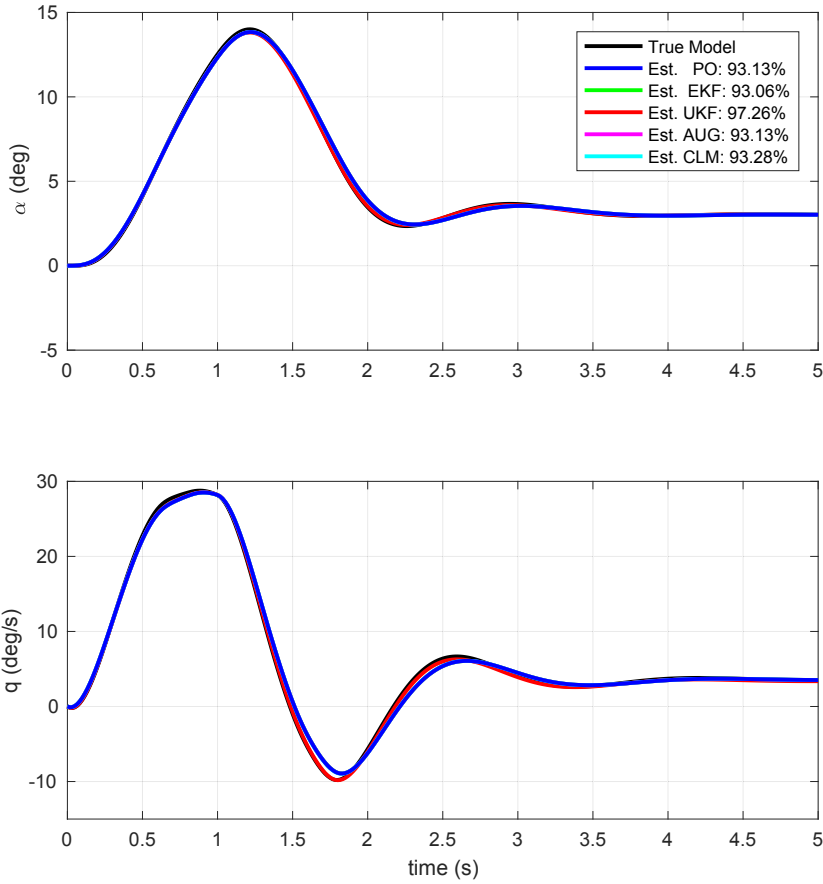


**Figure 8.6:** Simulated and true angle-of-attack and pitch angular velocity for noise-free validation data.

Different tuning parameter settings have been investigated. This has been done since the tuning is often done by the user. The tuning parameters for the EKF and UKF methods are  $R = 10^{-k}I_2$  for  $k = 1, 3, 5, 7, 9$  and  $Q = 10^{-5}I_2$  has been kept fixed. These settings have also been used for the EKF part in the AUG method. The tuning of the artificial noise variance  $\sigma_{w\theta}^2 = 10^{-k}$  for  $k = 1, 3, 5, 7, 9$  has been investigated. For the regularization tuning of the CLM method,  $\lambda_m = 10^k$  for  $k = -2, -1, 0, 1, 2$  have been used. The PO method has no tuning parameters as stated previously. In the results only the best tuning parameter settings are shown. The results for other settings can be found in Appendix G. It should also be noted that the estimated models are based on the mean of the MC simulations.

The results for SNR  $10^7$  to  $10^5$  do not differ much in appearance from the noise-free case when using the best tuning parameters. These results have been put in Appendix G. For SNR  $10^4$  the estimates are given in Figure 8.7 and Table 8.3. All methods are affected by the noise, but the PO, EKF and CLM methods still seem to give acceptable results. Both the AUG and the UKF methods do not predict the nonlinearity correctly. Also, the uncertainty of two standard deviations, given as dashed lines in the figure, are much wider for these two methods.

The result for the validation is shown in Figure 8.8. It is clear that all methods except the UKF method follow the true data well. This can also be seen in the model fit values given in the figure. The AUG method is doing well in the validation even though the nonlinearity is incorrect. This is probably due to the fact that the error in the nonlinearity is mostly a bias, i.e., the slope of the curve is similar to the correct slope. Also, the linear part of the AUG model seems to be reasonable. It is also worth mentioning that the sign of  $Z_{\delta_c}$  is wrong for the AUG method, but this does not seem to affect the result much.

The estimates for SNR  $10^3$  are shown in Figure 8.9 and Table 8.4. The UKF estimate is even worse than for SNR  $10^4$ . As can be seen, the linear part is wrong and the nonlinearity is not correctly estimated above  $\alpha = 4^\circ$ . The AUG method seems to make a correct estimation in contrast to earlier, but the CLM method has now some problems with the nonlinearity.

The validation shown in Figure 8.10 clearly supports the estimation results. The model fit for the UKF method is now down to 18.60%. The rest of the methods show a good model fit. It is hard to see the problem with the nonlinearity in the validation result for the CLM method.

In conclusion, the PO and EKF methods seem to be most robust against measurement noise. The AUG method has a small bias for the whole angle-of-attack range, and the other two methods have problems describing the nonlinearity correctly.

**Initial parameter offset:** It is unlikely that the initial guess of the parameters will be the exact truth, even if a lot of work has been done prior to the estimation. To investigate how the proposed methods are affected, a random initial offset of up to 10% of the linear terms and of the bias and slope of the nonlinearity have been investigated. The values are given in Figure 8.11 and Table 8.5. The noise setting SNR  $10^4$  has been chosen as a reference case.

The estimates for initial offsets  $\theta_{0,1} - \theta_{0,3}$  are shown in Figure 8.12 - 8.14 and Table 8.7 - 8.9, respectively. For these three cases the PO and EKF methods seem to be most robust. Depending on the case and tuning, the AUG and CLM methods can give accurate or inaccurate results. The UKF method does not give any accurate results at all. If this is due to the chosen SNR of  $10^4$  or the tuning setting or both is hard to say. For initial offsets  $\theta_{0,2}$  the result is similar to the result in the

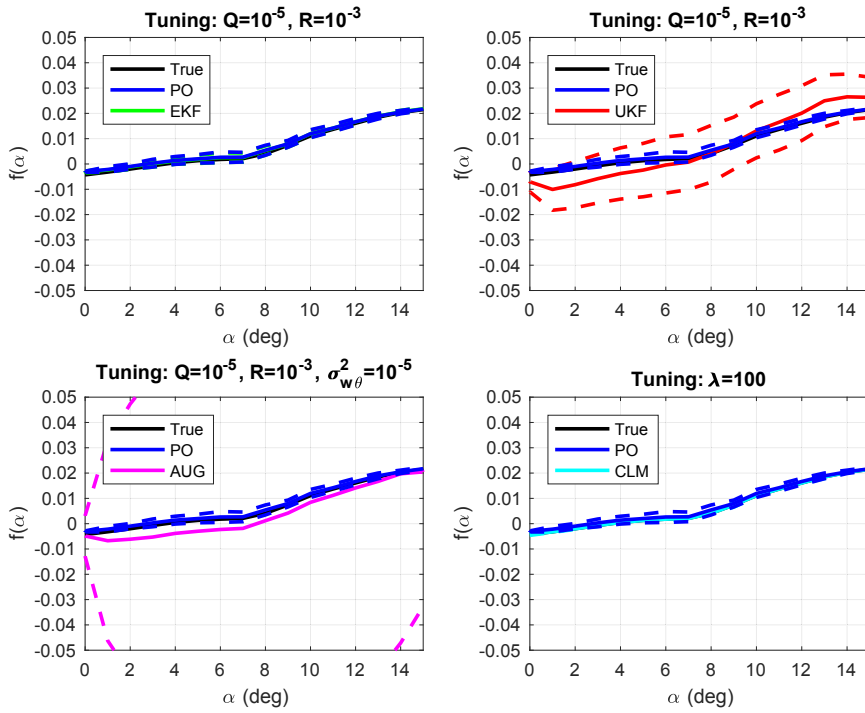


**Figure 8.7:** Estimated and true pitching moment for noisy data with SNR  $10^4$ .

**Table 8.3:** Estimated and true aerodynamic derivatives for noisy data with SNR  $10^4$ .

	True	PO	EKF	UKF	AUG	CLM
$Z_\alpha$	0.9804	0.9813	0.9828	0.9882	0.9796	0.9804
$Z_q$	0.0163	0.0159	0.0140	0.0127	0.0169	0.0163
$M_q$	0.9790	0.9767	0.9758	0.9758	0.9849	0.9771
$Z_{\delta_e}$	-0.0051	-0.0085	-0.0225	-0.0371	-0.0083	-0.0051
$Z_{\delta_c}$	-0.0005	0.0000	-0.0564	0.0006	0.0025	-0.0005
$M_{\delta_e}$	-0.5182	-0.5033	-0.5112	-0.6546	-0.5631	-0.5182
$M_{\delta_c}$	0.1376	0.1333	0.1131	0.1957	0.1511	0.1376

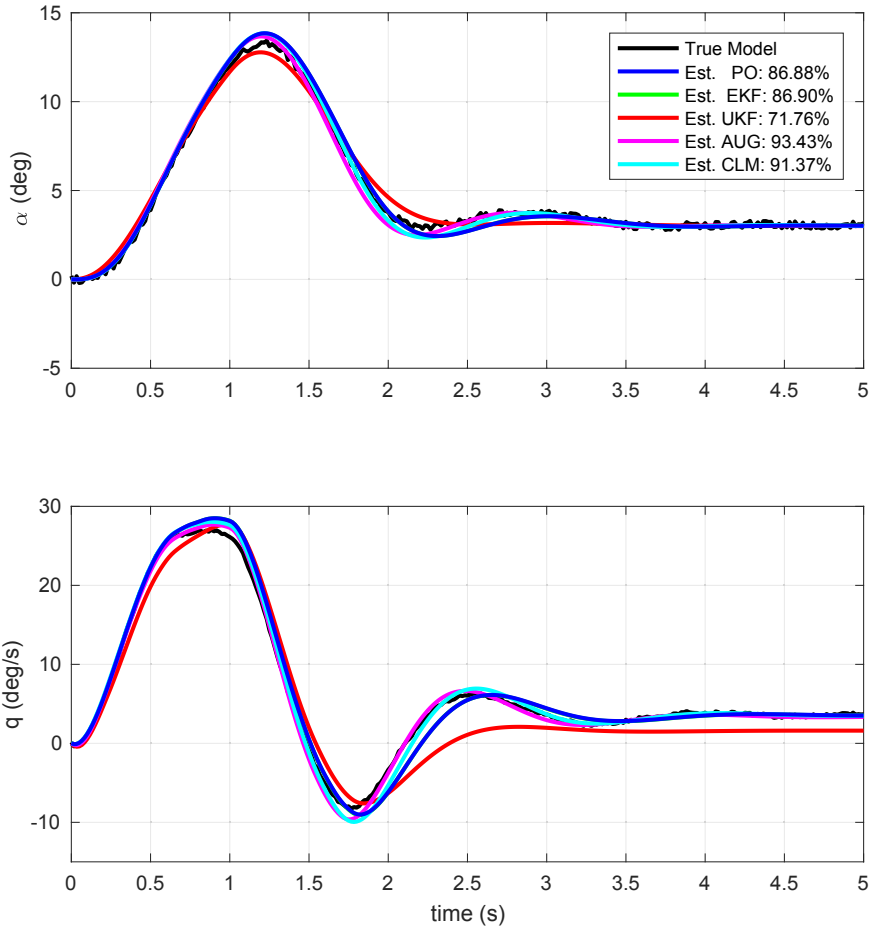


**Figure 8.8:** Simulated and true angle-of-attack and pitch angular velocity for noisy validation data with  $\text{SNR } 10^4$ .

measurement noise study shown in Figure 8.7. The tuning settings are the same for these two cases. Estimates with initial offsets  $\theta_{0,1}$  and  $\theta_{0,3}$  show similar results and also have the same tuning parameters, but different from initial offsets  $\theta_{0,2}$ . There is no additional information for  $\theta_{0,4}$  and  $\theta_{0,5}$ . They have therefore been put in Appendix G.

In conclusion, the above results show once more that the tuning can play a critical role for the resulting model estimates. This is also shown in Table 8.6 where the worst and best tuning settings for the different offsets are given. Even the EKF method is of course affected if wrongly tuned.

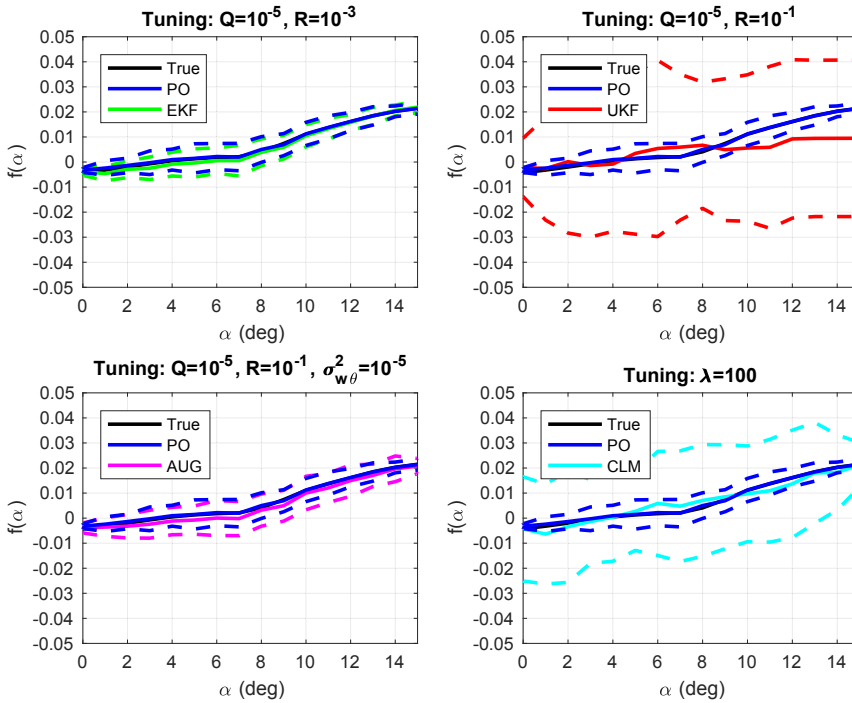


**Figure 8.9:** Estimated and true pitching moment for noisy data with SNR  $10^3$ .

**Table 8.4:** Estimated and true aerodynamic derivatives for noisy data with SNR  $10^3$ .

	True	PO	EKF	UKF	AUG	CLM
$Z_\alpha$	0.9804	0.9815	0.9852	1.0179	0.9808	0.9806
$Z_q$	0.0163	0.0158	0.0111	-0.0002	0.0162	0.0166
$M_q$	0.9790	0.9783	0.9779	1.0490	0.9818	0.9681
$Z_{\delta_e}$	-0.0051	-0.0086	-0.0441	-0.1525	-0.0079	-0.0060
$Z_{\delta_c}$	-0.0005	0.0037	0.1425	0.0511	0.0008	0.0008
$M_{\delta_e}$	-0.5182	-0.5050	-0.5545	0.0309	-0.5243	-0.5159
$M_{\delta_c}$	0.1376	0.1369	0.0447	2.6781	0.1385	0.1369

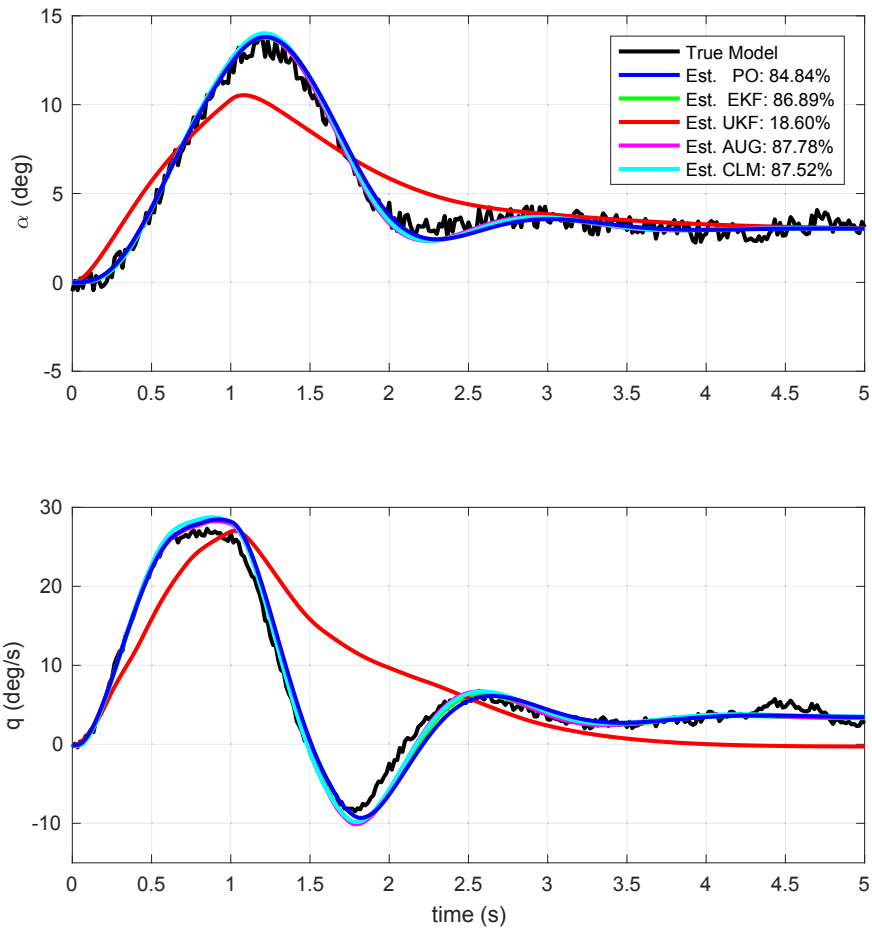


**Figure 8.10:** Simulated and true angle-of-attack and pitch angular velocity for noisy validation data with  $SNR 10^3$ .



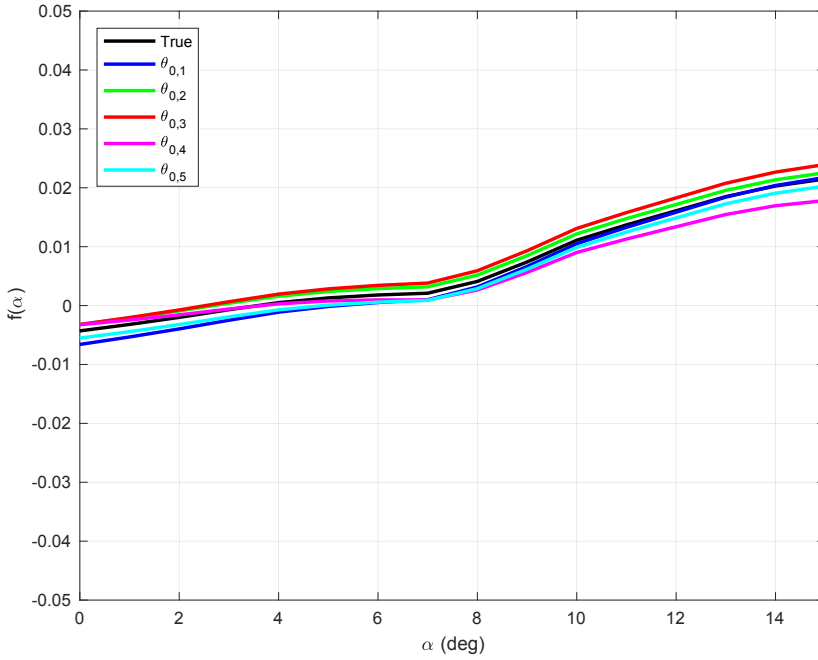


**Figure 8.11:** True pitching moment and initial offset in  $\theta_0$ .

**Table 8.5:** True aerodynamic derivatives and initial offset in  $\theta_0$ .

	True	$\theta_{0,1}$	$\theta_{0,2}$	$\theta_{0,3}$	$\theta_{0,4}$	$\theta_{0,5}$
$Z_\alpha$	0.9804	0.9824	0.9797	0.9821	0.9787	0.9819
$Z_q$	0.0163	0.0179	0.0151	0.0172	0.0160	0.0155
$M_q$	0.9790	0.9811	0.9753	0.9834	0.9815	0.9778
$Z_{\delta_e}$	-0.0051	-0.0046	-0.0052	-0.0055	-0.0051	-0.0052
$Z_{\delta_c}$	-0.0005	-0.0004	-0.0005	-0.0004	-0.0005	-0.0005
$M_{\delta_e}$	-0.5182	-0.4664	-0.5728	-0.4520	-0.4555	-0.5734
$M_{\delta_c}$	0.1376	0.1238	0.1657	0.1520	0.1460	0.1539

**Table 8.6:** Model fit for initial offset in  $\theta_0$ . A reference value for SNR  $10^4$  with no initial model offset is given and compared to the worst and best tuning for the estimates with initial offset for the investigated cases.

Method	SNR $10^4$	Model Fit lower	Model Fit upper
PO	86.88%	86.50%	86.84%
EKF	86.90%	59.42%	87.31%
UKF	71.76%	68.96%	88.74%
AUG	93.43%	< 0%	95.55%
CLM	91.37%	76.36%	87.32%

**Process noise simulation:** For the study of how process noise affects the estimations, only the PO and EKF methods are compared. This is due to the fact that the results from the measurement noise analysis show that the performance of the UKF method is uncertain depending on noise characteristics and tuning parameter settings. The CLM approach uses a constraint that is based on the dynamic equation  $x_{k+1} = f(x_k, u_k; \theta)$ . This does not take care of process noise. If process noise is present there will likely be a bias in the estimates. The AUG method is discarded since it is more complex and computationally heavy than the EKF approach.

To be able to investigate the properties of the two methods, 100 Monte Carlo (MC) simulations have been generated. One realization of the estimation data is shown in Figure 8.15 together with a validation data set. A slightly different type of maneuver has been used for the validation. It should be noted that more excitation is needed when process noise is present compared to the earlier case with only measurement noise. The differences can be seen when comparing Figure 8.15 with Figure 8.4.

For the new excitation, the reference controls the angle-of-attack, which is fairly smooth. The input and pitch angular velocity on the other hand are more affected by the noise, which corresponds to atmospheric turbulence. Different tuning settings for the EKF method have been investigated to see the effect they have on the estimation accuracy.  $R$  has been changed between  $R = 10^{-1}$  and  $R = 10^{-9}$  while  $Q = 10^{-5}$  has been kept constant. As can be seen in Figure 8.16 and Table 8.10 the PO approach gives estimates close to the true system for the case studied. The EKF approach on the other hand seems to find a minimum away from the true system. The estimated models are validated using the validation data sets. The result can be seen in Figures 8.17 - 8.19. Even though the PO method gives the better estimates, the differences between the two methods are not so significant as one could expect from the model estimates. This can also be seen in Table 8.11.

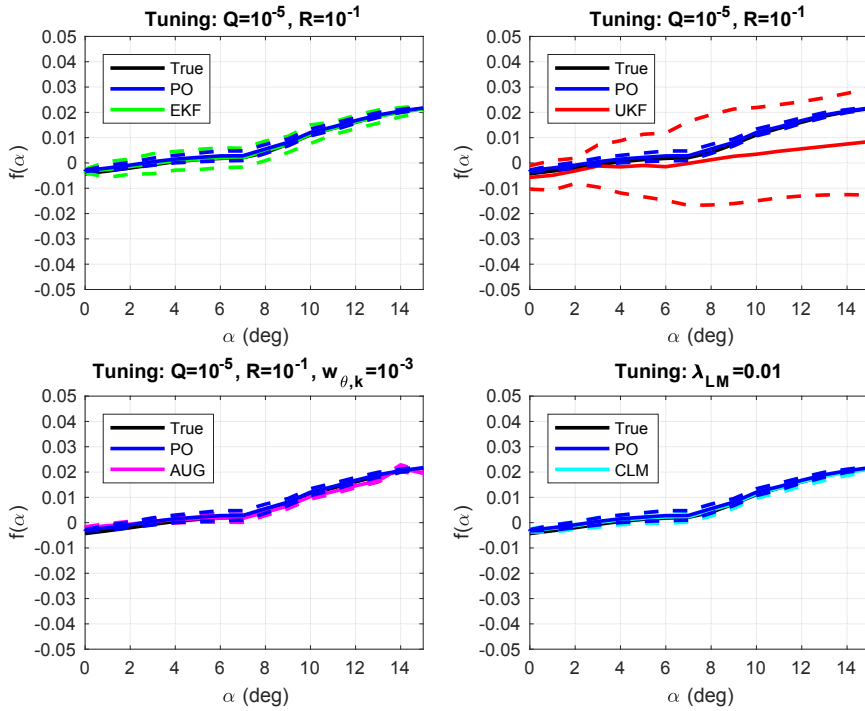


**Figure 8.12:** Estimated and true pitching moment for initial offset in  $\theta_{0,1}$ .

**Table 8.7:** Estimated and true aerodynamic derivatives for the initial offset in  $\theta_{0,1}$ .

	True	PO	EKF	UKF	AUG	CLM
$N_\alpha$	0.9804	0.9813	0.9740	0.9652	0.9801	0.9787
$N_q$	0.0163	0.0158	0.0251	0.0330	0.0168	0.0193
$M_q$	0.9790	0.9768	0.9792	1.0133	0.9812	0.9803
$N_{\delta_e}$	-0.0051	-0.0086	0.0594	0.0719	-0.0087	0.0163
$N_{\delta_c}$	-0.0005	-0.0000	0.2797	0.3565	0.0005	0.1038
$M_{\delta_e}$	-0.5182	-0.5013	-0.4981	-0.2849	-0.4718	-0.4821
$M_{\delta_c}$	0.1376	0.1324	0.1759	0.6742	0.1251	0.2262

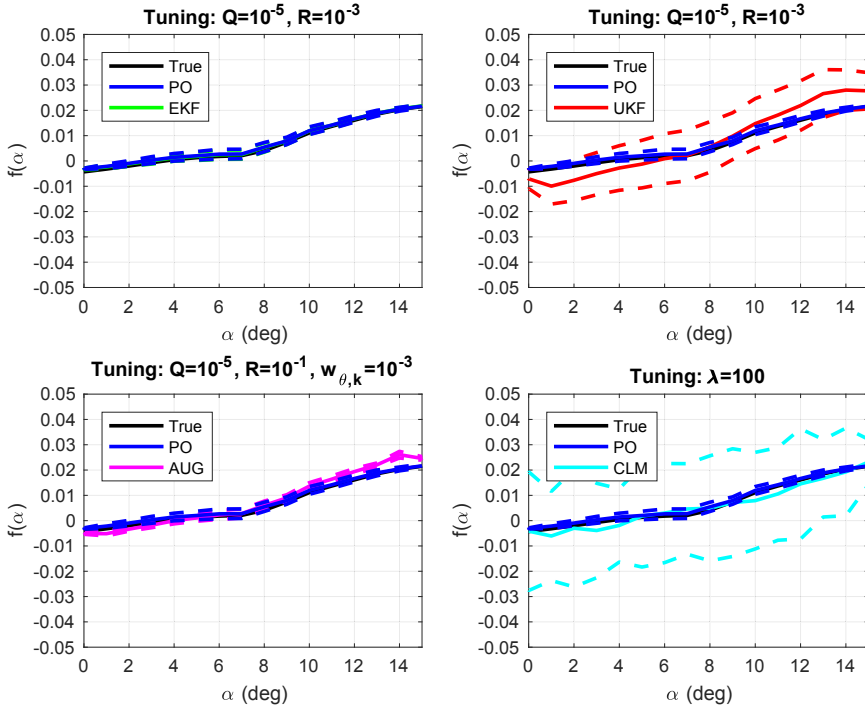


**Figure 8.13:** Estimated and true pitching moment for initial offset in  $\theta_{0,2}$ .

**Table 8.8:** Estimated and true aerodynamic derivatives for the initial offset in  $\theta_{0,2}$ .

	True	PO	EKF	UKF	AUG	CLM
$N_\alpha$	0.9804	0.9813	0.9827	0.9882	0.9798	0.9805
$N_q$	0.0163	0.0158	0.0142	0.0127	0.0171	0.0166
$M_q$	0.9790	0.9774	0.9770	0.9724	0.9749	0.9687
$N_{\delta_e}$	-0.0051	-0.0086	-0.0211	-0.0363	-0.0086	-0.0060
$N_{\delta_c}$	-0.0005	-0.0008	-0.0505	0.0027	0.0003	0.0006
$M_{\delta_e}$	-0.5182	-0.5001	-0.5090	-0.6631	-0.5709	-0.5612
$M_{\delta_c}$	0.1376	0.1465	0.1216	0.2021	0.1653	0.1622

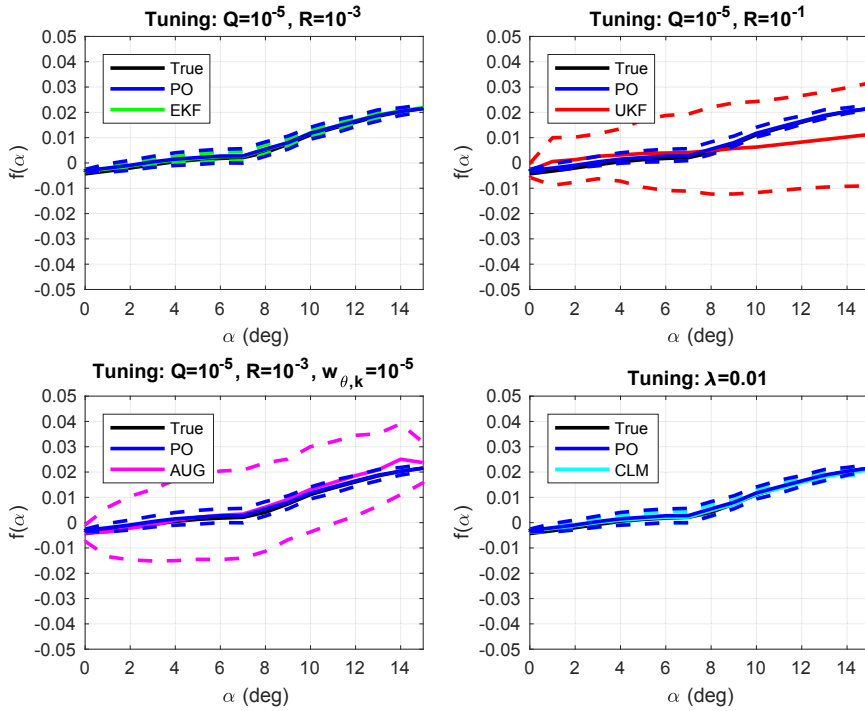
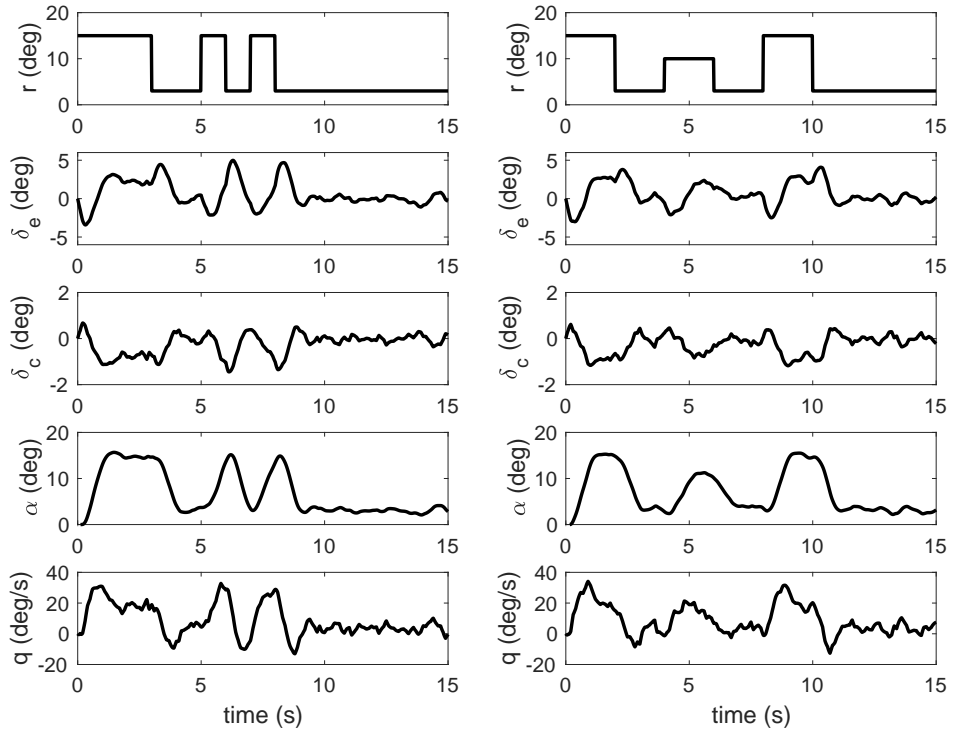


Figure 8.14: Estimated and true pitching moment for initial offset in  $\theta_{0,3}$ .

Table 8.9: Estimated and true aerodynamic derivatives for the initial offset in  $\theta_{0,3}$ .

	True	PO	EKF	UKF	AUG	CLM
$N_\alpha$	0.9804	0.9814	0.9840	0.9622	0.9794	0.9783
$N_q$	0.0163	0.0158	0.0124	0.0363	0.0175	0.0198
$M_q$	0.9790	0.9774	0.9766	1.0058	0.9758	0.9814
$N_{\delta_e}$	-0.0051	-0.0088	-0.0338	0.1094	-0.0070	0.0200
$N_{\delta_c}$	-0.0005	-0.0007	-0.1035	0.4656	0.0085	0.1192
$M_{\delta_e}$	-0.5182	-0.4977	-0.5121	-0.2075	-0.5369	-0.4746
$M_{\delta_c}$	0.1376	0.1441	0.1090	0.8361	0.1597	0.2580



**Figure 8.15:** Example of simulations with process noise, estimation data to the left and validation data to the right. At the top is the reference signal. Below this, the two inputs elevator and canard deflection are shown. The two bottom figures gives the outputs angle-of-attack and pitch angular velocity respectively.

One possible explanation can be the feedback system. This can also be seen when analyzing how close the different signals from the estimated models are to the validation data using the model fit formula for the separate signals

$$F_v(m, Z) = 100 \left( 1 - \frac{\|s_i - \hat{s}_i\|_2}{\|s_i - \bar{s}_i\|_2} \right). \quad (8.20)$$

Here  $s_i$ ,  $i \in [\delta_e, \delta_c, \alpha, q]$  is the validation input or output signal and  $\bar{s}_i$  is the mean of this signal. Furthermore,  $\hat{s}_i$  is the predicted signal from the model  $m$ . The result from this analysis is shown in Table 8.12. The table shows that the EKF have slightly lower fitness values than the PO approach.

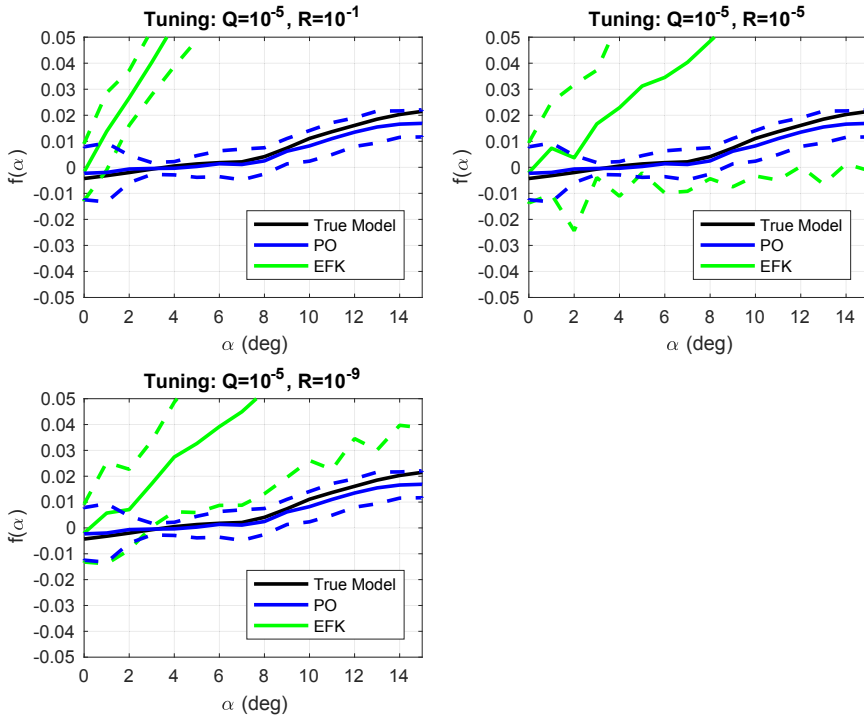


**Figure 8.16:** Estimation of the nonlinear part,  $f_m(\theta_8, \dots, \theta_{25}, \hat{\alpha}_k)$ , of the predictor (8.1). The true model is given in black. The results are based on 100 Monte Carlo simulations. The means are given as solid lines and  $\pm 2$  standard deviations are given as dashed lines. The PO result is shown in blue and the EKF result is shown in green. The PO approach gives better predictions of the true system characteristics compared to the EKF approach when atmospheric disturbances are present.

**Table 8.10:** Estimation of the linear part of the predictor (8.1). The results are based on 100 Monte Carlo simulations.

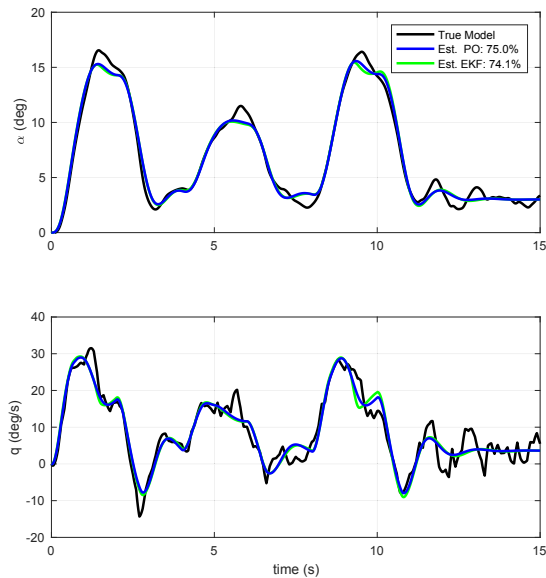
$\theta$	True	PO	EKF: $R = 10^{-1}$	EKF: $R = 10^{-5}$	EKF: $R = 10^{-9}$
$Z_\alpha$	0.9804	0.9799	0.9911	0.8566	0.7947
$Z_q$	0.0163	0.0166	0.0152	-0.1441	-0.2232
$M_q$	0.9790	0.9850	-0.0274	0.5744	0.5265
$Z_{\delta_e}$	-0.0051	-0.0042	-0.1042	1.1756	1.7530
$Z_{\delta_c}$	-0.0005	-0.0070	-0.4062	4.9494	7.3410
$M_{\delta_e}$	-0.5182	-0.4662	-7.8893	-3.4566	-3.8158
$M_{\delta_c}$	0.1376	0.1119	-30.7782	-12.2434	-13.7008

**Table 8.11:** Model Fit for process noise.

PO	EKF: $R = 10^{-1}$	EKF: $R = 10^{-5}$	EKF: $R = 10^{-9}$
75.0%	74.1%	67.6%	67.9%

**Table 8.12:** Model fit of input and output signals.

	True model	PO	EKF: $R = 10^{-1}$	EKF: $R = 10^{-5}$	EKF: $R = 10^{-9}$
$\delta_e$	66.63%	66.52%	63.44%	64.72%	66.25%
$\delta_c$	59.77%	59.92%	56.40%	58.66%	59.88%
$\alpha$	87.60%	87.58%	86.39%	87.08%	87.52%
$q$	68.56%	68.90%	66.30%	67.97%	68.85%

**Figure 8.17:** Validation data. PO is shown in blue and the EKF ( $R = 10^{-1}$ ) is shown in green.



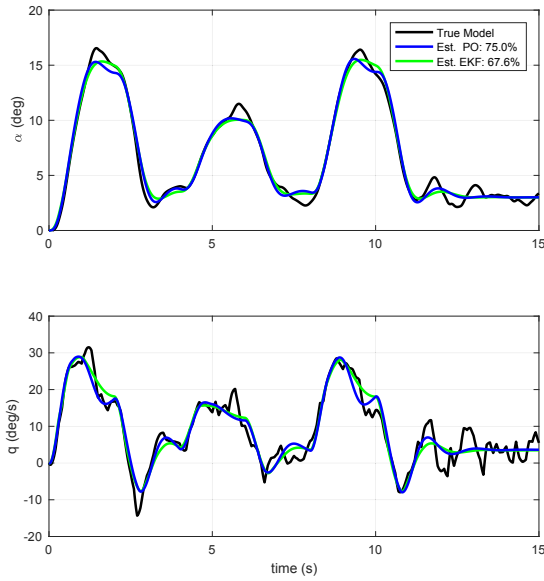


**Figure 8.18:** Validation data. PO is shown in blue and the EKF ( $R = 10^{-5}$ ) is shown in green.

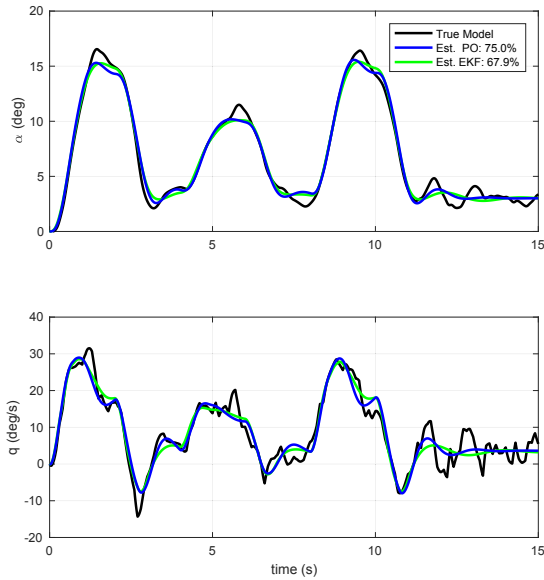


**Figure 8.19:** Validation data. PO is shown in blue and the EKF ( $R = 10^{-9}$ ) is shown in green.

### 8.3 Estimation on real data

The five methods have been evaluated on data from a flight test where a wind-up turn is performed. A wind-up turn is a flight maneuver where an initial roll of 90 degrees is performed followed by an almost pure, high angle-of-attack, pitching maneuver at almost constant speed. The identification is based on data collected after the initial roll has been performed. The sample frequency is 60 Hz and the dataset contains approximately 300 measurements, which are shown in Figure 8.20. Note that the leading edge deflection ( $\delta_{LE}$ ) has been added as an input compared to the previous investigation based on simulated data.

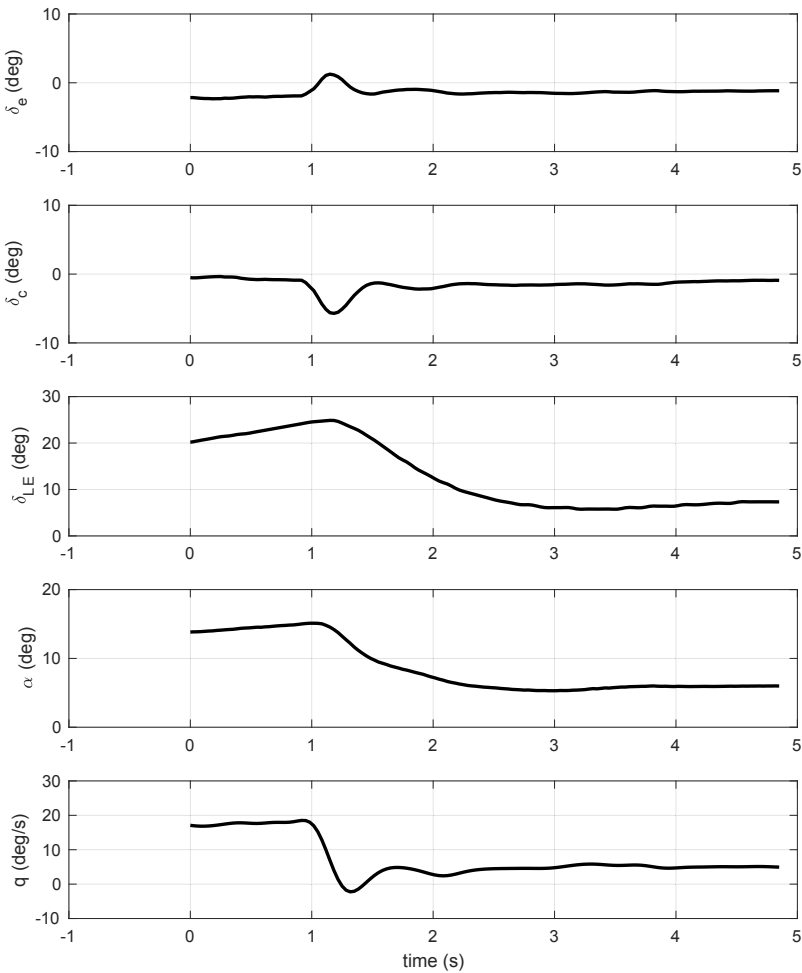


Figure 8.20: Input and output data from flight test.

The estimation result, based on this dataset, is shown in Figure 8.21 and Table 8.13. All the parameters were initialized using the values from the present model. As can be seen, all methods capture the nonlinearity around  $\alpha = 7$  (deg) and the slope of the curve. It is interesting to see that the methods predict that the nonlinearity should be more aggressive, i.e., the curve slope should change more abruptly, than what is in the present model. There are rather large variations of the estimated curves at higher angles-of-attack. This can be due to the fact that there were few data for angles-of-attack between 12 to 14 degrees. Comparing the different approaches, it is interesting to note that the PO and CLM approaches give a closer resemblance to the present model, which has been built up from numerical calculations, wind tunnel tests and flight tests during a period of more than 30 years.

## 8.4 Conclusions

Five approaches for direct system identification of unstable nonlinear systems have been presented. Three of the methods are variations of the prediction-error method (PEM). These are the parameterized observer (PO) approach and two approaches based on the Kalman filter, the extended Kalman filter (EKF) and the unscented Kalman filter (UKF). The fourth approach is a state estimation method, the augmented system approach (AUG) using the extended Kalman filter. The fifth method is a parameter and state estimation method, the constrained Levenberg-Marquardt (CLM) approach.

These methods have been evaluated on simulated data from an unstable nonlinear system and tested for measurement and process noise sensitivity as well as for initial value offsets. From these tests one can conclude that the PO and EKF approaches seem most robust. The approaches have also been tested on real data from a flight test near the speed of sound. Here, the PO and CLM approaches show promising results since a good resemblance to the present aerodynamic model was found. The other methods show some biases in the results compared to the present aerodynamic model for the JAS 39 Gripen.

All in all, the relatively simple PO approach seems to be most robust against noise and initial model offset for the studied cases. There is also the gain that engineers using the PO method do not have to be experts in the tuning of Kalman filters to get good results. With that said it has to be pointed out that this is a limited study and there might be cases for which the EKF approach outperforms the PO approach, but at the cost of tuning.

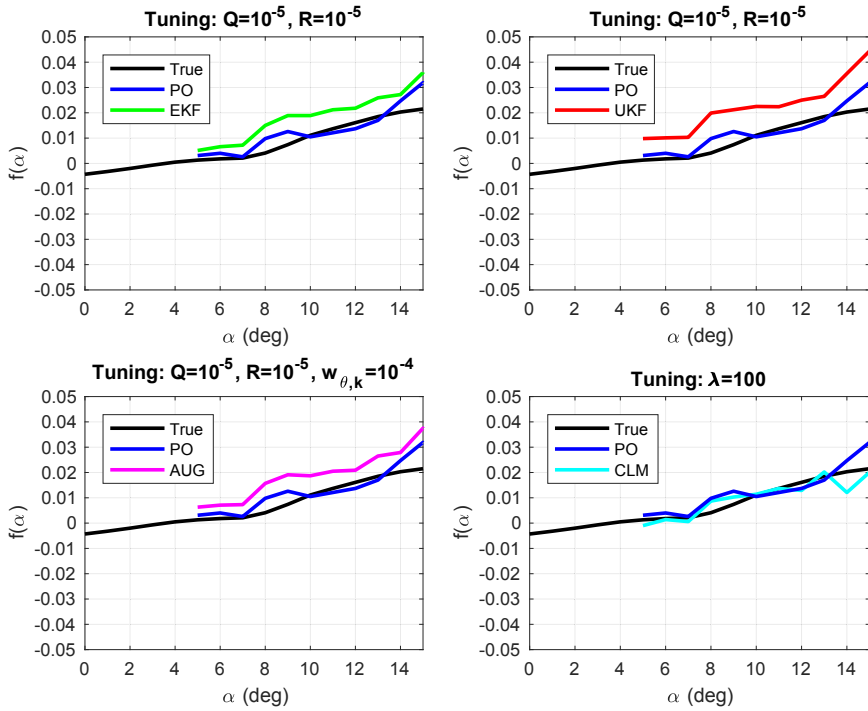


Figure 8.21: Estimated and present model for the pitching moment.

Table 8.13: Estimated and present model aerodynamic derivatives.

	Present	PO	EKF	UKF	AUG	CLM
$N_\alpha$	0.9804	0.9975	0.9984	0.9930	0.9930	0.9962
$N_q$	0.0163	0.0125	0.0116	0.0135	0.0134	0.0131
$M_q$	0.9790	0.8948	0.9095	0.8867	0.9040	0.9370
$N_{\delta_e}$	-0.0051	-0.0011	-0.0063	-0.0087	-0.0090	-0.0030
$N_{\delta_c}$	-0.0005	0.0072	0.0048	0.0013	0.0017	0.0013
$N_{\delta_{LE}}$	0.0001	-0.0068	-0.0078	-0.0058	-0.0057	-0.0071
$M_{\delta_e}$	-0.5182	-0.5512	-0.4837	-0.4528	-0.4828	-0.4968
$M_{\delta_c}$	0.1376	0.1730	0.1617	0.2279	0.1851	0.1242
$M_{\delta_{LE}}$	-0.0031	-0.0305	-0.0488	-0.0467	-0.0454	-0.0334



# 9

---

## Discussion

"If I have seen a little further it is by standing on the shoulders of giants."

- Isaac Newton (1643 - 1727)

*The aim* of this work was to improve the tools used in industry today, making the modeling process easier for the engineers, leading to a more time and cost effective way of working. To do this, two aspects have been considered.

The first aspect treats estimation of linear system characteristics during flight tests [Larsson and Enqvist, 2009]. This is an interesting topic that can save both time and reduce cost as well as being a tool for flight safety. This gives the possibility for the engineers to make decisions when the aircraft is still in the air. If, for example, the excitation is weak during a maneuver so that post-flight analysis would be hard or impossible and the tool give an indication of this, the test engineer can ask the pilot to make a new and stronger excitation. This means that the test does not have to be redone during another flight. A flight safety situation could be that the test engineer sees that stability and/or control characteristics are degrading in a way that calls for a more thorough analysis and the flight can be aborted in a safe way. Another use of this kind of method could be to implement it in an adaptive control setting. Then the online identification could be used to reconfigure the controller as the flight characteristics change either to a new flight condition or perhaps if the aircraft is damaged in some way. There is also a benefit of using this kind of method when working with demonstrator aircraft where prior knowledge of the flight characteristics might not be as good as for a real production test aircraft [Larsson et al., 2019].

In this thesis, improvements of an existing frequency domain method (Method A) have been suggested. This method is based on an ordinary least squares approach

and can therefore run into problem if noisy data is analyzed. An Instrumental Variable (IV) method has been included in a proposed modified method, which is also based on the use of data fusion (Method C). This takes care of noise that is colored, such as atmospheric turbulence, and/or correlated with the regressors for the studied cases. The benefits of using these improvements have been verified in simulations and the algorithm has been run on real flight test data. A time-domain method (Method B) has been compared to Method A. What can be done in the time domain can often be done in the frequency domain and vice versa. There might however be issues that make it easier to implement methods in one of the domains. Three master theses [Andersson, 2010, Larsson Cahlin, 2016, Nyman, 2016] have been performed at Saab to make a software-demonstrator in the real flight test-monitoring environment. These have looked at both the time domain method and parts of the improved frequency domain method. The frequency domain method seems to have some practical benefits in this environment, which have made this the method of choice.

The second aspect concerns post-flight analysis of more advanced maneuvers where nonlinear flight characteristics are part of the problem in the system identification process. This modeling is one of the important parts of the flight-testing besides verifying that the performance requirements are fulfilled. With accurate models, hundreds of thousands of simulations can be performed to find problems so that control system design can be used to improve the flight mechanical characteristics and thereby increasing the flight performance. This way of model-based working is effective since problems can be eliminated as early as possible. A lack of accuracy in the models will probably lead to a more robust control design with larger margins, which will reduce the flight performance.

To make post-flight estimation of nonlinear flight mechanical characteristics more effective a prediction-error method, using a parameterized observer gain, has been developed [Larsson and Enqvist, 2012b, 2016]. This method has been compared to four other direct methods. The methods have been compared and contrasted with respect to signal-to-noise ratio effects of measurement noise as well as to effects of parameter initiation. The effect of process noise has been analyzed, but here the study has been limited to the parameterized observer and the EKF approaches. The investigations have been done since a fighter aircraft, like the JAS 39 Gripen, can be tested under different weather conditions, but also since the existing flight dynamical model, even though it has been developed over a long period of time, will always contain some approximations leading to differences when compared to the true system. A benchmark problem has been implemented to test the methods for a simplified two degree-of-freedom setup. The simplification has been made so that only one nonlinearity is included in the system. The rest of the system and the input part have been left as linear. The result is a bit unexpected. The parameterized observer approach with no tuning parameters seems to be most robust against different kinds of noises and initial offsets, for the studied problems. To make the methods useful, further studies of six degrees-of-freedom problems with several nonlinearities have to be made.

Apart from the studies made in this thesis it can also be interesting to look at other types of methods, as for example indirect identification.

*The goal of the work described in this thesis was to provide aircraft companies with robust methods for identification of flight mechanical characteristics, making working life easier for the engineers working with this subject. The tools developed have taken the combined subject of system identification and aeronautical engineering a little further, and will hopefully prove to be valuable assets during future flight tests.*



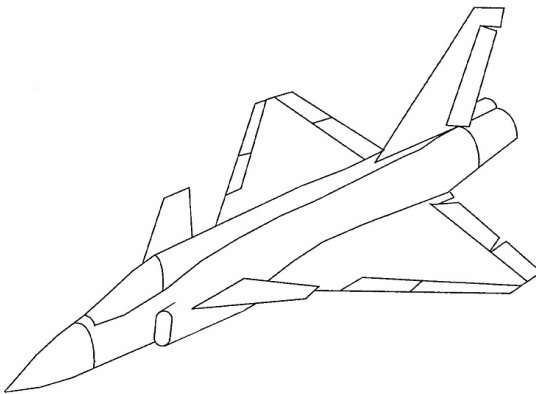


# A

---

## Nonlinear aircraft model

This appendix describes the nonlinear physics of the simulation model ADMIRE [Forsell and Nilsson, 2005]. ADMIRE is a Matlab/Simulink model that describes a generic fighter with a single engine and a close-coupled delta-canard configuration, similar to the Gripen fighter. The aircraft is shown in Figure A.1 together with the geometric, mass and inertia data.



### Reference geometry

$$S = 45.0 \text{ m}^2$$

$$b = 10.0 \text{ m}$$

$$\bar{c} = 5.2 \text{ m}$$

### Mass and inertia

$$m = 9100 \text{ kg}$$

$$I_{xx} = 21000 \text{ kgm}^2$$

$$I_{yy} = 81000 \text{ kgm}^2$$

$$I_{zz} = 101000 \text{ kgm}^2$$

$$I_{xy} = 0 \text{ kgm}^2$$

$$I_{yz} = 0 \text{ kgm}^2$$

$$I_{zx} = 2500 \text{ kgm}^2$$

**Figure A.1:** The ADMIRE aircraft and some of the key parameters.

Three envelop points, at an altitude of 6000 m, have been chosen to illustrate the difference between subsonic (Mach 0.5), transonic (Mach 0.9) and supersonic

(Mach 1.4) characteristics. Table A.1 shows the envelope data for the chosen points.

**Table A.1:** Envelope data at 6000 m.

Mach	V(m/s)	$\rho(\text{kg/m}^3)$	$q_a(\text{N/m}^2)$
0.5	158.2	0.6012	7523
0.9	284.8	0.6012	24376
1.4	443.0	0.6012	58983

In Chapter 3, it was stated that the forces and moments acting on the aircraft come from gravity (working on the mass), inertia, engine thrust and aerodynamics. The mass and inertia were given in Figure A.1. The thrust for ADMIRE is shown in Figure A.2 for the chosen envelope points. The thrust does not increase

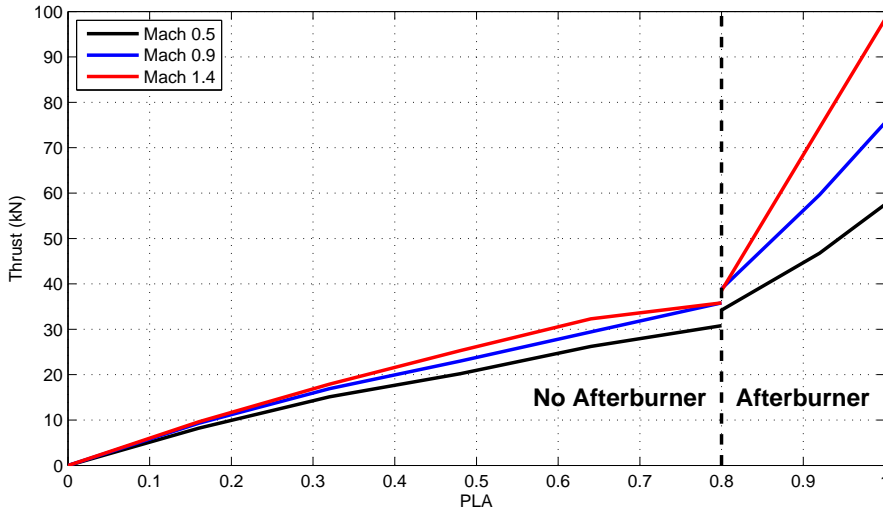


**Figure A.2:** The engine thrust as a function of Mach and PLA.

linearly with the  $PLA$  (Power Leverage Angle) setting, which can clearly be seen in the difference between Mach 0.9 and Mach 1.4 for a  $PLA$  setting of 0.8. It should be noted here that the  $PLA$  has here been made nondimensional, where  $PLA > 0.8$  represents a setting using the afterburner. The thrust ( $T_e$ ) is given as

$$T_e = \text{Thrust}(M, PLA) \quad (\text{A.1})$$

The aerodynamic model characteristics, which come from Backström [1997], are shown in Figures A.3 - A.8, where the effect of the wind vector ( $\alpha, \beta$ ) and control surface deflections ( $\delta_a, \delta_e, \delta_c, \delta_r$ ) are given. Furthermore, the damping characteristics ( $\dot{\alpha}, \dot{\beta}, \dot{p}, \dot{q}, \dot{r}$ ) are given in Tables A.2 - A.4. The aerodynamic tangential

force coefficient is given as

$$C_T = C_T(\alpha) + \Delta C_T(\delta_e) + \Delta C_T(\delta_c) + C_{T_{\dot{\alpha}}} \frac{\dot{\alpha}c}{2V} + C_{T_{\dot{q}}} \frac{qc}{2V} \quad (\text{A.2})$$

where the terms are  $C_T(\alpha) = C_T(\alpha, 0)$ ,  $\Delta C_T(\delta_e) = (C_T(\alpha, \delta_e) - C_T(\alpha, 0))$  and  $\Delta C_T(\delta_c) = (C_T(\alpha, \delta_c) - C_T(\alpha, 0))$ , respectively. With the same principle, the rest of the aerodynamic coefficients are given as

$$C_N = C_N(\alpha) + \Delta C_N(\delta_e) + \Delta C_N(\delta_c) + C_{N_{\dot{\alpha}}} \frac{\dot{\alpha}c}{2V} + C_{N_{\dot{q}}} \frac{qc}{2V} \quad (\text{A.3})$$

$$C_m = C_m(\alpha) + \Delta C_m(\delta_e) + \Delta C_m(\delta_c) + C_{m_{\dot{\alpha}}} \frac{\dot{\alpha}c}{2V} + C_{m_{\dot{q}}} \frac{qc}{2V} \quad (\text{A.4})$$

$$C_C = C_C(\beta) + \Delta C_C(\delta_a) + \Delta C_C(\delta_r) + C_{C_{\dot{\beta}}} \frac{\dot{\beta}c}{2V} + C_{C_{\dot{p}}} \frac{pc}{2V} + C_{C_{\dot{r}}} \frac{rc}{2V} \quad (\text{A.5})$$

$$C_l = C_l(\beta) + \Delta C_l(\delta_a) + \Delta C_l(\delta_r) + C_{l_{\dot{\beta}}} \frac{\dot{\beta}c}{2V} + C_{l_{\dot{p}}} \frac{pc}{2V} + C_{l_{\dot{r}}} \frac{rc}{2V} \quad (\text{A.6})$$

$$C_n = C_n(\beta) + \Delta C_n(\delta_a) + \Delta C_n(\delta_r) + C_{n_{\dot{\beta}}} \frac{\dot{\beta}c}{2V} + C_{n_{\dot{p}}} \frac{pc}{2V} + C_{n_{\dot{r}}} \frac{rc}{2V} \quad (\text{A.7})$$

Using (3.3), (3.11), (3.14) and (3.19) together with (A.1) - (A.7) and the data in Figure A.1 and Table A.1, it is possible to build a simulation model. It should be noted that this simulation model is only valid for angles-of-attack close to  $5^\circ$  and angles-of-sideslip around  $0^\circ$ . This is due to the fact that outside this envelope there are other dependencies, for example  $C_n$  could depend on the angle-of-attack.

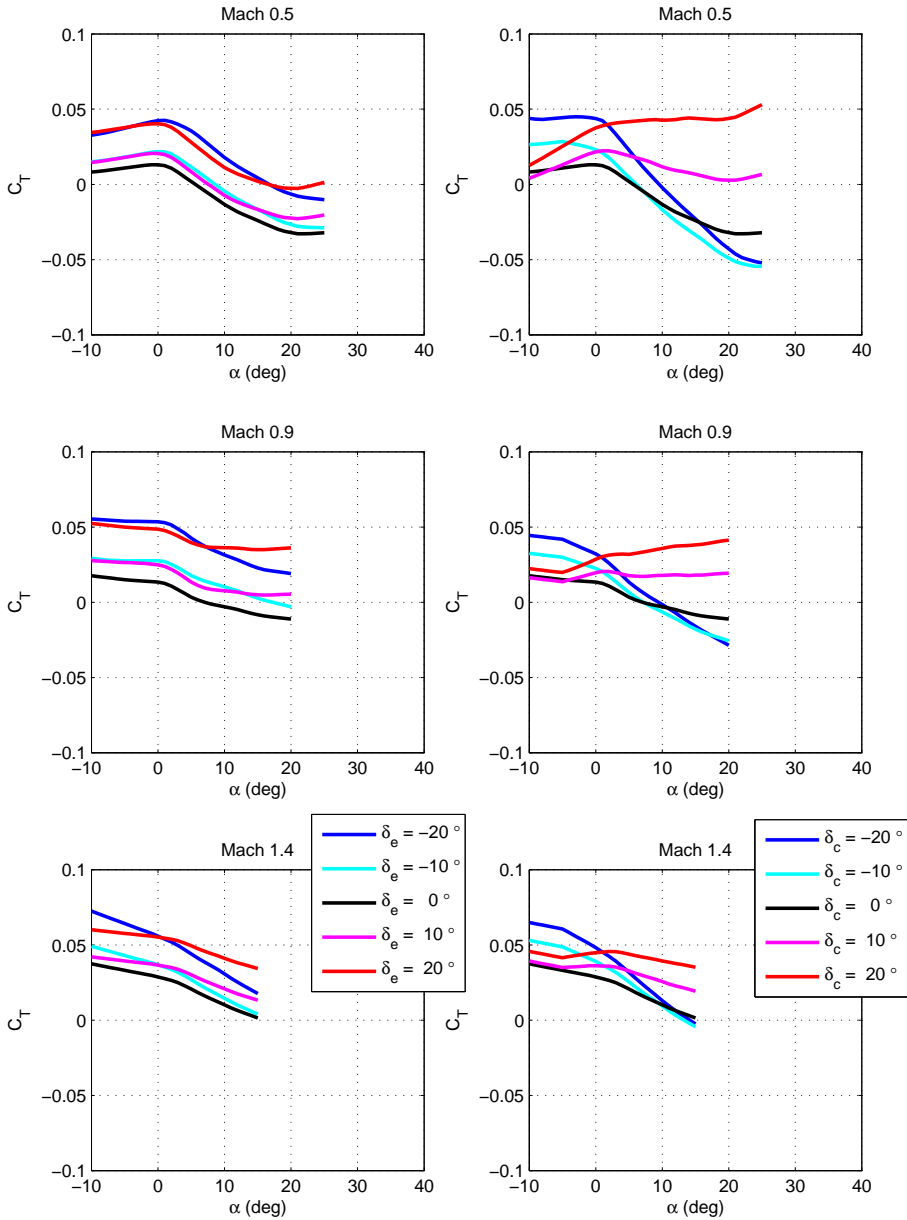


**Figure A.3:** Tangential force coefficient as a function of angle-of-attack  $\alpha$ , elevator deflection  $\delta_e$  and canard deflection  $\delta_c$ .

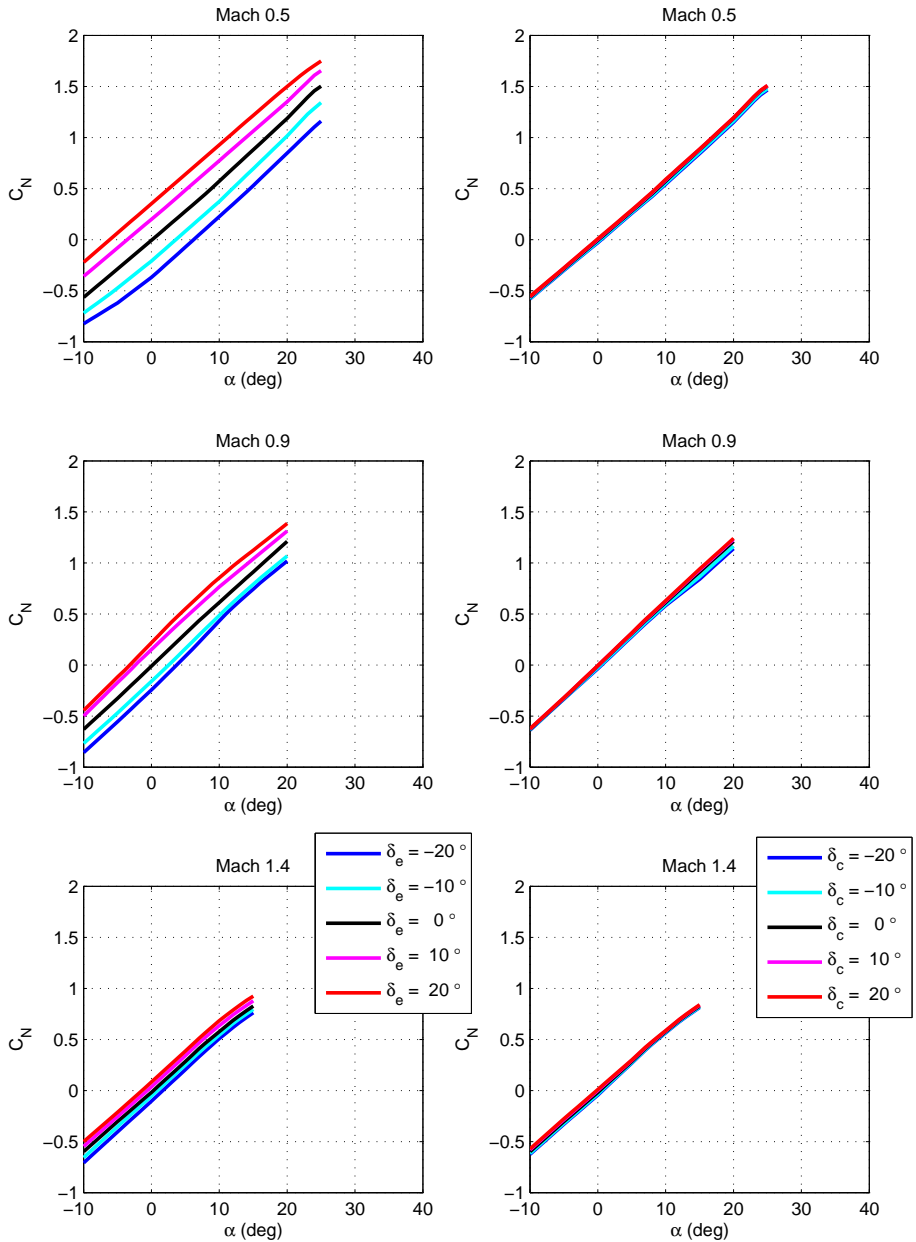


**Figure A.4:** Normal force coefficient as a function of angle-of-attack  $\alpha$ , elevator deflection  $\delta_e$  and canard deflection  $\delta_c$ .

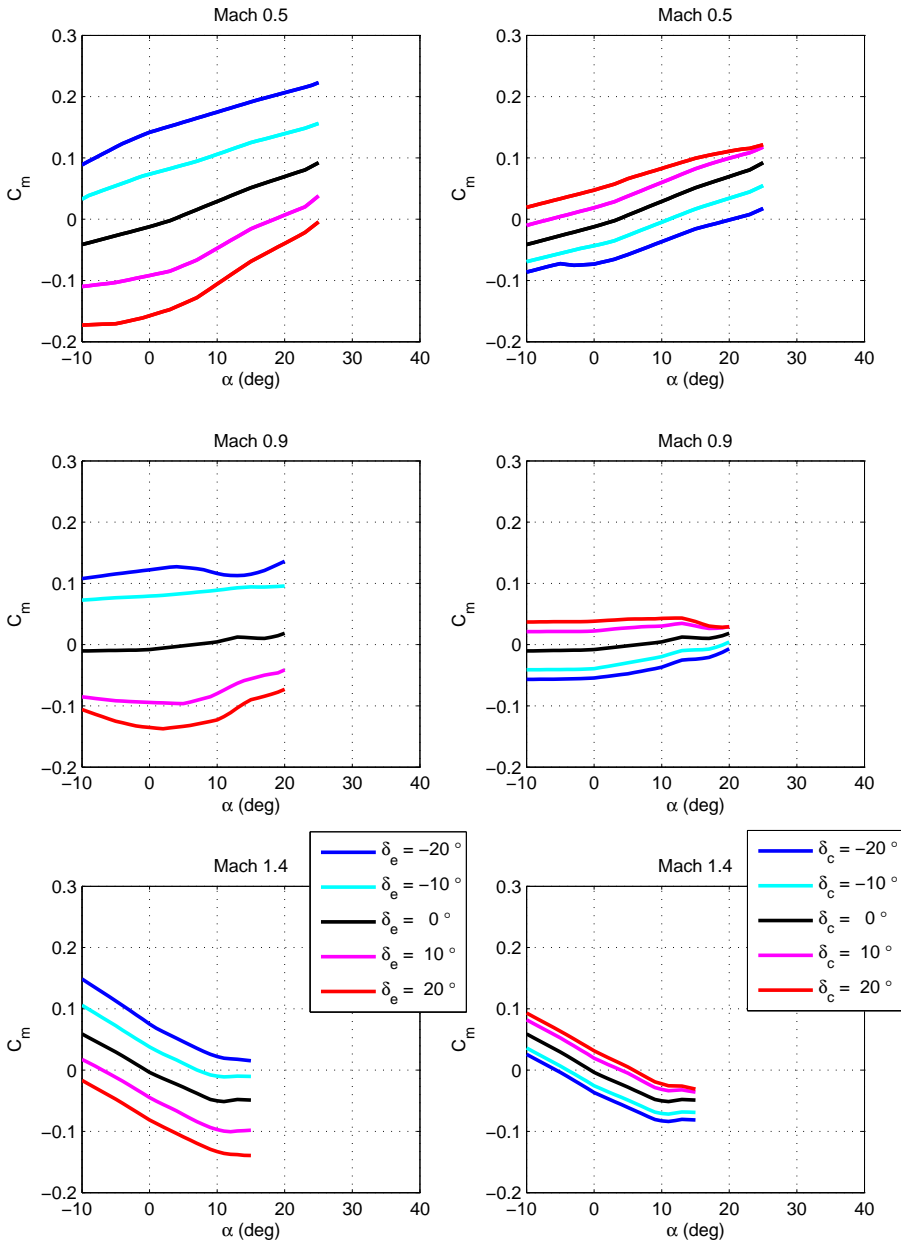


**Figure A.5:** Pitching moment coefficient as a function of angle-of-attack  $\alpha$ , elevator deflection  $\delta_e$  and canard deflection  $\delta_c$ .

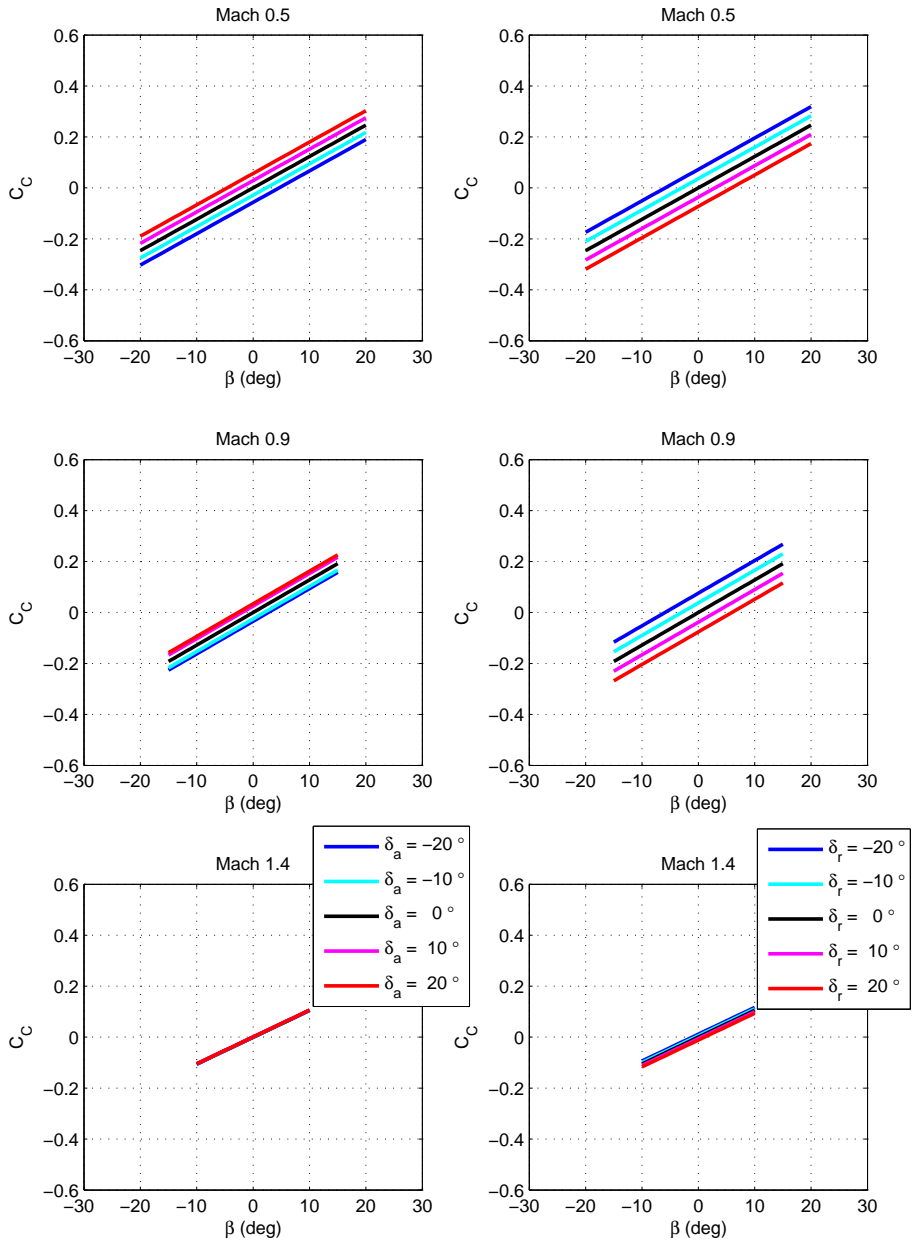


**Figure A.6:** Side force coefficient as a function of angle-of-sideslip  $\beta$ , aileron deflection  $\delta_a$  and rudder deflection  $\delta_r$ .



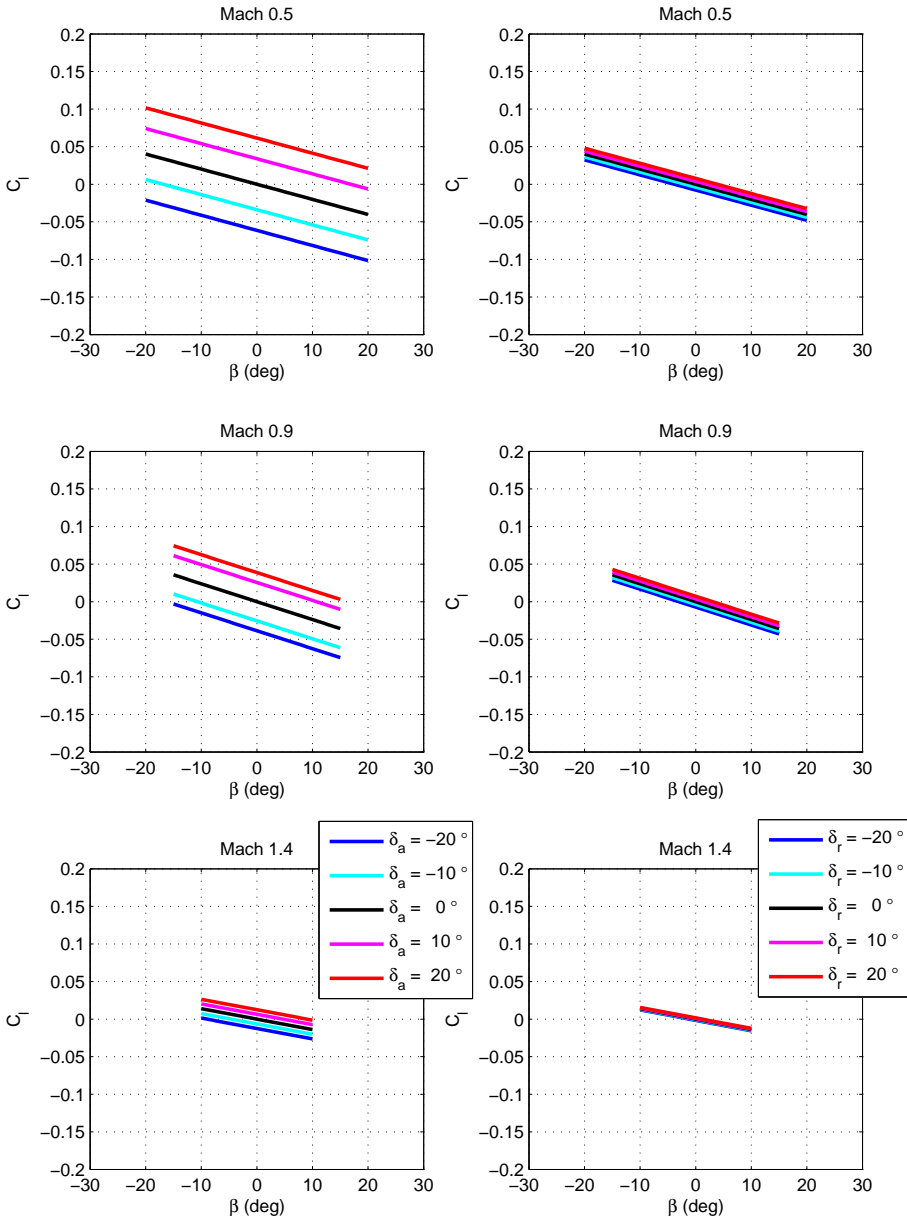


**Figure A.7:** Rolling moment coefficient as a function of angle-of-sideslip  $\beta$ , aileron deflection  $\delta_a$  and rudder deflection  $\delta_r$ .

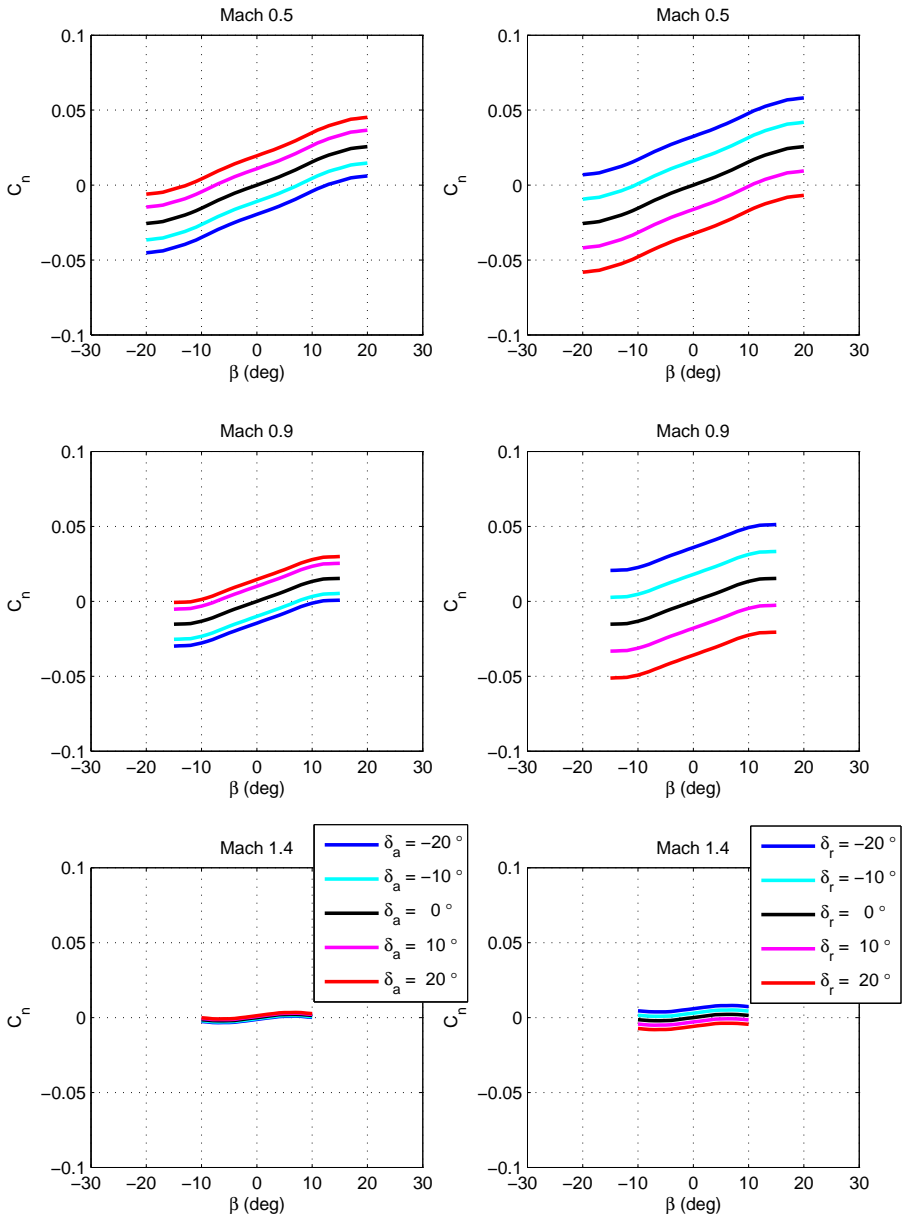


**Figure A.8:** Yawing moment coefficient as a function of angle-of-sideslip  $\beta$ , aileron deflection  $\delta_a$  and rudder deflection  $\delta_r$ .

**Table A.2:** Dynamic derivatives ( $C_{T\dot{\alpha}}$  etc.) at  $M 0.5$ .

	$\dot{\alpha}$	$\dot{\beta}$	$\dot{p}$	$\dot{q}$	$\dot{r}$
$C_T$					
$C_N$	1.65			3.54	
$C_m$	-0.54			-1.64	
$C_C$		0.35	-0.06		-0.52
$C_l$		0.00	-0.29		0.08
$C_n$		0.02	-0.06		-0.27

**Table A.3:** Dynamic derivatives ( $C_{T\dot{\alpha}}$  etc.) at  $M 0.9$ .

	$\dot{\alpha}$	$\dot{\beta}$	$\dot{p}$	$\dot{q}$	$\dot{r}$
$C_T$					
$C_N$	3.13			4.08	
$C_m$	-1.18			-2.70	
$C_C$		0.32	-0.03		-0.63
$C_l$		0.00	-0.32		0.13
$C_n$		-0.11	-0.08		-0.30

**Table A.4:** Dynamic derivatives ( $C_{T\dot{\alpha}}$  etc.) at  $M 1.4$ .

	$\dot{\alpha}$	$\dot{\beta}$	$\dot{p}$	$\dot{q}$	$\dot{r}$
$C_T$					
$C_N$	2.14			1.75	
$C_m$	0.42			-1.88	
$C_C$		0.11	0.00		-0.53
$C_l$		0.00	-0.26		0.19
$C_n$		-0.03	-0.08		-0.24

# B

---

## Some mathematics

In this appendix some mathematical details from Chapter 5 are presented.

To see **the asymptotic bias for the ordinary least squares method** with noisy regressors, consider the following simple regression problem for a scalar  $\Theta$

$$Y = \Theta\Phi + \varepsilon \quad (\text{B.1})$$

where  $\Phi$  is the true regressors. If the regressors are noisy  $\phi = \Phi + v$  then

$$Y = \Theta\Phi + \varepsilon = \Theta\phi + \varepsilon - \Theta v = \Theta(\phi - v) + \varepsilon \quad (\text{B.2})$$

The ordinary least squares solution can then be written as

$$\begin{aligned} \hat{\Theta} &= (\phi^T \phi)^{-1} \phi^T Y \\ &= (\phi^T \phi)^{-1} \phi^T (\Theta(\phi - v) + \varepsilon) \\ &= \Theta + (\phi^T \phi)^{-1} \phi^T (\varepsilon - \Theta v) \\ &= \Theta + ((\Phi + v)^T (\Phi + v))^{-1} (\Phi + v)^T (\varepsilon - \Theta v). \end{aligned} \quad (\text{B.3})$$

Under general excitation assumptions, the limit of  $\hat{\Theta}$  for the scalar problem is

$$\begin{aligned} \lim_{N \rightarrow \infty} \hat{\Theta} &= \lim_{N \rightarrow \infty} \Theta + ((\Phi + v)^T (\Phi + v))^{-1} (\Phi + v)^T (-\Theta v + \varepsilon) \\ &= \Theta (1 - \sigma_v^2 / (\sigma_v^2 + \sigma_\Phi^2)) \end{aligned} \quad (\text{B.4})$$

since  $E[\Phi^T \varepsilon] = E[\Phi^T v] = E[v^T \varepsilon] = 0$ ,  $E[\Phi^T \Phi] = N\sigma_\Phi^2$  and  $E[v^T v] = N\sigma_v^2$ . If  $\sigma_v^2 = 0$  then  $\lim_{N \rightarrow \infty} \hat{\Theta} = \Theta$ . Otherwise this equality does not hold since  $(1 - \sigma_v^2 / (\sigma_v^2 + \sigma_\Phi^2)) < 1$  in that case. The calculations for a non-scalar problem are more complex, but the principle is that the normal of the hyperplane spanned by the system is tilted compared to the case  $\sigma_v^2 = 0$ .

**The normalization** used in this thesis is described below.

Consider an IV problem of the form

$$\hat{\Theta} = (Z^T X)^{-1} Z^T Y \quad (\text{B.5})$$

where  $Z \in R^{m \times n}$ ,  $X \in R^{m \times n}$  and  $Y \in R^{m \times 1}$ . Let  $H \in R^{n \times n}$  be a diagonal matrix where the elements  $h_{jj}$  are the inverses of the maximum column elements  $\max(Z_{ij}, X_{ij}, i = 1, \dots, m)$ . Define  $A = ZH$  and  $B = XH$ . Let

$$\hat{\Theta}_H = (A^T B)^{-1} A^T Y \quad (\text{B.6})$$

Then,

$$\begin{aligned} \hat{\Theta}_H &= ((ZH)^T (XH))^{-1} (ZH)^T Y \\ &= (H^T Z^T XH)^{-1} (H^T Z^T) Y \\ &= H^{-1} (Z^T X)^{-1} (H^T)^{-1} H^T Z^T Y \\ &= H^{-1} (Z^T X)^{-1} Z^T Y = H^{-1} \hat{\Theta} \end{aligned} \quad (\text{B.7})$$

This means that

$$\hat{\Theta} = H \hat{\Theta}_H \quad (\text{B.8})$$

It can be numerically better to solve (B.6) than (B.5). The original estimates can then be retrieved by (B.8)

The same can be done for the information matrix.

$$\hat{I} = (X^T Z)(Z^T Z)^{-1}(Z^T X)/\hat{\sigma}^2 \quad (\text{B.9})$$

where

$$\hat{\sigma}^2 = (Y - X\hat{\Theta})^T (Y - X\hat{\Theta}) \quad (\text{B.10})$$

For this

$$\hat{I}_H = (B^T A)(A^T A)^{-1}(A^T B)/\hat{\sigma}_H^2 \quad (\text{B.11})$$

where

$$\begin{aligned} \hat{\sigma}_H^2 &= (Y - B\hat{\Theta}_H)^T (Y - B\hat{\Theta}_H) \\ &= (Y - XHH^{-1}\hat{\Theta})^T (Y - XHH^{-1}\hat{\Theta}) \\ &= (Y - X\hat{\Theta})^T (Y - X\hat{\Theta}) = \hat{\sigma}^2 \end{aligned} \quad (\text{B.12})$$

Then,

$$\begin{aligned} \hat{I}_H &= ((XH)^T (ZH))((ZH)^T (ZH))^{-1}((ZH)^T (XH))/\hat{\sigma}_H^2 \\ &= (H^T X^T ZH)(H^T Z^T ZH)^{-1}(H^T Z^T XH)/\hat{\sigma}_H^2 \\ &= (H^T X^T ZH)(H^{-1}(Z^T Z)^{-1}(H^T)^{-1})(H^T Z^T XH)/\hat{\sigma}_H^2 \\ &= H^T (X^T Z)(Z^T Z)^{-1} Z^T X H / \hat{\sigma}^2 = H^T \hat{I} H \end{aligned} \quad (\text{B.13})$$

This gives

$$\hat{I} = (H^T)^{-1} \hat{I}_H (H)^{-1} \quad (\text{B.14})$$

# C

---

## Sequential algorithms

This appendix present the three algorithms used in Chapter 5. This includes **Method A** (based on the works in Morelli [1999], Morelli [2010], Larsson and Enqvist [2012a] and Klein and Morelli [2016]), **Method B** (based on Klein and Morelli [2016] and Ljung [1999]) and **Method C** presented in this thesis.

**Algorithm 1** Method A

---

```

1: Begin program
2: Input
3:   Choose:  $\omega_i, i = 1, \dots, M$ 
4:   Choose:  $t_{pres}$  (should be a multiple of  $T_s$ )
5: Initialization
6:   Get data:  $u_0$  and  $y_0$ 
7:   Set:  $\phi_0 := \begin{bmatrix} y_0^T & u_0^T \end{bmatrix}$ 
8:   Set:  $T_s$  and  $n_p := n_y + n_u$ 
9:   Set:  $\tilde{\phi}_0(\omega_i) := 0_{1 \times n_p}, \tilde{Y}_0(\omega_i) := 0_{1 \times n_y}$  and  $\tilde{z}_0(\omega_i) := 0_{1 \times n_y}, i = 1, \dots, M$ 
10:  Set:  $n := 1$  and  $N := 1$ 
11: while RUN == TRUE do
12:   Get data:  $u_N$  and  $y_N$ 
13:   Set:  $u_N := u_N - u_0$ 
14:   Set:  $y_N := y_N - y_0$ 
15:   Set:  $\phi_N := \begin{bmatrix} y_N^T & u_N^T \end{bmatrix}$ 
16:   for  $i = 1 \rightarrow M$  do
17:     Transform:  $\tilde{\phi}_N(\omega_i) = \tilde{\phi}_{N-1}(\omega_i) + \phi_{N-1} e^{-j\omega_i(N-1)T_s}$ 
18:     Transform:  $\tilde{Y}_N(\omega_i) = \tilde{Y}_{N-1}(\omega_i) + y_{N-1} e^{-j\omega_i(N-1)T_s}$ 
19:     Set:  $\tilde{z}_N(\omega_i) := j\omega_i \tilde{Y}_N^T(\omega_i) + \frac{1}{T_s} (y_k^T e^{-j\omega_i k T_s} - y_0^T)$ 
20:   end for
21:   Set:  $\tilde{\Phi}_N := \begin{bmatrix} \tilde{\phi}_N^T(\omega_1) & \tilde{\phi}_N^T(\omega_2) & \dots & \tilde{\phi}_N^T(\omega_M) \end{bmatrix}^T$ 
22:   Set:  $\tilde{Z}_N := \begin{bmatrix} \tilde{Z}_{N,1} & \dots & \tilde{Z}_{N,n_y} \end{bmatrix} = \begin{bmatrix} \tilde{z}_N^T(\omega_1) & \tilde{z}_N^T(\omega_2) & \dots & \tilde{z}_N^T(\omega_M) \end{bmatrix}^T$ 
23:   if  $N = n(t_{pres}/T_s)$  then
24:     for  $k = 1 \rightarrow n_y$  do
25:       Solve Regression:  $\hat{\Theta}_k = (\Re(\tilde{\Phi}_N^* \tilde{\Phi}_N))^{-1} \Re(\tilde{\Phi}_N^* \tilde{Z}_{N,k})$ 
26:       Calculate:  $\hat{\sigma}_k^2 = \frac{1}{M-n_p} ((\tilde{Z}_{N,k} - \tilde{\Phi}_N \hat{\Theta}_k)^* (\tilde{Z}_{N,k} - \tilde{\Phi}_N \hat{\Theta}_k))$ 
27:       Calculate:  $\hat{C}_k(\hat{\Theta}_k) = \hat{\sigma}_k^2 \Re(\tilde{\Phi}_N^* \tilde{\Phi}_N)^{-1}$ 
28:       Calculate:  $s_{k,i} = \sqrt{\hat{C}_{k,ii}(\hat{\Theta})}, i = 1, \dots, n_p$ 
29:       Present:  $\hat{\Theta}_k \pm 2[s_{k,1} \dots s_{k,n_p}]^T$ 
30:     end for
31:     Set:  $n := n + 1$ 
32:   end if
33:   if OP = RUN then
34:     Set:  $N := N + 1$ 
35:   end if
36: end while
37: End program

```

---

---

**Algorithm 2 Method B**


---

```

1: Begin program
2: Input
3:   Choose:  $t_{pres}$ 
4:   Choose:  $P_{0,1}, \dots, P_{0,n_y}$  ( $P_{0,k}$  is a  $n_p \times n_p$  matrix) and  $\hat{\sigma}_0 = [\hat{\sigma}_{0,1} \ \dots \ \hat{\sigma}_{0,n_y}]$ 
5: Initialization
6:   Construct: Butterworth filter with a cut-off frequency at 2Hz
7:   Get data:  $u_0$  and  $y_0$ 
8:   Set:  $T_s$  and  $n_p := n_y + n_u$ 
9:   Initialize:  $\hat{\theta}_0 = [\hat{\theta}_{0,1} \ \dots \ \hat{\theta}_{0,n_y}] := 0_{n_p \times n_y}$ 
10:  Set:  $n := 1$  and  $N := 1$ 
11: while RUN == TRUE do
12:   Get data:  $u_N$  and  $y_N$ 
13:   Set:  $u_N := u_N - u_0$ 
14:   Set:  $y_N := y_N - y_0$  and  $y_{N-1} := y_{N-1} - y_0$ 
15:   Filter:  $u_N, y_N$  and  $y_{N-1}$ 
16:   Set:  $\phi_N := [y_N^T \ u_N^T]^T$ 
17:   Set:  $z_N := (y_N^T - y_{N-1}^T)/T_s$ 
18:   for  $k = 1 \rightarrow n_y$  do
19:     Calculate recursion:  $K_{N,k} = P_{N-1,k} \phi_N^T (\hat{\sigma}_{N-1,k}^2 + \phi_N P_{N-1,k} \phi_N^T)^{-1}$ 
20:     Calculate recursion:  $P_{N,k} = P_{N-1,k} - K_{N,k} \phi_N P_{N-1,k}$ 
21:     Calculate recursion:  $\hat{\theta}_{N,k} = \hat{\theta}_{N-1,k} + K_{N,k} (z_{N,k} - \phi_N \hat{\theta}_{N-1,k})$ 
22:     if  $N < 5n_p + 1$  then
23:       Calculate:  $\hat{\sigma}_{N,k}^2 = (\frac{1}{N})((N-1)\hat{\sigma}_{N-1,k}^2 + (z_{N,k} - \phi_N \hat{\theta}_{N,k})^2)$ 
24:     else if  $n = 5n_p + 1$  then
25:       Calculate:  $\hat{\sigma}_{N,k}^2 = (\frac{1}{n-n_p})((N-1)\hat{\sigma}_{N-1,k}^2 + (z_{N,k} - \phi_N \hat{\theta}_{N,k})^2)$ 
26:     else if  $N > 5n_p + 1$  then
27:       Calculate:  $\hat{\sigma}_{N,k}^2 = (\frac{1}{N-n_p})((N-1-n_p)\hat{\sigma}_{N-1,k}^2 + (z_{N,k} - \phi_N \hat{\theta}_{N,k})^2)$ 
28:     end if
29:     if  $N = n(t_{pres}/T_s)$  then
30:       Set:  $\hat{C}_k := P_{N,k}$ 
31:       Calculate:  $s_{k,i} = \sqrt{\hat{C}_{k,ii}(\hat{\theta})}$ ,  $i = 1, \dots, n_p$ 
32:       Present:  $\hat{\theta}_k \pm 2[s_{k,1} \ \dots \ s_{k,n_p}]^T$ 
33:       Set:  $n := n + 1$ 
34:     end if
35:   end for
36:   if RUN == TRUE then
37:     Set:  $N := N + 1$ 
38:   end if
39: end while
40: End program

```

---



To get an easier to read algorithm for Method C, some parts are given as separate sub-algorithms below. These are the parts for the calculations of the finite Fourier transform, the Complex Least Squares solver for the IV approach and the data fusion part. These are used as subroutines in the Method C algorithm.

---

**Algorithm 3** Finite Fourier Transform
 

---

- 1: **Input** [ $\tilde{F}_{N-1}(\omega)$ ,  $f_{N-1}$ ,  $\omega$ ,  $N$ ,  $T_s$ ]
  - 2: **Transform:**  $\tilde{F}_N(\omega) = \tilde{F}_{N-1}(\omega) + f_{N-1} e^{-j\omega(N-1)T_s}$
  - 3: **Output** [ $\tilde{F}_N(\omega)$ ]
- 

---

**Algorithm 4** Complex Least Squares with IV
 

---

- 1: **Input** [ $\tilde{\Phi}_N$ ,  $\tilde{\zeta}_N$ ,  $\tilde{Z}_N$ ,  $M$ ,  $n_p$ ]
  - 2:  $n_o \leftarrow$  no. of columns in  $\tilde{Z}_N$
  - 3: **for**  $k = 1 \rightarrow n_o$  **do**
  - 4: Solve regression:  $\hat{\Theta}_k = (\Re(\tilde{\zeta}_N^* \tilde{\Phi}_N))^{-1} \Re(\tilde{\zeta}_N^* \tilde{Z}_{N,k})$
  - 5: Calculate:  $\hat{\sigma}_k^2 = \frac{1}{M-n_p} ((\tilde{Z}_{N,k} - \tilde{\Phi}_N \hat{\Theta}_k)^* (\tilde{Z}_{N,k} - \tilde{\Phi}_N \hat{\Theta}_k))$
  - 6: Calculate:  $\hat{P}_k(\hat{\Theta}_k) = \hat{\sigma}_k^2 \Re(\tilde{\zeta}_N^* \tilde{\Phi}_N)^{-1} \Re(\tilde{\zeta}_N^* \tilde{\zeta}_N) \Re(\tilde{\Phi}_N^* \tilde{\zeta}_N)^{-1}$
  - 7: Calculate:  $\hat{I}_k = \hat{P}_k^{-1}$
  - 8: **end for**
  - 9: **Output** [ $\hat{\Theta}$ ,  $\hat{I}_k$ ]
- 

---

**Algorithm 5** Data Fusion
 

---

- 1: **Input** [ $\hat{\Theta}_1$ ,  $\hat{I}_1$ ,  $\hat{\Theta}_2$ ,  $\hat{I}_2$ ]
  - 2:  $n_y \leftarrow$  no. of columns in  $\hat{\Theta}_1$
  - 3: **for**  $k = 1 \rightarrow n_y$  **do**
  - 4: Calculate:  $\hat{I}_k = \hat{I}_{1,k} + \hat{I}_{2,k}$
  - 5: Calculate:  $\hat{\Theta}_k = \hat{I}_k^{-1} (\hat{I}_{1,k} \hat{\Theta}_{1,k} + \hat{I}_{2,k} \hat{\Theta}_{2,k})$
  - 6: Calculate:  $s_k = \sqrt{\hat{I}_{k,ii}^{-1}(\hat{\Theta})}$ ,  $i = 1, \dots, n_p$
  - 7: **end for**
  - 8: **Output** [ $\hat{\Theta}$ ,  $\hat{I}$ ,  $s$ ]
-

---

**Algorithm 6** Method C
 

---

```

1: Begin program
2: Settings  $\omega, T_{seq}, T_{int}$ 
3: Get:  $(t_0, u_0, y_0), (t_1, u_1, y_1)$  and  $(t_{IV,0}, u_{IV,0}, y_{IV,0})$ 
4: Initialization  $T_s = t_1 - t_0, M := n_\omega$  and  $n_p := n_y + n_u$ 
5: Set:  $(t_0 := 0, u_0 := 0, y_0 := 0)$  and  $(t_{IV,0} := 0, u_{IV,0} := 0, y_{IV,0} := 0)$ 
6: Set:  $\phi_0 := [y_0^T u_0^T]$  and  $\phi_{IV,0} := [y_{IV,0}^T u_{IV,0}^T]$ 
7: Set:  $\tilde{\phi}_0 := 0_{M \times n_p}, \tilde{Y}_0 := 0_{M \times n_y}, \tilde{z}_0 := 0_{M \times n_y}$  and  $\tilde{\phi}_{IV,0} := 0_{M \times n_p}$ 
8: Set:  $\hat{I}_1 := 0_{n_p \times n_p \times n_y}$  and  $\hat{\Theta}_1 := 0_{n_p \times n_y}$ 
9: Set:  $n := 1$  and  $N := 1$ 
10: while RUN == TRUE do
11: Get:  $(t_N, u_N, y_N)$  and  $(t_{IV,N}, u_{IV,N}, y_{IV,N})$ 
12: Set:  $t_N := t_N - t_0, u_N := u_N - u_0, y_N := y_N - y_0$ 
13: Set:  $t_{IV,N} := t_{IV,N} - t_{IV,0}, u_{IV,N} := u_{IV,N} - u_{IV,0}, y_{IV,N} := y_{IV,N} - y_{IV,0}$ 
14: Set:  $\phi_N := [y_N^T u_N^T]$  and  $\phi_{IV,N} := [y_{IV,N}^T u_{IV,N}^T]$ 
15: Algorithm 3  $[\tilde{\phi}_{N-1}(\omega), \phi_{N-1}, \omega, N, T_s] \rightarrow [\tilde{\phi}_N(\omega)]$ 
16: Algorithm 3  $[\tilde{\phi}_{IV,N-1}(\omega), \phi_{IV,N-1}, \omega, N, T_s] \rightarrow [\tilde{\phi}_{IV,N}(\omega)]$ 
17: Algorithm 3  $[\tilde{Y}_{N-1}(\omega), y_{N-1}, \omega, N, T_s] \rightarrow [\tilde{Y}_N(\omega)]$ 
18: Set:  $\tilde{z}_N(\omega) := j\omega \tilde{Y}_N^T(\omega) + \frac{1}{T_s}(y_N^T e^{-j\omega N T_s} - y_0^T)$ 
19: Set:  $\tilde{\Phi}_N := [\tilde{\phi}_N^T(\omega_1) \quad \tilde{\phi}_N^T(\omega_2) \quad \dots \quad \tilde{\phi}_N^T(\omega_M)]^T$ 
20: Set:  $\tilde{\zeta}_N := [\tilde{\phi}_{IV,N}^T(\omega_1) \quad \tilde{\phi}_{IV,N}^T(\omega_2) \quad \dots \quad \tilde{\phi}_{IV,N}^T(\omega_M)]^T$ 
21: Set:  $\tilde{Z}_N := [\tilde{Z}_{N,1} \quad \dots \quad \tilde{Z}_{N,n_y}] = [\tilde{z}_N^T(\omega_1) \quad \tilde{z}_N^T(\omega_2) \quad \dots \quad \tilde{z}_N^T(\omega_M)]^T$ 
22: if  $N = n(T_{int}/T_s)$  then
23:   for  $k = 1 \rightarrow n_y$  do
24:     Algorithm 4  $[\tilde{\Phi}_{N,k}, \tilde{\zeta}_{N,k}, \tilde{Z}_{N,k}, M, n_p] \rightarrow [\hat{\Theta}_{2,k}, \hat{I}_{2,k}]$ 
25:     Algorithm 5  $[\hat{\Theta}_{1,k}, \hat{I}_{1,k}, \hat{\Theta}_{2,k}, \hat{I}_{2,k}] \rightarrow [\hat{\Theta}_k, \hat{I}_k, s_k]$ 
26:     Present:  $\hat{\Theta}_k \pm 2[s_{k,1} \dots s_{k,n_p}]^T$ 
27:   end for
28:   if  $N = n(T_{seq}/T_s)$  then
29:     Set:  $\hat{I}_{1,k} := \hat{I}_k$  and  $\hat{\Theta}_{1,k} := \hat{\Theta}_k$ 
30:     Set:  $\tilde{\phi}_0 := 0_{M \times n_p}, \tilde{Y}_0 := 0_{M \times n_y}$  and  $\tilde{z}_0 := 0_{M \times n_y}$ 
31:   end if
32:   Set:  $n := n + 1$ 
33: end if
34: if RUN == TRUE then
35:   Set:  $N := N + 1$ 
36: end if
37: end while
38: End program

```

---



# D

---

## Complementary results to the sequential identification

In this appendix more detailed results for the methods A, IV and C from Chapter 5 are presented. This is done so that the interested reader can check for more information about the simulations that have been used to produce the results.

The following cases are given here:

### **F16 Open loop**

- Measurement noise
- Process noise

### **F16 Closed loop**

- Measurement noise
- Process noise

### **JAS 39 Gripen Open loop**

- Measurement noise
- Process noise

To make it easier, the definition figures and the model structures for the F16 and JAS 39 Gripen fighters are given on the next page. Note again that the normal force, denoted  $N$ , in the figures is the same as the negative vertical force, denoted  $Z$ , in the model structure, i.e.,  $Z = -N$ .

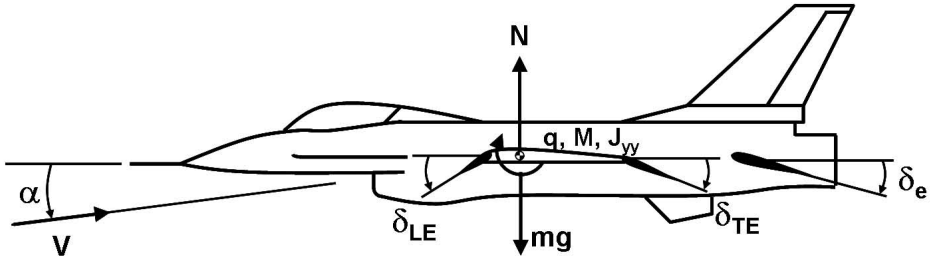


Figure D.1: Definition of the variables for the F-16.

$$\begin{aligned} \begin{bmatrix} \dot{\alpha}(t) \\ \dot{q}(t) \end{bmatrix} &= \begin{bmatrix} Z_{\alpha} & Z_q \\ M_{\alpha} & M_q \end{bmatrix} \begin{bmatrix} \alpha(t) \\ q(t) \end{bmatrix} + \begin{bmatrix} Z_{\delta_e} \\ M_{\delta_e} \end{bmatrix} [\delta_e(t)] + w(t) \\ \begin{bmatrix} \alpha_m(t) \\ q_m(t) \end{bmatrix} &= \begin{bmatrix} \alpha(t) \\ q(t) \end{bmatrix} + e(t) \end{aligned} \quad (D.1)$$

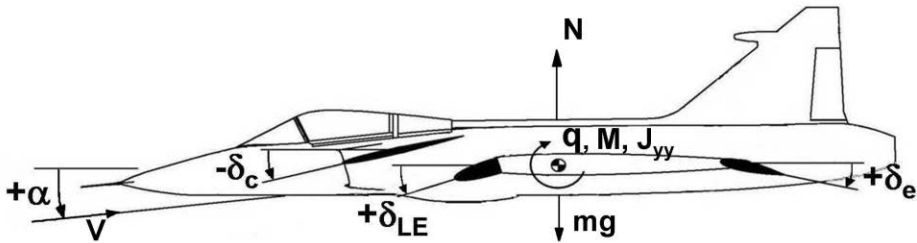
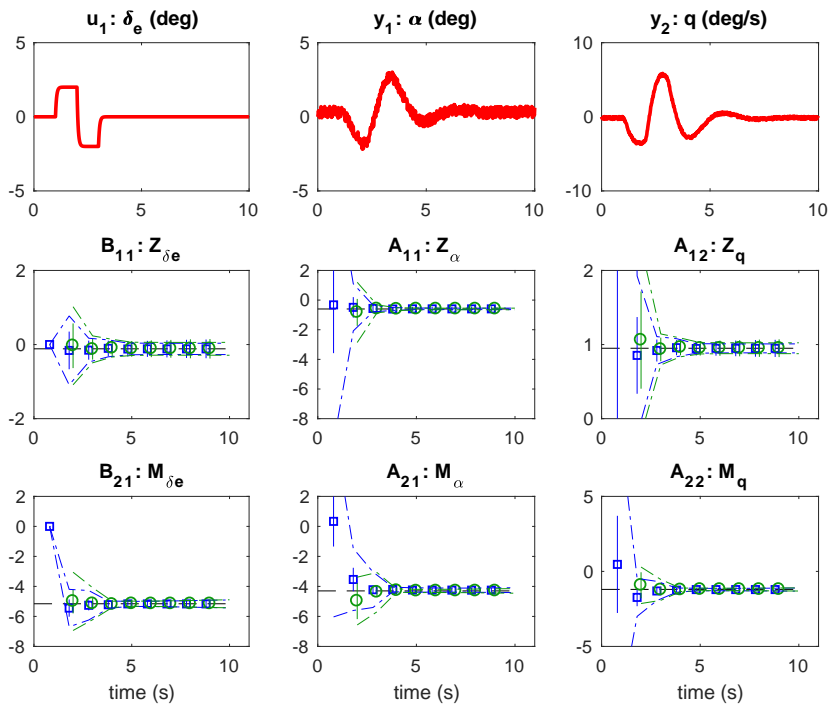


Figure D.2: Definition of the variables of JAS 39 Gripen.

$$\begin{aligned} \begin{bmatrix} \dot{\alpha}(t) \\ \dot{q}(t) \end{bmatrix} &= \begin{bmatrix} Z_{\alpha} & Z_q \\ M_{\alpha} & M_q \end{bmatrix} \begin{bmatrix} \alpha(t) \\ q(t) \end{bmatrix} + \begin{bmatrix} Z_{\delta_e} & Z_{\delta_c} \\ M_{\delta_e} & M_{\delta_c} \end{bmatrix} \begin{bmatrix} \delta_e(t) \\ \delta_c(t) \end{bmatrix} + w(t) \\ \begin{bmatrix} \alpha_m(t) \\ q_m(t) \end{bmatrix} &= \begin{bmatrix} \alpha(t) \\ q(t) \end{bmatrix} + e(t) \end{aligned} \quad (D.2)$$

## F16 Open loop

- Measurement noise



**Figure D.3:** Estimation of the F16 open loop model parameters for the measurement noise case, comparing Method A in blue with Method IV in green.

**Table D.1:** Estimation of the F16 open loop model parameters at time 9 s for the measurement noise case, comparing Method A with Method IV.

	True	Method A	Method IV
$Z_\alpha$	-0.600	$-0.592 \pm 0.176$	$-0.599 \pm 0.178$
$Z_q$	0.950	$0.948 \pm 0.123$	$0.950 \pm 0.127$
$Z_{\delta_e}$	-0.115	$-0.117 \pm 0.267$	$-0.115 \pm 0.279$
$M_\alpha$	-4.300	$-4.250 \pm 0.161$	$-4.300 \pm 0.163$
$M_q$	-1.200	$-1.211 \pm 0.112$	$-1.203 \pm 0.117$
$M_{\delta_e}$	-5.157	$-5.167 \pm 0.245$	$-5.159 \pm 0.256$

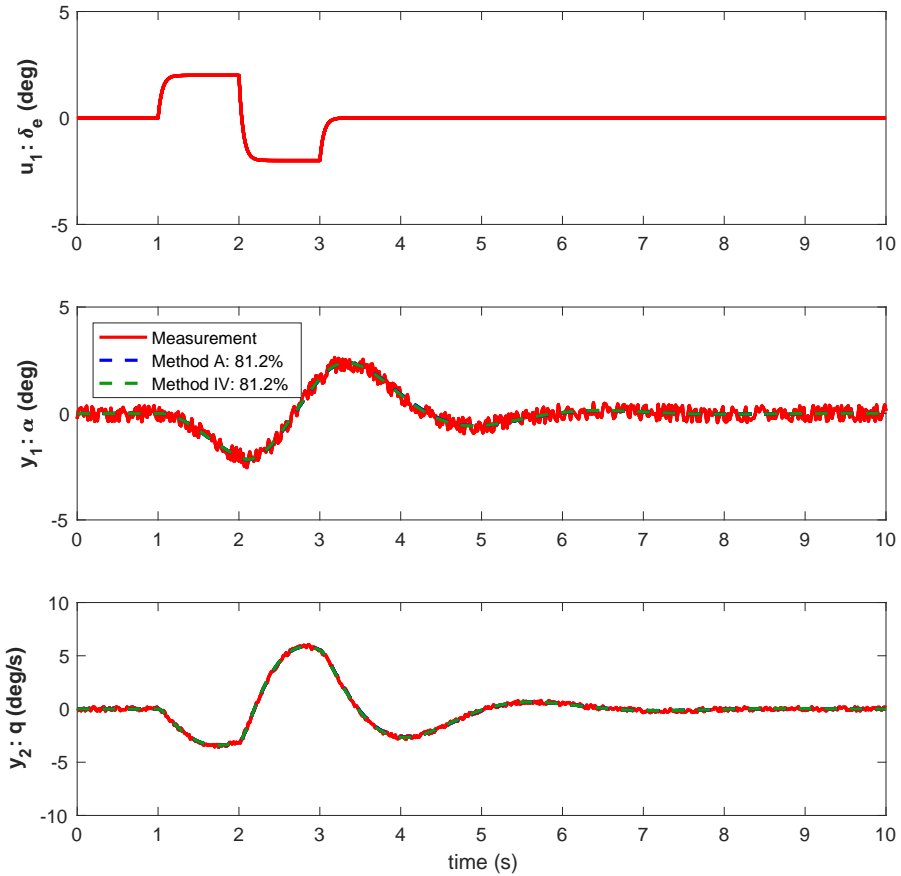


**Figure D.4:** Validation of the F16 open loop model parameters for the measurement noise case, comparing Method A in blue with Method IV in green.

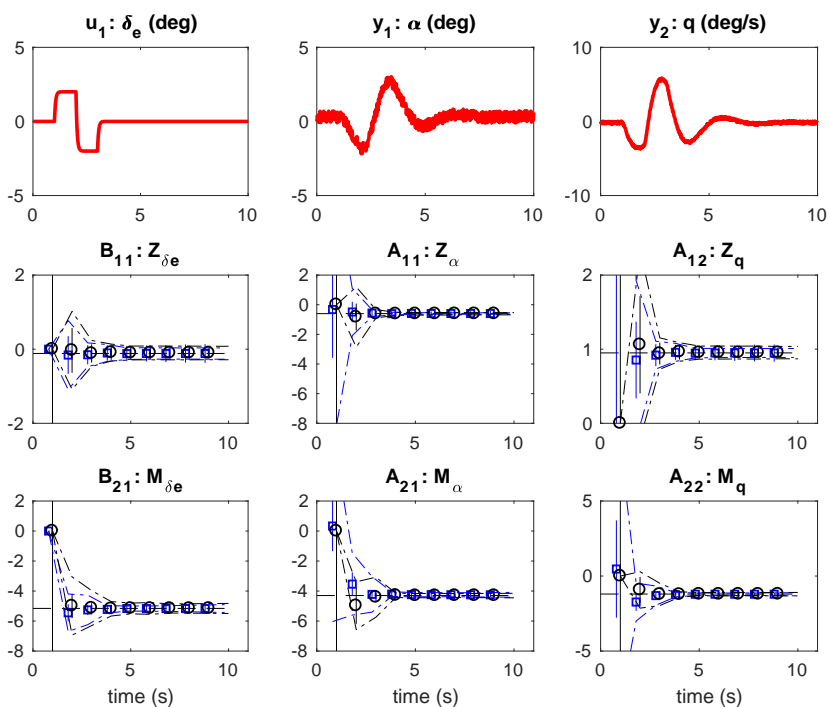


**Figure D.5:** Estimation of the F16 open loop model parameters for the measurement noise case, comparing Method A in blue with Method C in black.

**Table D.2:** Estimation of the F16 open loop model parameters at time 9 s for the measurement noise case, comparing Method A with Method C.

	True	Method A	Method C
$Z_\alpha$	-0.600	$-0.592 \pm 0.176$	$-0.608 \pm 0.096$
$Z_q$	0.950	$0.948 \pm 0.123$	$0.954 \pm 0.071$
$Z_{\delta_e}$	-0.115	$-0.117 \pm 0.267$	$-0.103 \pm 0.143$
$M_\alpha$	-4.300	$-4.250 \pm 0.161$	$-4.302 \pm 0.102$
$M_q$	-1.200	$-1.211 \pm 0.112$	$-1.207 \pm 0.074$
$M_{\delta_e}$	-5.157	$-5.167 \pm 0.245$	$-5.158 \pm 0.154$



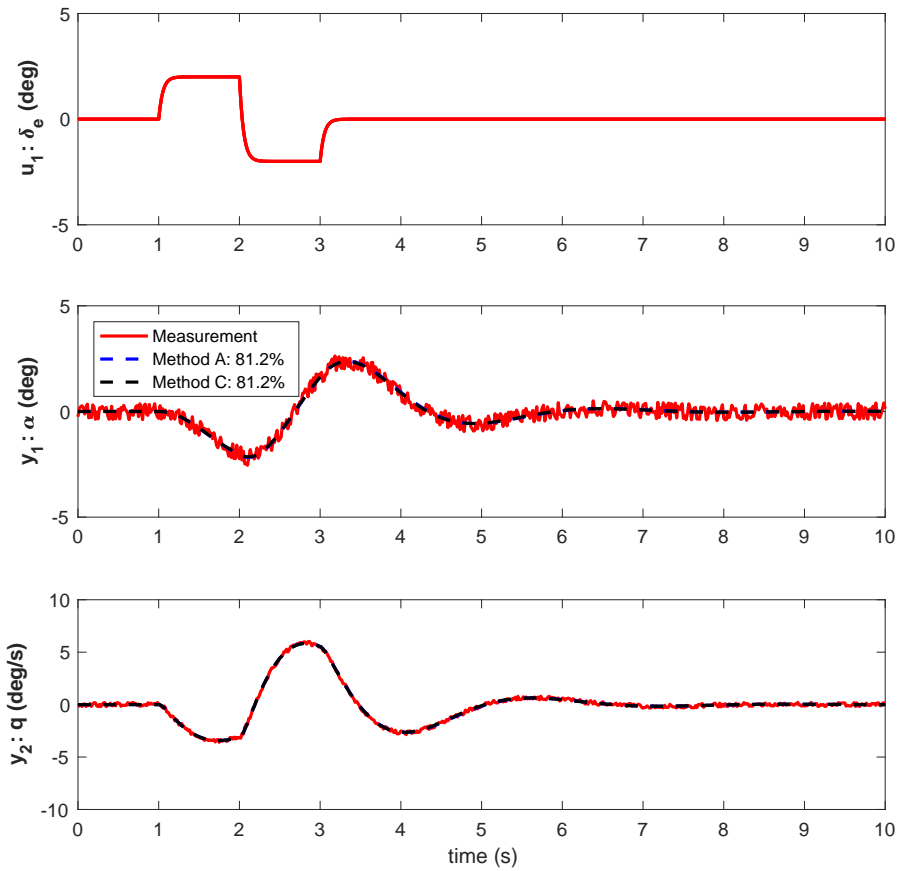


**Figure D.6:** Validation of the F16 open loop model parameters for the measurement noise case, comparing Method A in blue with Method C in black.

- Process noise

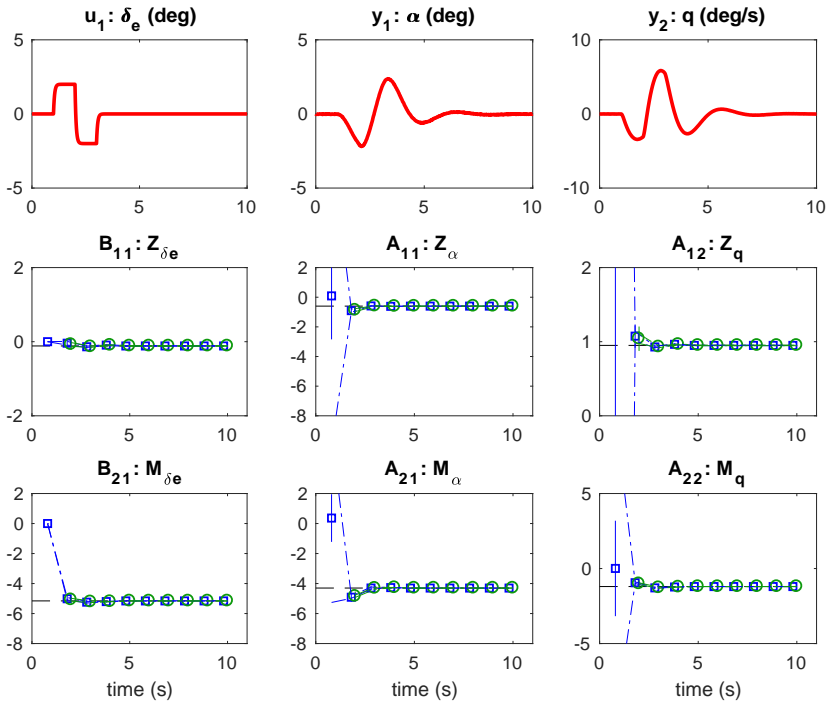


**Figure D.7:** Estimation of the F16 open loop model parameters for the no process noise case, comparing Method A in blue with Method IV in green.

**Table D.3:** Estimation of the F16 open loop model parameters at time 10 s for the no process noise case, comparing Method A with Method IV.

	True	Method A	Method IV
$Z_\alpha$	-0.600	$-0.600 \pm 0.009$	$-0.600 \pm 0.009$
$Z_q$	0.950	$0.950 \pm 0.006$	$0.950 \pm 0.007$
$Z_{\delta_e}$	-0.115	$-0.115 \pm 0.014$	$-0.115 \pm 0.014$
$M_\alpha$	-4.300	$-4.302 \pm 0.008$	$-4.302 \pm 0.009$
$M_q$	-1.200	$-1.201 \pm 0.006$	$-1.202 \pm 0.006$
$M_{\delta_e}$	-5.157	$-5.158 \pm 0.013$	$-5.160 \pm 0.013$

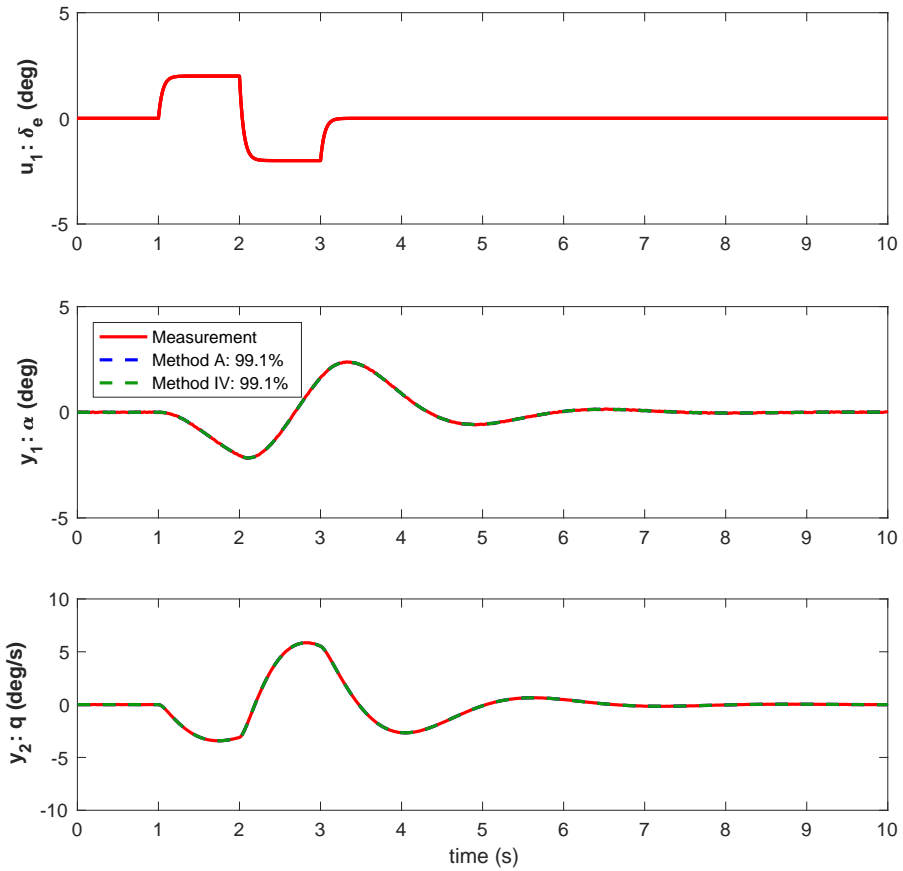


**Figure D.8:** Validation of the F16 open loop model parameters for the no process noise case, comparing Method A in blue with Method IV in green.

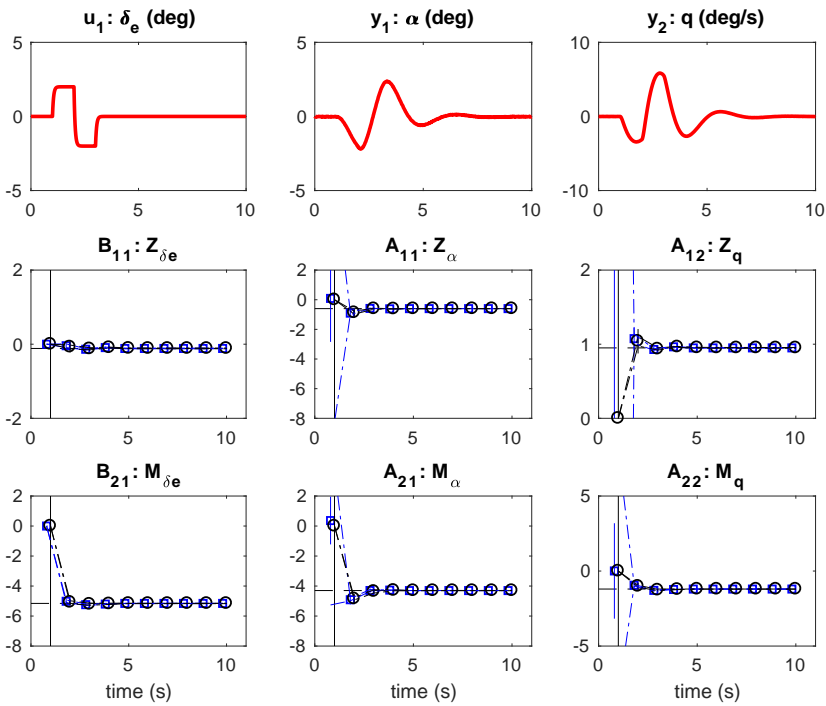


**Figure D.9:** Estimation of the F16 open loop model parameters for the no process noise case, comparing Method A in blue with Method C in black.

**Table D.4:** Estimation of the F16 open loop model parameters at time 10 s for the no process noise case, comparing Method A with Method C.

	True	Method A	Method C
$Z_\alpha$	-0.600	$-0.600 \pm 0.009$	$-0.601 \pm 0.006$
$Z_q$	0.950	$0.950 \pm 0.006$	$0.951 \pm 0.004$
$Z_{\delta_e}$	-0.115	$-0.115 \pm 0.014$	$-0.114 \pm 0.009$
$M_\alpha$	-4.300	$-4.302 \pm 0.008$	$-4.302 \pm 0.006$
$M_q$	-1.200	$-1.201 \pm 0.006$	$-1.202 \pm 0.005$
$M_{\delta_e}$	-5.157	$-5.158 \pm 0.013$	$-5.160 \pm 0.010$

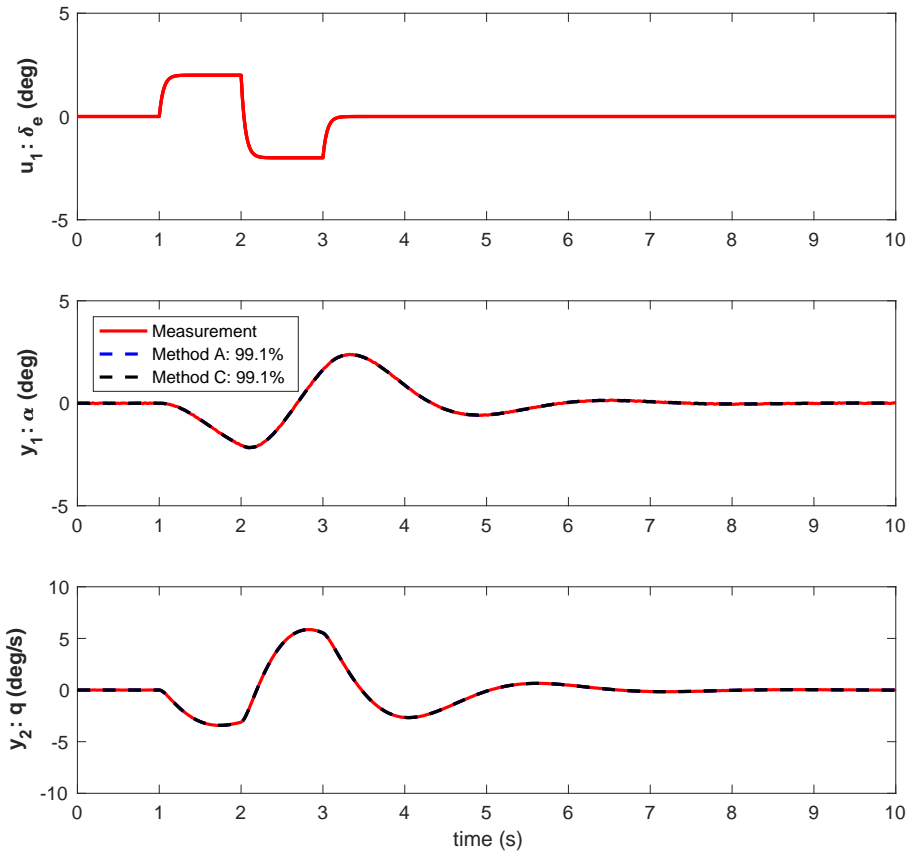


**Figure D.10:** Validation of the F16 open loop model parameters for the no process noise case, comparing Method A in blue with Method C in black.

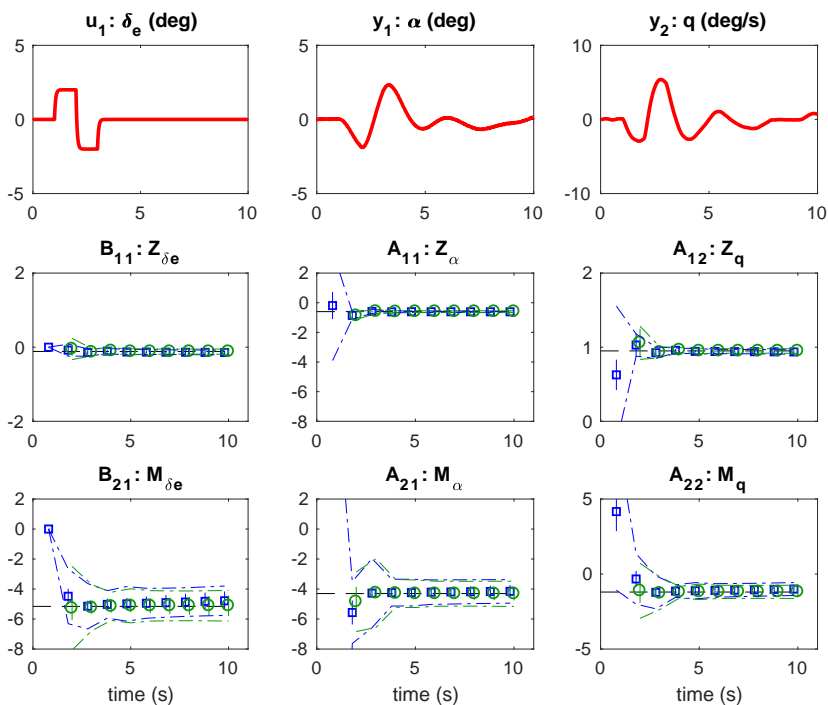


**Figure D.11:** Estimation of the F16 open loop model parameters for the light process noise case, comparing Method A in blue with Method IV in green.

**Table D.5:** Estimation of the F16 open loop model parameters at time 10 s for the light process noise case, comparing Method A with Method IV.

	True	Method A	Method IV
$Z_\alpha$	-0.600	$-0.612 \pm 0.030$	$-0.599 \pm 0.033$
$Z_q$	0.950	$0.936 \pm 0.021$	$0.949 \pm 0.023$
$Z_{\delta_e}$	-0.115	$-0.143 \pm 0.045$	$-0.120 \pm 0.050$
$M_\alpha$	-4.300	$-4.153 \pm 0.415$	$-4.315 \pm 0.447$
$M_q$	-1.200	$-1.000 \pm 0.282$	$-1.186 \pm 0.315$
$M_{\delta_e}$	-5.157	$-4.782 \pm 0.621$	$-5.115 \pm 0.689$

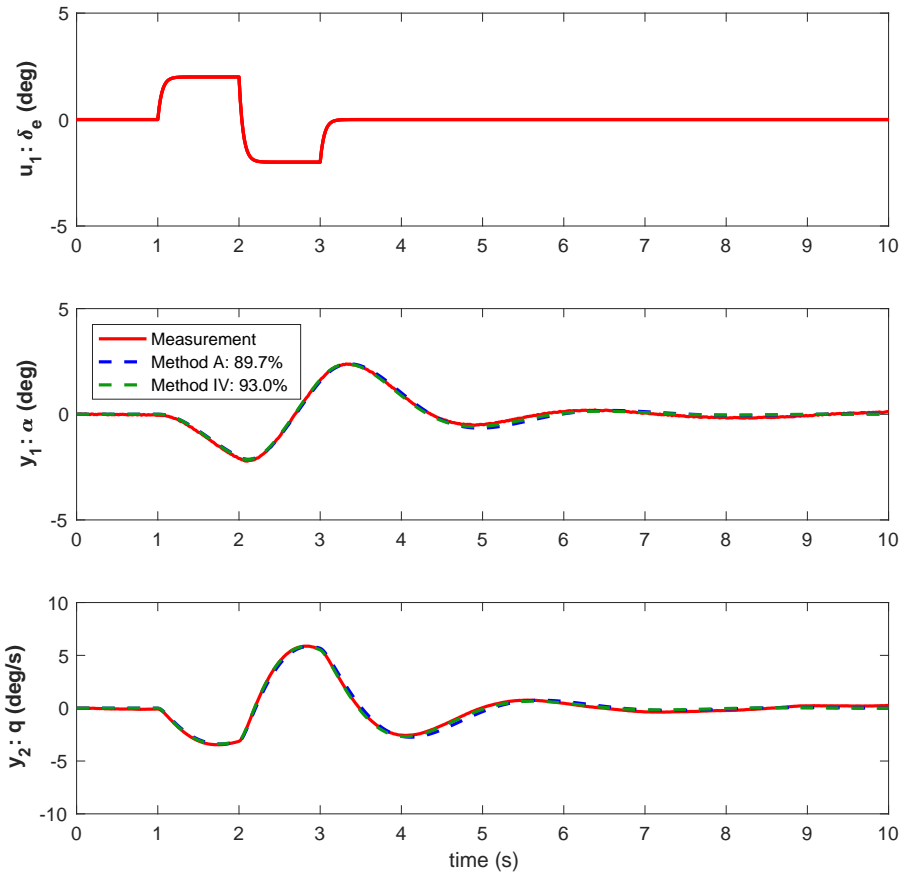


**Figure D.12:** Validation of the F16 open loop model parameters for the light process noise case, comparing Method A in blue with Method IV in green.

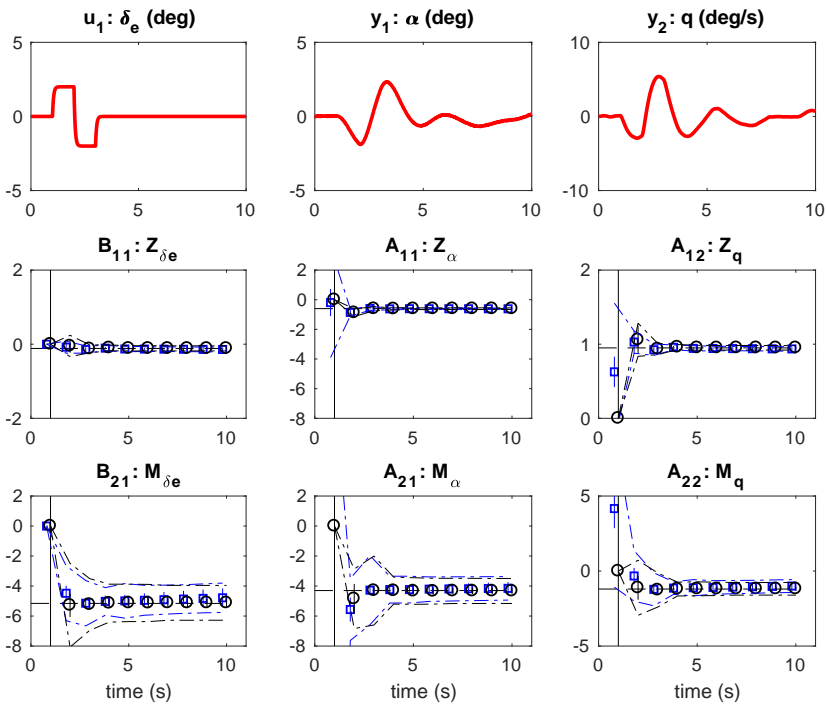


**Figure D.13:** Estimation of the F16 open loop model parameters for the light process noise case, comparing Method A in blue with Method C in black.

**Table D.6:** Estimation of the F16 open loop model parameters at time 10 s for the light process noise case, comparing Method A with Method C.

	True	Method A	Method C
$Z_\alpha$	-0.600	$-0.612 \pm 0.030$	$-0.605 \pm 0.017$
$Z_q$	0.950	$0.936 \pm 0.021$	$0.951 \pm 0.012$
$Z_{\delta_e}$	-0.115	$-0.143 \pm 0.045$	$-0.113 \pm 0.025$
$M_\alpha$	-4.300	$-4.153 \pm 0.415$	$-4.328 \pm 0.197$
$M_q$	-1.200	$-1.000 \pm 0.282$	$-1.184 \pm 0.144$
$M_{\delta_e}$	-5.157	$-4.782 \pm 0.621$	$-5.119 \pm 0.262$



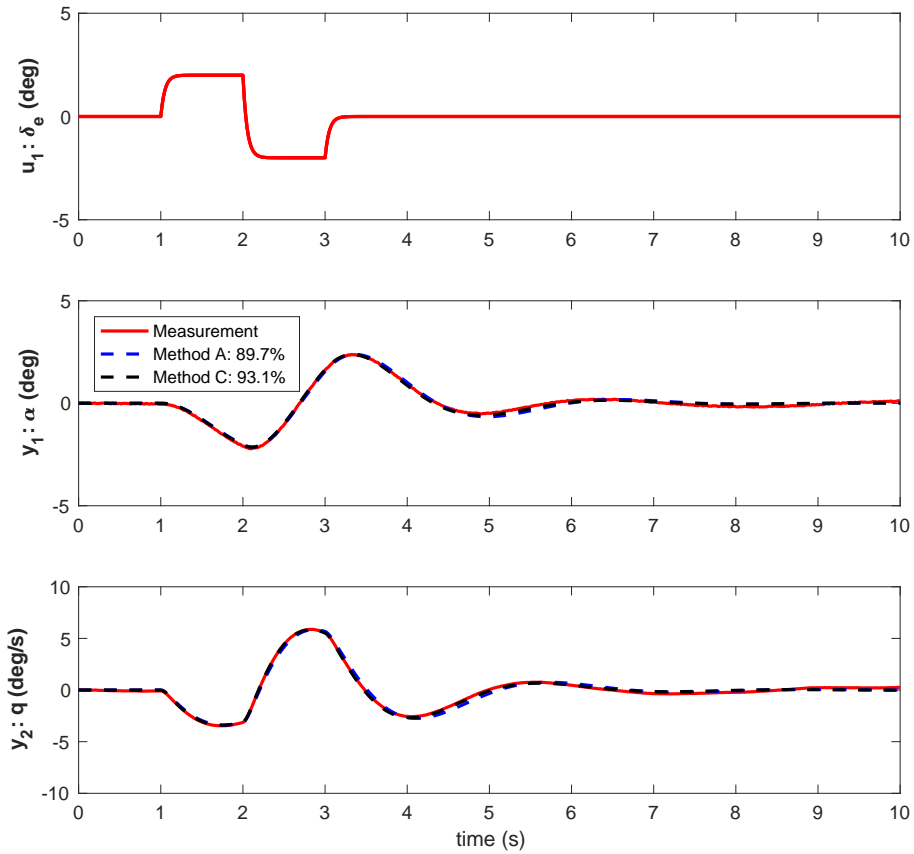


**Figure D.14:** Validation of the F16 open loop model parameters for the light process noise case, comparing Method A in blue with Method C in black.

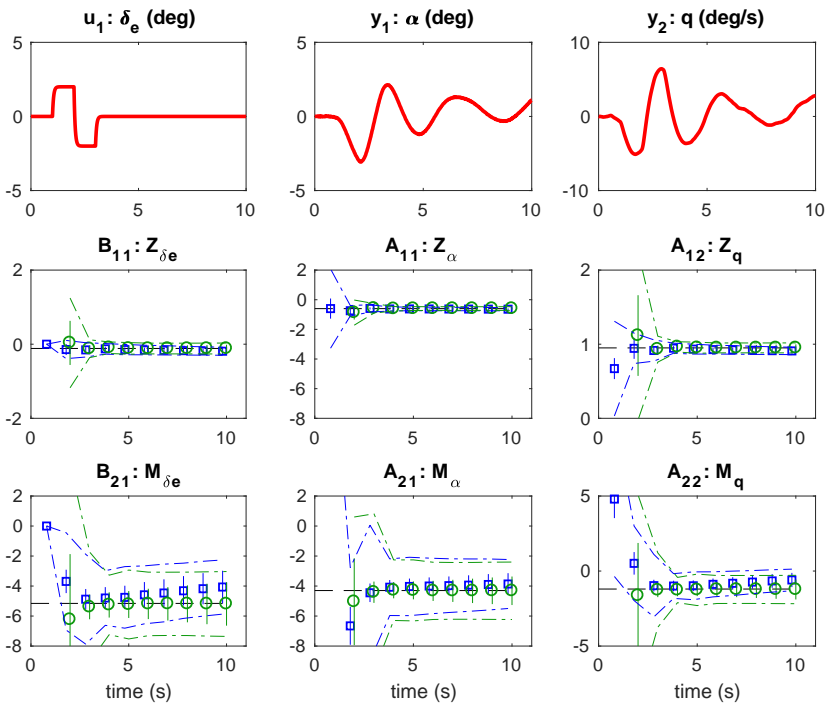


**Figure D.15:** Estimation of the F16 open loop model parameters for the medium process noise case, comparing Method A in blue with Method IV in green.

**Table D.7:** Estimation of the F16 open loop model parameters at time 10 s for the medium process noise case, comparing Method A with Method IV.

	True	Method A	Method IV
$Z_\alpha$	-0.600	$-0.638 \pm 0.051$	$-0.595 \pm 0.067$
$Z_q$	0.950	$0.909 \pm 0.034$	$0.950 \pm 0.047$
$Z_{\delta_e}$	-0.115	$-0.190 \pm 0.076$	$-0.116 \pm 0.102$
$M_\alpha$	-4.300	$-3.864 \pm 0.721$	$-4.316 \pm 0.950$
$M_q$	-1.200	$-0.595 \pm 0.473$	$-1.231 \pm 0.664$
$M_{\delta_e}$	-5.157	$-4.065 \pm 1.084$	$-5.195 \pm 1.445$

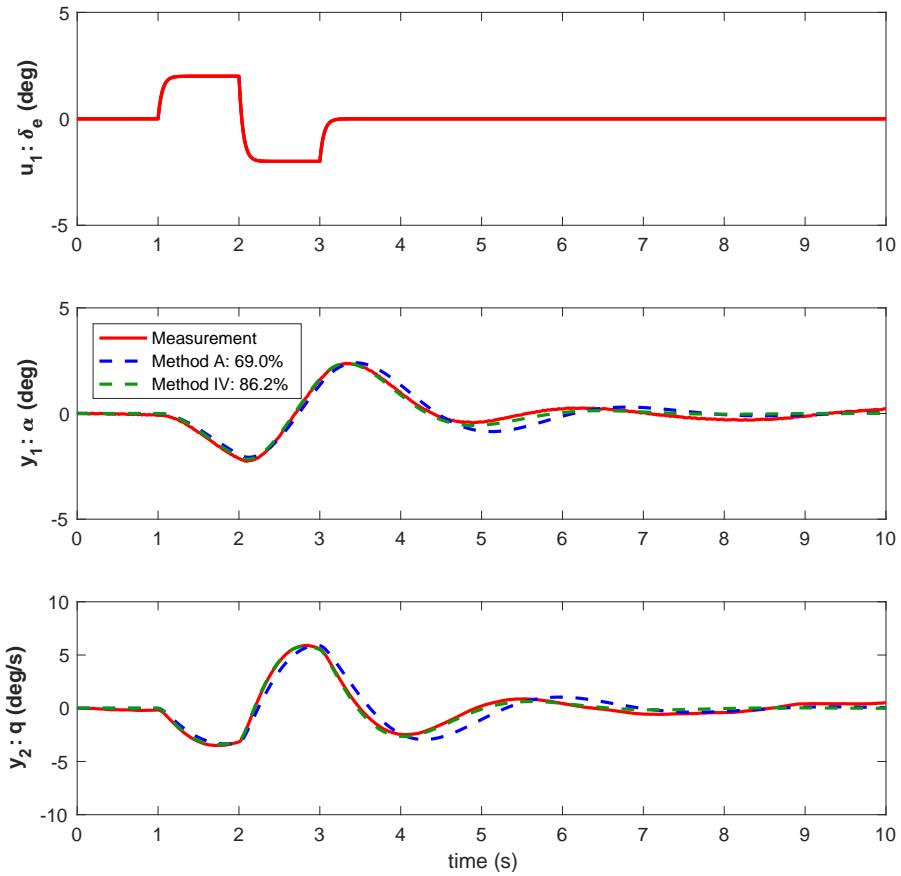


**Figure D.16:** Validation of the F16 open loop model parameters for the medium process noise case, comparing Method A in blue with Method IV in green.

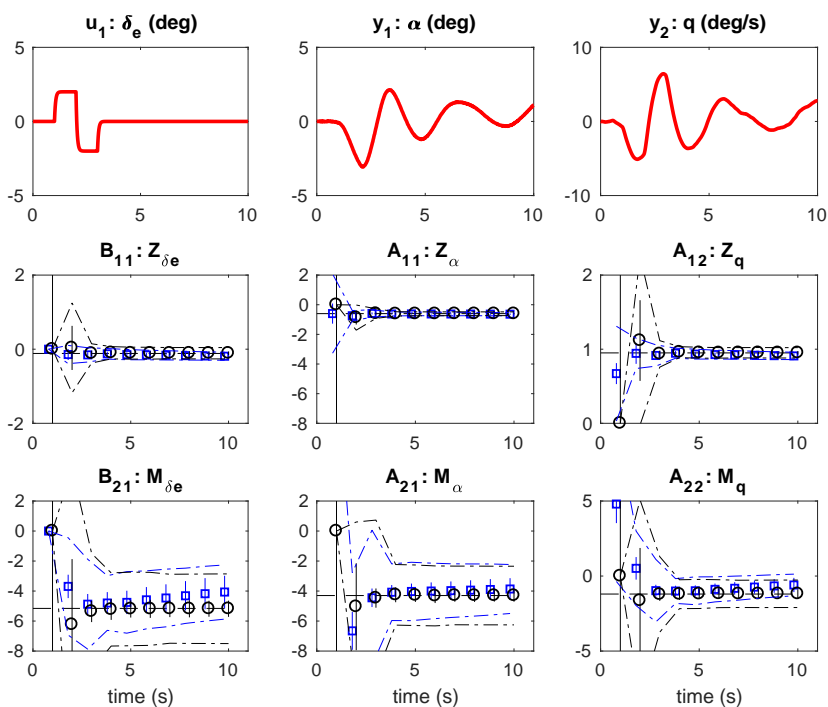


**Figure D.17:** Estimation of the F16 open loop model parameters for the medium process noise case, comparing Method A in blue with Method C in black.

**Table D.8:** Estimation of the F16 open loop model parameters at time 10 s for the medium process noise case, comparing Method A with Method C.

	True	Method A	Method C
$Z_\alpha$	-0.600	$-0.638 \pm 0.051$	$-0.609 \pm 0.033$
$Z_q$	0.950	$0.909 \pm 0.034$	$0.951 \pm 0.023$
$Z_{\delta_e}$	-0.115	$-0.190 \pm 0.076$	$-0.109 \pm 0.046$
$M_\alpha$	-4.300	$-3.864 \pm 0.721$	$-4.300 \pm 0.411$
$M_q$	-1.200	$-0.595 \pm 0.473$	$-1.183 \pm 0.295$
$M_{\delta_e}$	-5.157	$-4.065 \pm 1.084$	$-5.179 \pm 0.540$

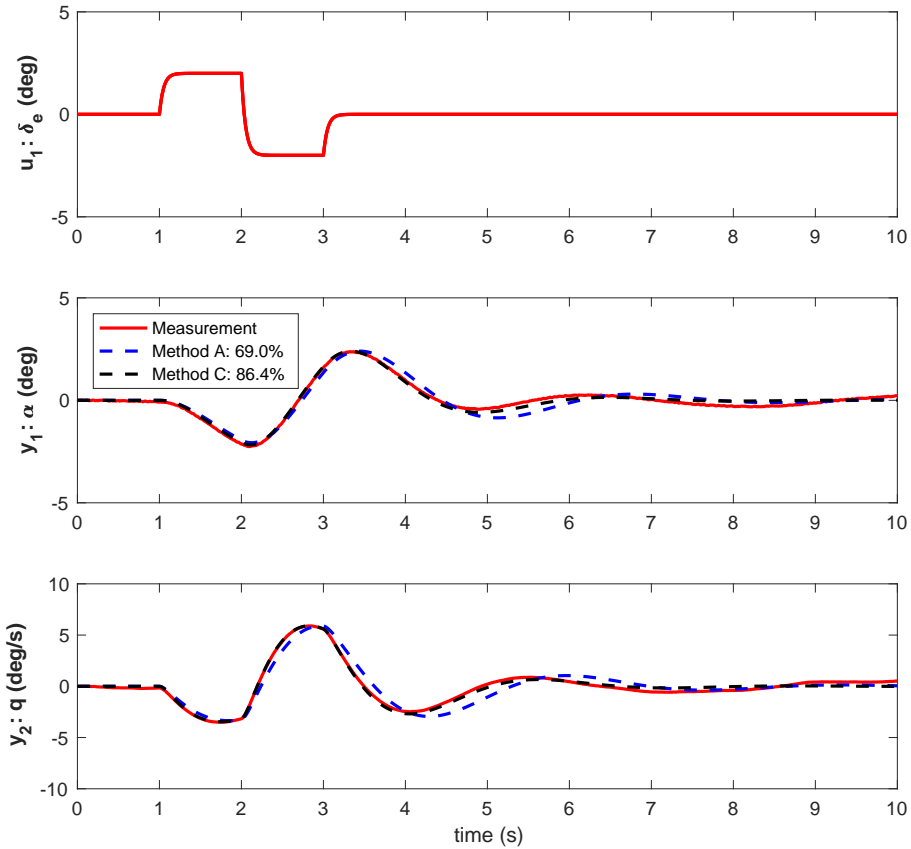


**Figure D.18:** Validation of the F16 open loop model parameters for the medium process noise case, comparing Method A in blue with Method C in black.

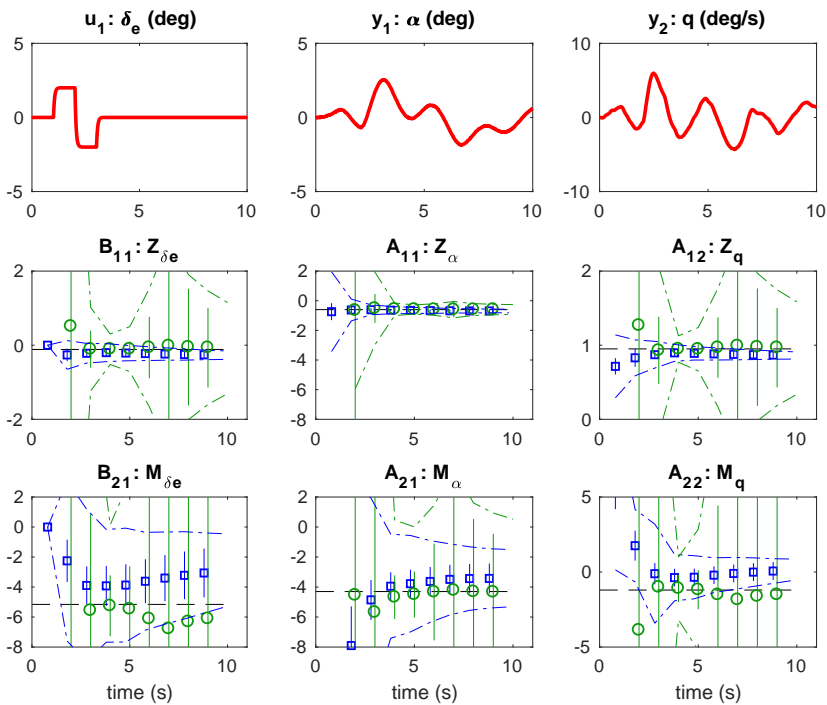


**Figure D.19:** Estimation of the F16 open loop model parameters for the severe process noise case, comparing Method A in blue with Method IV in green.

**Table D.9:** Estimation of the F16 open loop model parameters at time 10 s for the severe process noise case, comparing Method A with Method IV.

	True	Method A	Method IV
$Z_\alpha$	-0.600	$-0.693 \pm 0.068$	$-0.592 \pm 0.239$
$Z_q$	0.950	$0.862 \pm 0.040$	$0.961 \pm 0.385$
$Z_{\delta_e}$	-0.115	$-0.269 \pm 0.112$	$-0.078 \pm 0.782$
$M_\alpha$	-4.300	$-3.410 \pm 1.010$	$-4.356 \pm 3.406$
$M_q$	-1.200	$0.152 \pm 0.598$	$-1.429 \pm 5.628$
$M_{\delta_e}$	-5.157	$-2.902 \pm 1.676$	$-5.960 \pm 11.486$

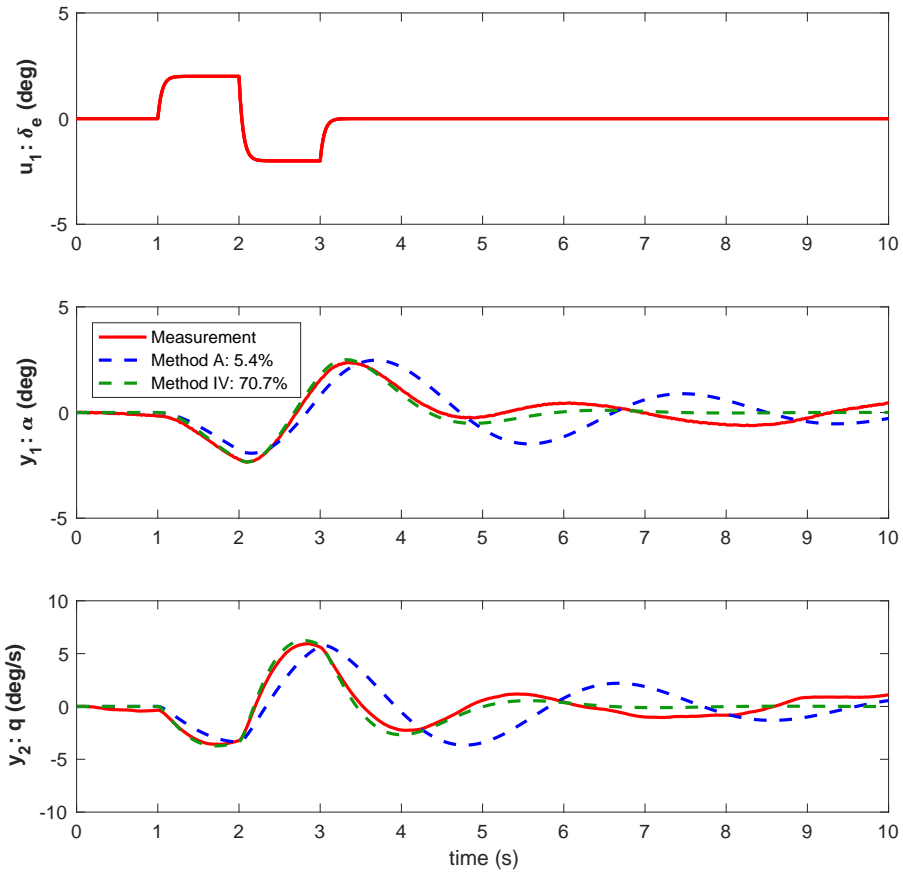


**Figure D.20:** Validation of the F16 open loop model parameters for the severe process noise case, comparing Method A in blue with Method IV in green.

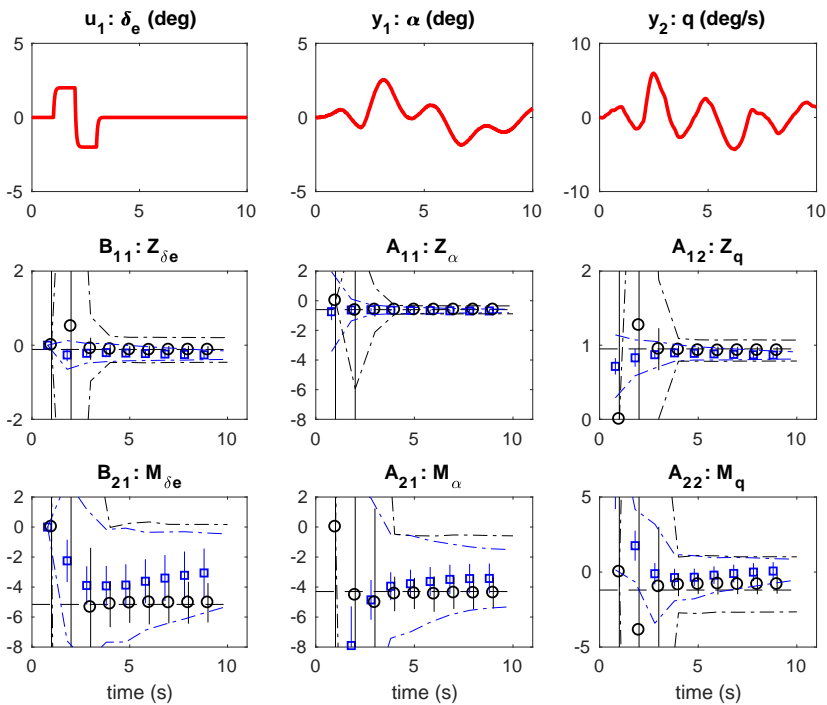


**Figure D.21:** Estimation of the F16 open loop model parameters for the severe process noise case, comparing Method A in blue with Method C in black.

**Table D.10:** Estimation of the F16 open loop model parameters at time 10 s for the severe process noise case, comparing Method A with Method C.

	True	Method A	Method C
$Z_\alpha$	-0.600	$-0.693 \pm 0.068$	$-0.615 \pm 0.080$
$Z_q$	0.950	$0.862 \pm 0.040$	$0.928 \pm 0.049$
$Z_{\delta_e}$	-0.115	$-0.269 \pm 0.112$	$-0.129 \pm 0.105$
$M_\alpha$	-4.300	$-3.410 \pm 1.010$	$-4.399 \pm 1.045$
$M_q$	-1.200	$0.152 \pm 0.598$	$-0.820 \pm 0.629$
$M_{\delta_e}$	-5.157	$-2.902 \pm 1.676$	$-5.049 \pm 1.324$



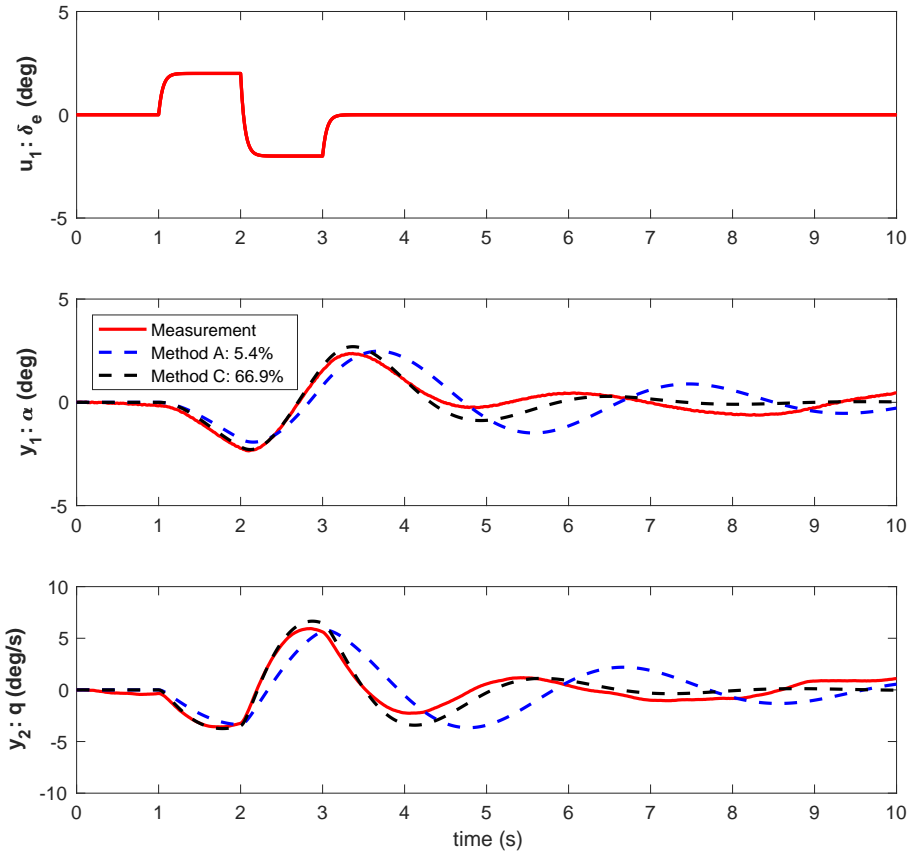


**Figure D.22:** Validation of the F16 open loop model parameters for the severe process noise case, comparing Method A in blue with Method C in black.

## F16 Closed loop

- Measurement noise

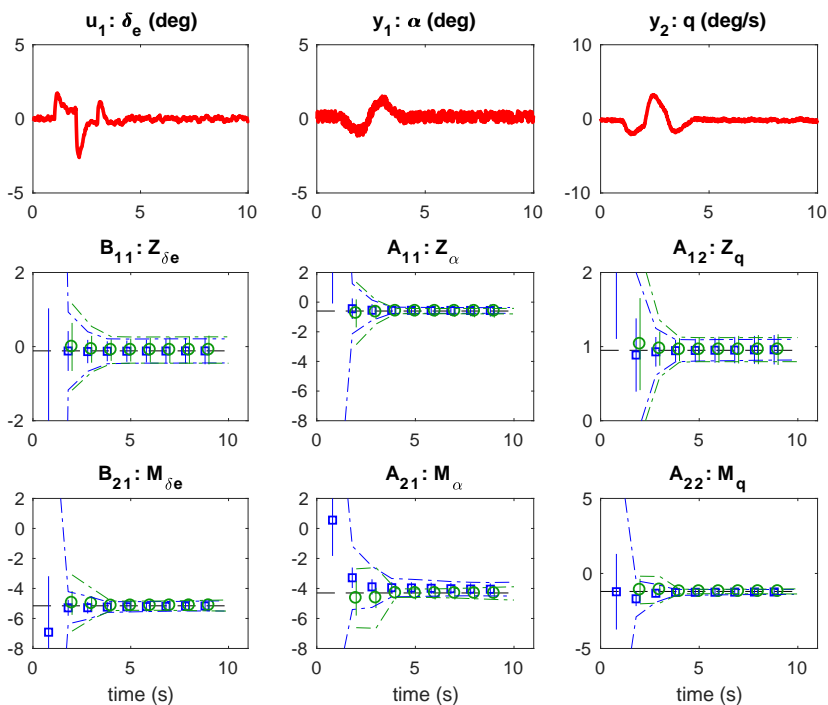


**Figure D.23:** Estimation of the F16 closed loop model parameters for the measurement noise case, comparing Method A in blue with Method IV in green.

**Table D.11:** Estimation of the F16 closed loop model parameters at time 9 s for the measurement noise case, comparing Method A with Method IV.

	True	Method A	Method IV
$Z_\alpha$	-0.600	$-0.556 \pm 0.429$	$-0.608 \pm 0.450$
$Z_q$	0.950	$0.958 \pm 0.206$	$0.959 \pm 0.215$
$Z_{\delta_e}$	-0.115	$-0.116 \pm 0.375$	$-0.092 \pm 0.403$
$M_\alpha$	-4.300	$-4.045 \pm 0.396$	$-4.330 \pm 0.427$
$M_q$	-1.200	$-1.233 \pm 0.190$	$-1.197 \pm 0.204$
$M_{\delta_e}$	-5.157	$-5.164 \pm 0.346$	$-5.138 \pm 0.382$

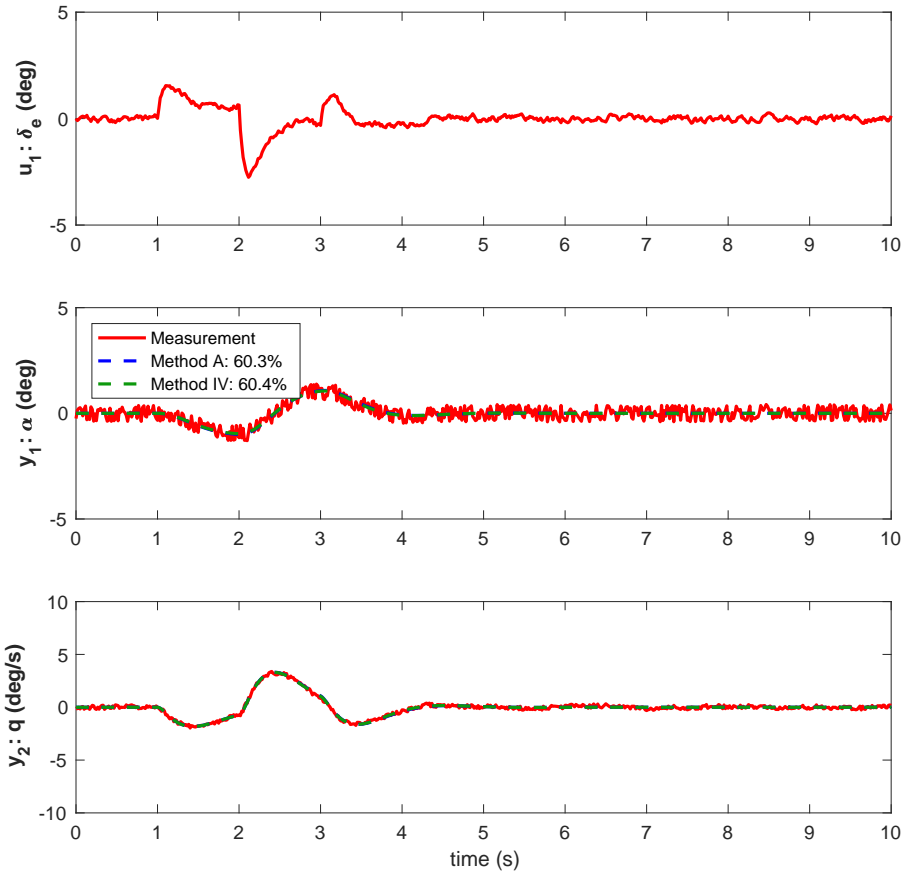


**Figure D.24:** Validation of the F16 closed loop model parameters for the measurement noise case, comparing Method A in blue with Method IV in green.

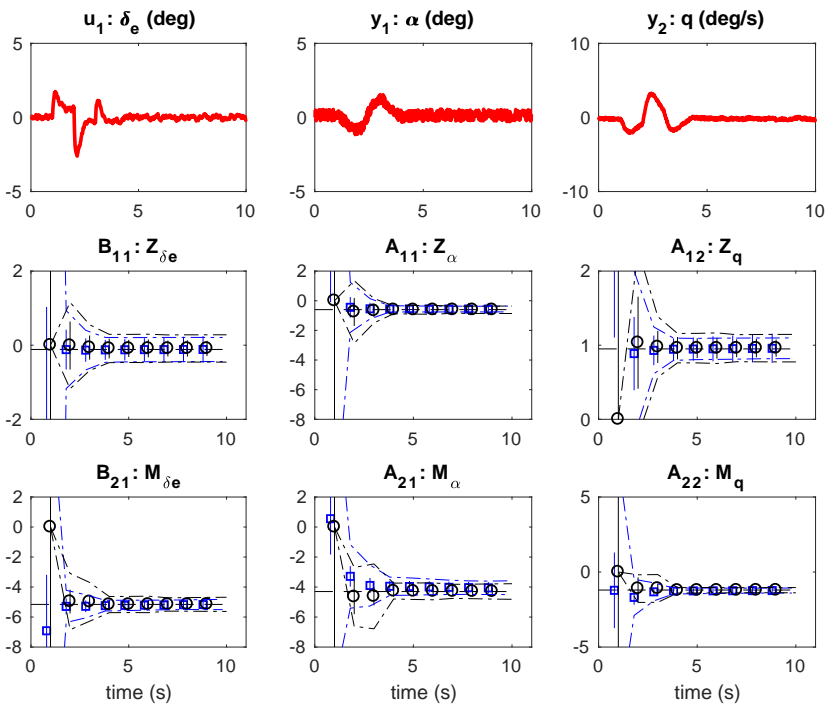


**Figure D.25:** Estimation of the F16 closed loop model parameters for the measurement noise case, comparing Method A in blue with Method C in black.

**Table D.12:** Estimation of the F16 closed loop model parameters at time 9 s for the measurement noise case, comparing Method A with Method C.

	True	Method A	Method C
$Z_\alpha$	-0.600	$-0.556 \pm 0.429$	$-0.611 \pm 0.233$
$Z_q$	0.950	$0.958 \pm 0.206$	$0.960 \pm 0.118$
$Z_{\delta_e}$	-0.115	$-0.116 \pm 0.375$	$-0.088 \pm 0.207$
$M_\alpha$	-4.300	$-4.045 \pm 0.396$	$-4.298 \pm 0.249$
$M_q$	-1.200	$-1.233 \pm 0.190$	$-1.208 \pm 0.125$
$M_{\delta_e}$	-5.157	$-5.164 \pm 0.346$	$-5.154 \pm 0.223$

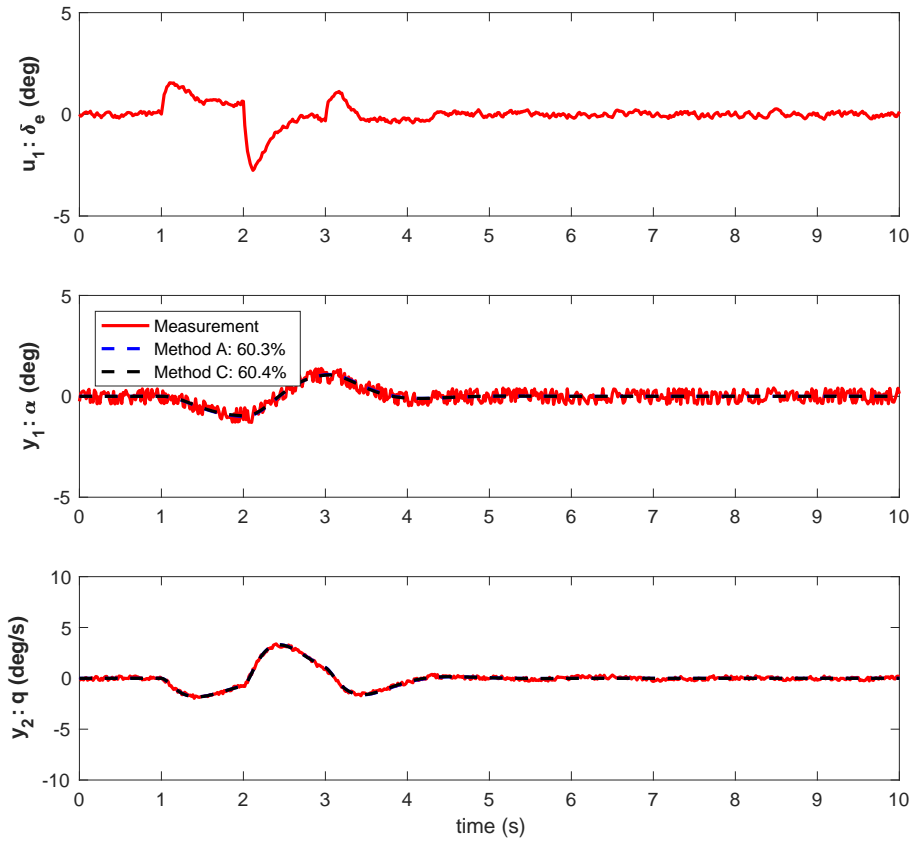


**Figure D.26:** Validation of the F16 closed loop model parameters for the measurement noise case, comparing Method A in blue with Method C in black.

- Process noise

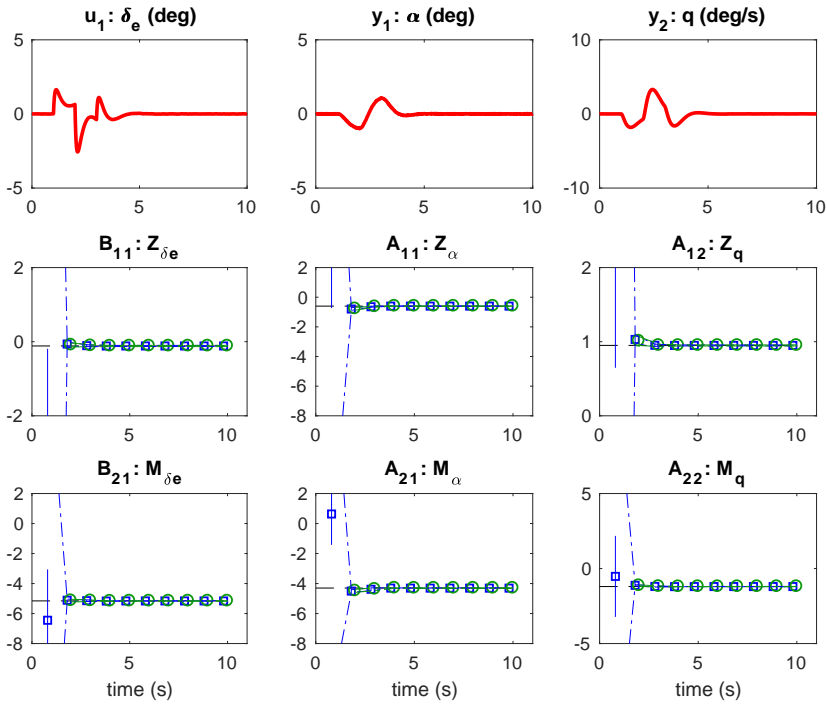


**Figure D.27:** Estimation of the F16 closed loop model parameters for the no process noise case, comparing Method A in blue with Method IV in green.

**Table D.13:** Estimation of the F16 closed loop model parameters at time 10 s for the no process noise case, comparing Method A with Method IV.

	True	Method A	Method IV
$Z_\alpha$	-0.600	$-0.600 \pm 0.023$	$-0.600 \pm 0.023$
$Z_q$	0.950	$0.950 \pm 0.011$	$0.950 \pm 0.011$
$Z_{\delta_e}$	-0.115	$-0.116 \pm 0.019$	$-0.116 \pm 0.021$
$M_\alpha$	-4.300	$-4.307 \pm 0.021$	$-4.306 \pm 0.022$
$M_q$	-1.200	$-1.202 \pm 0.010$	$-1.203 \pm 0.010$
$M_{\delta_e}$	-5.157	$-5.160 \pm 0.018$	$-5.164 \pm 0.019$

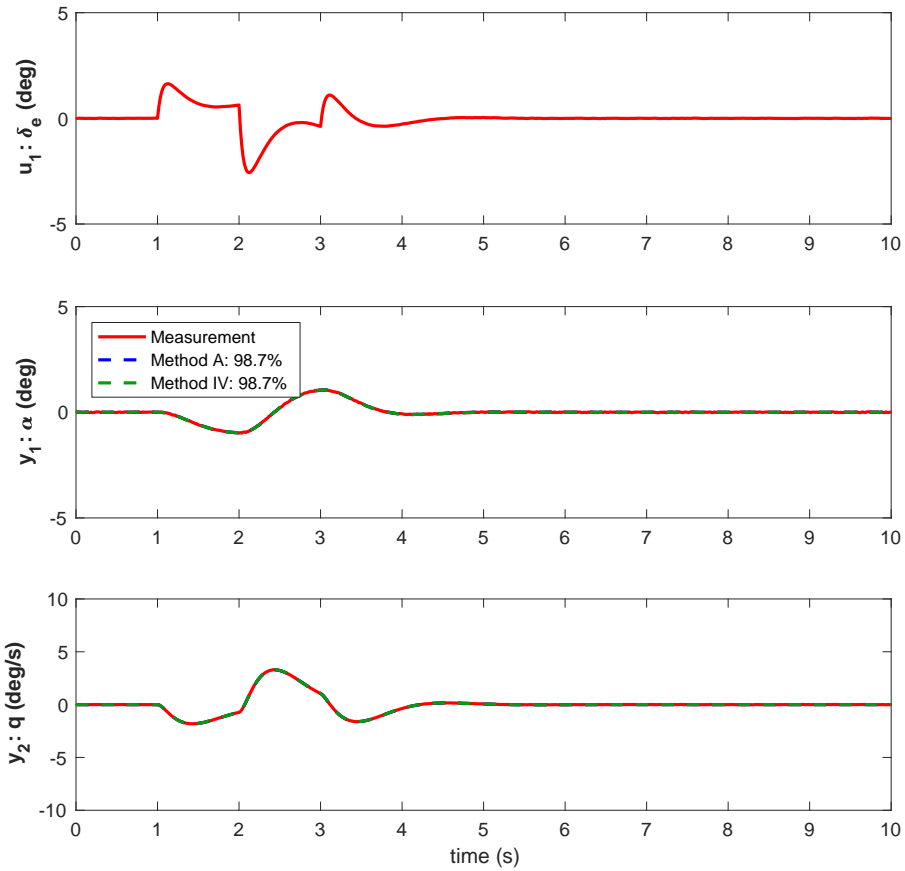


**Figure D.28:** Validation of the F16 closed loop model parameters for the no process noise case, comparing Method A in blue with Method IV in green.

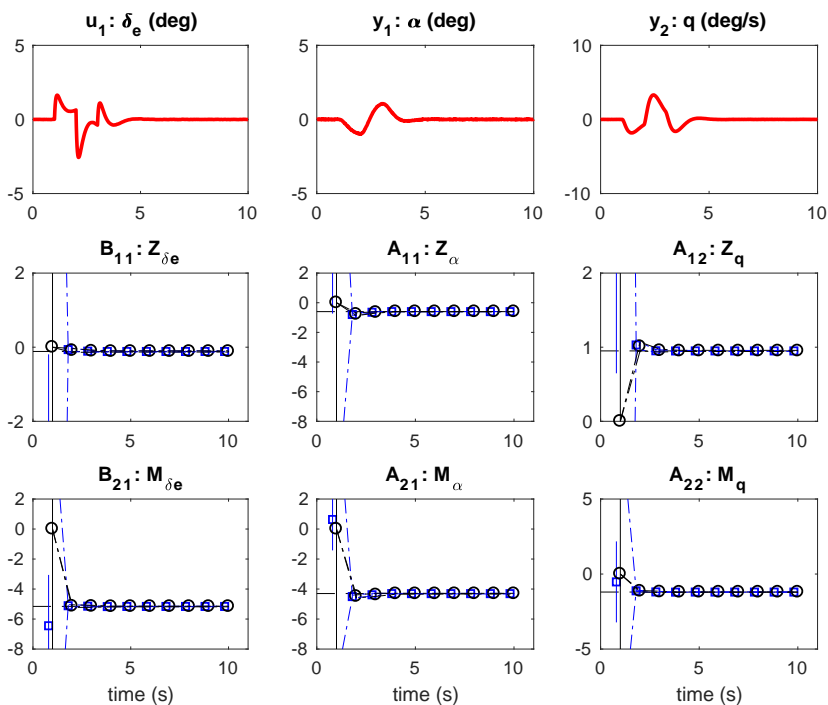


**Figure D.29:** Estimation of the F16 closed loop model parameters for the no process noise case, comparing Method A in blue with Method C in black.

**Table D.14:** Estimation of the F16 closed loop model parameters at time 10 s for the no process noise case, comparing Method A with Method C.

	True	Method A	Method C
$Z_\alpha$	-0.600	$-0.600 \pm 0.023$	$-0.602 \pm 0.013$
$Z_q$	0.950	$0.950 \pm 0.011$	$0.950 \pm 0.006$
$Z_{\delta_e}$	-0.115	$-0.116 \pm 0.019$	$-0.115 \pm 0.011$
$M_\alpha$	-4.300	$-4.307 \pm 0.021$	$-4.309 \pm 0.014$
$M_q$	-1.200	$-1.202 \pm 0.010$	$-1.203 \pm 0.007$
$M_{\delta_e}$	-5.157	$-5.160 \pm 0.018$	$-5.164 \pm 0.012$



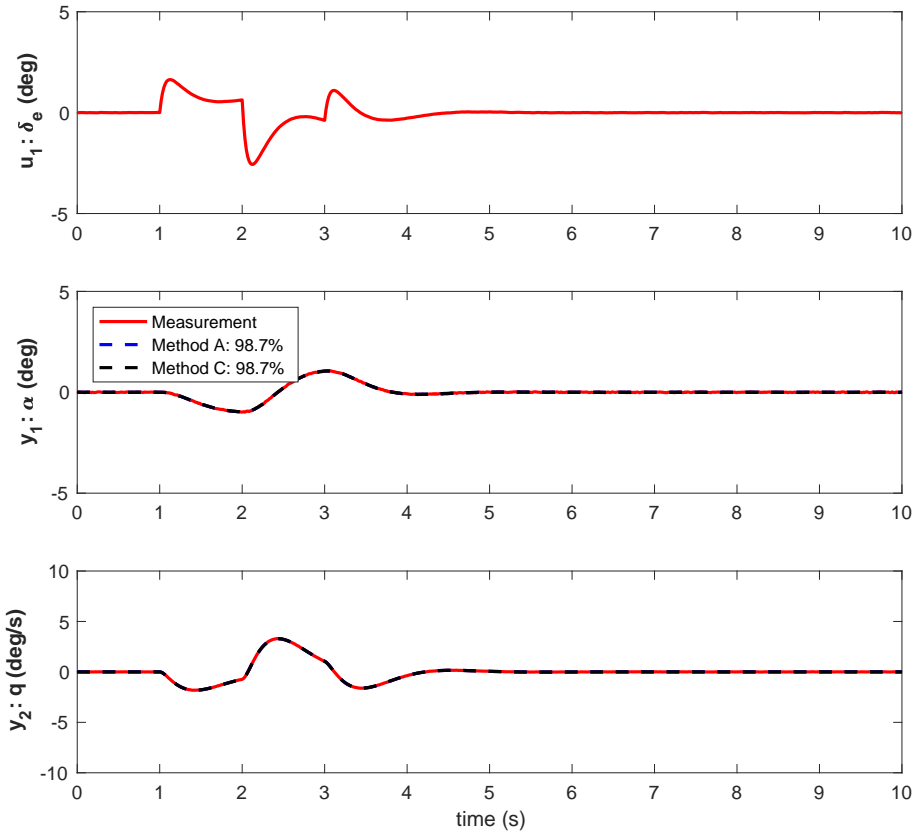


**Figure D.30:** Validation of the F16 closed loop model parameters for the no process noise case, comparing Method A in blue with Method C in black.

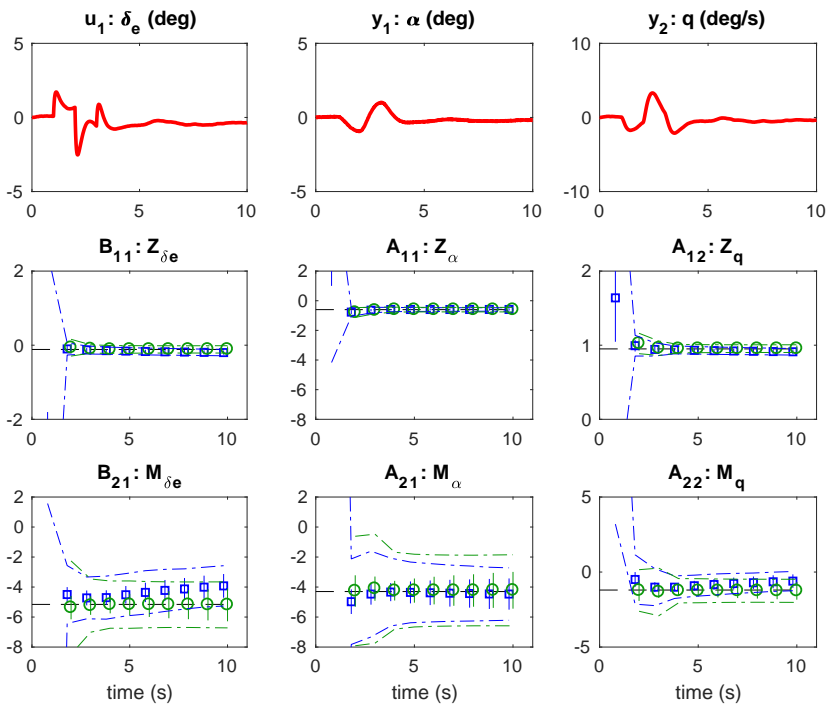


**Figure D.31:** Estimation of the F16 closed loop model parameters for the light process noise case, comparing Method A in blue with Method IV in green.

**Table D.15:** Estimation of the F16 closed loop model parameters at time 10 s for the light process noise case, comparing Method A with Method IV.

	True	Method A	Method IV
$Z_\alpha$	-0.600	$-0.590 \pm 0.074$	$-0.602 \pm 0.086$
$Z_q$	0.950	$0.911 \pm 0.032$	$0.954 \pm 0.042$
$Z_{\delta_e}$	-0.115	$-0.199 \pm 0.056$	$-0.113 \pm 0.077$
$M_\alpha$	-4.300	$-4.467 \pm 1.040$	$-4.216 \pm 1.225$
$M_q$	-1.200	$-0.606 \pm 0.449$	$-1.251 \pm 0.591$
$M_{\delta_e}$	-5.157	$-3.921 \pm 0.790$	$-5.189 \pm 1.093$

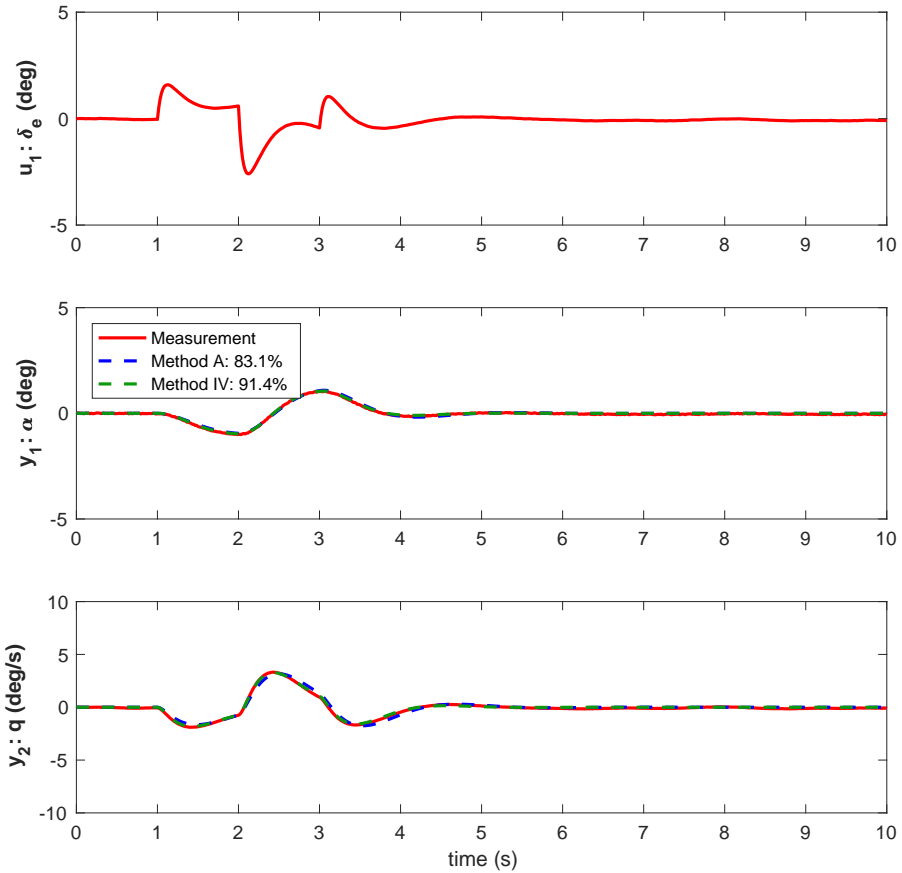


**Figure D.32:** Validation of the F16 closed loop model parameters for the light process noise case, comparing Method A in blue with Method IV in green.

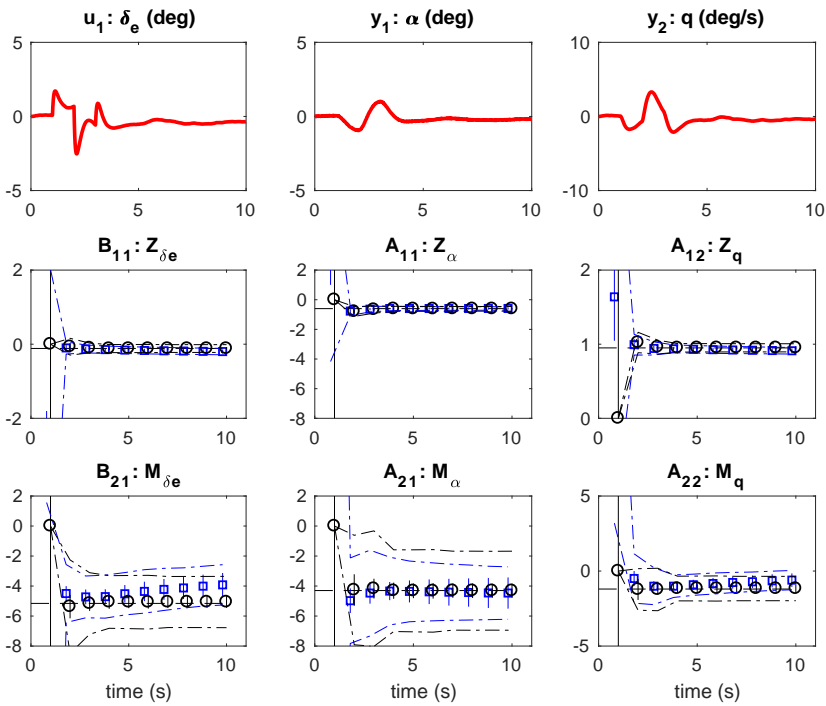


**Figure D.33:** Estimation of the F16 closed loop model parameters for the light process noise case, comparing Method A in blue with Method C in black.

**Table D.16:** Estimation of the F16 closed loop model parameters at time 10 s for the light process noise case, comparing Method A with Method C.

	True	Method A	Method C
$Z_\alpha$	-0.600	$-0.590 \pm 0.074$	$-0.613 \pm 0.039$
$Z_q$	0.950	$0.911 \pm 0.032$	$0.951 \pm 0.020$
$Z_{\delta_e}$	-0.115	$-0.199 \pm 0.056$	$-0.117 \pm 0.033$
$M_\alpha$	-4.300	$-4.467 \pm 1.040$	$-4.312 \pm 0.465$
$M_q$	-1.200	$-0.606 \pm 0.449$	$-1.166 \pm 0.247$
$M_{\delta_e}$	-5.157	$-3.921 \pm 0.790$	$-5.065 \pm 0.390$

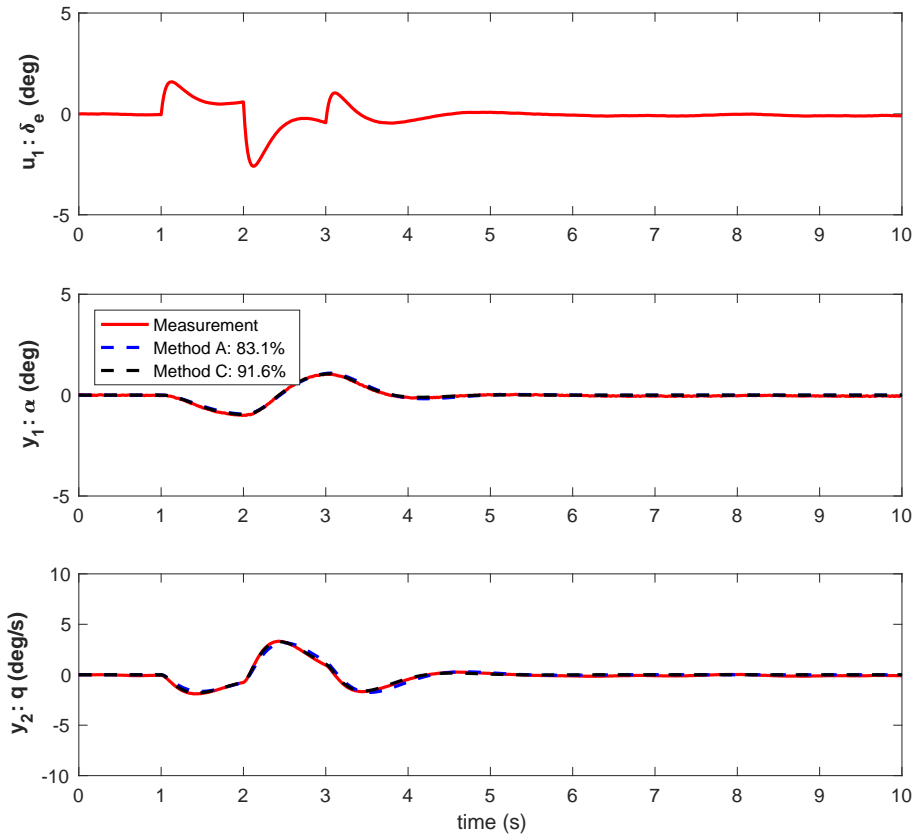


**Figure D.34:** Validation of the F16 closed loop model parameters for the light process noise case, comparing Method A in blue with Method C in black.

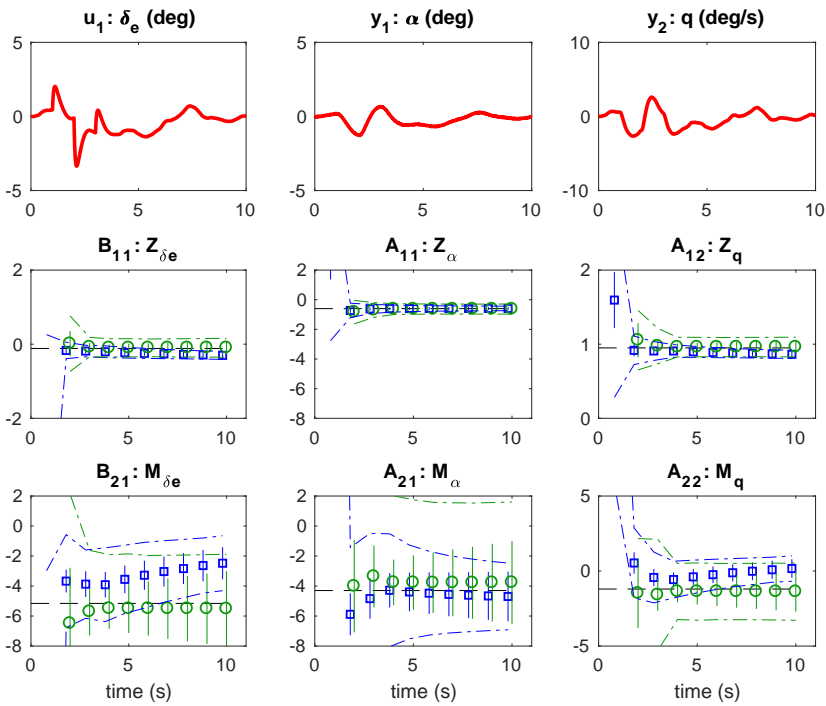


**Figure D.35:** Estimation of the F16 closed loop model parameters for the medium process noise case, comparing Method A in blue with Method IV in green.

**Table D.17:** Estimation of the F16 closed loop model parameters at time 10 s for the medium process noise case, comparing Method A with Method IV.

	True	Method A	Method IV
$Z_\alpha$	-0.600	$-0.587 \pm 0.113$	$-0.630 \pm 0.188$
$Z_q$	0.950	$0.863 \pm 0.042$	$0.962 \pm 0.091$
$Z_{\delta_e}$	-0.115	$-0.302 \pm 0.073$	$-0.097 \pm 0.171$
$M_\alpha$	-4.300	$-4.694 \pm 1.649$	$-3.764 \pm 2.775$
$M_q$	-1.200	$0.166 \pm 0.617$	$-1.375 \pm 1.332$
$M_{\delta_e}$	-5.157	$-2.478 \pm 1.063$	$-5.520 \pm 2.517$

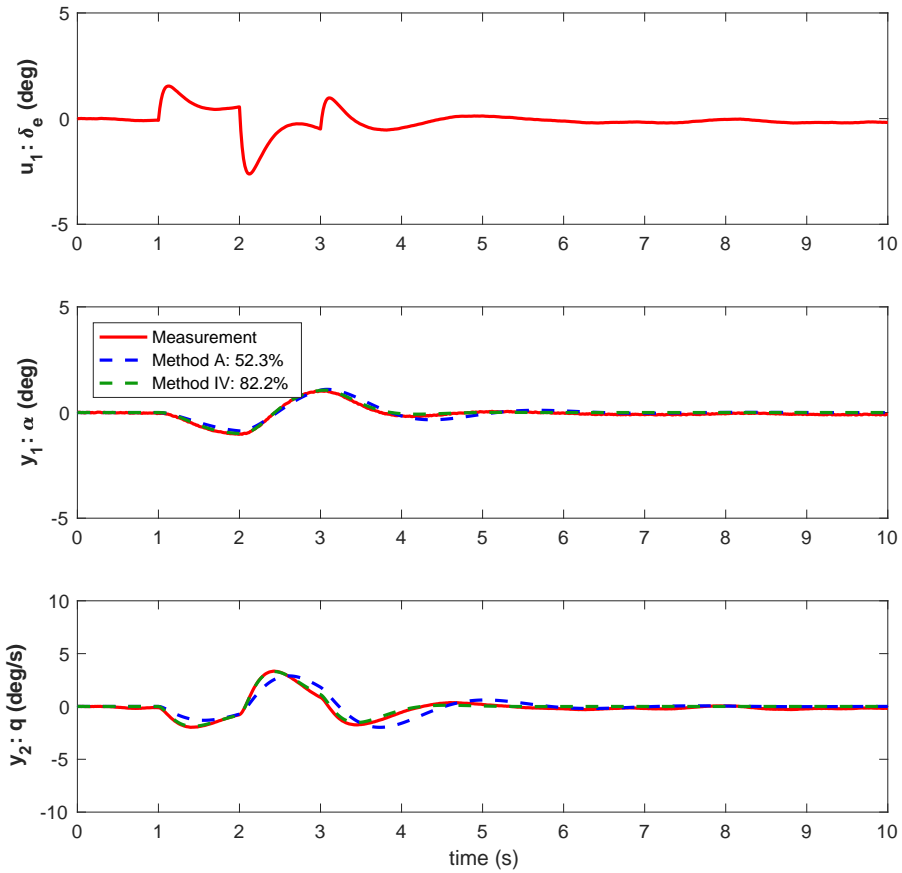


**Figure D.36:** Validation of the F16 closed loop model parameters for the medium process noise case, comparing Method A in blue with Method IV in green.

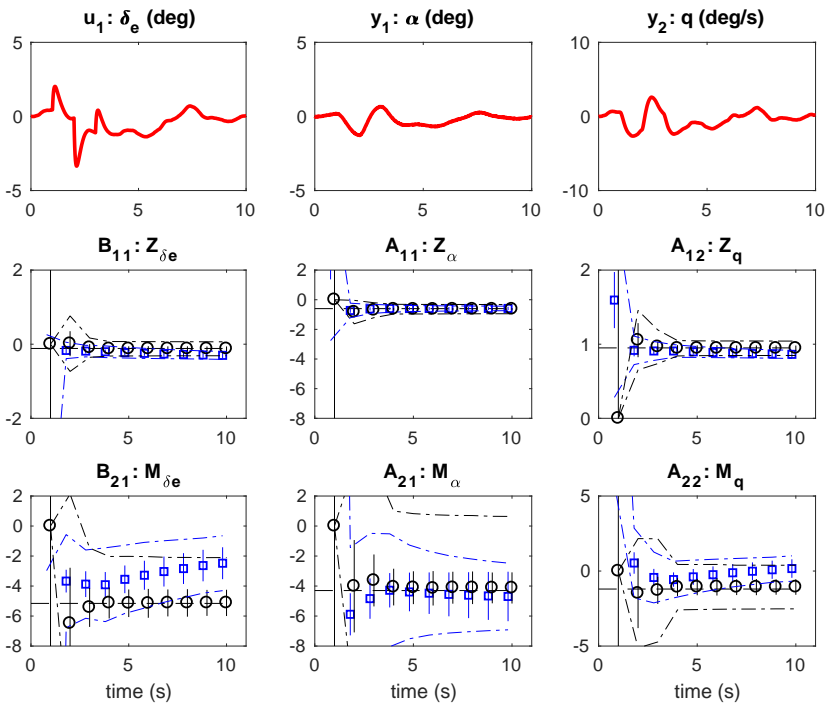


**Figure D.37:** Estimation of the F16 closed loop model parameters for the medium process noise case, comparing Method A in blue with Method C in black.

**Table D.18:** Estimation of the F16 closed loop model parameters at time 10 s for the medium process noise case, comparing Method A with Method C.

	True	Method A	Method C
$Z_\alpha$	-0.600	$-0.587 \pm 0.113$	$-0.635 \pm 0.074$
$Z_q$	0.950	$0.863 \pm 0.042$	$0.945 \pm 0.037$
$Z_{\delta_e}$	-0.115	$-0.302 \pm 0.073$	$-0.124 \pm 0.063$
$M_\alpha$	-4.300	$-4.694 \pm 1.649$	$-4.127 \pm 1.038$
$M_q$	-1.200	$0.166 \pm 0.617$	$-1.066 \pm 0.518$
$M_{\delta_e}$	-5.157	$-2.478 \pm 1.063$	$-5.123 \pm 0.876$



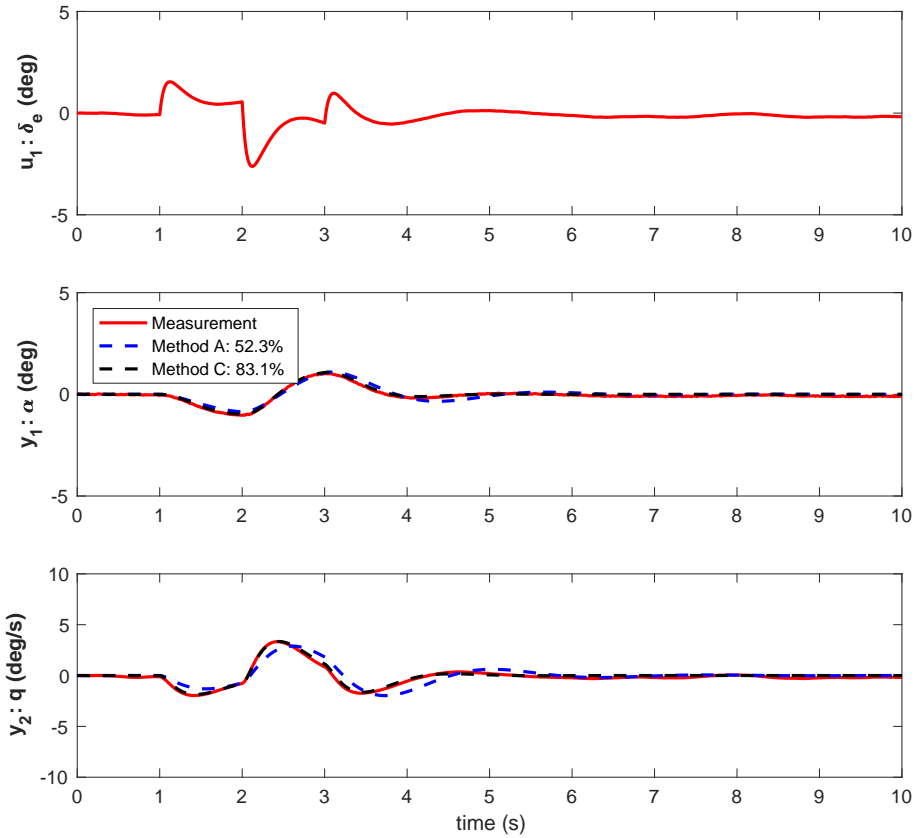


**Figure D.38:** Validation of the F16 closed loop model parameters for the medium process noise case, comparing Method A in blue with Method C in black.

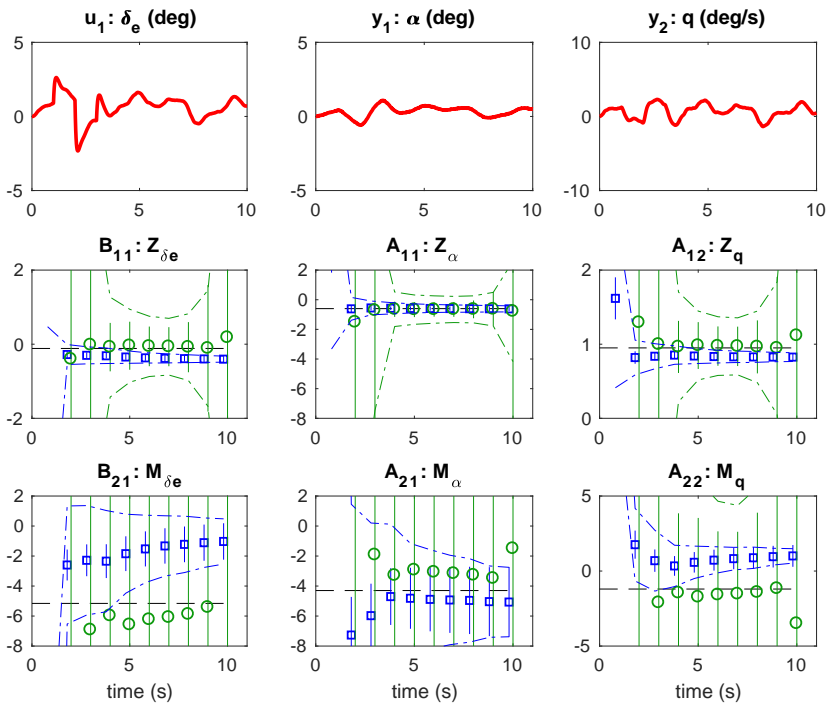


**Figure D.39:** Estimation of the F16 closed loop model parameters for the severe process noise case, comparing Method A in blue with Method IV in green.

**Table D.19:** Estimation of the F16 closed loop model parameters at time 10 s for the severe process noise case, comparing Method A with Method IV.

	True	Method A	Method IV
$Z_\alpha$	-0.600	$-0.616 \pm 0.156$	$-0.7808 \pm 16.86$
$Z_q$	0.950	$0.826 \pm 0.048$	$1.1159 \pm 19.84$
$Z_{\delta_e}$	-0.115	$-0.403 \pm 0.080$	$0.1790 \pm 34.04$
$M_\alpha$	-4.300	$-5.066 \pm 2.336$	$-1.5018 \pm 233.3$
$M_q$	-1.200	$1.009 \pm 0.725$	$-3.5015 \pm 274.1$
$M_{\delta_e}$	-5.157	$-1.028 \pm 1.213$	$-9.4085 \pm 470.5$

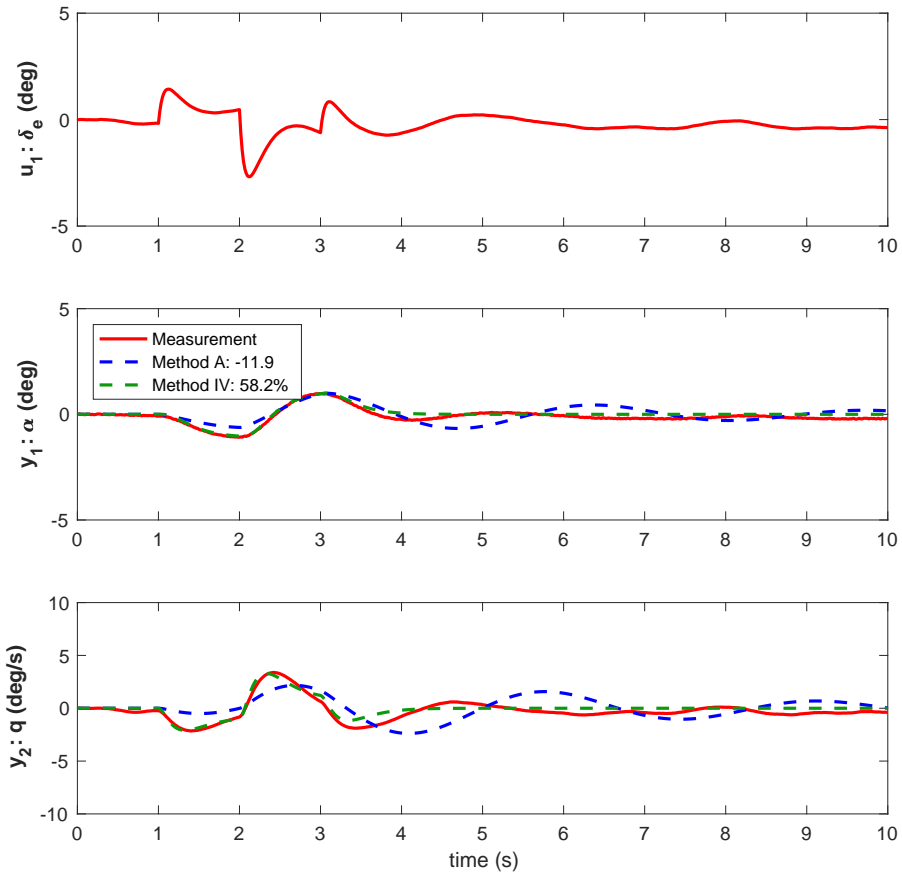


**Figure D.40:** Validation of the F16 closed loop model parameters for the severe process noise case, comparing Method A in blue with Method IV in green.

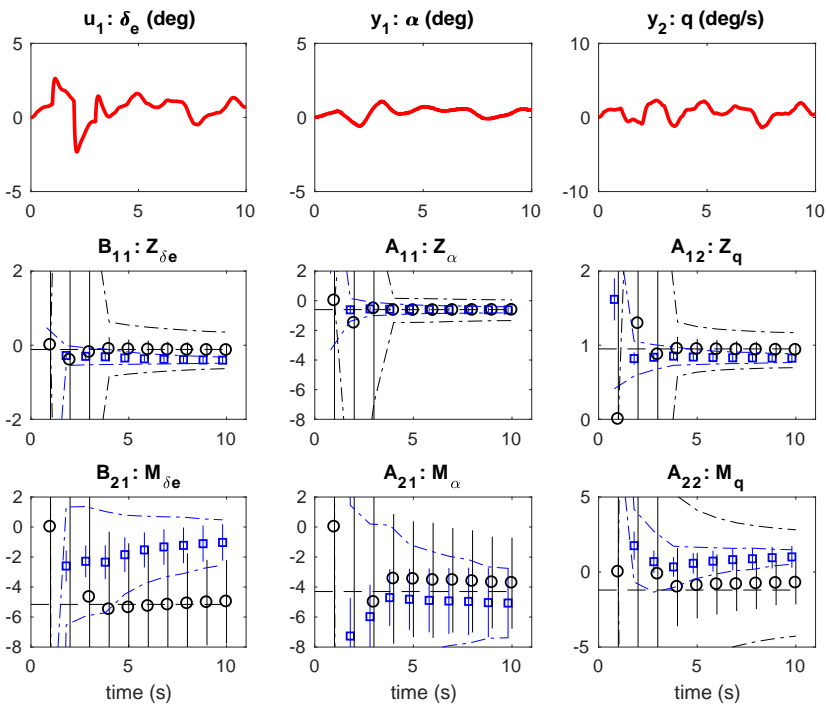


**Figure D.41:** Estimation of the F16 closed loop model parameters for the severe process noise case, comparing Method A in blue with Method C in black.

**Table D.20:** Estimation of the F16 closed loop model parameters at time 10 s for the severe process noise case, comparing Method A with Method C.

	True	Method A	Method C
$Z_\alpha$	-0.600	$-0.616 \pm 0.156$	$-0.640 \pm 0.208$
$Z_q$	0.950	$0.826 \pm 0.048$	$0.933 \pm 0.097$
$Z_{\delta_e}$	-0.115	$-0.403 \pm 0.080$	$-0.140 \pm 0.183$
$M_\alpha$	-4.300	$-5.066 \pm 2.336$	$-3.738 \pm 3.035$
$M_q$	-1.200	$1.009 \pm 0.725$	$-0.728 \pm 1.430$
$M_{\delta_e}$	-5.157	$-1.028 \pm 1.213$	$-4.987 \pm 2.777$

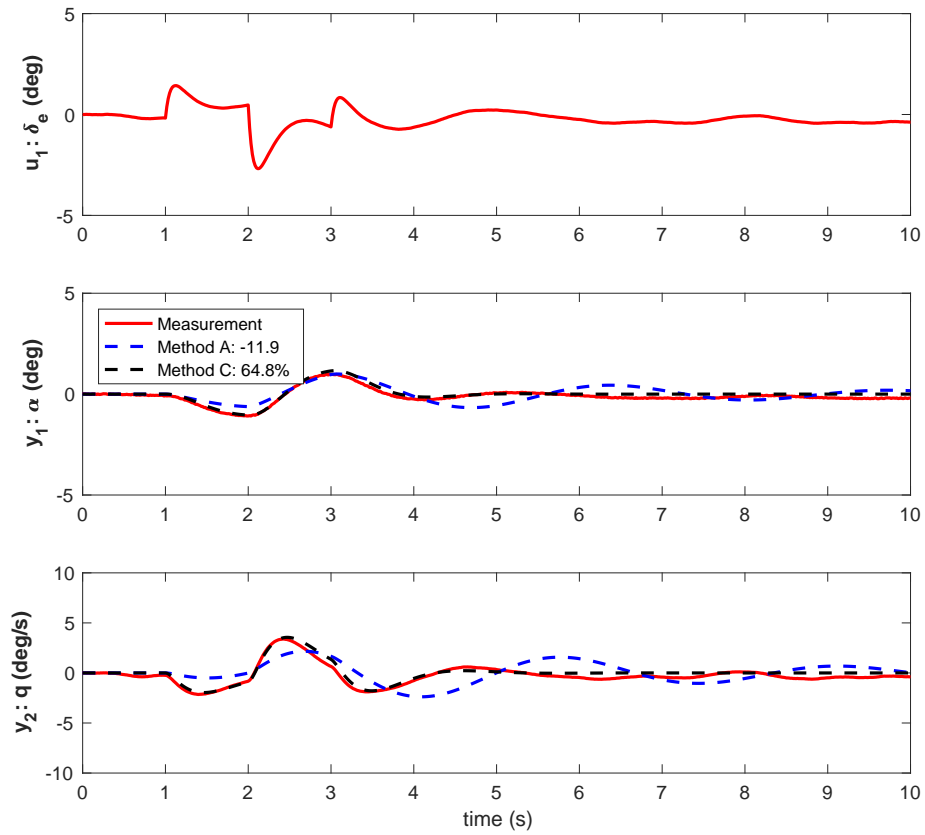


**Figure D.42:** Validation of the F16 closed loop model parameters for the severe process noise case, comparing Method A in blue with Method C in black.

## JAS 39 Gripen Closed loop

- Measurement noise

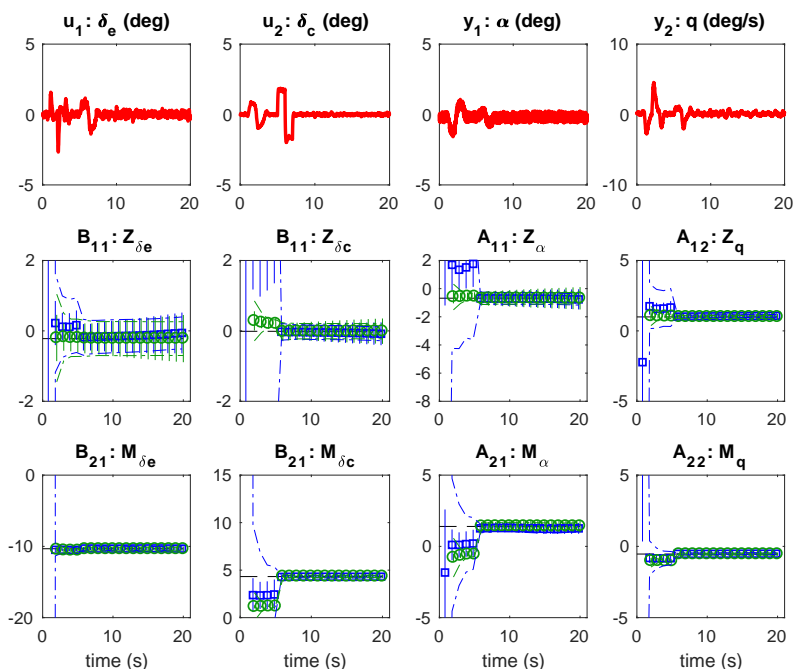


**Figure D.43:** Estimation of the JAS 39 Gripen closed loop model parameters for the measurement noise case, comparing Method A in blue with Method IV in green.

**Table D.21:** Estimation of the JAS 39 Gripen closed loop model parameters at time 19 s for the measurement noise case, comparing Method A with Method IV.

	True	Method A	Method IV
$Z_\alpha$	-0.679	$-0.761 \pm 0.715$	$-0.686 \pm 0.793$
$Z_q$	0.992	$1.068 \pm 0.198$	$0.994 \pm 0.213$
$Z_{\delta_e}$	-0.220	$-0.059 \pm 0.579$	$-0.219 \pm 0.671$
$Z_{\delta_c}$	-0.012	$-0.082 \pm 0.324$	$-0.009 \pm 0.361$
$M_\alpha$	1.339	$1.265 \pm 0.381$	$1.420 \pm 0.424$
$M_q$	-0.537	$-0.511 \pm 0.106$	$-0.544 \pm 0.114$
$M_{\delta_e}$	-10.330	$-10.311 \pm 0.309$	$-10.370 \pm 0.359$
$M_{\delta_c}$	4.324	$4.311 \pm 0.173$	$4.338 \pm 0.193$

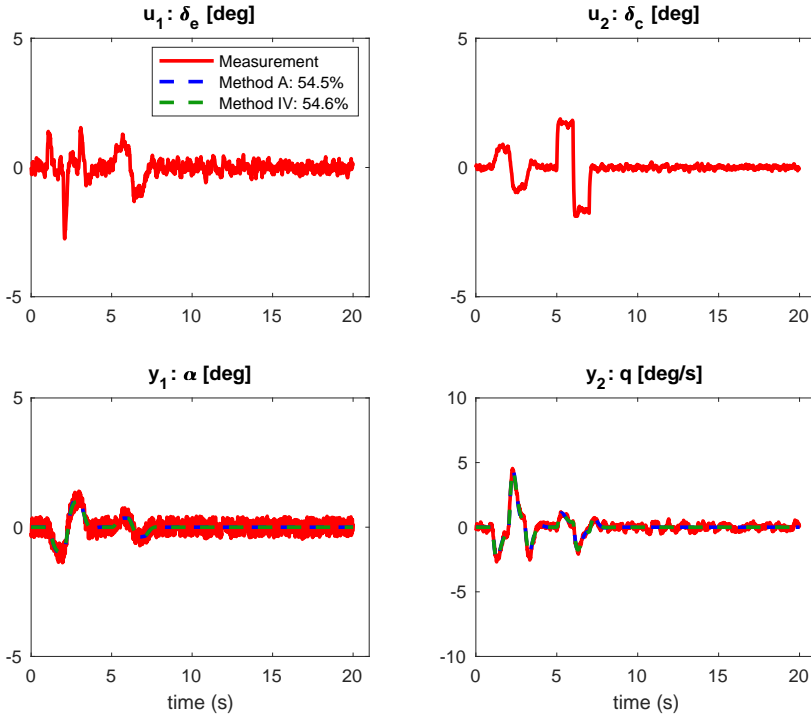


**Figure D.44:** Validation of the JAS 39 Gripen closed loop model parameters for the measurement noise case, comparing Method A in blue with Method IV in green.

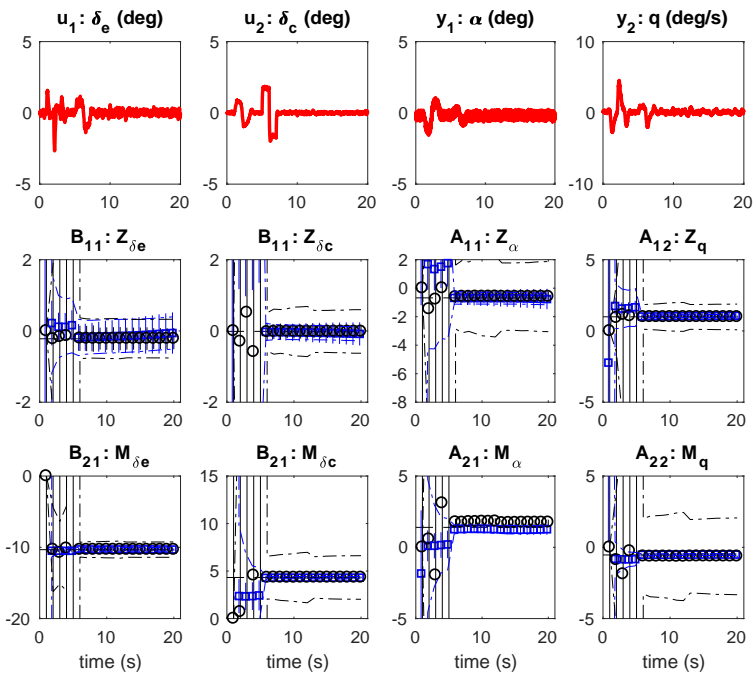


**Figure D.45:** Estimation of the JAS 39 Gripen closed loop model parameters for the measurement noise case, comparing Method A in blue with Method C in black.

**Table D.22:** Estimation of the JAS 39 Gripen closed loop model parameters at time 19 s for the measurement noise case, comparing Method A with Method C.

	True	Method A	Method C
$Z_\alpha$	-0.679	$-0.761 \pm 0.715$	$-0.592 \pm 0.353$
$Z_q$	0.992	$1.068 \pm 0.198$	$0.984 \pm 0.094$
$Z_{\delta_e}$	-0.220	$-0.059 \pm 0.579$	$-0.215 \pm 0.297$
$Z_{\delta_c}$	-0.012	$-0.082 \pm 0.324$	$-0.014 \pm 0.177$
$M_\alpha$	1.339	$1.265 \pm 0.381$	$1.751 \pm 0.188$
$M_q$	-0.537	$-0.511 \pm 0.106$	$-0.633 \pm 0.050$
$M_{\delta_e}$	-10.330	$-10.311 \pm 0.309$	$-10.328 \pm 0.158$
$M_{\delta_c}$	4.324	$4.311 \pm 0.173$	$4.324 \pm 0.096$



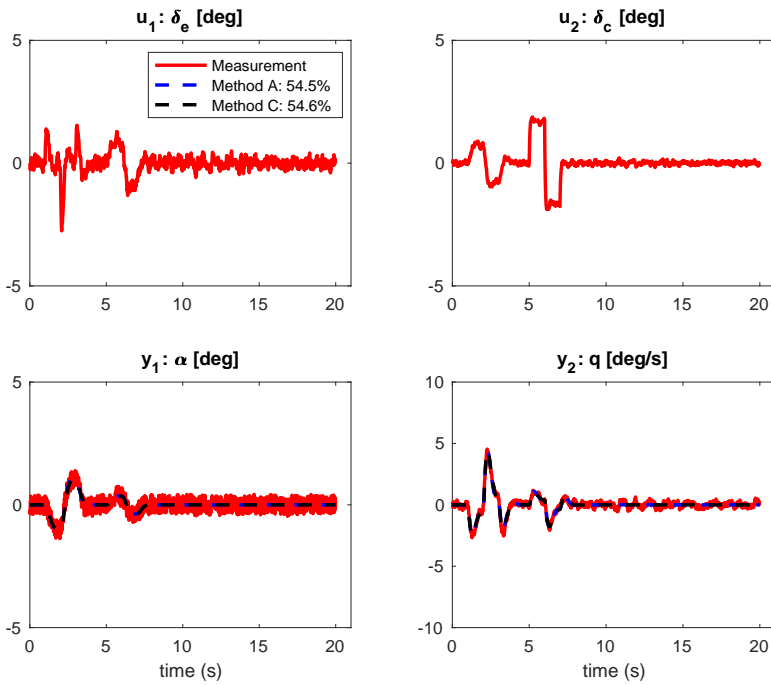


**Figure D.46:** Validation of the JAS 39 Gripen closed loop model parameters for the measurement noise case, comparing Method A in blue with Method C in black.

- Process noise

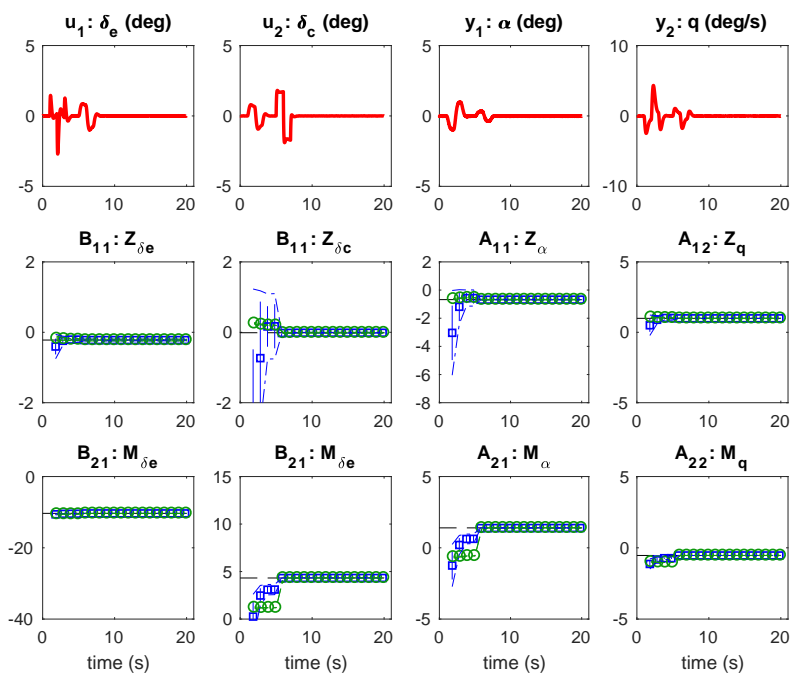


**Figure D.47:** Estimation of the JAS 39 Gripen closed loop model parameters for the no process noise case, comparing Method A in blue with Method IV in green.

**Table D.23:** Estimation of the JAS 39 Gripen closed loop model parameters at time 20 s for the no process noise case, comparing Method A with Method IV.

	True	Method A	Method IV
$Z_\alpha$	-0.679	$-0.679 \pm 0.038$	$-0.679 \pm 0.039$
$Z_q$	0.992	$0.992 \pm 0.010$	$0.992 \pm 0.011$
$Z_{\delta_e}$	-0.220	$-0.220 \pm 0.030$	$-0.220 \pm 0.033$
$Z_{\delta_c}$	-0.012	$-0.012 \pm 0.017$	$-0.012 \pm 0.018$
$M_\alpha$	1.339	$1.391 \pm 0.024$	$1.403 \pm 0.026$
$M_q$	-0.537	$-0.537 \pm 0.007$	$-0.539 \pm 0.007$
$M_{\delta_e}$	-10.330	$-10.342 \pm 0.020$	$-10.356 \pm 0.022$
$M_{\delta_c}$	4.324	$4.329 \pm 0.011$	$4.335 \pm 0.012$

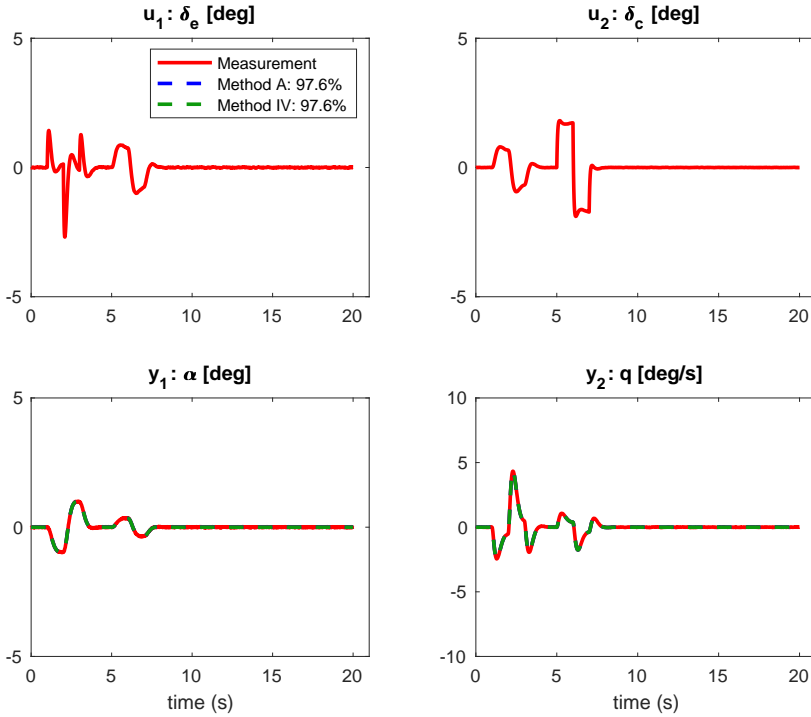


**Figure D.48:** Validation of the JAS 39 Gripen closed loop model parameters for the no process noise case, comparing Method A in blue with Method IV in green.

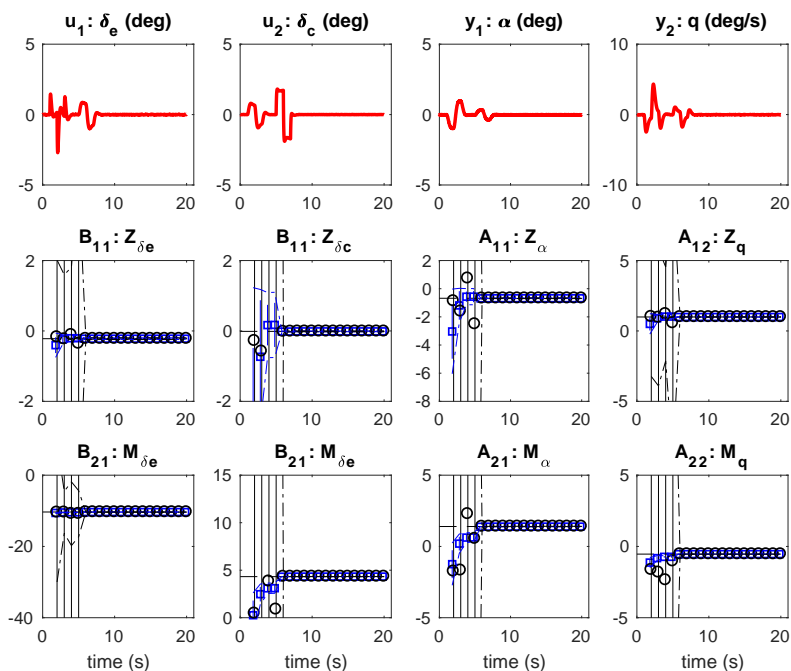


**Figure D.49:** Estimation of the JAS39 closed loop model parameters for the no process noise case, comparing Method A in blue with Method C in black.

**Table D.24:** Estimation of the JAS 39 Gripen closed loop model parameters at time 20 s for the no process noise case, comparing Method A with Method C.

	True	Method A	Method C
$Z_\alpha$	-0.679	$-0.679 \pm 0.038$	$-0.679 \pm 0.019$
$Z_q$	0.992	$0.992 \pm 0.010$	$0.992 \pm 0.005$
$Z_{\delta_e}$	-0.220	$-0.220 \pm 0.030$	$-0.220 \pm 0.016$
$Z_{\delta_c}$	-0.012	$-0.012 \pm 0.017$	$-0.012 \pm 0.009$
$M_\alpha$	1.339	$1.391 \pm 0.024$	$1.403 \pm 0.014$
$M_q$	-0.537	$-0.537 \pm 0.007$	$-0.539 \pm 0.004$
$M_{\delta_e}$	-10.330	$-10.342 \pm 0.020$	$-10.356 \pm 0.011$
$M_{\delta_c}$	4.324	$4.329 \pm 0.011$	$4.335 \pm 0.006$

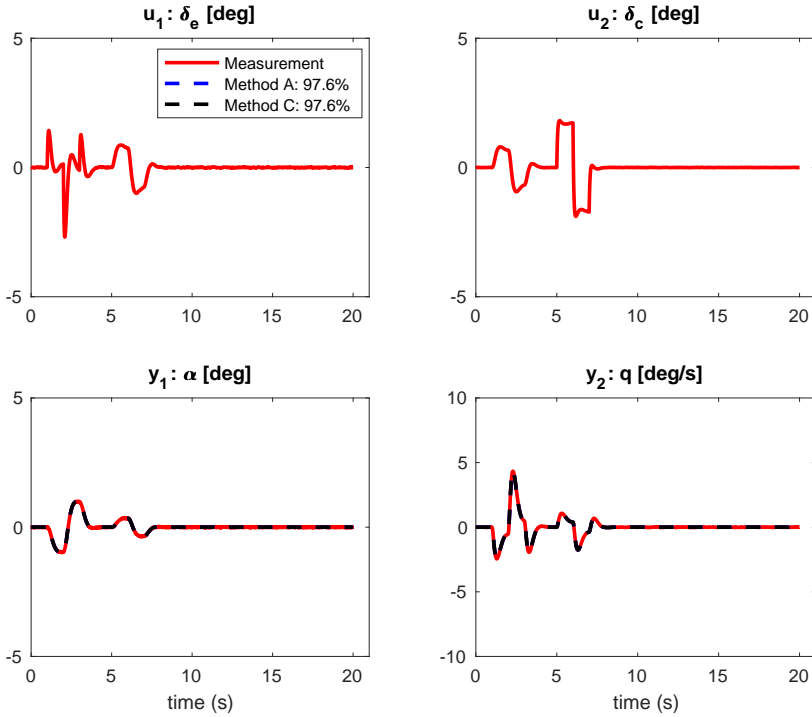


**Figure D.50:** Validation of the JAS 39 Gripen closed loop model parameters for the no process noise case, comparing Method A in blue with Method C in black.

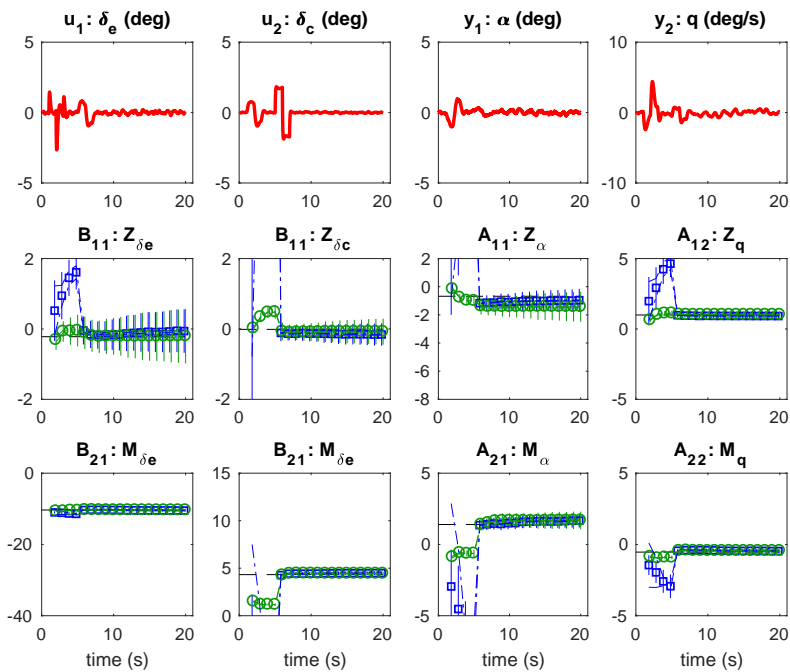


**Figure D.51:** Estimation of the JAS 39 Gripen closed loop model parameters for the light process noise case, comparing Method A in blue with Method IV in green.

**Table D.25:** Estimation of the JAS 39 Gripen closed loop model parameters at time 20 s for the light process noise case, comparing Method A with Method IV.

	True	Method A	Method IV
$Z_\alpha$	-0.679	$-0.958 \pm 0.807$	$-1.429 \pm 1.070$
$Z_q$	0.992	$0.914 \pm 0.210$	$1.017 \pm 0.274$
$Z_{\delta_e}$	-0.220	$-0.060 \pm 0.617$	$-0.204 \pm 0.773$
$Z_{\delta_c}$	-0.012	$-0.158 \pm 0.318$	$-0.076 \pm 0.370$
$M_\alpha$	1.339	$1.674 \pm 0.486$	$1.687 \pm 0.616$
$M_q$	-0.537	$-0.462 \pm 0.126$	$-0.447 \pm 0.158$
$M_{\delta_e}$	-10.330	$-10.476 \pm 0.371$	$-10.367 \pm 0.445$
$M_{\delta_c}$	4.324	$4.486 \pm 0.191$	$4.438 \pm 0.213$

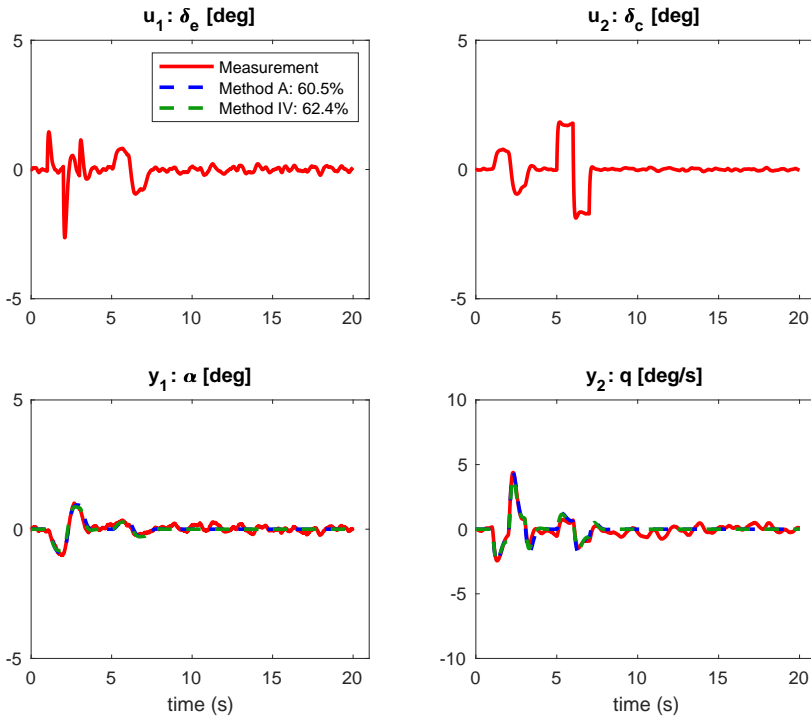


**Figure D.52:** Validation of the JAS 39 Gripen closed loop model parameters for the light process noise case, comparing Method A in blue with Method IV in green.

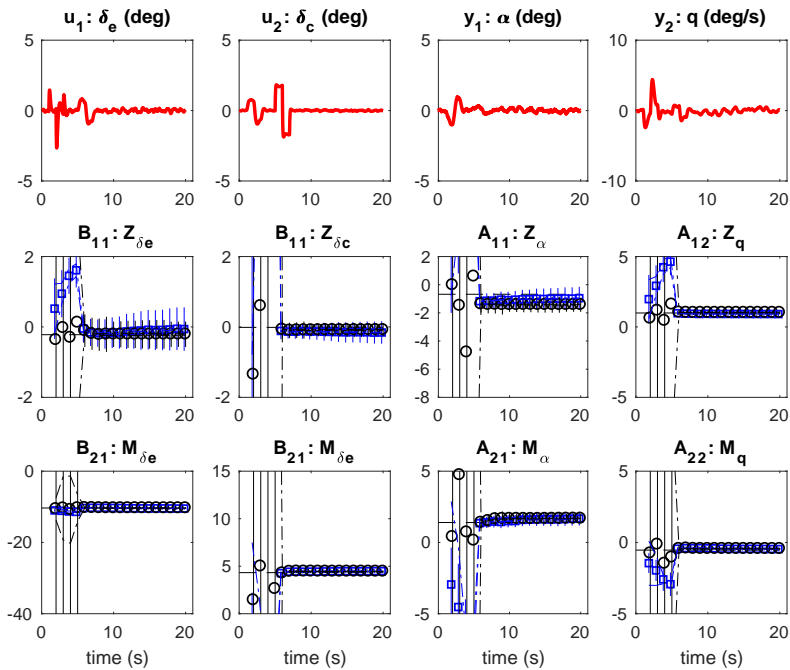


**Figure D.53:** Estimation of the JAS 39 Gripen closed loop model parameters for the light process noise case, comparing Method A in blue with Method C in black.

**Table D.26:** Estimation of the JAS 39 Gripen closed loop model parameters at time 20 s for the light process noise case, comparing Method A with Method C.

	True	Method A	Method C
$Z_\alpha$	-0.679	$-0.958 \pm 0.807$	$-1.425 \pm 0.501$
$Z_q$	0.992	$0.914 \pm 0.210$	$1.015 \pm 0.128$
$Z_{\delta_e}$	-0.220	$-0.060 \pm 0.617$	$-0.208 \pm 0.362$
$Z_{\delta_c}$	-0.012	$-0.158 \pm 0.318$	$-0.083 \pm 0.174$
$M_\alpha$	1.339	$1.674 \pm 0.486$	$1.679 \pm 0.328$
$M_q$	-0.537	$-0.462 \pm 0.126$	$-0.445 \pm 0.084$
$M_{\delta_e}$	-10.330	$-10.476 \pm 0.371$	$-10.361 \pm 0.237$
$M_{\delta_c}$	4.324	$4.486 \pm 0.191$	$4.445 \pm 0.114$



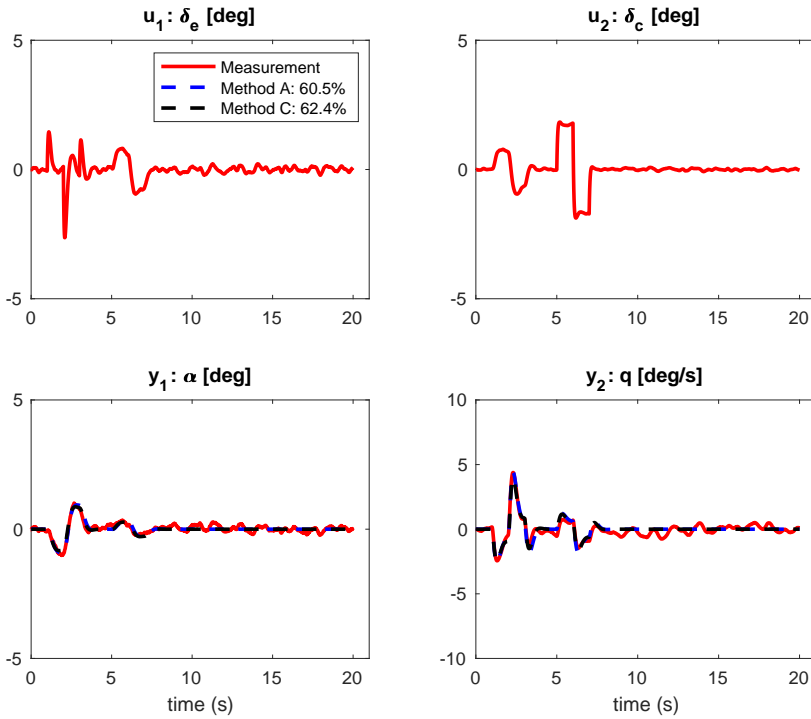


**Figure D.54:** Validation of the JAS 39 Gripen closed loop model parameters for the light process noise case, comparing Method A in blue with Method C in black.

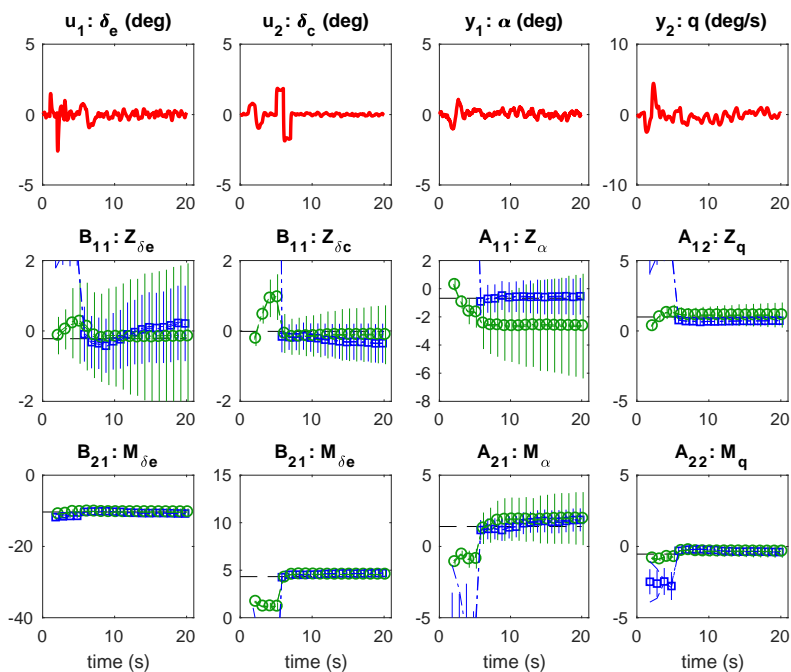


**Figure D.55:** Estimation of the JAS 39 Gripen closed loop model parameters for the medium process noise case, comparing Method A in blue with Method IV in green.

**Table D.27:** Estimation of the JAS 39 Gripen closed loop model parameters at time 20 s for the medium process noise case, comparing Method A with Method IV.

	True	Method A	Method IV
$Z_\alpha$	-0.679	$-0.537 \pm 1.300$	$-2.655 \pm 3.716$
$Z_q$	0.992	$0.726 \pm 0.324$	$1.128 \pm 0.890$
$Z_{\delta_e}$	-0.220	$0.214 \pm 1.072$	$-0.152 \pm 2.072$
$Z_{\delta_c}$	-0.012	$-0.349 \pm 0.556$	$-0.109 \pm 0.835$
$M_\alpha$	1.339	$1.867 \pm 0.806$	$1.952 \pm 1.859$
$M_q$	-0.537	$-0.392 \pm 0.201$	$-0.347 \pm 0.445$
$M_{\delta_e}$	-10.330	$-10.759 \pm 0.664$	$-10.357 \pm 1.037$
$M_{\delta_c}$	4.324	$4.694 \pm 0.344$	$4.543 \pm 0.418$

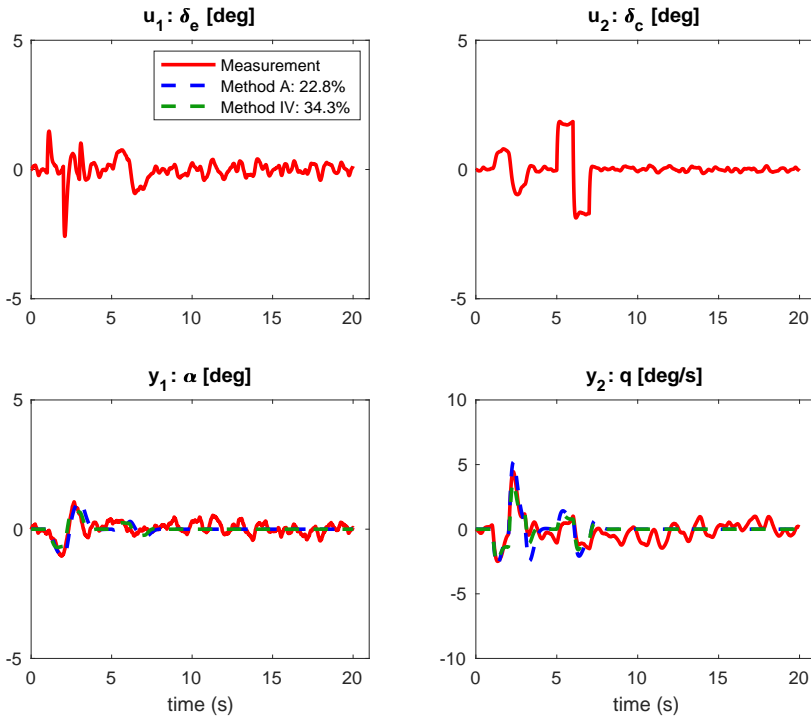


**Figure D.56:** Validation of the JAS 39 Gripen closed loop model parameters for the medium process noise case, comparing Method A in blue with Method IV in green.

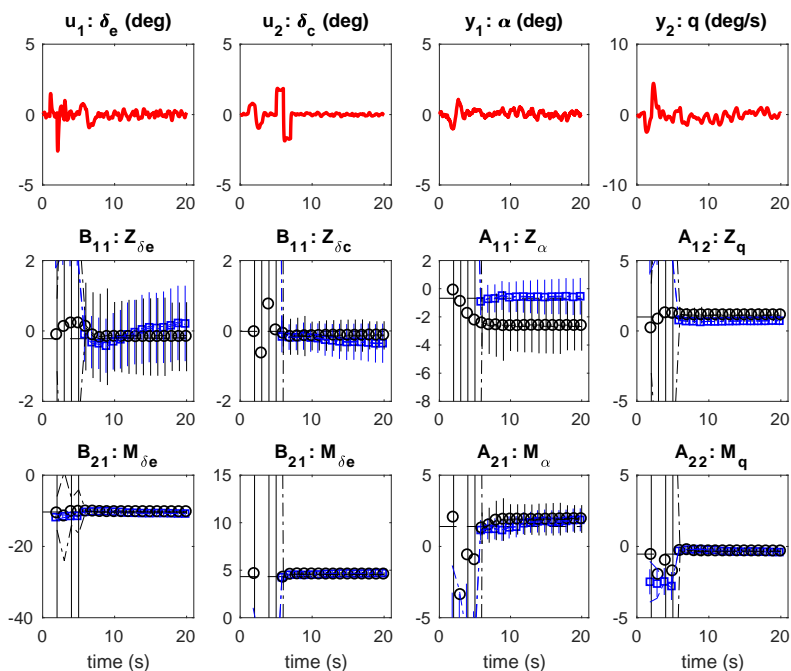


**Figure D.57:** Estimation of the JAS 39 Gripen closed loop model parameters for the medium process noise case, comparing Method A in blue with Method C in black.

**Table D.28:** Estimation of the JAS 39 Gripen closed loop model parameters at time 20 s for the medium process noise case, comparing Method A with Method C.

	True	Method A	Method C
$Z_\alpha$	-0.679	$-0.537 \pm 1.300$	$-2.639 \pm 1.760$
$Z_q$	0.992	$0.726 \pm 0.324$	$1.123 \pm 0.421$
$Z_{\delta_e}$	-0.220	$0.214 \pm 1.072$	$-0.164 \pm 0.980$
$Z_{\delta_c}$	-0.012	$-0.349 \pm 0.556$	$-0.127 \pm 0.402$
$M_\alpha$	1.339	$1.867 \pm 0.806$	$1.924 \pm 0.975$
$M_q$	-0.537	$-0.392 \pm 0.201$	$-0.340 \pm 0.233$
$M_{\delta_e}$	-10.330	$-10.759 \pm 0.664$	$-10.341 \pm 0.543$
$M_{\delta_c}$	4.324	$4.694 \pm 0.344$	$4.558 \pm 0.222$

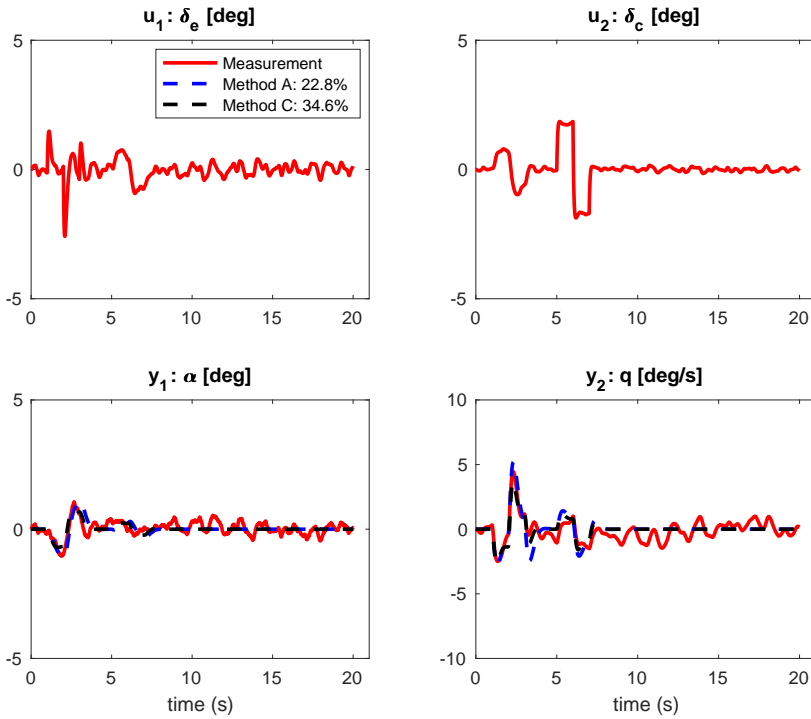


**Figure D.58:** Validation of the JAS 39 Gripen closed loop model parameters for the medium process noise case, comparing Method A in blue with Method C in black.

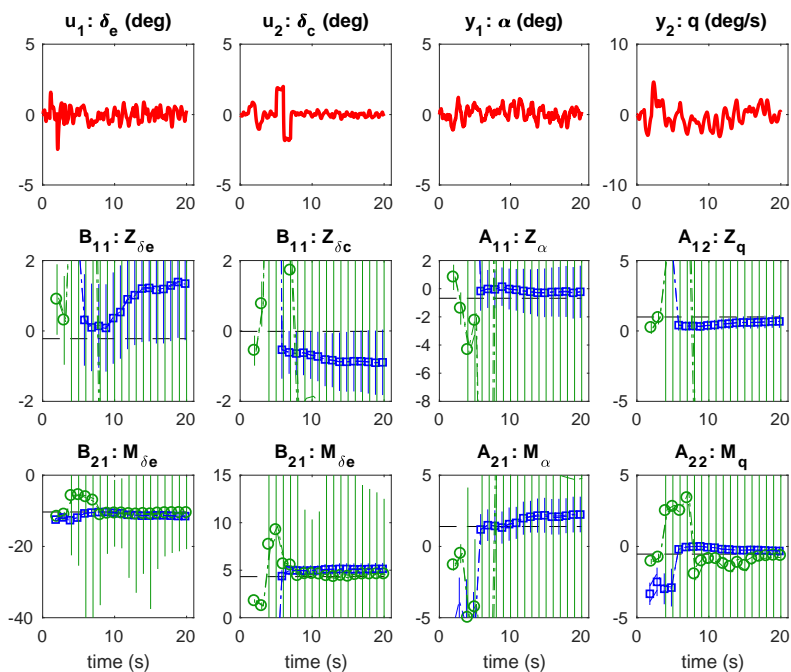


**Figure D.59:** Estimation of the JAS 39 Gripen closed loop model parameters for the severe process noise case, comparing Method A in blue with Method IV in green.

**Table D.29:** Estimation of the JAS 39 Gripen closed loop model parameters at time 20 s for the severe process noise case, comparing Method A with Method IV.

	True	Method A	Method IV
$Z_\alpha$	-0.679	$-0.220 \pm 1.855$	$36.323 \pm 853.21$
$Z_q$	0.992	$0.677 \pm 0.458$	$-6.704 \pm 161.11$
$Z_{\delta_e}$	-0.220	$1.345 \pm 1.607$	$-5.524 \pm 89.879$
$Z_{\delta_c}$	-0.012	$-0.891 \pm 0.930$	$-3.024 \pm 70.199$
$M_\alpha$	1.339	$2.242 \pm 1.251$	$5.464 \pm 96.370$
$M_q$	-0.537	$-0.318 \pm 0.309$	$-0.657 \pm 18.198$
$M_{\delta_e}$	-10.330	$-11.485 \pm 1.084$	$-10.596 \pm 10.150$
$M_{\delta_c}$	4.324	$5.139 \pm 0.627$	$4.583 \pm 7.930$

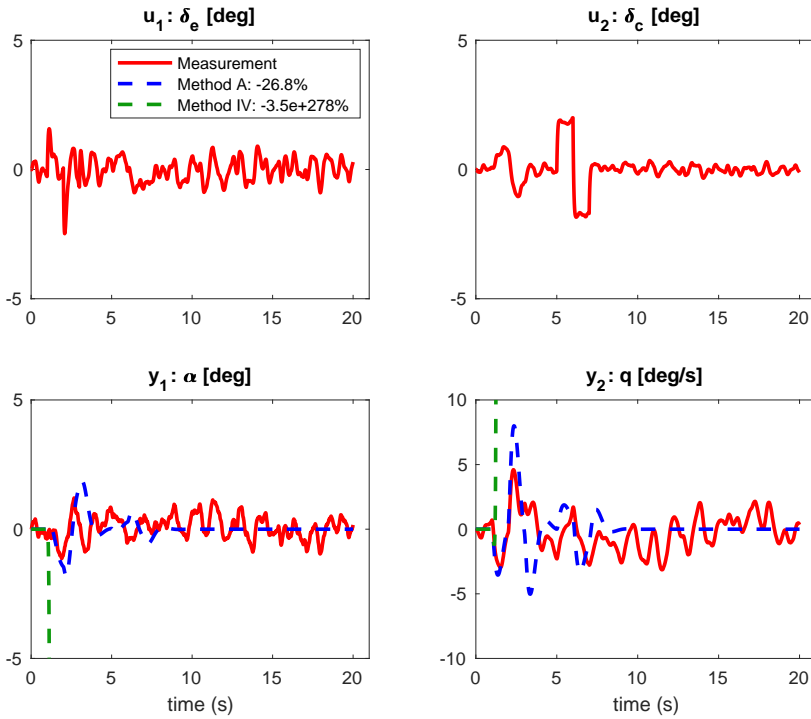


**Figure D.60:** Validation of the JAS 39 Gripen closed loop model parameters for the severe process noise case, comparing Method A in blue with Method IV in green.

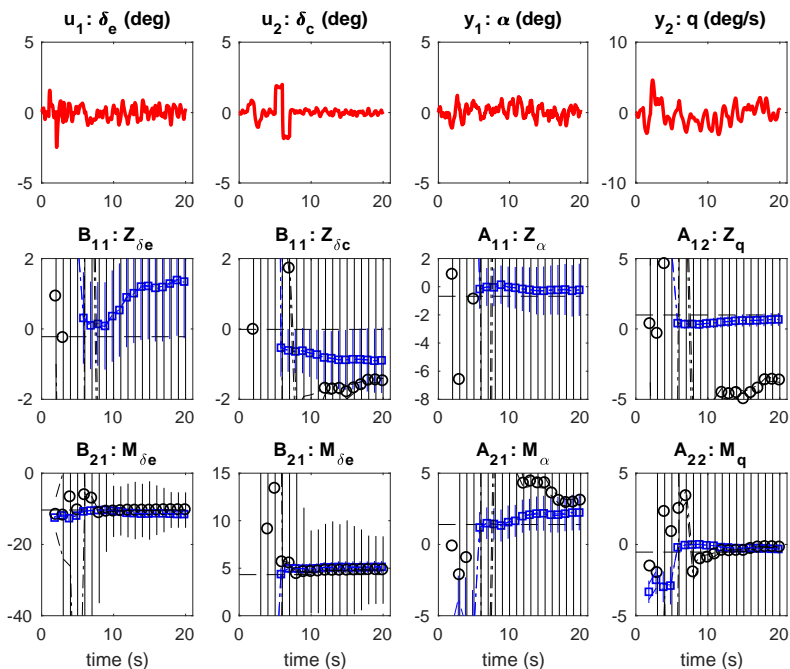


**Figure D.61:** Estimation of the JAS 39 Gripen closed loop model parameters for the severe process noise case, comparing Method A in blue with Method C in black.

**Table D.30:** Estimation of the JAS 39 Gripen closed loop model parameters at time 20 s for the severe process noise case, comparing Method A with Method C.

	True	Method A	Method C
$Z_\alpha$	-0.679	$-0.220 \pm 1.855$	$20.250 \pm 339.71$
$Z_q$	0.992	$0.677 \pm 0.458$	$-3.649 \pm 63.834$
$Z_{\delta_e}$	-0.220	$1.345 \pm 1.607$	$-3.867 \pm 36.241$
$Z_{\delta_c}$	-0.012	$-0.891 \pm 0.930$	$-1.481 \pm 24.395$
$M_\alpha$	1.339	$2.242 \pm 1.251$	$3.083 \pm 46.639$
$M_q$	-0.537	$-0.318 \pm 0.309$	$-0.207 \pm 8.791$
$M_{\delta_e}$	-10.330	$-11.485 \pm 1.084$	$-10.352 \pm 4.971$
$M_{\delta_c}$	4.324	$5.139 \pm 0.627$	$4.804 \pm 3.547$



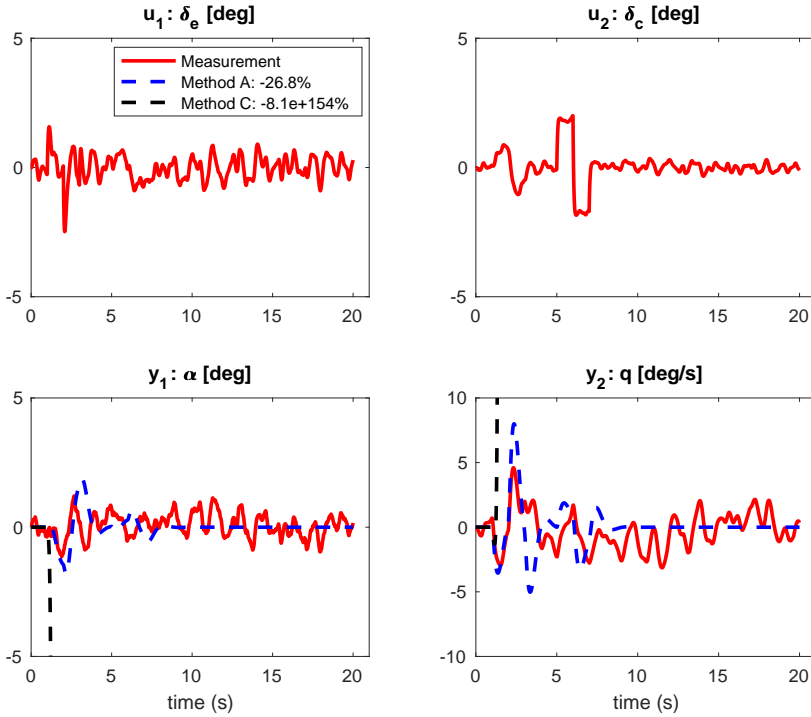


**Figure D.62:** Validation of the JAS 39 Gripen closed loop model parameters for the severe process noise case, comparing Method A in blue with Method C in black.

# E

---

## GFF test card

This appendix shows one of the test cards used in the GFF flight test campaign as an example. The test card is useful since it gives a structured way of planning and conducting the test and it also acts as a notebook for collecting comments during the test campaign. These notes can be valuable when revisiting the test data.


TEST CARD ID: System Identification		Aircraft: GFF		
Radio test freq:		Test id: GFF	Test type: FQ	Pilot: David Lundström
Test Object: GFF		Test Conductor: Alejandro Sobrón	Date: 17-10-31	
Configuration: GoPro camera added under the nose. Orange fluorescent tape on the top side outer part of the wing.		Test heading: System Identification	Sub heading: Multisine crest factor optimized input	
Restrictions and remarks: Max nz=4,8		Summary of test results: In general the test went as planned. Test pos. 7 had to be repeated since it was aborted due to ground proximity the first time. The outside temperature was about 5° C during the test. It was a bit Turbulete in the air, which can be seen in the angel-of-attack and angle-of-sideslip measurements. The %Fuel noted in the test card is unceartain since it is based on calculations and not on measurements.		

Figure E.1: Test card front.

<b>Pos</b> <b>0</b>	<b>Alt.</b> 0-80 m	<b>Speed</b> 0-40 m/s	<b>Header</b> Ground check and Take-off	<b>Exp Time</b> 0 s	<b>%Fuel</b> 100	<b>Test type</b> Take-off
Ground check, Taxi and Take-off OK.						
<b>Pos</b> <b>1</b>	<b>Alt.</b> 80 m	<b>Speed</b> 40 m/s	<b>Header</b> Multisine crest factor optimized	<b>Exp Time</b> 327 s	<b>%Fuel</b> 84.1	<b>Test type</b> System identification
Crest factor optimized multisine, <b>parallel</b> , <b>ID CR1</b> , 3 periods, Amplitude <b>A1 de and dc</b> 100% OK.						
<b>Pos</b> <b>2</b>	<b>Alt.</b> 80 m	<b>Speed</b> 40 m/s	<b>Header</b> Multisine crest factor optimized	<b>Exp Time</b> 382 s	<b>%Fuel</b> 74.4	<b>Test type</b> System identification
Crest factor optimized multisine, <b>parallel</b> , <b>ID CR1</b> , 3 periods, Amplitude <b>A1 de and dc</b> 100% OK.						
<b>Pos</b> <b>3</b>	<b>Alt.</b> 80 m	<b>Speed</b> 40 m/s	<b>Header</b> Multisine crest factor optimized	<b>Exp Time</b> 431 s	<b>%Fuel</b> 66.6	<b>Test type</b> System identification
Crest factor optimized multisine, <b>parallel</b> , <b>ID CR2</b> , 3 periods, Amplitude <b>A1 de and dc</b> 100% OK.						

Figure E.2: Test card page 1.

<b>Pos</b> 4	<b>Alt.</b> 80 m	<b>Speed</b> 40 m/s	<b>Header</b> Multisine crest factor optimized	<b>ExpTime</b> 480 s	<b>%Fuel</b> 58.3	<b>Test type</b> System identification
Crest factor optimized multisine, <b>separated, ID CR1</b> , 3 periods, Amplitude <b>A1 de and dc 100%</b> OK.						
<b>Pos</b> 5	<b>Alt.</b> 80 m	<b>Speed</b> 40 m/s	<b>Header</b> Multisine crest factor optimized	<b>ExpTime</b> 531 s	<b>%Fuel</b> 50.0	<b>Test type</b> System identification
Crest factor optimized multisine, <b>separated, ID CR1</b> , 3 periods, Amplitude <b>A1 de and dc 100%</b> OK.						
<b>Pos</b> 6	<b>Alt.</b> 80 m	<b>Speed</b> 40 m/s	<b>Header</b> Multisine crest factor optimized	<b>ExpTime</b> 578 s	<b>%Fuel</b> 42.3	<b>Test type</b> System identification
Crest factor optimized multisine, <b>separated, ID CR2</b> , 3 periods, Amplitude <b>A1 de and dc 100%</b> OK.						
<b>Pos</b> 7	<b>Alt.</b> 80 m	<b>Speed</b> 40 m/s	<b>Header</b> Double pulse partial input	<b>ExpTime</b> 619 s	<b>%Fuel</b> 35.2	<b>Test type</b> System identification
Double pulse, <b>separated</b> , 1 period, Amplitude <b>A2 de 40% and A3 dc 40%</b> Repeated due to ground proximity. Repetition ExpTime 666 s and %Fuel 27.5.						

Figure E.3: Test card page 2.

<b>Pos</b> 8	<b>Alt.</b> 80-0 m	<b>Speed</b> 40-0 m/s	<b>Header</b> Landing and post flight check	<b>Exp Time</b> 762 s	<b>%Fuel</b> 11.3	<b>Test type</b> Landing and post flight
Approach and landing. Download and check measurements. Check battery levels. Check amount of fuel left. OK.						
<b>Pos</b> 9	<b>Alt.</b>	<b>Speed</b>	<b>Header</b>	<b>Exp Time</b>	<b>%Fuel</b>	<b>Test type</b>
<b>Pos</b> 10	<b>Alt.</b>	<b>Speed</b>	<b>Header</b>	<b>Exp Time</b>	<b>%Fuel</b>	<b>Test type</b>
<b>Pos</b> 11	<b>Alt.</b>	<b>Speed</b>	<b>Header</b>	<b>Exp Time</b>	<b>%Fuel</b>	<b>Test type</b>

Figure E.4: Test card page 3.



# F

---

## Kalman filters

The present appendix provides basics needed to follow the Kalman filter calculations in the rest of the thesis. In the linear case, the Kalman filter [Kalman, 1960] is optimal in the sense that it will minimize the mean of the squared error of the predicted states if the noise is white and has a normal distribution. Also, the filter has to be tuned, i.e., the relationship between the process noise covariance ( $Q$ ) and measurement noise covariance ( $R$ ) has to be found and set correctly. In this case the linear filter will converge and give the optimal predictions of the states. For the nonlinear case used in this thesis, the Extended Kalman Filter and the Unscented Kalman Filter have been implemented. There is no general proof that these filters have any of the properties mentioned for the linear Kalman filter. The following model is used

$$\begin{aligned}x_{k+1} &= f(x_k, u_k; \theta) + w_k, \\y_k &= h(x_k, u_k) + e_k,\end{aligned}\tag{F.1}$$

where  $\theta$  contains the unknown model parameters to be identified,  $e_k$  and  $w_k$  are assumed to be white noise with zero mean and covariance matrix  $R$  and  $Q$ ,  $x_k$  is a  $n_x \times 1$  state vector,  $u_k$  is an  $n_u \times 1$  input vector and  $y_k$  is an  $n_y \times 1$  output vector.

A predictor for (F.1) can be written as

$$\begin{aligned}\hat{x}_{k+1}(\theta) &= f(\hat{x}_k(\theta), u_k; \theta) + K_k(\theta)\varepsilon_k(\theta), \\ \hat{y}_k(\theta) &= h(\hat{x}_k(\theta), u_k), \\ \varepsilon_k(\theta) &= y_k - \hat{y}_k(\theta)\end{aligned}\tag{F.2}$$

Here, the prediction error  $\varepsilon(\theta)$  is also called the innovation and represents the part of  $y_k$  that cannot be predicted from past measurements. The Kalman filter is often implemented in a way that first predicts the states in a time update using



the dynamic model  $\hat{x}_{k|k-1} = f(\hat{x}_{k-1}(\theta), u_{k-1}; \theta)$  and then make a correction based on the innovation  $\hat{x}_k = \hat{x}_{k|k-1} + K_k(\theta)(y_k - h(\hat{x}_{k|k-1}(\theta), u_{k-1}))$  in a measurement update where the information from the predicted states and the measurements are fused to give a new and more accurate prediction of the states, i.e., the predicted state covariance  $P_k(\theta)$  is reduced.

## F.1 Extended Kalman filter (EKF)

The EKF is an extension of the Kalman Filter to nonlinear systems. The main idea is to compute the Kalman gain  $K_k(\theta)$  at each time step using a linearized model. This linearization is performed by computing the partial derivatives of  $f$  with respect to  $x$  and  $u$  evaluated for  $\hat{x}_k$  and  $u_k$ , giving the matrices  $A_k(\theta)$  and  $B_k(\theta)$ , respectively. Similarly, matrices  $C_k(\theta)$  and  $D_k(\theta)$  can be obtained by linearizing  $h$ . This gives the linearized model

$$\begin{aligned} x_{k+1,lin} &= A_k(\theta)x_{k,lin} + B_k(\theta)u_k \\ y_{k,lin} &= C_k(\theta)x_{k,lin} + D_k(\theta)u_k + e_k \end{aligned} \quad (\text{F.3})$$

Using (F.3) and (F.1) both without any direct input-output relation ( $D_k(\theta) = 0$ ) gives the following EKF algorithm [Khalil, 2002]

**Initialization** ( $k = 0$ ):

$$\begin{aligned} \hat{x}_{1|0}(\theta) &= x_0, \\ P_{1|0}(\theta) &= P_0 \end{aligned} \quad (\text{F.4})$$

**Measurement update:**

Correction by fusion of prediction and measurements for ( $k$ )

$$\begin{aligned} K_k(\theta) &= [P_{k|k-1}(\theta)C_k^T(\theta)][C_k(\theta)P_{k|k-1}(\theta)C_k^T(\theta) + R]^{-1} \\ \hat{x}_k &= \hat{x}_{k|k-1}(\theta) + K_k(\theta)(y_k - C_k\hat{x}_{k|k-1}(\theta)) \\ P_k(\theta) &= P_{k|k-1}(\theta) - K_k(\theta)C_k^T(\theta)P_{k|k-1}(\theta) \end{aligned} \quad (\text{F.5})$$

**Time update:**

Prediction of states for ( $k + 1$ ) given predictions for ( $k$ )

$$\begin{aligned} \hat{x}_{k+1|k}(\theta) &= f(\hat{x}_k(\theta), u_k; \theta) \\ P_{k+1|k}(\theta) &= A_k(\theta)P_k(\theta)A_k^T(\theta) + Q \end{aligned} \quad (\text{F.6})$$

The measurement and time update are then iterated as  $k$  increases.

Another way to do the iterations is to make the measurement and time updates at the same time in a single recursion

$$\begin{aligned}
 K_k(\theta) &= [A_k(\theta)P_k(\theta)C_k^T(\theta)][C_k(\theta)P_k(\theta)C_k^T(\theta) + R]^{-1} \\
 P_{k+1}(\theta) &= A_k(\theta)P_k(\theta)A_k^T(\theta) + Q - K_k(\theta)[C_k(\theta)P_k(\theta)C_k^T(\theta) + R]K_k^T(\theta) \\
 \hat{x}_{k+1}(\theta) &= f(\hat{x}_k(\theta), u_k; \theta) + K_k(\theta)\varepsilon_k(\theta) \\
 \hat{y}_k(\theta) &= h(\hat{x}_k(\theta), u_k; \theta)
 \end{aligned} \tag{F.7}$$

The initialization has to be done as previously. This is the way the EKF has been implemented in this thesis.

## F.2 Unscented Kalman filter (UKF)

When the system is highly nonlinear, the EKF method suffers from the fact that the covariance are propagated through a linearization of the system instead of the actual nonlinear system. The UKF uses an unscented transformation that samples the covariance and propagates it through the actual nonlinearities.

The unscented transformation of  $x$ ,  $z = g(x)$ , uses so called sigma points

$$x^i = \begin{cases} \hat{x} - (\sqrt{(n_x + \lambda)P})_i & \text{if } i < 0 \\ \hat{x} & \text{if } i = 0 \\ \hat{x} + (\sqrt{(n_x + \lambda)P})_i & \text{if } i > 0 \end{cases} \tag{F.8}$$

To represent the mean and covariance

$$E(z) \approx \frac{1}{2} \sum_{i=-n_x}^{-1} \frac{\lambda}{n_x + \lambda} z^i + \frac{\lambda}{n_x + \lambda} z^0 + \frac{1}{2} \sum_{i=1}^{n_x} \frac{\lambda}{n_x + \lambda} z^i \tag{F.9}$$

$$\begin{aligned}
 P(z) &\approx \frac{1}{2} \sum_{i=-n_x}^{-1} \frac{1}{n_x + \lambda} (z^i - E(z))(z^i - E(z)) + \\
 &\quad \left( \frac{\lambda}{n_x + \lambda} + (1 - \alpha^2 + \beta) \right) (z^0 - E(z))(z^0 - E(z)) + \\
 &\quad \frac{1}{2} \sum_{i=1}^{n_x} \frac{1}{n_x + \lambda} (z^i - E(z))(z^i - E(z))
 \end{aligned} \tag{F.10}$$

Here, the scaling parameter  $\lambda$  is defined as  $\lambda = \alpha^2(n_x + \kappa) - n_x$ . The parameters in this expression are  $\alpha$ , which controls the sigma point spread,  $\beta$  incorporates information of the distribution and  $\kappa$  is a secondary parameter. The standard values often used for these parameters are  $10^{-3}$ , 2 and 0 respectively.

This gives

$$g(x) \sim N(E(z), P(z)) \quad (\text{F.11})$$

The UKF algorithm then becomes as follows

**Initialization** ( $k = 0$ ):

$$\begin{aligned} \hat{x}_{1|0}(\theta) &= x_0, \\ P_{1|0}(\theta) &= P_0 \end{aligned} \quad (\text{F.12})$$

**Measurement update:**

Correction by fusion of prediction and measurements for ( $k$ )

$$\bar{x} = \begin{pmatrix} \hat{x}_k \\ e_k \end{pmatrix} \sim N \left( \begin{pmatrix} \hat{x}_{k|k-1} \\ 0 \end{pmatrix}, \begin{pmatrix} P_{k|k-1} & 0 \\ 0 & R \end{pmatrix} \right) \quad (\text{F.13})$$

$$z = \begin{pmatrix} x_k \\ y_k \end{pmatrix} = \begin{pmatrix} x_k \\ h(x_k, u_k, e_k) \end{pmatrix} \quad (\text{F.14})$$

Using the unscented transformation gives

$$z \sim N \left( \begin{pmatrix} \hat{x}_{k|k-1} \\ \hat{y}_{k|k-1} \end{pmatrix}, \begin{pmatrix} P_{k|k-1}^{xx} & P_{k|k-1}^{xy} \\ P_{k|k-1}^{yx} & P_{k|k-1}^{yy} \end{pmatrix} \right) \quad (\text{F.15})$$

The update is then given by

$$K_k = P_{k|k-1}^{xy} (P_{k|k-1}^{yy})^{-1} \quad (\text{F.16})$$

$$\hat{x}_k = \hat{x}_{k|k-1} + K_k (y_k - \hat{y}_{k|k-1}) \quad (\text{F.17})$$

$$P_k^{xx} = P_{k|k-1}^{xx} - K_k P_{k|k-1}^{yy} K_k^T \quad (\text{F.18})$$

**Time update:**

Prediction of states for ( $k + 1$ ) given predictions for ( $k$ )

$$\bar{x} = \begin{pmatrix} \hat{x}_k \\ v_k \end{pmatrix} \sim N \left( \begin{pmatrix} \hat{x}_k \\ 0 \end{pmatrix}, \begin{pmatrix} P_k & 0 \\ 0 & Q \end{pmatrix} \right) \quad (\text{F.19})$$

$$z = x_{k+1|k} = f(x_k, u_k, v_k) \quad (\text{F.20})$$

Using the unscented transformation gives

$$z \sim N(\hat{x}_{k+1|k}, P_{k+1|k}) \quad (\text{F.21})$$

The measurement and time update are then iterated as  $k$  increases. The time and measurement update structure has been kept in the used implementation.

# G

## Complementary results to the identification of unstable nonlinear systems

In this appendix complementary results to Chapter 8 are presented. To be able to understand the results, it is recommended that Section 8.2 is read. In that section, the simulation model and maneuvers for estimation and verification are described. The methods are denoted with PO (Parametrized Observer), EKF (Extended Kalman Filter), UKF (Unscented Kalman Filter), AUG (AUGmented state estimation) and CLM (Constrained Levenberg-Marquardt). Two types of investigations have been made. The first concerning SNR (Signal-to-Noise Ratio) and the second concerning  $\theta_0$  (initial model parameter offset). For these the model fit is given. In addition to this the results for SNR $10^5$ ,  $10^6$  and  $10^7$ , which were left out in Section 8.2, are given. One aspect of the comparison was to look at the influence of tuning parameters for the different methods. For the methods using some version of the Kalman filter, a fixed value of the process noise tuning parameter  $Q = 10^{-5}$  was used. The other tuning parameter settings used are given in Table G.1. This is by no means an exhaustive investigation looking for optimal settings, but gives some indication of possible problems.

**Table G.1:** Investigated tuning parameters.

PO, EKF, UKF, AUG	R1	R2	R3	R4	R5
	$10^{-9}$	$10^{-7}$	$10^{-5}$	$10^{-3}$	$10^{-1}$
CLM	$\lambda 1$	$\lambda 2$	$\lambda 3$	$\lambda 4$	$\lambda 5$
	0.01	0.1	1	10	100
AUG	W1	W2	W3	W4	W5
	$10^{-9}$	$10^{-7}$	$10^{-5}$	$10^{-3}$	$10^{-1}$

## G.1 Tuning results from the noise (SNR) sensitivity study

The parameter estimation in the SNR investigation is based on 100 MC (Monte Carlo) simulations for each method, SNR and tuning parameter setting. The outcome has then been validated on separate data sets. The mean of the Model fit is shown in Table G.2. As can be seen, there five different SNR settings have been investigated. As mentioned in Chapter 8, SNR  $10^4$  is assumed to be the worst case using data direct from flight test for the investigated maneuvers. After post-processing data SNR  $10^6$  or SNR  $10^7$  are more likely signal-to-noise ratios. SNR  $10^3$  has been added to get a feeling for how the methods work on other possible types of maneuvers with lower level of excitation.

In general, the results are more robust for higher SNR, which is not surprising. All methods except AUG seem to be insensitive to the tuning for SNR greater than  $10^5$ . Looking into the table the best results for the different methods and SNR settings are given in bold font. For all methods except the CLM, i.e., those methods that use some version of the Kalman filter, the results show that a tuning with higher  $R$  ( $R \rightarrow R5$ ), that is those putting more weight on using the information in the dynamic model, seems to give better results.

An important conclusion is that having more tuning parameters can possible lead to better results, but at the cost that the user has to have a very good knowledge of how to set these parameters. Otherwise the results can be corrupted. It is interesting to see that the PO method, which has no tuning parameters, is robust against the investigated SNR settings. The EKF rhas a similar behavior, but making the wrong tuning for noisy data decrease the accuracy in the results. The UKF gives less robust results for the more noisy data (SNR lower than  $10^4$ ), but has otherwise similar results as both PO and EKF. The CLM method seems almost as robust against different SNR settings as the PO method and the results are best for the largest regularization parameter tuning used ( $\lambda_{LM} = \lambda5 = 100$ ). A strange result is that the model fit seems to have an unmotivated dip for  $\lambda_{LM} = \lambda4 = 10$ . No reason for this behavior have been found so far. The AUG method has the highest number of tuning parameters. When using the best settings a model fit above 90% can be obtained for most SNR values, but the variation in the results for different tuning parameters is too big to be robust from a user perspective.

An interesting aspect that will be left to future work is when the results are good enough. For example, when is it possible to use the results for a control law design. Would it for example be possible to use some kind of figures of merit for the estimated model that help in the control law design.

**Table G.2: Model fit for different SNR.**

Met.	Tuning	SNR = 10 <sup>3</sup>	SNR = 10 <sup>4</sup>	SNR = 10 <sup>5</sup>	SNR = 10 <sup>6</sup>	SNR = 10 <sup>7</sup>	
PO	–	<b>84.84 ± 1.33</b>	<b>86.88 ± 0.43</b>	<b>86.63 ± 0.12</b>	<b>86.54 ± 0.04</b>	<b>86.50 ± 0.01</b>	
EKF	R1	< 0	71.88 ± 0.35	85.42 ± 0.12	86.43 ± 0.04	86.48 ± 0.01	
	R2	< 0	72.09 ± 0.35	85.44 ± 0.12	86.43 ± 0.04	86.48 ± 0.01	
	R3	10.38 ± 0.61	81.64 ± 0.41	86.14 ± 0.12	86.46 ± 0.04	86.47 ± 0.01	
	R4	<b>86.89 ± 1.25</b>	<b>86.90 ± 0.43</b>	86.55 ± 0.12	86.52 ± 0.04	86.51 ± 0.01	
	R5	85.93 ± 1.30	86.64 ± 0.43	<b>86.58 ± 0.12</b>	<b>86.59 ± 0.04</b>	<b>86.84 ± 0.01</b>	
UKF	R1	< 0	68.86 ± 0.27	<b>86.93 ± 0.12</b>	87.47 ± 0.04	88.69 ± 0.01	
	R2	< 0	68.87 ± 0.27	86.85 ± 0.12	<b>87.57 ± 0.04</b>	88.63 ± 0.01	
	R3	< 0	69.82 ± 0.27	86.83 ± 0.12	87.54 ± 0.04	<b>88.82 ± 0.01</b>	
	R4	< 0	<b>71.76 ± 0.29</b>	86.18 ± 0.11	85.25 ± 0.04	79.52 ± 0.01	
	R5	<b>18.60 ± 0.46</b>	64.78 ± 0.31	83.80 ± 0.11	79.59 ± 0.03	84.40 ± 0.01	
CLM	λ1	28.34 ± 0.59	86.36 ± 0.43	86.55 ± 0.12	86.60 ± 0.04	86.60 ± 0.01	
	λ2	87.41 ± 1.16	86.84 ± 0.43	86.59 ± 0.12	86.60 ± 0.04	86.60 ± 0.01	
	λ3	<b>87.52 ± 1.12</b>	86.79 ± 0.43	86.72 ± 0.12	86.75 ± 0.04	86.75 ± 0.01	
	λ4	81.12 ± 1.07	82.50 ± 0.33	83.13 ± 0.10	82.28 ± 0.03	82.19 ± 0.01	
	λ5	<b>87.52 ± 1.12</b>	<b>91.37 ± 0.37</b>	<b>91.53 ± 0.11</b>	<b>91.29 ± 0.03</b>	<b>91.23 ± 0.01</b>	
AUG	W1	R1	< 0	< 0	72.73 ± 24.4	86.33 ± 0.04	86.50 ± 0.01
		R2	< 0	< 0	84.57 ± 23.3	86.32 ± 0.04	86.50 ± 0.01
		R3	< 0	71.54 ± 26.6	87.16 ± 0.12	86.56 ± 0.04	86.51 ± 0.01
		R4	< 0	< 0	85.30 ± 0.12	85.30 ± 0.04	85.44 ± 0.01
		R5	86.87 ± 1.26	87.60 ± 0.43	87.55 ± 0.12	87.58 ± 0.04	87.58 ± 0.01
	W2	R1	< 0	< 0	< 0	85.91 ± 0.04	86.42 ± 0.01
		R2	< 0	< 0	< 0	85.88 ± 0.04	86.42 ± 0.01
		R3	< 0	< 0	85.54 ± 0.12	86.41 ± 0.04	86.45 ± 0.01
		R4	< 0	< 0	86.72 ± 0.12	86.55 ± 0.04	86.52 ± 0.01
		R5	86.76 ± 1.26	87.66 ± 0.43	87.64 ± 0.12	87.65 ± 0.04	87.66 ± 0.01
	W3	R1	< 0	< 0	< 0	78.93 ± 11.3	87.28 ± 0.01
		R2	< 0	< 0	< 0	84.02 ± 8.49	87.27 ± 0.01
		R3	< 0	< 0	70.89 ± 10.2	86.45 ± 0.04	87.15 ± 0.01
		R4	42.52 ± 10.8	<b>93.43 ± 0.27</b>	87.92 ± 0.12	87.14 ± 0.04	87.06 ± 0.01
		R5	<b>87.78 ± 1.19</b>	88.24 ± 0.43	87.92 ± 0.12	87.94 ± 0.04	87.95 ± 0.01
	W4	R1	< 0	< 0	< 0	< 0	< 0
		R2	< 0	< 0	< 0	< 0	< 0
		R3	< 0	< 0	< 0	79.72 ± 0.04	90.99 ± 0.01
		R4	< 0	41.69 ± 0.15	90.17 ± 0.09	90.44 ± 0.04	89.91 ± 0.01
		R5	75.55 ± 0.85	93.12 ± 0.41	90.21 ± 0.12	90.07 ± 0.04	90.10 ± 0.01
W5	R1	< 0	< 0	< 0	< 0	87.57 ± 0.01	
	R2	< 0	< 0	< 0	< 0	87.70 ± 0.01	
	R3	< 0	< 0	< 0	< 0	90.70 ± 0.01	
	R4	< 0	< 0	29.26 ± 0.05	83.34 ± 0.04	<b>92.20 ± 0.01</b>	
	R5	< 0	48.15 ± 0.16	<b>93.64 ± 0.10</b>	<b>90.69 ± 0.04</b>	90.83 ± 0.01	

## G.2 Complementary results for the SNR sensitivity study

The results given in this section, for SNR  $10^7$ ,  $10^6$  and  $10^5$ , has been left out of the main part of this thesis because the outcome is similar to that of the noise-free case using the best tuning parameters. As mentioned in the previous section most methods seem to be insensitive to the tuning for these SNRs. The results of the estimated models are given in Figures G.1, G.3 and G.5 together with Tables G.3, G.5 and G.7. As can be seen, all model estimates are fairly close to the true system. For the nonlinear part, CLM is the method that is least smooth, but it is still close to the true system. Both CLM and AUG give the best estimates of the linear parameters  $Z_\alpha$  and  $M_{\delta_c}$ . These are important parameters that have a large influence on the simulation results. This can be seen in the validation shown in Figures G.2, G.4 and G.6 together with Tables G.4, G.6 and G.8. Here, CLM and AUG have a model fit above 90%. The other methods are not much worse with a model fit above 86%. All-in-all, the results seem to be usable. The parameter that possibly is harder to estimate is  $Z_{\delta_c}$ . Some of the methods have problems in estimating the correct sign, but this parameter is less important and do not influence the simulation much.

## G.3 Tuning results from the initial offset ( $\theta_0$ ) sensitivity study

To investigate how sensitive the methods are to the initiation of the model parameters 100 MC (Monte Carlo) simulations have been made for each method, tuning parameter setting and different initial offset. The five used offsets can be seen in Figure G.7 and Table G.9. The parameters and the nonlinearities are disturbed up to 10% from the true value. This corresponds to possible model deviations of the current aerodynamic database for JAS 39 Gripen, which would be used for determining the initial parameters in an identification using real flight test data. A SNR of  $10^4$  has been used for the simulations.

As in the SNR investigation the PO method seems to be robust against initial parameter offsets. This is indeed an interesting result. The EKF follow this pattern but for  $R = R5 = 10^{-1}$ , i.e., when the method puts more weight on the dynamic model. Here, the results seem to depend on the initial offset. The same is true for the UKF method. This seems to be natural for the methods that use some version of the Kalman filter since if the initial model is uncertain then if the method puts weight on using the information in the dynamic model then the result gets less robust. For the CLM method the results are robust for  $\lambda_{LM} \leq 1$ . Above this level the resulting model fit change about 10% depending on the initial parameters. Again, the AUG method gives a kind of mixed result. If the tuning parameters are set as well as possible, the result can be excellent, but if not the results can be really bad.

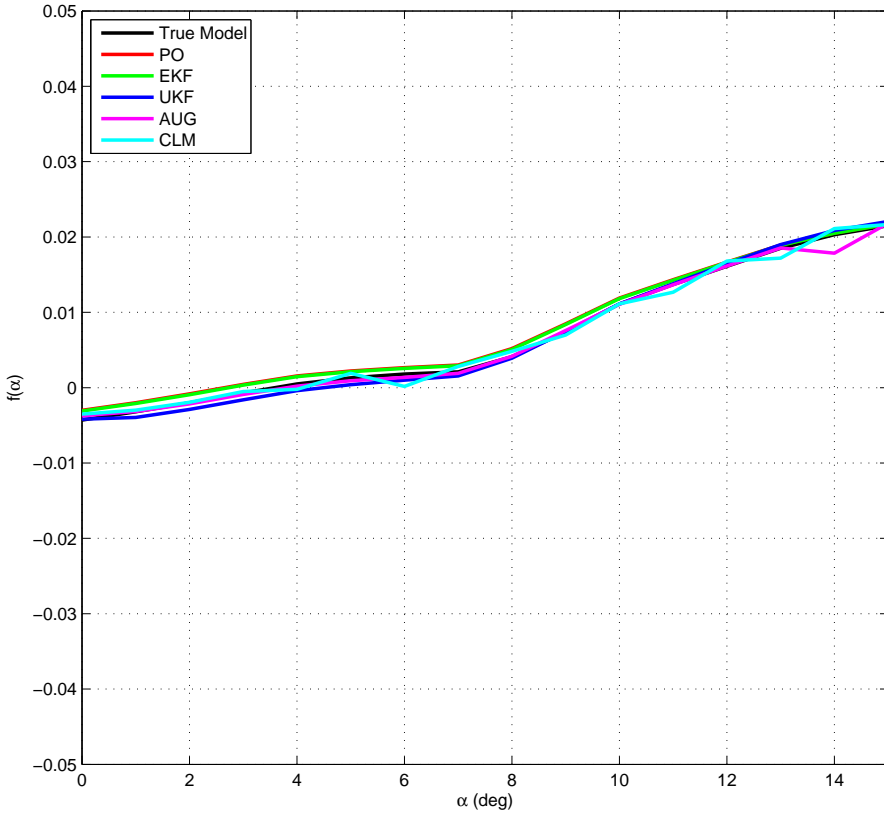


**Figure G.1:** Estimated and true aerodynamic derivatives for noisy data with SNR  $10^7$ .

**Table G.3:** Estimated and true aerodynamic derivatives for noisy data with SNR  $10^7$ .

	True	PO	EKF	UKF	AUG	CLM
$Z_\alpha$	0.9804	0.9814	0.9813	0.9815	0.9809	0.9800
$Z_q$	0.0163	0.0158	0.0159	0.0157	0.0162	0.0165
$M_q$	0.9790	0.9769	0.9771	0.9787	0.9780	0.9777
$Z_{\delta_e}$	-0.0051	-0.0087	-0.0082	-0.0095	-0.0093	-0.0048
$Z_{\delta_c}$	-0.0005	0.0003	0.0012	-0.0023	-0.0093	-0.0048
$M_{\delta_e}$	-0.5182	-0.5011	-0.5026	-0.5338	-0.5185	-0.5188
$M_{\delta_c}$	0.1376	0.1336	0.1330	0.1404	0.1377	0.1379



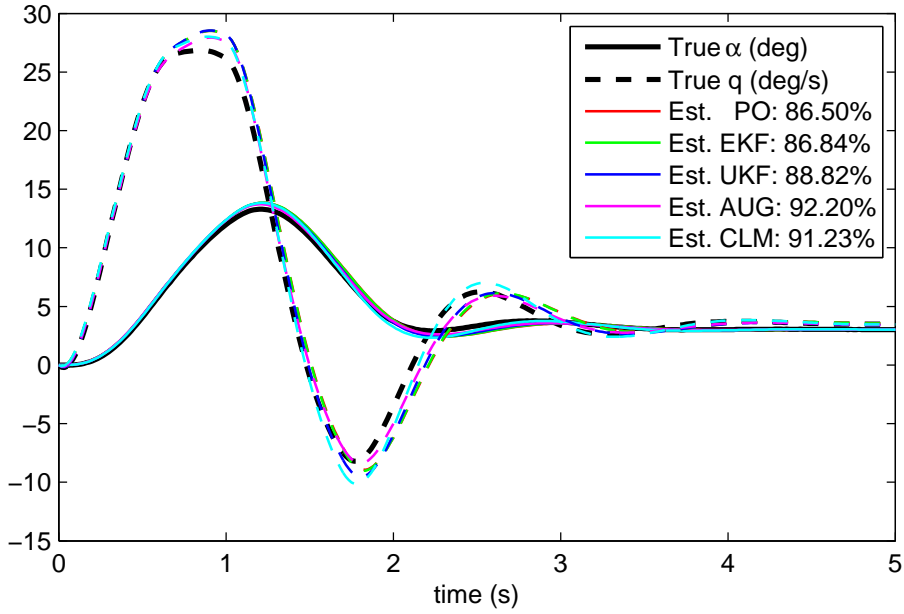
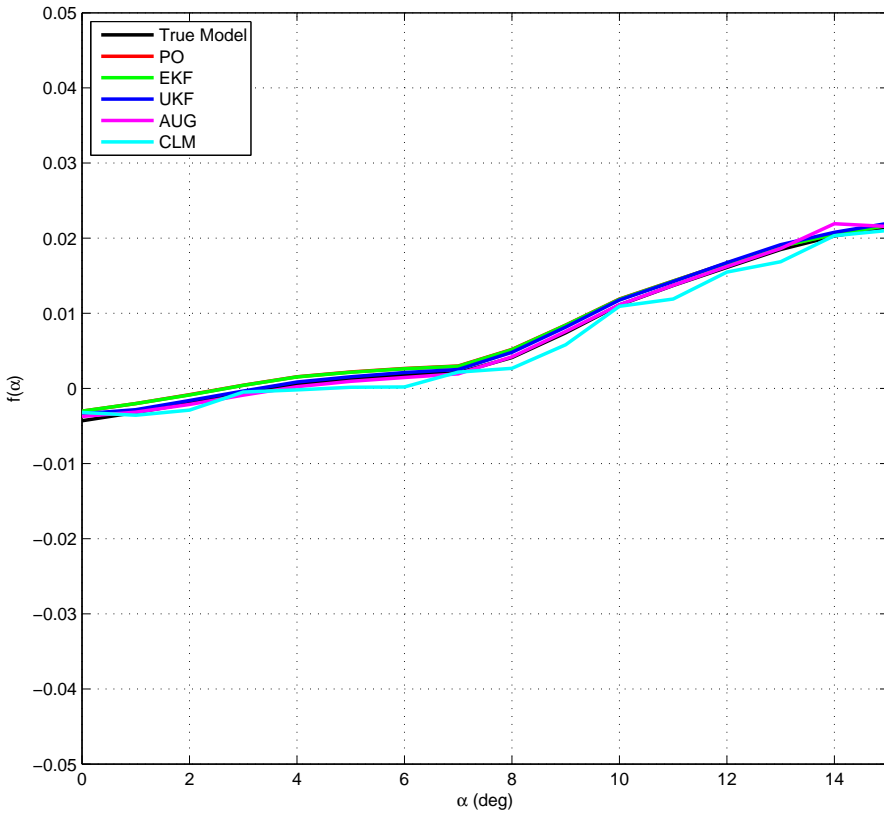


Figure G.2: Simulated noisy validation data for  $SNR 10^7$ .

Table G.4: Model fit and tuning for noisy data with  $SNR 10^7$ .

Method	Tuning	Model Fit val.	Model Fit est.
PO	<i>none</i>	$86.50 \pm 0.02\%$	$85.39 \pm 0.03\%$
EKF	$R = 1 \cdot 10^{-1}$	$86.84 \pm 0.02\%$	$85.79 \pm 0.03\%$
UKF	$R = 1 \cdot 10^{-5}$	$88.82 \pm 0.02\%$	$86.08 \pm 0.03\%$
AUG	$R = 1 \cdot 10^{-3}, w_k = 1 \cdot 10^{-1}$	$92.20 \pm 0.02\%$	$82.79 \pm 0.02\%$
CLM	$\lambda_{LM} = 100$	$91.23 \pm 0.02\%$	$89.97 \pm 0.02\%$



**Figure G.3:** Estimated and true aerodynamic derivatives for noisy data with SNR  $10^6$ .

**Table G.5:** Estimated and true aerodynamic derivatives for noisy data with SNR  $10^6$ .

	True	PO	EKF	UKF	AUG	CLM
$Z_\alpha$	0.9804	0.9812	0.9813	0.9814	0.9803	0.9796
$Z_q$	0.0163	0.0160	0.0159	0.0158	0.0165	0.0167
$M_q$	0.9790	0.9769	0.9769	0.9773	0.9789	0.9795
$Z_{\delta_e}$	-0.0051	-0.0075	-0.0084	-0.0088	-0.0071	-0.0030
$Z_{\delta_c}$	-0.0005	0.0051	0.0013	0.0004	0.0000	-0.0011
$M_{\delta_e}$	-0.5182	-0.5016	-0.5015	-0.5154	-0.5184	-0.5180
$M_{\delta_c}$	0.1376	0.1319	0.1336	0.1360	0.1377	0.1377

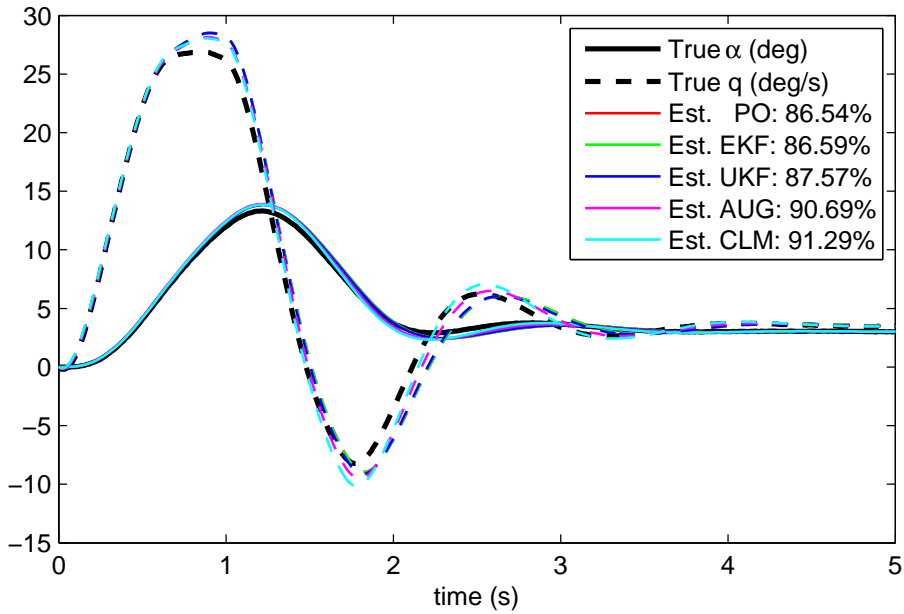


**Figure G.4:** Simulated and true angle-of-attack and pitch angular velocity for noisy validation data with SNR  $10^6$ .

**Table G.6:** Model fit and tuning for noisy data with SNR  $10^6$

Method	Tuning	Model Fit val.	Model Fit est.
PO	<i>none</i>	$86.54 \pm 0.08\%$	$85.69 \pm 0.08\%$
EKF	$R = 1 \cdot 10^{-1}$	$86.59 \pm 0.08\%$	$85.84 \pm 0.08\%$
UKF	$R = 1 \cdot 10^{-7}$	$87.57 \pm 0.08\%$	$86.07 \pm 0.09\%$
AUG	$R = 1 \cdot 10^{-1}, w_k = 1 \cdot 10^{-1}$	$90.69 \pm 0.07\%$	$86.08 \pm 0.07\%$
CLM	$\lambda_{LM} = 100$	$91.29 \pm 0.06\%$	$91.15 \pm 0.07\%$

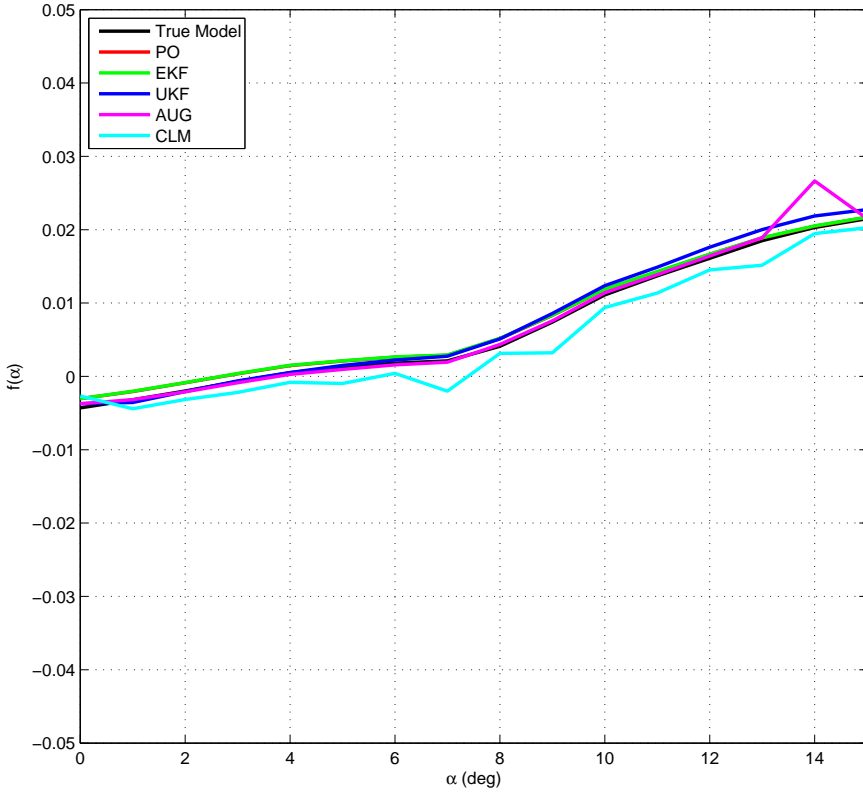


**Figure G.5:** Estimated and true aerodynamic derivatives for noisy data with  $\text{SNR } 10^5$ .

**Table G.7:** Estimated and true aerodynamic derivatives for noisy data with  $\text{SNR } 10^5$ .

	True	PO	EKF	UKF	AUG	CLM
$Z_\alpha$	0.9804	0.9813	0.9817	0.9821	0.9794	0.9805
$Z_q$	0.0163	0.0159	0.0153	0.0155	0.0178	0.0163
$M_q$	0.9790	0.9770	0.9769	0.9762	0.9794	0.9822
$Z_{\delta_e}$	-0.0051	-0.0086	-0.0124	-0.0177	-0.0128	-0.0060
$Z_{\delta_c}$	-0.0005	0.0005	-0.0154	0.0013	0.0013	-0.0004
$M_{\delta_e}$	-0.5182	-0.5017	-0.5021	-0.5318	-0.5215	-0.5211
$M_{\delta_c}$	0.1376	0.1344	0.1320	0.1403	0.1384	0.1385

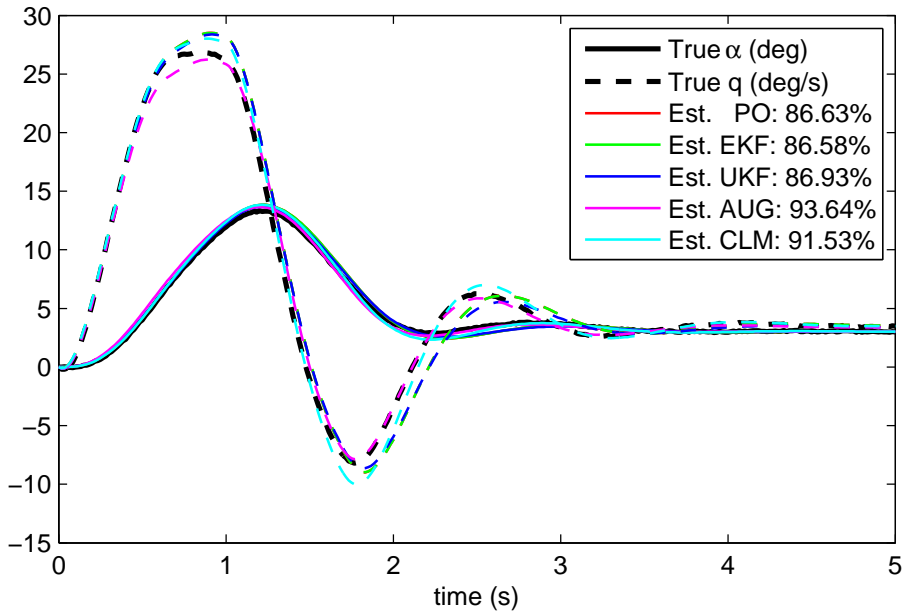


**Figure G.6:** Simulated and true angle-of-attack and pitch angular velocity for noisy validation data with SNR  $10^5$ .

**Table G.8:** Model fit and tuning for noisy data with SNR  $10^5$ .

Method	Tuning	Model Fit val.	Model Fit est.
PO	<i>none</i>	$86.63 \pm 0.24\%$	$86.27 \pm 0.22\%$
EKF	$R = 1 \cdot 10^{-1}$	$86.58 \pm 0.24\%$	$86.11 \pm 0.22\%$
UKF	$R = 1 \cdot 10^{-9}$	$86.93 \pm 0.24\%$	$84.66 \pm 0.17\%$
AUG	$R = 1 \cdot 10^{-1}, w_k = 1 \cdot 10^{-1}$	$93.64 \pm 0.21\%$	$81.30 \pm 0.24\%$
CLM	$\lambda_{LM} = 100$	$91.53 \pm 0.22\%$	$89.87 \pm 0.21\%$

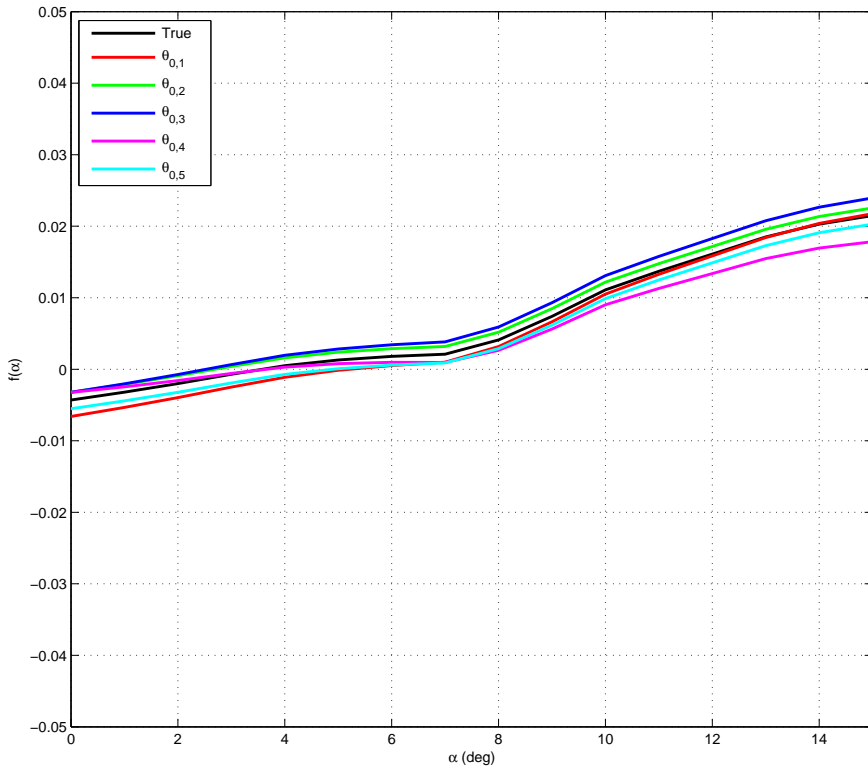


**Figure G.7:** True pitching moment and initial offset in  $\theta_0$ .

**Table G.9:** True aerodynamic derivatives and initial offset in  $\theta_0$ .

	True	$\theta_{0,1}$	$\theta_{0,2}$	$\theta_{0,3}$	$\theta_{0,4}$	$\theta_{0,5}$
$Z_\alpha$	0.9804	0.9824	0.9797	0.9821	0.9787	0.9819
$Z_q$	0.0163	0.0179	0.0151	0.0172	0.0160	0.0155
$M_q$	0.9790	0.9811	0.9753	0.9834	0.9815	0.9778
$Z_{\delta_e}$	-0.0051	-0.0046	-0.0052	-0.0055	-0.0051	-0.0052
$Z_{\delta_c}$	-0.0005	-0.0004	-0.0005	-0.0004	-0.0005	-0.0005
$M_{\delta_e}$	-0.5182	-0.4664	-0.5728	-0.4520	-0.4555	-0.5734
$M_{\delta_c}$	0.1376	0.1238	0.1657	0.1520	0.1460	0.1539

**Table G.10:** Model fit for different  $\theta_0$ .

Met.	Tuning	$\theta_{0,1}$	$\theta_{0,2}$	$\theta_{0,3}$	$\theta_{0,4}$	$\theta_{0,5}$	
PO	–	$86.53 \pm 0.43$	$86.84 \pm 0.43$	$86.52 \pm 0.43$	$86.50 \pm 0.43$	$86.51 \pm 0.43$	
EKF	R1	$71.83 \pm 0.35$	$71.76 \pm 0.35$	$71.73 \pm 0.35$	$71.78 \pm 0.35$	$71.70 \pm 0.35$	
	R2	$72.08 \pm 0.35$	$72.00 \pm 0.35$	$72.01 \pm 0.35$	$71.99 \pm 0.35$	$72.16 \pm 0.35$	
	R3	$81.61 \pm 0.41$	$81.59 \pm 0.41$	$81.55 \pm 0.41$	$81.61 \pm 0.41$	$81.68 \pm 0.41$	
	R4	$86.90 \pm 0.43$	$86.91 \pm 0.43$	$86.90 \pm 0.43$	$86.90 \pm 0.43$	$86.91 \pm 0.43$	
	R5	$87.31 \pm 0.43$	$86.63 \pm 0.43$	$59.42 \pm 0.19$	$83.99 \pm 0.38$	$86.63 \pm 0.43$	
UKF	R1	$69.18 \pm 0.25$	$69.08 \pm 0.24$	$69.63 \pm 0.25$	$69.05 \pm 0.24$	$69.67 \pm 0.24$	
	R2	$68.96 \pm 0.24$	$69.66 \pm 0.24$	$69.08 \pm 0.24$	$69.07 \pm 0.24$	$69.45 \pm 0.24$	
	R3	$69.29 \pm 0.25$	$71.27 \pm 0.25$	$69.86 \pm 0.25$	$69.45 \pm 0.25$	$69.60 \pm 0.24$	
	R4	$70.04 \pm 0.27$	$72.46 \pm 0.26$	$72.19 \pm 0.27$	$70.68 \pm 0.28$	$71.39 \pm 0.26$	
	R5	$83.23 \pm 0.33$	$69.15 \pm 0.26$	$88.74 \pm 0.21$	$69.13 \pm 0.33$	$83.47 \pm 0.35$	
CLM	$\lambda_1$	$86.35 \pm 0.43$	$86.56 \pm 0.43$	$86.34 \pm 0.43$	$86.42 \pm 0.43$	$86.45 \pm 0.43$	
	$\lambda_2$	$86.89 \pm 0.43$	$86.92 \pm 0.43$	$86.91 \pm 0.43$	$86.80 \pm 0.43$	$86.83 \pm 0.43$	
	$\lambda_3$	$86.56 \pm 0.43$	$86.80 \pm 0.43$	$86.57 \pm 0.43$	$86.57 \pm 0.43$	$86.79 \pm 0.43$	
	$\lambda_4$	$76.69 \pm 0.32$	$86.72 \pm 0.33$	$76.36 \pm 0.31$	$77.92 \pm 0.32$	$86.84 \pm 0.33$	
	$\lambda_5$	$81.57 \pm 0.29$	$87.32 \pm 0.28$	$79.66 \pm 0.28$	$84.39 \pm 0.30$	$86.68 \pm 0.29$	
AUG	W1	R1	< 0	< 0	< 0	< 0	< 0
		R2	< 0	< 0	< 0	< 0	< 0
		R3	< 0	< 0	< 0	< 0	$74.16 \pm 0.01$
		R4	< 0	< 0	< 0	$57.13 \pm 0.03$	$87.52 \pm 0.01$
		R5	$82.99 \pm 1.33$	$89.28 \pm 0.40$	$83.84 \pm 0.12$	$84.33 \pm 0.04$	$89.55 \pm 0.01$
	W2	R1	< 0	< 0	< 0	< 0	< 0
		R2	< 0	< 0	< 0	< 0	< 0
		R3	< 0	< 0	< 0	< 0	$22.06 \pm 0.00$
		R4	< 0	< 0	< 0	< 0	< 0
		R5	$82.82 \pm 1.33$	$89.64 \pm 0.39$	$83.63 \pm 0.12$	$84.12 \pm 0.04$	$89.89 \pm 0.01$
	W3	R1	< 0	< 0	< 0	< 0	< 0
		R2	< 0	< 0	< 0	< 0	< 0
		R3	$17.08 \pm 0.22$	< 0	< 0	< 0	< 0
		R4	< 0	$95.24 \pm 0.20$	$94.51 \pm 0.11$	$94.32 \pm 0.03$	$54.09 \pm 0.01$
		R5	$82.57 \pm 1.34$	$90.73 \pm 0.36$	$83.00 \pm 0.12$	$83.69 \pm 0.04$	$90.54 \pm 0.01$
	W4	R1	< 0	< 0	< 0	< 0	< 0
		R2	< 0	< 0	< 0	< 0	< 0
		R3	< 0	< 0	< 0	< 0	< 0
		R4	$37.52 \pm 0.44$	$41.48 \pm 0.15$	$42.08 \pm 0.05$	$41.83 \pm 0.02$	$41.66 \pm 0.00$
		R5	$85.21 \pm 1.37$	$95.55 \pm 0.26$	$85.54 \pm 0.13$	$88.44 \pm 0.04$	$95.17 \pm 0.01$
	W5	R1	< 0	< 0	< 0	< 0	< 0
		R2	< 0	< 0	< 0	< 0	< 0
		R3	< 0	< 0	< 0	< 0	< 0
		R4	< 0	< 0	< 0	< 0	< 0
		R5	$49.02 \pm 0.53$	$47.52 \pm 0.16$	$48.84 \pm 0.05$	$47.65 \pm 0.02$	$48.40 \pm 0.00$

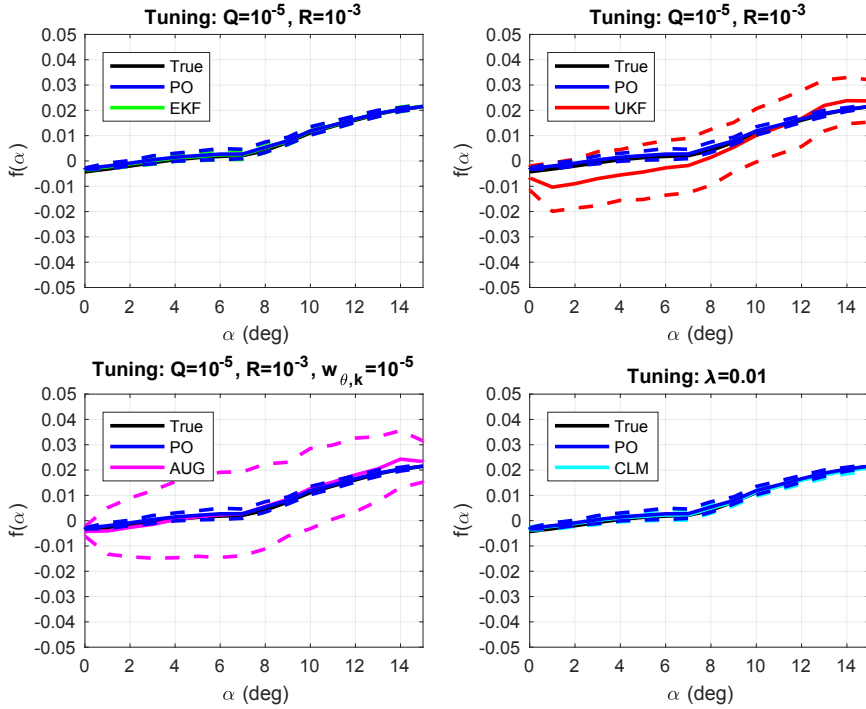


**Figure G.8:** Estimated and true pitching moment for initial offset in  $\theta_{0,4}$ .

**Table G.11:** Estimated and true aerodynamic derivatives for the initial offset in  $\theta_{0,4}$ .

	True	PO	EKF	UKF	AUG	CLM
$N_\alpha$	0.9804	0.9813	0.9833	0.9881	0.9800	0.9785
$N_q$	0.0163	0.0159	0.0134	0.0127	0.0170	0.0194
$M_q$	0.9790	0.9776	0.9778	0.9829	0.9770	0.9813
$N_{\delta_e}$	-0.0051	-0.0084	-0.0265	-0.0369	-0.0087	0.0174
$N_{\delta_c}$	-0.0005	0.0012	-0.0732	0.0003	0.0019	0.1084
$M_{\delta_e}$	-0.5182	-0.4955	-0.5032	-0.6285	-0.5397	-0.4731
$M_{\delta_c}$	0.1376	0.1560	0.1455	0.2305	0.1637	0.2600



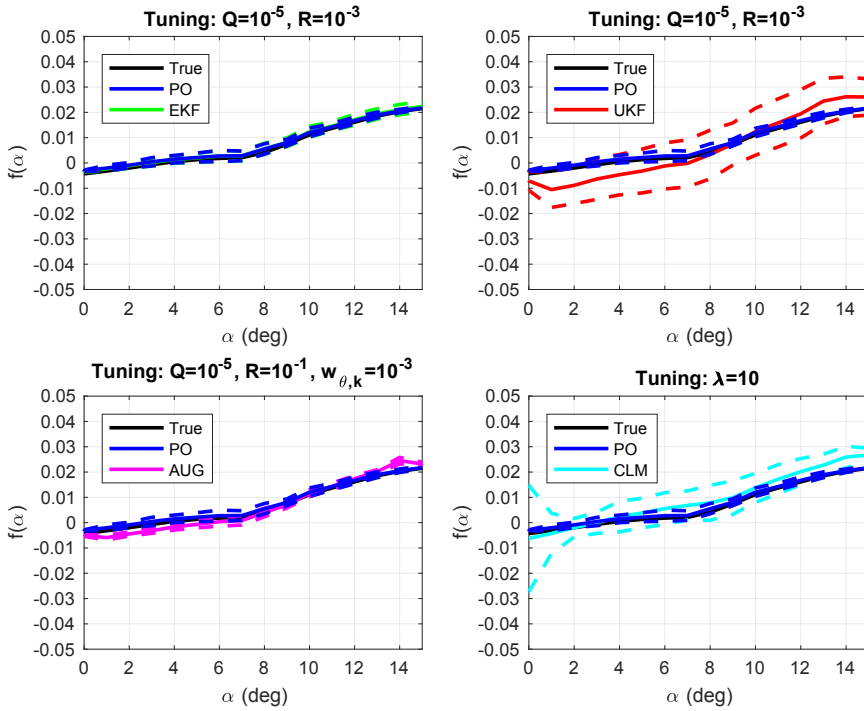


**Figure G.9:** Estimated and true pitching moment for initial offset in  $\theta_{0,5}$ .

**Table G.12:** Estimated and true aerodynamic derivatives for the initial offset in  $\theta_{0,5}$ .

	True	PO	EKF	UKF	AUG	CLM
$N_\alpha$	0.9804	0.9812	0.9854	0.9730	0.9802	0.9811
$N_q$	0.0163	0.0160	0.0107	0.0251	0.0168	0.0160
$M_q$	0.9790	0.9769	0.9742	1.0304	0.9790	0.9657
$N_{\delta_e}$	-0.0051	-0.0073	-0.0467	0.0537	-0.0088	-0.0084
$N_{\delta_c}$	-0.0005	0.0058	-0.1569	0.2451	0.0003	-0.0008
$M_{\delta_e}$	-0.5182	-0.5021	-0.5296	-0.0848	-0.5718	-0.5523
$M_{\delta_c}$	0.1376	0.1314	0.0364	1.5136	0.1535	0.1481

---

## Bibliography

- M. R-H Abdalmoaty. *Learning Stochastic Nonlinear Dynamical Systems Using Non-stationary Linear Predictors*. Licentiate thesis, KTH, Stockholm, 2017. Cited on page 146.
- I. Andersson. *Real-Time Aerodynamic System identification*. Saab Aeronautics; Linköping, Sweden, 2010. (Company internal report). Cited on pages 78 and 188.
- K. Andersson, M. Karlsson, and M. Staaf. Aerodynamic and flight dynamic real-time analysis during spin and carefree maneuvering tests of the Saab JAS 39 Gripen. In *Proceedings of the 23rd Congress of ICAS, International Council of Aeronautical Sciences*, 2002. Cited on page 48.
- H. Backström. Report on the usage of the generic aerodata model. Technical Report iss. 2, Saab, 1997. (Company internal report). Cited on pages 5 and 192.
- R. M. Bailey, R. W. Hostetler, K. N. Barnes, C. M. Belcastro, and C. M. Belcastro. Experimental validation: Subscale aircraft ground facilities and integrated test capability. In *Proceedings of the AIAA Guidance, Navigation, and Control Conference*, 2005. AIAA 2005-6433. Cited on page 121.
- Basappa and R. V. Jategaonkar. Evaluation of recursive methods for aircraft parameter estimation. In *Proceedings of the AIAA Atmospheric Flight Mechanics Conference and Exhibit*, August 2004. AIAA 2004-5063. Cited on page 59.
- P. Biswas, P. Grieder, and J. Löfberg. A survey on stability analysis of discrete-time affine systems. In *Proceedings of the 16th Triennial World Congress*, 2005. Cited on pages 149 and 153.
- N. Bof, R Carli, and L Schenato. Lyapunov theory for discrete time systems. Technical Report iss. 1, University of Padova; Padova, Italy, 2018. arXiv:1809.05289v1. Cited on page 148.
- J. R. Chambers. Modeling flight - the role of dynamically scaled free-flight models in support of NASA's aerospace programs. *NASA, Washington DC*, 2009. Cited on page 121.

- P. A. Cook. *Nonlinear Dynamical Systems*. Prentice Hall, Inc., Second edition, 1994. Cited on page 12.
- F. E. C. Culick. What the Wright brothers did and did not understand about flight mechanics - in modern terms. In *Proceedings of the 37th AIAA/ASME/SAE/SAEE Joint Propulsion Conference and Exhibit*, Salt Lake City, Utah, USA, July 2001. Cited on page 2.
- W. M. DeBusk, G. Chowdhary, and E. N. Johnson. Real-time system identification of a small multi-engine aircraft. In *Proceedings of the AIAA Infotech@Aerospace Conference*, April 2010. AIAA-2010-3472. Cited on page 59.
- R. F. Dorr, R. Francillon, and J. Miller. *Saab J35 Draken*. Aerofax Inc., 1987. Cited on page 122.
- B. Duignan. *Occam's razor*. Encyclopædia Britannica, inc., On-line edition, 2018. Cited on page 143.
- B. Etkin. *Dynamics of Atmospheric Flight*. John Wiley and Sons, Inc., First edition, 1972. Cited on page 29.
- G. Feng. Stability analysis of piecewise discrete-time linear systems. *IEEE Transactions on Automatic Control*, 47(7):1108–1112, 2002. Cited on page 149.
- L. Forssell and U. Nilsson. ADMIRE the aero-data model in a research environment version 4.0, model description. Technical report, FOI, 2005. Cited on pages 5, 35, and 191.
- L. S. Forssell and Å. Hydén. Flight control system validation using global nonlinear optimization algorithms. In *Proceedings of the 2003 European Control Conference (ECC)*, pages 1269–1273, September 2003. Cited on page 5.
- U. Forssell and L. Ljung. Identification of unstable systems using output error and Box-Jenkins model structures. *IEEE Transactions on Automatic Control*, 45(1):131–147, January 2000. Cited on page 145.
- M. Gilson and P. Van den Hof. Instrumental variable methods for closed-loop system identification. *Automatica*, 41(2):241–249, February 2005. Cited on page 80.
- N. J. Gordon, D. J. Salmond, and A. F. M. Smith. Novel approach to nonlinear/non-Gaussian Bayesian state estimation. *IEE Proceedings F - Radar and Signal Processing*, 140(2):107–113, April 1993. Cited on page 158.
- F. Gustafsson. Particle filter theory and practice with positioning applications. *IEEE Aerospace and Electronic Systems Magazine*, 25(7):53–82, 2010. Cited on page 158.
- F. Gustafsson. *Statistical Sensor Fusion*. Studentlitteratur AB, Lund., 2012. Cited on pages 93 and 140.

- D. Haessig and B. Friedland. A method for simultaneous state and parameter estimation in nonlinear systems. In *Proceedings of the American Control Conference*, 1997. Cited on page 161.
- A. Hagenblad, L Ljung, and A Wills. Maximum likelihood identification of Wiener models. *Automatica*, 44(11):2697–2705, February 2008. Cited on page 158.
- P. G. Hamel and R. V. Jategaonkar. Evolution of flight vehicle system identification. *Journal of Aircraft*, 33(1):9–28, January-February 1996. Cited on page 8.
- J. Hamilton. *F-16 Fighting Falcon*. ABDO Daughters, First edition, 2012. Cited on page 6.
- J. P. Hespanha. *Linear Systems Theory*. Princeton University Press, New Jersey, Second edition, 2018. Cited on page 84.
- R. V. Jategaonkar. *Flight Vehicle System Identification, A Time Domain Methodology*. American Institute of Aeronautics and Astronautics Inc., 2015. Cited on page 8.
- Z. P. Jiang, E.D. Sontag, and Y. Wang. Input-to-state stability for discrete-time nonlinear systems. In *Proceedings of the 14th IFAC World Congress*, 1999. Cited on page 152.
- M. Johansson. *Piecewise Linear Control Systems*. PhD thesis, Lund University, Sweden, 1999. Cited on page 149.
- J. Jørgensen. *Saab 35 Draken, the ultimate portfolio*. Nordic Airpower, First edition, 2015. Cited on page 7.
- C. Jouannet, P. Berry, T. Melin, K. Amadori, D. Lundström, and I. Staack. Subscale flight testing used in conceptual design. *Aircraft Engineering and Aerospace Technology*, 84(3):192–199, 2012. Cited on pages 7, 122, and 130.
- S. J. Julier, J. K. Uhlmann, and H. F. Durrant-Whyte. A new extension of the Kalman filter to nonlinear systems. In *Proceedings of the 1995 American Control Conference*, volume 1-6, pages 1628–1632, June 1995. Cited on page 160.
- T. Kailath, A. H. Sayed, and B. Hassibi. *Linear Estimation*. Prentice Hall PTR, First edition, 2000. Cited on page 159.
- R. E. Kalman. A new approach to linear filtering and prediction problems. *Transactions of the ASME-Journal of Basic Engineering*, 46(Series D):35–45, March 1960. Cited on pages 23, 73, 159, and 277.
- G. Keijsper. *Saab Gripen - Sweden's 21st Century Multi-role Aircraft*. Aerofax, First edition, 2004. Cited on page 5.
- H. K. Khalil. *Nonlinear Systems*. Prentice Hall, Inc., Third edition, 2002. Cited on pages 12, 148, and 278.

- V. Klein and E. A. Morelli. *Aircraft System Identification, Theory and Practice*. American Institute of Aeronautics and Astronautics Inc., 2016. Cited on pages 8, 59, 61, 62, 63, 65, 72, 73, 119, 127, and 203.
- I. Kollár, R. Pintelon, and J. Schoukens. Frequency domain system identification toolbox for matlab: Characterizing nonlinear errors of linear models. In *Proceedings of SYSID 2006*, March 2006. Cited on page 126.
- G. Kristiansson. Modeling of the Unsteady Aerodynamics at High Angles of Attack for the Saab JAS 39 Gripen. Technical report, Saab Aeronautics; Linköping, Sweden, 2006. (Company internal report). Cited on page 57.
- R. Larsson. *System Identification of Flight Mechanical Characteristics*. Licentiate thesis, Linköping University, 2013. Cited on page 9.
- R. Larsson and M. Enqvist. Real-time aerodynamic model parameter identification. In *Society of Flight Test Engineers International Symposium*, Linköping and Stockholm, Sweden, September 2009. Cited on page 187.
- R. Larsson and M. Enqvist. Sequential aerodynamic model parameter identification. In *Proceedings of the 16th IFAC Symposium on System Identification*, pages 1413–1418, Brussels, Belgium, July 2012a. Cited on pages 68, 127, and 203.
- R. Larsson and M. Enqvist. Nonlinear aerodynamic modeling of unstable aircraft using flight test data. In *Proceedings of the 28th Congress of the International Council of the Aeronautical Sciences*, Brisbane, Australia, September 2012b. Cited on page 188.
- R. Larsson and M. Enqvist. An easy to use engineering method for identification of complex flight dynamics from flight test data. In *Proceedings of 16th AIAA Aviation Technology, Integration, and Operations Conference, AIAA Aviation 2016*, Washington DC, USA, June 2016. Cited on page 188.
- R. Larsson, Z. Sjanic, M. Enqvist, and L. Ljung. Direct prediction-error identification of unstable nonlinear systems applied to flight test data. In *Proceedings of the 15th IFAC Symposium on System Identification*, pages 144–149, Saint-Malo, France, July 2009. Cited on page 143.
- R. Larsson, A. Sobron, D. Lundström, and M. Enqvist. Multisine inputs for a sub-scale demonstrator aircraft. *Submitted to Control Engineering Practice*, March 2019. Cited on page 187.
- S. Larsson Cahlin. Real-time estimation of aerodynamic parameters. Technical report, Linköping University, Sweden, 2016. Master Thesis. Cited on page 188.
- M. Lazar and W.P.M.H. Heemels. Global input-to-state stability and stabilization of discrete-time piecewise affine systems. *Nonlinear Analysis: Hybrid Systems*, 2(3):721–734, 2008. Cited on page 149.

- L. Ljung. Convergence analysis of parametric identification methods. *IEEE Transactions on Automatic Control*, AC-23(5):770–783, October 1978. Cited on page 22.
- L. Ljung. *System Identification, Theory for the User*. Prentice Hall PTR, Second edition, 1999. Cited on pages 11, 21, 24, 72, 80, 124, 138, 145, 146, 159, and 203.
- L. Ljung. Perspective on system identification. In *Proceedings of the 17th IFAC World Congress*, Seoul, South Korea, July 2008. Cited on page 11.
- L. Ljung and J. Sjöberg. A system identification perspective on neural nets. In *Proceedings of the 1992 IEEE-SP Workshop*, 1992. Cited on page 158.
- D. Lundström. *Aircraft Design Automation and Subscale Testing*. Linköping Studies in Science and Technology, Dissertation No. 1480, 2012. Cited on page 121.
- D. Lundström, A. Sobron, P. Krus, C. Jouannet, and R. Gil Annes da Silva. Subscale flight testing of a generic fighter aircraft. 2016. Cited on page 131.
- A. M. Lyapunov. The General Problem of Stability of Motion (in Russian). *Kharkov Mathematical Society*, Collected Works II:250 p, 1892. Cited on page 147.
- P. P. Menon, G. D. Bates, and I. Postlethwaite. Hybrid evolutionary optimisation methods for the clearance of nonlinear flight control laws. In *Proceedings of the 44th IEEE Conference on Decision and Control, and the European Control Conference 2005*, pages 4053–4058, December 2005. Cited on page 5.
- T. K. Moon. The expectation-maximization algorithm. *IEEE Signal Processing Magazine*, 13(6):47–60, November 1996. Cited on page 158.
- P. Del Moral. Non-linear filtering: Interacting particle solution. *Markov Processes Related Fields*, 2(4):555–580, April 1996. Cited on page 158.
- E. A. Morelli. Real-time parameter estimation in the frequency domain. In *Proceedings of the AIAA Guidance, Navigation, and Control Conference*, August 1999. AIAA-99-4043. Cited on pages 59, 64, 65, 68, and 203.
- E. A. Morelli. Real-time aerodynamic parameter estimation without air flow angle measurements. Technical report, NASA Langley Research Center; Hampton, USA, 2010. Cited on pages 68 and 203.
- E. A. Morelli. Flight test maneuvers for efficient aerodynamic modeling. In *Proceedings of the AIAA Atmospheric Flight Mechanics Conference*, August 2011. AIAA 2011-6672. Cited on page 126.
- E. A. Morelli and V. Klein. Application of System Identification to Aircraft at NASA Langley Research Center. *Journal of Aircraft*, 42(1):12–25, January-February 2005. Cited on page 138.

- A. V. Mulders, J. Schoukens, M. Volckaert, and M. Diehl. Two nonlinear optimization methods for black box identification compared. *Automatica*, 46(10): 1675–1681, October 2010. Cited on pages 23 and 162.
- K. S. Narendra and K Parthasarathy. Identification and control of dynamic systems using neural networks. *IEEE Transactions on Neural Networks*, 1(1):4–27, March 1990. Cited on page 158.
- R. C. Nelson. *Flight Stability and Automatic Control*. McGraw-Hill, Second edition, 1998. Cited on pages 25, 29, and 43.
- J. Nocedal and S. J. Wright. *Numerical Optimization*. Springer Series in Operations Research. SpringerScience+Business Media, LLC, Second edition, 2006. Cited on pages 22 and 162.
- L. Nyman. *Estimation of Aerodynamic Parameters in Real-Time: Implementation and Comparison of a Sequential Frequency Domain Method and a Batch Method*. Linköping University, Sweden, 2016. Master Thesis. Cited on page 188.
- R. Pintelon and J. Schoukens. *System Identification, A Frequency Domain Approach*. John Wiley & Sons, Inc, Second edition, 2012. Cited on page 11.
- R. Pintelon, J. Schoukens, and G. Vandersteen. Frequency domain system identification using arbitrary signals. *IEEE Transactions on Automatic Control*, 42(12):1717–1720, December 1997. Cited on page 68.
- P. H. Rangegowda, J. Valluru, S. C. Patwardhan, and S. Mukhopadhyay. Simultaneous state and parameter estimation using receding-horizon nonlinear kalman filter. In *Proceedings of the 10th IFAC International Symposium on Advanced Control of Chemical Processes*, 2018. Cited on page 161.
- J. Roll. *Local and Piecewise Affine Approaches to System Identification*. PhD Thesis, Linköping University, Linköping, Sweden, 2003. Cited on page 18.
- T. B. Schön, A. Wills, and B. Ninness. Maximum likelihood nonlinear system estimation. In *Proceedings of the 14th IFAC Symposium on System Identification*, 2006. Cited on page 158.
- T. B. Schön, A Wills, and B. Ninness. System identification of nonlinear state-space models. *Automatica*, 47(1):39–49, January 2011. Cited on pages 145 and 158.
- J. Schoukens, M. Vaes, and R. Pintelon. Linear system identification in a nonlinear setting: Nonparametric analysis of the nonlinear distortions and their impact on the best linear approximation. *IEEE Control Systems, Vol. 36 Iss: 3*, 2016. Cited on page 127.
- D. Simon. *Optimal State Estimation: Kalman,  $H_\infty$  and Nonlinear Approaches*. John Wiley & Sons, Inc., First edition, 2006. Cited on page 161.

- S. Skogestad and I. Postlethwaite. *Multivariable robust control, Analysis and Design*. John Wiley Sons, Ltd., Second edition, 2005. Cited on page 164.
- G. L. Smith, S. F. Schmidt, and L. A. McGee. Application of statistical filter theory to the optimal estimation of position and velocity on board a circumlunar vehicle. Technical Report TR R-135, NASA, 1962. Cited on page 159.
- A. Sobron. *On Subscale Flight Testing: Applications in Aircraft Conceptual Design*. Licentiate thesis, Linköping University Electronic Press, 2018. Cited on page 121.
- A. Sobron, D. Lundström, P. Krus, R. Larsson, and C. Jouannet. Methods for efficient flight testing and modelling of remotely piloted aircraft within visual line-of-sight. In *Proceedings of the 31th Congress of the International Council of the Aeronautical Sciences*, 2018. Cited on page 130.
- T. Söderström and P. Stoica. *System Identification*. Prentice Hall PTR, Second edition, 1989. Cited on page 11.
- T. Söderström and P. Stoica. Instrumental variable methods for system identification. *Circuits Systems and Signal Processing*, 22(1):1–9, 2002. Cited on page 24.
- B. L. Stevens and F. L. Lewis. *Aircraft Control and Simulation*. John Wiley Sons, Inc., First edition, 1992. Cited on pages 29 and 112.
- M. B. Tischler and R. K. Remple. *Aircraft and Rotorcraft System Identification, Engineering Methods with Flight Test Examples*. American Institute of Aeronautics and Astronautics Inc., 2012. Cited on page 8.
- J. Upton. *Warbird Tech – Lockheed F-104 Starfighter*. Specialty Press, First edition, 2003. Cited on page 6.
- G. Welch and G. Bishop. An introduction to the Kalman filter. Technical Report TR 95-041, Department of Computer Science, University of North Carolina at Chapel Hill, July 2006. Cited on page 24.
- W. H. Young. On classes of summable functions and their Fourier series. *Proceedings of the Royal Society of London. Series A, Containing Papers of a Mathematical and Physical Character*, 87(594):225–229, 1912. Cited on page 153.





**PhD Dissertations**  
**Division of Automatic Control**  
**Linköping University**

**M. Millnert:** Identification and control of systems subject to abrupt changes. Thesis No. 82, 1982. ISBN 91-7372-542-0.

**A. J. M. van Overbeek:** On-line structure selection for the identification of multivariable systems. Thesis No. 86, 1982. ISBN 91-7372-586-2.

**B. Bengtsson:** On some control problems for queues. Thesis No. 87, 1982. ISBN 91-7372-593-5.

**S. Ljung:** Fast algorithms for integral equations and least squares identification problems. Thesis No. 93, 1983. ISBN 91-7372-641-9.

**H. Jonson:** A Newton method for solving non-linear optimal control problems with general constraints. Thesis No. 104, 1983. ISBN 91-7372-718-0.

**E. Trulsson:** Adaptive control based on explicit criterion minimization. Thesis No. 106, 1983. ISBN 91-7372-728-8.

**K. Nordström:** Uncertainty, robustness and sensitivity reduction in the design of single input control systems. Thesis No. 162, 1987. ISBN 91-7870-170-8.

**B. Wahlberg:** On the identification and approximation of linear systems. Thesis No. 163, 1987. ISBN 91-7870-175-9.

**S. Gunnarsson:** Frequency domain aspects of modeling and control in adaptive systems. Thesis No. 194, 1988. ISBN 91-7870-380-8.

**A. Isaksson:** On system identification in one and two dimensions with signal processing applications. Thesis No. 196, 1988. ISBN 91-7870-383-2.

**M. Viberg:** Subspace fitting concepts in sensor array processing. Thesis No. 217, 1989. ISBN 91-7870-529-0.

**K. Forsman:** Constructive commutative algebra in nonlinear control theory. Thesis No. 261, 1991. ISBN 91-7870-827-3.

**F. Gustafsson:** Estimation of discrete parameters in linear systems. Thesis No. 271, 1992. ISBN 91-7870-876-1.

**P. Nagy:** Tools for knowledge-based signal processing with applications to system identification. Thesis No. 280, 1992. ISBN 91-7870-962-8.

**T. Svensson:** Mathematical tools and software for analysis and design of nonlinear control systems. Thesis No. 285, 1992. ISBN 91-7870-989-X.

**S. Andersson:** On dimension reduction in sensor array signal processing. Thesis No. 290, 1992. ISBN 91-7871-015-4.

**H. Hjalmarsson:** Aspects on incomplete modeling in system identification. Thesis No. 298, 1993. ISBN 91-7871-070-7.

**I. Klein:** Automatic synthesis of sequential control schemes. Thesis No. 305, 1993. ISBN 91-7871-090-1.

**J.-E. Strömberg:** A mode switching modelling philosophy. Thesis No. 353, 1994. ISBN 91-7871-430-3.

**K. Wang Chen:** Transformation and symbolic calculations in filtering and control. Thesis No. 361, 1994. ISBN 91-7871-467-2.

**T. McKelvey:** Identification of state-space models from time and frequency data. Thesis No. 380, 1995. ISBN 91-7871-531-8.

**J. Sjöberg:** Non-linear system identification with neural networks. Thesis No. 381, 1995. ISBN 91-7871-534-2.

**R. Germundsson:** Symbolic systems – theory, computation and applications. Thesis No. 389, 1995. ISBN 91-7871-578-4.

**P. Pucar:** Modeling and segmentation using multiple models. Thesis No. 405, 1995. ISBN 91-7871-627-6.

**H. Fortell:** Algebraic approaches to normal forms and zero dynamics. Thesis No. 407, 1995. ISBN 91-7871-629-2.

**A. Helmersson:** Methods for robust gain scheduling. Thesis No. 406, 1995. ISBN 91-7871-628-4.

**P. Lindskog:** Methods, algorithms and tools for system identification based on prior knowledge. Thesis No. 436, 1996. ISBN 91-7871-424-8.

**J. Gunnarsson:** Symbolic methods and tools for discrete event dynamic systems. Thesis No. 477, 1997. ISBN 91-7871-917-8.

**M. Jirstrand:** Constructive methods for inequality constraints in control. Thesis No. 527, 1998. ISBN 91-7219-187-2.

**U. Forssell:** Closed-loop identification: Methods, theory, and applications. Thesis No. 566, 1999. ISBN 91-7219-432-4.

**A. Stenman:** Model on demand: Algorithms, analysis and applications. Thesis No. 571, 1999. ISBN 91-7219-450-2.

**N. Bergman:** Recursive Bayesian estimation: Navigation and tracking applications. Thesis No. 579, 1999. ISBN 91-7219-473-1.

**K. Edström:** Switched bond graphs: Simulation and analysis. Thesis No. 586, 1999. ISBN 91-7219-493-6.

**M. Larsson:** Behavioral and structural model based approaches to discrete diagnosis. Thesis No. 608, 1999. ISBN 91-7219-615-5.

**F. Gunnarsson:** Power control in cellular radio systems: Analysis, design and estimation. Thesis No. 623, 2000. ISBN 91-7219-689-0.

**V. Einarsson:** Model checking methods for mode switching systems. Thesis No. 652, 2000. ISBN 91-7219-836-2.

**M. Norrlöf:** Iterative learning control: Analysis, design, and experiments. Thesis No. 653, 2000. ISBN 91-7219-837-0.

**F. Tjärnström:** Variance expressions and model reduction in system identification. Thesis No. 730, 2002. ISBN 91-7373-253-2.

**J. Löfberg:** Minimax approaches to robust model predictive control. Thesis No. 812, 2003. ISBN 91-7373-622-8.

**J. Roll:** Local and piecewise affine approaches to system identification. Thesis No. 802, 2003. ISBN 91-7373-608-2.

**J. Elbornsson:** Analysis, estimation and compensation of mismatch effects in A/D converters. Thesis No. 811, 2003. ISBN 91-7373-621-X.

**O. Härkegård:** Backstepping and control allocation with applications to flight control. Thesis No. 820, 2003. ISBN 91-7373-647-3.

**R. Wallin:** Optimization algorithms for system analysis and identification. Thesis No. 919, 2004. ISBN 91-85297-19-4.

**D. Lindgren:** Projection methods for classification and identification. Thesis No. 915, 2005. ISBN 91-85297-06-2.

**R. Karlsson:** Particle Filtering for Positioning and Tracking Applications. Thesis No. 924, 2005. ISBN 91-85297-34-8.

**J. Jansson:** Collision Avoidance Theory with Applications to Automotive Collision Mitigation. Thesis No. 950, 2005. ISBN 91-85299-45-6.

**E. Geijer Lundin:** Uplink Load in CDMA Cellular Radio Systems. Thesis No. 977, 2005. ISBN 91-85457-49-3.

**M. Enqvist:** Linear Models of Nonlinear Systems. Thesis No. 985, 2005. ISBN 91-85457-64-7.

**T. B. Schön:** Estimation of Nonlinear Dynamic Systems — Theory and Applications. Thesis No. 998, 2006. ISBN 91-85497-03-7.

**I. Lind:** Regressor and Structure Selection — Uses of ANOVA in System Identification. Thesis No. 1012, 2006. ISBN 91-85523-98-4.

**J. Gillberg:** Frequency Domain Identification of Continuous-Time Systems Reconstruction and Robustness. Thesis No. 1031, 2006. ISBN 91-85523-34-8.

**M. Gerdin:** Identification and Estimation for Models Described by Differential-Algebraic Equations. Thesis No. 1046, 2006. ISBN 91-85643-87-4.

**C. Grönwall:** Ground Object Recognition using Laser Radar Data – Geometric Fitting, Performance Analysis, and Applications. Thesis No. 1055, 2006. ISBN 91-85643-53-X.

**A. Eidehall:** Tracking and threat assessment for automotive collision avoidance. Thesis No. 1066, 2007. ISBN 91-85643-10-6.

**F. Eng:** Non-Uniform Sampling in Statistical Signal Processing. Thesis No. 1082, 2007. ISBN 978-91-85715-49-7.

**E. Wernholt:** Multivariable Frequency-Domain Identification of Industrial Robots. Thesis No. 1138, 2007. ISBN 978-91-85895-72-4.

**D. Axehill:** Integer Quadratic Programming for Control and Communication. Thesis No. 1158, 2008. ISBN 978-91-85523-03-0.

**G. Hendeby:** Performance and Implementation Aspects of Nonlinear Filtering. Thesis No. 1161, 2008. ISBN 978-91-7393-979-9.

**J. Sjöberg:** Optimal Control and Model Reduction of Nonlinear DAE Models. Thesis No. 1166, 2008. ISBN 978-91-7393-964-5.

**D. Törnqvist:** Estimation and Detection with Applications to Navigation. Thesis No. 1216, 2008. ISBN 978-91-7393-785-6.

**P-J. Nordlund:** Efficient Estimation and Detection Methods for Airborne Applications. Thesis No. 1231, 2008. ISBN 978-91-7393-720-7.

**H. Tidfelt:** Differential-algebraic equations and matrix-valued singular perturbation. Thesis No. 1292, 2009. ISBN 978-91-7393-479-4.

**H. Ohlsson:** Regularization for Sparseness and Smoothness — Applications in System Identification and Signal Processing. Thesis No. 1351, 2010. ISBN 978-91-7393-287-5.

**S. Moberg:** Modeling and Control of Flexible Manipulators. Thesis No. 1349, 2010. ISBN 978-91-7393-289-9.

**J. Wallén:** Estimation-based iterative learning control. Thesis No. 1358, 2011. ISBN 978-91-7393-255-4.

**J. D. Hol:** Sensor Fusion and Calibration of Inertial Sensors, Vision, Ultra-Wideband and GPS. Thesis No. 1368, 2011. ISBN 978-91-7393-197-7.

**D. Ankelhed:** On the Design of Low Order H-infinity Controllers. Thesis No. 1371, 2011. ISBN 978-91-7393-157-1.

**C. Lundquist:** Sensor Fusion for Automotive Applications. Thesis No. 1409, 2011. ISBN 978-91-7393-023-9.

**P. Skoglar:** Tracking and Planning for Surveillance Applications. Thesis No. 1432, 2012. ISBN 978-91-7519-941-2.

**K. Granström:** Extended target tracking using PHD filters. Thesis No. 1476, 2012. ISBN 978-91-7519-796-8.

**C. Lyzell:** Structural Reformulations in System Identification. Thesis No. 1475, 2012. ISBN 978-91-7519-800-2.

**J. Callmer:** Autonomous Localization in Unknown Environments. Thesis No. 1520, 2013. ISBN 978-91-7519-620-6.

**D. Petersson:** A Nonlinear Optimization Approach to H2-Optimal Modeling and Control. Thesis No. 1528, 2013. ISBN 978-91-7519-567-4.

**Z. Sjanic:** Navigation and Mapping for Aerial Vehicles Based on Inertial and Imaging Sensors. Thesis No. 1533, 2013. ISBN 978-91-7519-553-7.

**F. Lindsten:** Particle Filters and Markov Chains for Learning of Dynamical Systems. Thesis No. 1530, 2013. ISBN 978-91-7519-559-9.

**P. Axelsson:** Sensor Fusion and Control Applied to Industrial Manipulators. Thesis No. 1585, 2014. ISBN 978-91-7519-368-7.

**A. Carvalho Bittencourt:** Modeling and Diagnosis of Friction and Wear in Industrial Robots. Thesis No. 1617, 2014. ISBN 978-91-7519-251-2.

**M. Skoglund:** Inertial Navigation and Mapping for Autonomous Vehicles. Thesis No. 1623, 2014. ISBN 978-91-7519-233-8.

**S. Khoshfetrat Pakazad:** Divide and Conquer: Distributed Optimization and Robustness Analysis. Thesis No. 1676, 2015. ISBN 978-91-7519-050-1.

**T. Ardehshiri:** Analytical Approximations for Bayesian Inference. Thesis No. 1710, 2015. ISBN 978-91-7685-930-8.

**N. Wahlström:** Modeling of Magnetic Fields and Extended Objects for Localization Applications. Thesis No. 1723, 2015. ISBN 978-91-7685-903-2.

**J. Dahlin:** Accelerating Monte Carlo methods for Bayesian inference in dynamical models. Thesis No. 1754, 2016. ISBN 978-91-7685-797-7.

**M. Kok:** Probabilistic modeling for sensor fusion with inertial measurements. Thesis No. 1814, 2016. ISBN 978-91-7685-621-5.

**J. Linder:** Indirect System Identification for Unknown Input Problems: With Applications to Ships. Thesis No. 1829, 2017. ISBN 978-91-7685-588-1.

**M. Roth:** Advanced Kalman Filtering Approaches to Bayesian State Estimation. Thesis No. 1832, 2017. ISBN 978-91-7685-578-2.

**I. Nielsen:** Structure-Exploiting Numerical Algorithms for Optimal Control. Thesis No. 1848, 2017. ISBN 978-91-7685-528-7.

**D. Simon:** Fighter Aircraft Maneuver Limiting Using MPC: Theory and Application. Thesis No. 1881, 2017. ISBN 978-91-7685-450-1.

**C. Veibäck:** Tracking the Wanders of Nature. Thesis No. 1958, 2018. ISBN 978-91-7685-200-2.

**C. Andersson Naesseth:** Machine learning using approximate inference: Variational and sequential Monte Carlo methods. Thesis No. 1969, 2018. ISBN 978-91-7685-161-6.

**Y. Jung:** Inverse system identification with applications in predistortion. Thesis No. 1966, 2018. ISBN 978-91-7685-171-5.

**Y. Zhao:** Gaussian Processes for Positioning Using Radio Signal Strength Measurements. Thesis No. 1968, 2019. ISBN 978-91-7685-162-3.

## **FACULTY OF SCIENCE AND ENGINEERING**

Linköping Studies in Science and Technology, Dissertation No. 1990, 2019  
Department of Electrical Engineering

Linköping University  
SE-581 83 Linköping, Sweden

[www.liu.se](http://www.liu.se)